Development of Rare Earth Free and Rare Earth Balance Permanent Magnets

Permanentmagnete auf Basis von Seltenerd-freien Legierungen und Legierungen mit häufig vorkommenden Seltenen Erden

Zur Erlangung des akademischen Grades Doktor-Ingenieur (Dr.-Ing.)

Genehmigte Dissertation im Fachbereich Material- und Geowissenschaften

von Bahar Fayyazi M. Sc.

Geboren am 13.09.1988 in Teheran

Darmstadt 2021

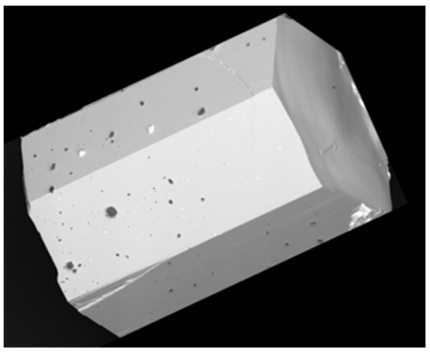

TECHNISCHE UNIVERSITÄT DARMSTADT

FUNKTIONALE MATERIALIEN

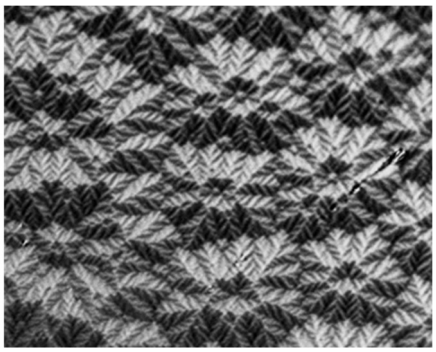

Development of Rare Earth Free and Rare Earth Balance Permanent Magnets

Genehmigte Dissertation im Fachbereich Material- und Geowissenschaften von Bahar Fayyazi

1. Gutachten: Prof. Dr. Oliver Gutfleisch (Technische Universität Darmstadt)
2. Gutachten: Prof. George Hadjipanayis (University of Delaware)

Tag der Einreichung: 14.04.2021
Tag der Prüfung: 02.07.2021

Darmstadt

Bitte zitieren Sie dieses Dokument als:
URN: urn:nbn:de:tuda-tuprints-192081
URL: https://tuprints.ulb.tu-darmstadt.de/id/eprint/19208

Dieses Dokument wird bereitgestellt von tuprints,
E-Publishing-Service der TU Darmstadt
http://tuprints.ulb.tu-darmstadt.de
tuprints@ulb.tu-darmstadt.de

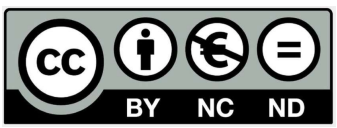

Die Veröffentlichung steht unter folgender Creative Commons Lizenz:
Namensnennung – Keine kommerzielle Nutzung – Keine Bearbeitung 4.0 International

http://creativecommons.org/licenses/by-nc-nd/4.0

Erklärung zur Dissertation

Hiermit erkläre ich, Bahar Fayyazi, dass ich die Vorliegende Dissertation selbstständig verfasst habe und keine anderen als die angegebenen Hilfsmittel verwendet habe. Alle wörtlich oder inhaltliche übernommenen Stellen sind als solche gekennzeichnet.

Ich versichere zudem, dass diese Arbeit in gleicher oder ähnlicher Form keiner Prüfungsbehörde vorgelegt wurde.

Darmstadt den 14.04.2021

Bahar Fayyazi

Abstract

In the quest for a sustainable permanent magnetic material, two material systems were extensively studied. The first part of the thesis investigates the Fe-Sn based systems as potential RE-free candidates. The Fe-Sn binary and several multinary systems such as $(FeX)_5Sn$ and $(FeX)_3(SnY)$ were extensively screened for the discovery of a new hard magnetic material using high-throughput Reactive Crucible Melting (RCM) technique as well as other non-equilibrium methods. The follow-up experimental screening strategies were supported by theoretical calculations carried out by other scientists. For high-throughput characterization, these synthesis techniques were combined with energy dispersive X-ray spectroscopy as well as magneto-optical Kerr microscopy which enabled the identification of phases with uniaxial magnetic anisotropy, for example Fe_3Sn_2 in the binary system. The reliability of the reactive crucible melting method was evaluated by a comparison of the phases forming in the reactive crucible with phases appearing in conventionally melted samples. It has been shown that under some circumstances, the phase relations might not always be correctly reproduced. The Fe_5Sn_3 phase, existing in the equilibrium phase diagram at 800°C and forming in conventionally melted alloys, does not exist in the diffusion zone of the reactive crucible. The problem of "missing phases" is discussed. In addition, by observation of domain structure and by employing different analytical models based on domain theory, the anisotropies of phases with uniaxial anisotropy were evaluated. It has been shown that the consideration of the magnitude of anisotropy is crucial for the selection of a proper model and realistic assessment of anisotropy energy. With the example of materials with high and intermediate uniaxial anisotropy, the applicability of 3 analytical models "Kittel", "Szymczak" and "Bodenberger-Hubert" were investigated.

Another major activity to study the Fe-Sn system was the investigation of structural and intrinsic magnetic properties of its binary ferromagnetic compounds by synthesis and characterization of Fe_3Sn, Fe_5Sn_3, and Fe_3Sn_2 single crystals. Derived from single crystal X-ray diffraction and Transmission Electron Microscopy (TEM), a new structural model is proposed for the Fe_5Sn_3 crystals - the threefold twinning of an orthorhombic unit cell with (3+1) dimensional space group Pbcm(α00)0s0. The spontaneous magnetization (M_s) and the anisotropy constants K_1 and K_2 of Fe_3Sn, Fe_5Sn_3, and Fe_3Sn_2 single crystals were determined in a wide temperature range using *M(H)* dependencies and the Sucksmith-Thompson technique. A large however planar anisotropy of K_1 = -1.16 MJm^{-3} appreciable for a rare earth free system and a negligible uniaxial anisotropy of K_1 = +0.05 MJm^{-3} were evaluated for Fe_3Sn and Fe_3Sn_2 compounds, respectively.

The second part of the thesis investigates the effect of partial substitution of Ce and Co in the Nd-Fe-B system. By synthesis and characterization of $(Nd_{1-x}Ce_x)_2(Fe_{1-y}Co_y)_{14}B$ single crystals, the structural and intrinsic magnetic properties were investigated for y = 0 and x = 0, 0.15, 0.36, 0.63 and 1 as well as y = 0.1 and x = 0 and 0.15. The effect of doping with Ce and Co on crystal lattice parameters a and c, M_s, H_a, T_C, T_{SPT}, and K_1 were evaluated. Additionally, for $Nd_2Fe_{14}B$ and by analysis of single crystal magnetization curves measured under the field of up to 50 T along four different orientations, five associating anisotropy constants were extracted using theoretical models and based on minimization of the total energy of the system.

All intrinsic magnetic properties were gradually decreased by an increase in Ce proportion when it was solely introduced to the structure. Furthermore, Ce substitution resulted in a decrease in spin reorientation transition temperature where anisotropy switches from uniaxial to an easy cone. The addition of Co has not only increased the Curie temperature but also improved the thermal stability of the intrinsic magnetic properties. The reduction of anisotropy energy with Ce substitution could partially be compensated by co-doping together with Co, especially at high temperatures. The improved intrinsic properties of the co-doped $Nd_2Fe_{14}B$ was also reflected in their extrinsic magnetic properties by characterization of mechanochemically synthesized sub-micron particles. For the sample with $(Nd_{0.82}Ce_{0.18})_2(Fe_{0.85}Co_{0.15})_{14}B$ composition, an improved temperature coefficient of coercivity of β = -0.4 %/K was achieved. Comparing these results with single crystal data, it can be verified that the enhanced high-temperature performance of NdFeB-based magnets co-doped with Ce and Co, which have also been observed in various literature, is due to an improvement in intrinsic magnetic properties.

Kurzfassung

Auf der Suche nach einem nachhaltigen permanentmagnetischen Material wurden zwei Materialsysteme eingehend analysiert. Der erste Teil der Arbeit untersucht Fe-Sn-basierte Systeme als potenzielle RE-freie Kandidaten. Das Fe-Sn-Binärsystem und mehrere multinäre Systeme wie $(FeX)_5Sn$ und $(FeX)_3(SnY)$ wurden ausgiebig in Hinblick auf die Entdeckung neuer, hartmagnetischer Materialien untersucht. Verwendet wurde hierfür das kombinatorische reaktive Schmelztiegelverfahren sowie andere Nichtgleichgewichtsmethoden. Die folgenden experimentellen Screening-Strategien wurden durch theoretische Berechnungen anderer Wissenschaftler unterstützt. Zur Hochdurchsatzcharakterisierung wurden diese Synthesemethoden mit energiedispersiver Röntgenspektroskopie sowie magnetooptischer Kerr-Mikroskopie kombiniert, die die Identifizierung von Phasen mit einachsiger magnetokristalliner Anisotropie, beispielsweise Fe_3Sn_2 im binären System, ermöglichte. Die Zuverlässigkeit des reaktiven Schmelztiegelverfahrens wurde durch Vergleich der im Reaktivtiegel gebildeten Phasen mit Phasen bewertet, die in konventionell geschmolzenen Proben auftreten. Es wurde unter bestimmten Umständen gezeigt, dass die Phasenbeziehungen möglicherweise nicht immer korrekt reproduziert werden. Die Fe_5Sn_3-Phase, die sich im Phasendiagramm bei 800°C sowie in konventionell geschmolzenen Legierungen bildet, existiert in der Diffusionszone des Reaktivtiegels nicht. Das Problem der „fehlenden Phasen“ wird diskutiert. Zusätzlich wurde durch Beobachtung der Domänenstruktur und durch Verwendung verschiedener auf der Domänentheorie basierender analytischer Modelle, die Anisotropie von Phasen mit uniaxialer Anisotropie bewertet. Es zeigte sich, dass die Berücksichtigung der Größe der Anisotropie für die Auswahl eines geeigneten Modells und die realistische Bewertung der Anisotropieenergie von entscheidender Bedeutung ist. Am Beispiel von Materialien mit hoher und mittlerer uniaxialer Anisotropie wurde die Anwendbarkeit von drei analytischen Modellen, „Kittel“, „Szymczak“ und „Bodenberger-Hubert“ untersucht.

Um die strukturellen und intrinsischen magnetischen Eigenschaften von binären ferromagnetischen Fe-Sn-Phasen zu untersuchen, wurden einkristalline Proben von Fe_3Sn, Fe_5Sn_3, und Fe_3Sn_2 hergestellt und charakterisiert. Abgeleitet von Einkristall-Röntgenbeugung und Transmissionselektronenmikroskopie (TEM) wird ein neues Strukturmodell für die Fe_5Sn_3-Kristalle

aufgestellt - die dreifache Zwillingsbildung einer orthorhombischen Einheitszelle mit (3 + 1) dimensionaler Raumgruppe Pbcm(α00)0s0. Die spontane Magnetisierung (M_s) und die Anisotropie Konstanten K_1 und K_2 von Fe_3Sn, Fe_5Sn_3, und Fe_3Sn_2-Einkristallen wurden in einem weiten Temperaturbereich bestimmt. Zur Bewertung der Anisotropie Konstanten wurde das Sucksmith-Thompson-Modell verwendet. Für die Fe_3Sn-Phase wurde eine große, jedoch planare Anisotropie von K_1 = -1,16 MJm^{-3}, die für ein Seltenerd-freies System beachtlich ist und für Fe_3Sn_2 eine vernachlässigbare uniaxiale Anisotropie von K_1 = +0,05 MJm^{-3} bewertet.

Der zweite Teil der Arbeit untersucht den Effekt der partiellen Substitution von Ce und Co im Nd-Fe-B-System. Durch Synthese und Charakterisierung von $(Nd_{1-x}Ce_x)_2(Fe_{1-y}Co_y)_{14}B$ -Einkristallen wurden die strukturellen und intrinsischen magnetischen Eigenschaften für y = 0 und x = 0, 0,15, 0,36, 0,63 und 1 sowie y = 0,1 und x = 0, 0,15 untersucht. Der Einfluss der Dotierung mit Ce und Co auf die Kristallgitterparameter a und c, M_s, H_a, T_C, T_{SPT} und K_1 wurde bewertet. Zusätzlich wurden für $Nd_2Fe_{14}B$ fünf assoziierende Anisotropie Konstanten extrahiert. Hierfür wurden unter Verwendung theoretischer Modelle und basierend auf der Minimierung der Gesamtenergie des Systems Einkristall-Magnetisierungskurven analysiert, die unter einem Feld von bis zu 50 T entlang vier verschiedener Orientierungen gemessen wurden.

Alle intrinsischen magnetischen Eigenschaften wurden durch eine Erhöhung des Ce-Anteils kontinuierlich verringert. Darüber hinaus führte die Ce-Substitution zu einer Abnahme der Spin-Umuorientierungs-Übergangstemperatur, bei der sich der Anisotropietyp von „leichte Achse“ zu „leichter Kegel“ ändert.

Die Zugabe von Co erhöhte nicht nur die Curie-Temperatur, sondern verbesserte auch die thermische Stabilität anderer intrinsischer magnetischer Eigenschaften. Die Verringerung der Anisotropieenergie durch Ce-Substitution konnte teilweise durch co-Dotierung mit Co kompensiert werden, insbesondere bei höheren Temperaturen. Die verbesserten intrinsischen Eigenschaften des co-dotierten $Nd_2Fe_{14}B$ spiegelten sich auch in ihren extrinsischen magnetischen Eigenschaften durch Charakterisierung mechanochemisch synthetisierter Submikron-Partikel wieder. Für die Probe mit einer Zusammensetzung von $(Nd_{0.82}Ce_{0.18})_2(Fe_{0.85}Co_{0.15})_{14}B$ konnte ein verbesserter Temperaturkoeffizient der Koerzitivfeldstärke von β = -0,4 %/K erzielt werden. Wenn diese Ergebnisse mit Einkristalldaten verglichen werden, kann geschlossen werden, dass die verbesserte Hochtemperaturleistung von den mit Ce und Co co-dotierten Magneten auf NdFeB-Basis, die auch in verschiedenen Literaturstellen beobachtet wurden, auf eine Verbesserung der intrinsischen Eigenschaften zurückzuführen ist.

Table of content

List of figures

List of tables

List of abbreviations

BSE	Back-Scattered Electron
CEF	Crystal Electric Field
DAM	Dual Alloy Method
DFT	Density Functional Theory
EA	Easy Axis
EDX	Energy Dispersive X-ray spectroscopy
EELS	Electron Energy Loss Spectroscopy
FIB	Focused Ion Beam
FOMP	First Order Magnetization Process
GB	Grain Boundary
HA	Hard Axis
HAADF	High Angle Annular Dark Field
HEBM	High Energy Ball Milling
HRE	Heavy Rare Earth
LED	Light Emitting Diodes
LRE	Light Rare Earth
MAE	Magnetocrystalline Anisotropy Energy
MFM	Magnetic Force Microscopy
MOKE	Magneto-Optical Kerr Effect magnetometry
OMA	Orbital Moment Anisotropy
PLL	Phase-Lock-Loop
PPMS	Physical Property Measurement System
RCM	Reactive Crucible Melting
RE	Rare Earth
SE	Secondary Electron
SEM	Scanning Electron Microscope
SRT	Spin Reorientation Transition
STEM	Scanning Transmission Electron Microscope
TEM	Transmission Electron Microscope
TM	Transition Metal
VSM	Vibrating Sample Magnetometry
XRD	X-Ray Diffraction

List of symbols

A	exchange stiffness
a, b, c	lattice parameters
$(BH)_{max}$	maximum energy product
B_n^m	CEF parameters
D	magnetic domain width
$D(E_f)$	density of state at fermi level
D_b	basic domain width
d_c	critical single domain particle size
D_s	surface domain width
E	electric field
E_a	anisotropy energy
E_d	magnetostatic energy
E_{ex}	exchange energy
E_Z	Zeeman energy
g	Landé factor
H	magnetic field
H_a	anisotropy field
H_c	coercivity
H_{CEF}	crystal electric field Hamiltonian
H_{cr}	critical magnetic field
H_d	demagnetizing field
H_{ext}	external magnetic field
J	total angular momentum
J_{ex}	exchange integral
K	magnetocrystalline anisotropy
K_B	Boltzmann constant
K_d	stray field energy coefficient
K_i	anisotropy constants
L	magnetic domain thickness
L_s	critical magnetic domain thickness
m	magnetization
M_s	spontaneous magnetization

N	demagnetization factor
O_n^m	Stevens equivalent operator
Q	quality factor
r_n	orbital radius with order n
s	spin quantum number
T_C	Curie temperature
T_f	spin glass transition temperature
T_m	melting temperature
T_{SRT}	spin reorientation transition temperature
V	volume
V_{lor}	Lorentz force
α_J, β_J, γ_J	Stevens factor θ_n with n = 2, 4, 6, respectively
β	Temperature coefficient of coercivity
θ	angle between magnetization and easy magnetization direction
θ_n	Stevens factor
μ^*	rotational permeability
μ_0	permeability constant of the vacuum
μ_B	Bohr magneton
μ_{eff}	effective magnetic moment
Φ	angle between external magnetic field and easy magnetization direction
γ	domain wall energy
σ	domain wall width
φ	angle between magnetization and basal plane

1. Introduction

High-performance permanent magnets are critical components for modern energy technologies such as wind turbines and electro-mobility. Certain conditions must be satisfied for a perspective material for permanent magnetic applications considering its intrinsic magnetic properties. These conditions are 1) large saturation magnetization 2) high Curie temperature and 3) strong magnetic anisotropy of easy-axis type. Most promising properties are found in Rare Earth (RE) content compounds as can be seen in Figure 1-1, summarizing the room temperature saturation magnetization and anisotropy field of some hard-magnetic materials. Among all materials, those based on the $Nd_2Fe_{14}B$ compound currently dominate the world's high-performance magnet market. Since the discovery of $Nd_2Fe_{14}B$ which dates back to 37 years ago, intensive studies have been carried out for turning the excellent intrinsic properties of this compound to desirable extrinsic properties i.e. high remanence and coercivity (Herbst 1991). The performance of hard magnets is generally described in terms of energy product BH_{max} which is the key figure of merit of the permanent magnets (Gutfleisch 2011). Figure 1-2 shows the temperature evolution of some permanent magnets' energy products illustrating although NdFeB magnets are leading materials at low temperatures however their performance drops steeply by temperature. The temperature stability of the compound can be increased by addition of Heavy Rare Earth (HRE) elements such as Dy and Tb which are considered highly critical (Coey 2012, Gutfleisch 2011).

Due to the chemical similarity of the RE elements, they are found and mined together. Accordingly, their separation and overall process of RE extraction are extremely complex and expensive (especially for HRE). This process has brought not only economic problems but also leads to severe environmental and ecological problems because of utilizing strong and toxic acids for RE extraction and contamination of waste products of RE ores with radioactive elements such as Th and U. Another important issue which also causes a critical condition for RE elements is the monopolistic position of China in supplying world's rare earth elements. Although RE element reserves are distributed throughout the world (China has only 50% of the world's reserves), however, due to their lower ecological standards and lower cost operations, China supplies more than 95% of the world's RE (EU-Commission 2017). This precarious situation has put the non-Chinese world in trouble as in 2010 China has started to limit its RE exports due to growing domestic consumption and trade restrictions. Consequently, the RE prices were drastically increased by the factor of 10 within a few months.

Although since 2011 the RE prices did not change dramatically, there have been always fluctuations associating with China's politics. Along with continuously growing worldwide RE demand which by keeping the current trade is predicted to exceed the RE supply by the end of this decade (Mancheri 2019), it is indispensable to search for a new material. For screening through a large number of yet unexamined material compositions, conventionally used one-alloy-at-a-time synthesis methods need to be replaced by other experimental techniques i.e. high-throughput and combinatorial methods aiming to drastically increase the efficiency of synthesis, optimization and characterization of new materials. In this thesis, the bulk combinatorial Reactive Crucible Melting (RCM) synthesis technique is combined with Scanning Electron Microscopy (SEM) and Kerr microscopy for high-throughput

identification of uniaxial ferromagnetic phases with desirable hard magnetic properties assignable from quantitative analysis of their domain patterns.

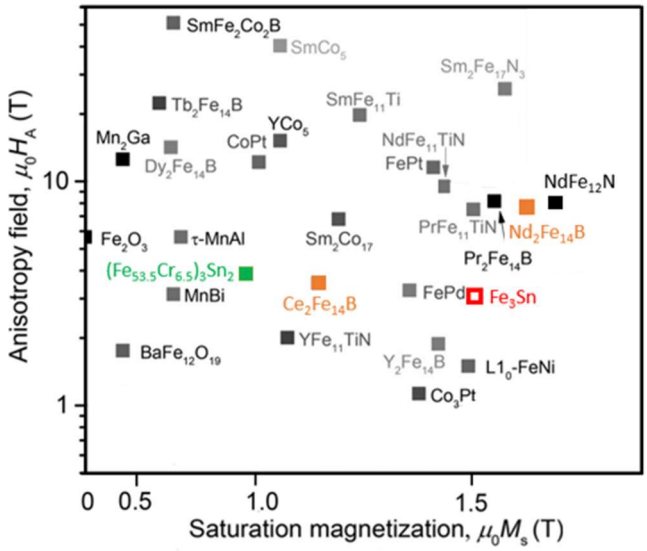

Figure 1-1. The intrinsic magnetic properties of some promising intermetallic compounds (Hirayama 2017). The materials investigated in this thesis are colored. The motivation for studying Fe-Sn compounds comes from the interesting reported properties for (Fe,Cr)$_3$Sn$_2$ in (Goll 2015) and for Fe$_3$Sn in (Sales 2014). The open square denotes the planar anisotropy of the Fe$_3$Sn compound.

In order to select a proper material for developing new permanent magnets - considering the RE supply chain vulnerabilities, two strategies were followed in this thesis.

1) Discovery of new materials which do not rely on RE elements (RE free magnets)

To ensure high magnetic moment and high T_C in RE-free hard magnetic material, including a large concentration of Transition Metals (TM) e.g. Fe, Co, Ni and Mn is essential. However, achieving a sufficiently strong easy-axis anisotropy in Fe (Co)-rich materials most often is not feasible due to the relatively small spin-orbit coupling of 3d metals in comparison to the REs. Moreover, due to a large crystal field, the orbital angular momentum of 3d electrons are usually quenched. There are only a few exceptions in 3d-rich compounds, which show large Magnetocrystalline Anisotropy Energy (MAE) which are shown in Figure 1-2.

The Fe-Sn ferromagnetic compounds Fe$_3$Sn, Fe$_5$Sn$_3$, and Fe$_3$Sn$_2$ have been reported to be potential candidates for permanent magnetic applications. In addition to possessing high Curie temperature (T_C > 600 K), as highlighted in Figure 1-1, promising properties are referred to Fe$_3$Sn$_2$ compound with small Cr substitution by analysis of its domain structure (Goll 2015, Goll 2018) and to Fe$_3$Sn compound by measuring oriented powder samples. However, a precise investigation of magnetocrystalline anisotropy, which requires a magnetization measurement on high-quality single crystals along different crystallographic orientations, has not been done prior to this work (Fayyazi 2019). Although Fe$_3$Sn shows an undesirable easy plane anisotropy, by combining theoretical calculations and experimental methods, the effect of different alloying elements for turning the anisotropy from planar

to uniaxial was investigated (Vekilova *-and Fayyazi* 2019). Furthermore, by DFT high-throughput screening through Fe-Sn binary system, potential hard magnetic candidate phases which may be stabilized upon alloying were identified (Fayyazi 2019). Among them, the theoretically predicted Fe_5Sn phase was extensively searched to be stabilized experimentally using the RCM method as well as non-equilibrium methods such as rapidly quenching and high energy ball milling techniques. Furthermore, the reliability and applicability of the RCM method for constructing the phase relations were evaluated by comparison of the phase composition forming in the reactive crucible with phases appearing in conventionally melted samples and with the phases represented in the reported Fe-Sn phase diagram (Fayyazi 2017). I also examined the authenticity of magnetic domain analysis for the assessment of magnetocrystalline anisotropy using different analytical models as it is the main strength of the RCM method for the discovery of potential hard magnetic compounds.

2) Development of materials with less critical/less demanded RE elements (RE lean magnets)

The world's most demanded RE elements are Nd, Pr, Dy, Tb, Y, and Eu, which are significantly used to produce magnets and luminescent materials. It is mentioned that RE elements are found together; highly demanded RE with other rare earth elements such as Ce and La. The latter elements are used to a much lesser extent in modern technology and therefore an excess of these elements is currently available which should be consumed. This phenomenon is called *rare earth balance* (Binnemans 2014). At the same time, Ce is the most abundant rare earth element and has the lowest cost among all rare earth elements. Therefore, the development of (Ce-Nd)-based permanent magnets are not only cost-efficient but also is a strategic way to utilize the natural RE resources. At room temperature, the spontaneous magnetization of $Ce_2Fe_{14}B$ is 26% lower than M_s of $Nd_2Fe_{14}B$ phase, the anisotropy field of $Ce_2Fe_{14}B$ is 3 times lower than H_a of $Nd_2Fe_{14}B$, and Curie temperature of $Ce_2Fe_{14}B$ is 424 K whereas for $Nd_2Fe_{14}B$ T_C is 585 K (Herbst 1991). This means that Ce substitution leads to a deterioration of the intrinsic properties in $Nd_2Fe_{14}B$ based compounds. Although substitution of Nd with Ce is believed to be a tradeoff between cost and magnetic properties, however, various studies show that Ce substitution may be advantageous for obtaining desirable extrinsic properties especially when Fe is also partially substituted by Co. A great motivation for co-doping of Ce and Co initiated from a study by Pathak et al. (Pathak 2015) which shows improved temperature stability of (Nd,Ce)(Fe,Co)B melt-spun ribbons, hot pressed and die-upset magnets (Figure 1-2. b). Maybe interesting to note that since 2015 number of publications per year on Ce substitution is more than doubled compared to previous years. Nevertheless, except this thesis, there is no study on measurement of $(NdCe)_2(FeCo)_{14}B$ quinary and quinary single crystals for accurate determination of their intrinsic magnetic properties which was an obstacle for further rational design of this class of materials (Fayyazi 2016, Gómez Eslava *-and Fayyazi* 2021). The obtained intrinsic properties were then compared with the extrinsic properties in mechanochemically synthesized nanoparticles of the very same compositions.

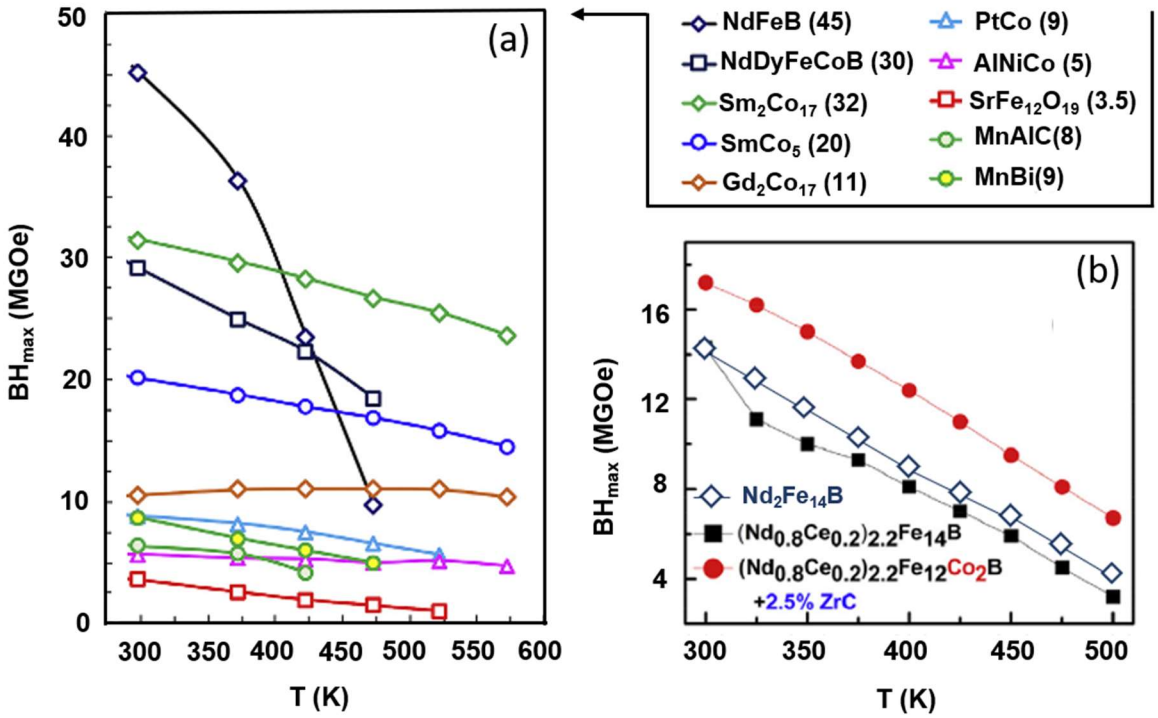

Figure 1-2. The temperature-dependent BH_{max} of (a) some permanent magnets (Cui 2018) and (b) Ce and Co Nd-Fe-B melt-spun ribbons reported in (Pathak 2016, Pathak 2015). The values in parentheses are BH_{max} at room temperature.

2. Fundamental

2.1. Magnetism of ferromagnetic materials

The main challenge in making a permanent magnet is to find a ferromagnetic phase with desirable intrinsic properties which can be turned to good extrinsic properties via proper microstructural design. In ferromagnetism, a spontaneous parallel alignment of adjacent spin moments has resulted from interatomic interactions between electrons. This arrangement occurs below the magnetic ordering temperature, called Curie temperature T_C. To describe magnetism in the nanoscale initially is important to introduce some micromagnetic length scales and parameters. The description of the micromagnetic parameters was taken from various textbooks (Buschow 2003, Coey 2010, Cullity 2008, Hubert 2014, Spaldin 2010).

2.1.1. Micromagnetic length scales and parameters

The strength of the exchange interaction is an important characteristic of a ferromagnetic material. The exchange energy which forces the spin moments to align can be described in a continuum picture as:

$$E_{ex} = \int A(\nabla \vec{m})^2 \, dV \qquad \textit{Equation 1}$$

where $\vec{m}$ is a unit vector in the direction of the magnetization and A is material-specific exchange constant also called exchange stiffness which describes the energy of a ferromagnetic coupling and is given in energy per unit length (J/m). Exchange stiffness is related to the Curie temperature of the material and can be approximated by:

$$A \approx \frac{K_B T_C}{2a} \qquad \textit{Equation 2}$$

here K_B is Boltzmann constant and a is the lattice parameter often in a cubic structure. To calculate A in other structures, the number of atoms in the unit cell should be considered. Determination of A is very important for many micromagnetic analysis such as quantitative characterization of the exchange interaction strength, domain wall width and domain wall energy. The exchange interactions resulted from spin-spin coupling are isotropic however spin of the electrons also couples with orbital momentum (spin-orbit coupling) where orbitals themselves strongly coupled to the lattice (orbit-lattice coupling). These interactions result in an anisotropic resistance of magnetic moments to get rotated from specific crystallographic orientations. The associated energy needed to rotate magnetic moments from its preferred magnetization direction (easy axis) is called Magnetocrystalline Anisotropy Energy (MAE). This energy in dependence of the magnetization angle can be parameterized in terms of anisotropy constants and expressed in terms of a series expansion of the direction cosines of M_s relative to the crystal axes:

$$E_a = K_1 sin^2(\theta) + K_2 sin^4(\theta) + \cdots \qquad \textit{Equation 3}$$

where K_i, i = 1, 2, 3, … are anisotropy constants expressed in J/m^3 and θ is the angle of the magnetization vector to the *c*-axis. More details on the magnetocrystalline anisotropy will be given in 2.2.3.

Another essential energy term acting on a ferromagnet is magnetostatic energy which is the main driving force for the formation of the magnetic domains. This energy is associated with the formation of magnetic stray fields and demagnetizing field on the surface and inside a homogeneously magnetized volume which depends on the shape of the sample. The magnetostatic energy can be expressed as a volume integral of the demagnetizing field H_d and the magnetization M.

$$E_d = -1/2 \int \mu_0 H_d M \, dV \qquad \textit{Equation 4}$$

The introduced micromagnetic energies, exchange, magnetocrystalline anisotropy and magnetostatic energy are always present in a ferromagnet while there are other energy terms which might contribute to the total free energy such as magnetostriction and Zeeman energy. The potential energy of a magnetized body under an external magnetic field is described as Zeeman energy:

$$E_Z = -\mu_0 \int_{Sample} M H_{ext} dV \qquad \textit{Equation 5}$$

here H_{ext} is the external magnetic field and M is the local magnetization. Since the minimization of the total energy is always favored in thermodynamics, using the introduced energy terms, many important micromagnetic parameters can be explored which are closely related to the concept of formation of magnetic domains which is the main focus of the next section.

2.1.2. Magnetic domains

The concept of magnetic domains is historically first introduced to explain why two pieces of Iron do not attract to each other. In 1907, Pierre-Ernest Weiss suggested the existence of regions with aligned magnetic moments (domains) which are oriented differently in the volume leading to the loss of net magnetization. In anisotropic magnetic materials, the domains align along the easy axes. Formation of magnetic domains is mainly in order to minimize the energy terms such as magnetostatic, exchange and anisotropy energies. As long as magnetic poles are created in the magnet, there is a stray field generated outside of it. The stray fields store a large amount of magnetostatic energy which should be reduced by the division of large uniformly magnetized regions into small ones. Splitting of the uniformly magnetized sample into domains associates with the formation of thin regions called domain walls where the magnetization rotates from one easy direction to another. Formation of the domains continues until the domain wall energy exceeds the saved magnetostatic energy and consequently, minimum energy can be achieved only with a specific number of domains within a specimen. The domain structure was first calculated quantitively by Landau and Lifshitz, can be regarded as the starting point of domain theory (Landau 1935). Depending on the rotation direction of magnetic moments with respect to domain wall - parallel or perpendicular, the domain wall is regarded as Bloch or Néel wall, respectively. Formation of the Bloch wall is more favorable in the bulk samples as it does

not create any stray fields within the wall. Figure 2-1 depicts the formation of 180° Bloch domain wall separating two magnetic domains. The energy associating with the formation of this kind of domain wall can be calculated as:

$$\gamma = 4\sqrt{AK} \qquad \textit{Equation 6}$$

where *A* is the material exchange stiffness and *K* is its magnetocrystalline anisotropy.

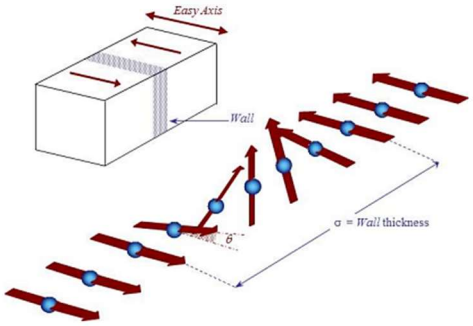

Figure 2-1. Schematic representation of a 180° domain wall adapted from (Cullity 2008)

The width of the domain wall is a consequence of the equilibrium between two competitive energies, anisotropy energy and exchange energy. Anisotropy energy tends to keep the magnetization along with the easy direction and therefore decreases the wall thickness. On the other hand, exchange energy which is resulted from an interaction between different spin orientations tends to elongate the domain width in order to minimize its energy. According to this energy balance, the resulting domain wall width can be calculated as:

$$\sigma = \pi\sqrt{\frac{A}{K}} \qquad \textit{Equation 7}$$

As mentioned, only an optimized size of the magnetic domain leads to the minimization of the total energy. Accordingly, different analytical domain models are developed to determine the formed domain pattern and size. The simplest models are developed for materials with uniaxial anisotropy. Figure 2-2 shows the domain pattern forming in a uniaxial material with a small, moderate, and strong degree of anisotropy which can be expressed by an important dimensionless quantity known as quality factor *Q:*

$$Q = \frac{K}{K_d} = \frac{2K}{\mu_0 M_s^2} \qquad \textit{Equation 8}$$

Q is the ratio between the anisotropy energy coefficient *K* and the stray field energy coefficient K_d. The quality factor is most often used for the classification of materials in the micromagnetic analysis. For materials with large uniaxial anisotropy (permanent magnetic materials $Q \geq 1$), Kittel open structure might be most stable where magnetic moments do not deviate from the easy direction and the

structure looks like stripes of alternating magnetization. For material with small uniaxial anisotropy, the Landau model with closure domains are favorable as the surface domains lie in the surface plane to eliminate the magnetostatic energy. For an intermediate range of *Q* values, the resulting domain pattern is complicated and can be the combination of both Kittel and Landau models. Three possible modifications are shown in Figure 2-2 where in (i) comparing to the totally open structure, the stray field is relatively reduced by tilting the magnetization by an angle at the expense of anisotropy energy. Another modification has reduced the closure domain size (ii) and model (iii) has combined (i) and (ii). The latter model describes the domain structure of one of the focus materials of this thesis and therefore will be described in more detail in section 4.3.

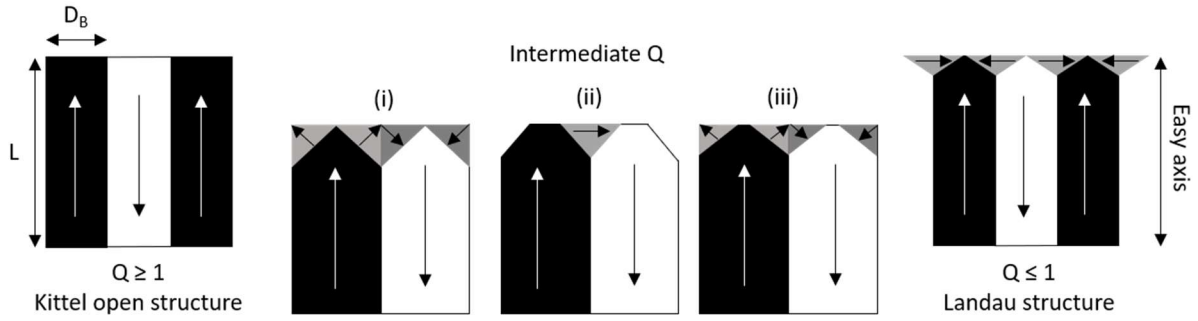

Figure 2-2. Resulting magnetic domain configuration for materials with different quality factors. For materials with relatively small anisotropy, closure structure form at the surface.

As domains are forming to minimize the magnetostatic energy with the expense of domain wall energy, there should be a point in which by decreasing the particle size, these two energy terms are balanced. This means that a single domain state is favorable and one can calculate the single domain particle size, specific to its material properties. For an isolated spherical particle with a uniaxial anisotropy, the single domain particle size can be calculated as:

$$d_c = 18\frac{\gamma}{\mu_0 M_s^2} \qquad \textit{Equation 9}$$

Determination of this quantity is of importance for permanent magnets as the field required to demagnetize a single domain particle in an ideal case associates with a coherent rotation of its magnetic moments (Stoner and Wohlfarth model). This contrasts with other coercivity mechanisms accompanied by nucleation of reversed domains (nucleation type) and pinning of domain wall movement (pinning type). Stoner and Wohlfarth model (Stoner 1948) suggests that to obtain maximum coercivity, the size of grains or particles should be close to the critical single domain and defined the upper limit of coercivity values as $H_c = H_a$. Based on the Stoner-Wohlfarth model, for a uniaxial ellipsoid particle with an easy direction along its major axis and using Equation 3 and Equation 5, the magnetic field energy required to align the magnetization along its hard direction can be written as:

$$E = K_1 \sin^2(\theta) + K_2 \sin^4(\theta) - \mu_0 M_s H_{ext} \cos(\Phi - \theta) \qquad \textit{Equation 10}$$

here, Φ is the angle between the external field and easy axis. By setting $\Phi = \pi/2$ and $\theta = 0$, the anisotropy field can be calculated by minimizing the energy $\frac{\partial E}{\partial \theta} = 0$:

$$H_a = \frac{2K_1 + 4K_2}{\mu_0 M_s} \qquad \textit{Equation 11}$$

In reality, the maximum achievable coercivity is only 20-30% of the theoretical limit (H_a) which this discrepancy is known as Brown paradox.

2.2. Magnetism of rare earth 4f and transition metals 3d electrons

Metallic compounds consisting rare earth elements and 3d transition metals are the main materials for permanent magnet applications. The favorable properties of these compounds such as high magnetization and high Curie temperature are mainly related to 3d sublattice and high magnetocrystalline anisotropy is related to RE sublattice (4f). Therefore, to have all desirable properties, a strong magnetic coupling between both sublattices is required.

2.2.1. Localized vs itinerant magnetism

The electronic configuration of the rare earth elements is $4f^0 5d^1 6s^2$ for La to $4f^{14} 5d^1 6s^2$ for Lu where the 4f shell is getting progressively filled. The radius of the 4f shell is much smaller than the atomic radius and well buried within the higher shells therefore they barely contribute to chemical bonding. Hence, the 4f electrons which carry the magnetic moments are localized and the electronic configuration shows an integral number of electrons. The 4f magnetic moment consists of spin *S* and orbital *L* moments where they couple by spin-orbit interaction to create a total angular momentum *J* and the resulting magnetic moment is proportional to $|L - S| < J < |L + S|$ and the effective magnetic moment can be calculated as $\mu_{eff} = g\mu_B\sqrt{J(J+1)}$ where *g* is the Landé factor and μ_B is Bohr magneton. The spin-orbit interaction is a relativistic effect and increases with the velocity of electrons. Therefore, this effect is generally stronger for heavy atoms due to the higher energy of the orbiting electrons which is a fraction of their rest-mass energy. This interaction is the main origin of the magnetocrystalline anisotropy in RE elements. Contrary to RE where magnetism originates from their localized 4f electrons, in transition metals, the unfilled d shell with delocalized (itinerant) electrons is responsible for magnetism. There, the 3d shell is the outermost shell and contributes to the bonding. The model describing the magnetism of atoms with delocalized electrons is based on the formation of energy bands (band structure). This concept is a starting point for discussing the ferromagnetism in metals such as Fe, Co and Ni which show non-integral values of magnetic moments providing evidence for the itinerant character of their moment carrying electrons. In ferromagnets, in the absence of magnetic fields, spontaneous splitting of spin-up and spin-down sub-bands occurs where part of electrons moves from one sub-band to another. The fulfilling condition for this phenomenon is given by stoner criterion ($ID(E_f) > 1$) which states that the system shows ferromagnetic order when the density of states at the fermi level as well as the atomic exchange integral are both large. The resulting magnetic moment is given by the difference in the integrated density of states and can be non-integer.

The delocalized model corresponds to the magnetism of 3d and 4d metals and also applied to Cerium which can have $4f^0$ or $4f^1$ electron (Coey 2010). This issue will be discussed elsewhere.

As mentioned earlier for transition metals, the 3d shell is the outermost shell of the atom. Therefore, they experience an inhomogeneous crystal electric field produced by ions in the surrounding. For 3d transition metals, the crystal field is much stronger than the spin-orbit coupling. This field causes orbitals to be strongly coupled to the crystal lattice. As a result, they are no longer able to reorient themselves to the applied magnetic field and do not contribute to the resulting magnetic moment. This phenomenon is referred as quenching of orbital angular momentum. As spins are only weekly coupled to the lattice, they contribute to the resulting magnetic moment which can be calculated as $\mu_{eff} = g\mu_B\sqrt{S(S+1)}$.

2.2.2. Exchange interaction

The overlap between charge clouds of two adjacent atoms leads to direct exchange interaction between them. This is particularly the case for 3d metals, due to their large extent of charge cloud. As 3d spins are held aligned to each other (when $J_{ex} > 0$) via strong exchange interactions and only can be disordered by thermal energy, the magnitude of J_{ex} is proportional to Curie temperature. For example, large and positive values of J_{ex} obtained for Fe-Sn ferromagnetic compounds are the reason behind their high Curie temperatures (Vekilova 2019).

In 3d-4f compounds, the exchange interactions are mainly from 3d-3d, 3d-4f and very weakly from 4f-4f interactions. It has been found that 4f-3d exchange interaction is indirect and happens through RE 5d spins which due to their spatially extended orbitals, they hybridize with the TM 3d orbitals antiferromagnetically. As 4f and 5d electrons are coupled by the interatomic exchange interaction ferromagnetically, the spin of RE 4f electrons couples antiferromagnetically with TM 3d spin moment. The delocalized model describes the 3d moments as spin moments however, for 4f moments one must consider both spin moment and orbital moment. For heavy RE, $J = L + S$, meaning that the total 4f moment is also coupled antiparallel to the 3d moment, however for light RE, $J = L - S$ and the total 4f moment couples ferromagnetically to the 3d moment. In 3d-4f compounds, 3d-3d exchange interaction determines the Curie temperature whereas the indirect 3d-4f exchange slightly modifies the Curie temperature also stabilizes the rare earth anisotropy against thermal excitations (Skomski 2009).

2.2.3. Magnetocrystalline anisotropy

The real-space motion of the electrons (orbital moment) is influenced by spin-orbit coupling and also adopts to the crystalline environment (crystal-field interactions). A combined effect of spin-orbit coupling and Crystal Electric Field (CEF) is the source of magnetocrystalline anisotropy of most ferromagnets.

RE-TM intermetallic compounds

For RE-TM compounds, the anisotropy originates mainly from RE sublattice due to its non-zero orbital momentum. For magnetic moment carrying RE metals (except Gd with $L = 0$), the 4f electron charge density is not spherical. This is explained by the single-ion model of anisotropy, which describes that

electrostatic potential acting on RE ions depends on its position in the crystal structure and as a result of crystal-field interaction, particular orbitals become stable and the shape of the 4f charge clouds become non-spherical. These asymmetric 4f charge clouds then orient themselves along particular crystallographic orientations to minimize their electrostatic interactions with the crystal lattice. Eventually, as a consequence of strong spin-orbit coupling of REs, a preferential alignment of spin momentum and accordingly magnetic moment along a specific crystalline direction can be obtained. To analyze the RE-sublattice anisotropy, a Hamiltonian with terms of CEF and exchange is required $H = H_{ex} + H_{CEF}$.

The H_{CEF} can be expressed in terms of CEF parameters B_n^m and the Stevens equivalent operators O_n^m which are the function of the angular momentum operator and they are known for each RE ions (Hutchings 1964).

$$H_{CEF} = \sum B_n^m O_n^m = \theta_n < r_n > A_n^m O_n^m \qquad \textit{Equation 12}$$

For f electrons (l = 3), n cannot exceed 6 and must be even to consider symmetry. CEF parameters B_n^m is different for one RE to another and can be expressed as $\theta_n < r_n > A_n^m$ where θ_n is Stevens factor characterizing each RE element. The notation for θ_n with n = 2, 4, 6 are usually given by α_J, β_J and γ_J, respectively. The shape of the 4f cloud is oblate when $\alpha_J < 0$ and is prolate when $\alpha_J > 0$ and depends only on the quantum number of RE 4f shell (number of f electrons). Figure 2-3 represents the physical meaning of the single-ion model for 4f rare earth ions.

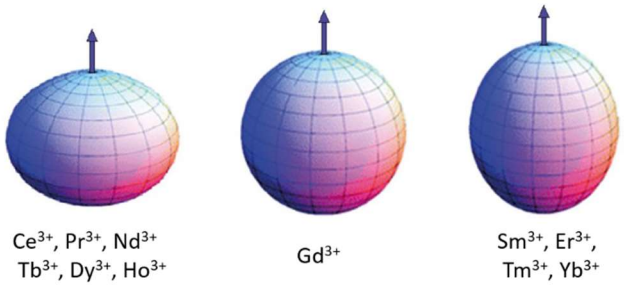

Figure 2-3. Angular distribution of the 4f electron charge density of different rare earth ions (Morgunov 2016)

In Equation 12, $< r_n >$ is the mean value of the 4f radius of order n which is known for each RE (Freeman 1979) . A_n^m is CEF coefficient represents charge distribution in the environment reflecting the strength of crystal-field interaction.

To relate CEF parameters to the macroscopic expression of anisotropy energy and anisotropy constants K_i (Equation 3), in lowest order approximation K_1 and K_2 can be written as (Buschow 2003):

$$K_1 = -3/2\alpha_J r_{4f}^2 A_2^0 < O_2^0 > -5\beta_J r_{4f}^4 A_4^0 < O_4^0 >, \qquad \textit{Equation 13}$$
$$K_2 = -35/8\beta_J r_{4f}^4 A_4^0 < O_4^0 >$$

These equations express the interaction of 4f moments and the electric-field gradient. As 4f charge distribution couples rigidly to the spin by spin-orbit coupling and it depends on the magnetization

angles, therefore a good measure of the magnetocrystalline anisotropy can be obtained by determination of the strength of the crystal field A_n^m at the rare earth site which is related to the macroscopic anisotropy constants K_i.

The anisotropy of 3d sublattice in RE-TM compounds also associates with orbital angular momentum which as explained is very small and often quenched. Due to complications of band structure calculations, the anisotropy of 3d sublattice can be experimentally obtained by magnetic measurement of RE-TM compounds with non-magnetic RE e.g. Y, La and Lu.

RE-free intermetallic compounds

In the absence of RE elements i.e. in RE free compounds, achieving strong magnetic anisotropy is difficult due to orbital angular momentum being quenched in most of the cases. There are a couple of strategies which one might need to consider while developing RE free hard magnetic materials (Kuz'min 2014). Uniaxial anisotropy can be only found in compounds having crystal symmetries lower than cubic otherwise, second-order anisotropy energy is zero. Therefore, a way to obtain magnetocrystalline anisotropy is inducing non-cubicity in cubic structures (e.g. under tension or by alloying). The other strategy considers the increase of Curie temperature, spontaneous magnetization, and anisotropy in most of the materials via volume expansion (e.g. introducing interstitial light elements). Nitrogenation of $Nd(FeX)_{12}$ is a well-known example of this effect which leads to an increase in anisotropy with a factor of 8 (Yang 1991). As already mentioned, spin-orbit coupling is larger for heavier elements. Therefore, a combination of 3d elements which provide high T_C and M_s, with larger non-RE elements might increase the anisotropy. Relatively large magnetocrystalline anisotropy of Fe_3Sn compound is a consequence of its noticeable spin-orbit coupling as reported in (Fayyazi 2019, Vekilova 2019). Other examples are $L1_0$ FePt and MnBi which are also reported as potential RE-free permanent magnetic materials (Cui 2018). Another strategy which is followed in this thesis is searching for a desirable material in a more intelligent way by not using time-consuming conventional synthesis and characterizing routes but by using high-throughput and combinatorial methods which enable synthesis and examination of a large number of systems at the same time.

Magnetocrystalline Anisotropy Energy (MAE)

Depending on crystal symmetry, anisotropy energy can be expressed mathematically as:

$$E_{a,Tet} = K_1 \sin^2\theta + (K_2 + K_2' \cos 4\varphi) \sin^4\theta + (K_3 + K_3' \cos 4\varphi) \sin^6\theta \qquad \textit{Equation 14}$$

$$E_{a,Hex} = K_1 \sin^2\theta + K_2 \sin^4\theta + K_3 \sin^6\theta + K'_3 \sin^6\theta \sin 6\varphi \qquad \textit{Equation 15}$$

for tetragonal and hexagonal symmetry, respectively. In these equations, θ is the angle between the magnetization vector with the *c*-axis and φ is the angle between the projection of magnetization in the Basal plane and the *a*-axis.

The easy magnetization direction can be unique (uniaxial anisotropy) or lie in the lattice plane (easy-plane anisotropy) or can be tilted by any angle from a crystal axis (easy-cone anisotropy). The anisotropy can change its type via a process called spin reorientation transition (SRT) driven by a temperature change. In a compound with multiple sublattices, the competition between favorable anisotropy of the sublattices may change the easy magnetization direction. In RE-TM compounds, the

contribution of RE anisotropy is more pronounced at low temperatures and it drops faster than that of the transition metal sublattice by increasing temperature. Therefore, spin reorientation transition is likely to occur in 3d-4f compounds if the two magnetic sublattices give contributions of opposite signs to the magnetic anisotropy.

By considering the system whose anisotropy energy could be described by the two first anisotropy terms K_1 and K_2 (like most of the cases), anisotropy is uniaxial, cone and planar when:

$K_1 > 0$ and $K_1 > -K_2 \rightarrow \theta = 0$

$K_1 < 0$ and $K_2 > -K_1/2 \rightarrow \theta = sin^{-1}\sqrt{|K_1|/2K_2}$

K_1 and $K_2 < 0$, $K_1 > 0$ and $K_1 < -K_2$, $K_1 < 0$ and $K_2 < -K_1/2 \rightarrow \theta = 90$

These conditions are depicted in Figure 2-4.

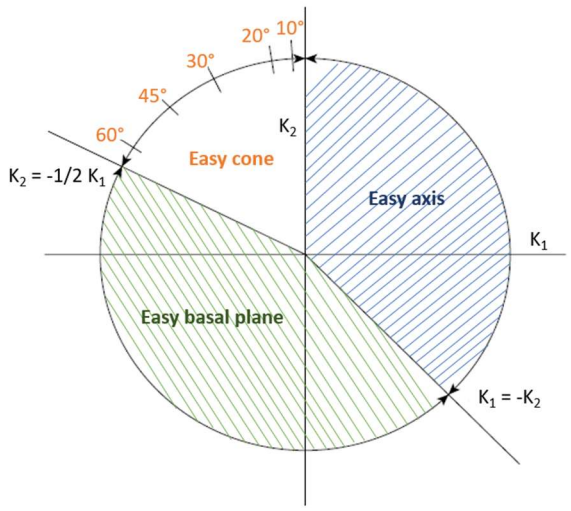

Figure 2-4. The easy magnetization direction for all possible values of K_1 and K_2 in hexagonal crystals. The figure is adapted from (Cullity 2008).

The anisotropy constants and accordingly anisotropy energies can be obtained experimentally by field-dependent magnetization measurement along different crystallographic orientations. The first two anisotropy constants K_1 and K_2 can be deduced by the Sucksmith-Thompson method (Sucksmith 1954) which will be explained in 3.2.4.

2.3. Material systems

To ensure the high performance of a potential permanent magnetic material, the intrinsic magnetic properties of the main phase should be an anisotropy of a uniaxial type with $K_1 > 1$ MJ/m^3, a saturation magnetization of more than 1.5 T (1.2 MA/m) and a Curie temperature greater than 550 K. These properties are more or less met in RE-TM compounds and the main challenge is the development of RE lean materials with a reasonable tradeoff between cost, criticality and properties. For RE free compounds, a high magnetic moment and high T_C can be governed by including a large concentration

of transition metals. However, as discussed achieving a sufficiently strong easy-axis anisotropy in TM-rich materials is quite challenging due to the quenching of orbital angular momenta of 3d electrons. There are only few exceptions in 3d-rich compounds, which show large MAE (Kuz'min 2014). Examples of known RE-free hard magnetic compounds with a desirable anisotropy are MnAl, FeNi, FePt, CoPt and MnBi. However due to various reasons e.g. high expense of Pt, the low magnetization of Mn-based compound and instability of the desired $L1_0$ structure in FeNi, so far none of them could be transferred into industrial applications (Cui 2018). Therefore, the main strategy for finding new 3d-rich phases suitable for permanent magnet application is the screening through a large number of possible compositions and searching among them for materials with desirable intrinsic properties.

2.3.1. The Fe-Sn system

The Fe-Sn binary system consists of 3 ferromagnetic compounds with considerable magnetic properties. The ferromagnetic compounds are Fe_3Sn, Fe_5Sn_3 and Fe_3Sn_2 phases all being metastable at room temperature. It is important to note that the existence of a highly metastable Fe_3Sn compound in the system is overlooked in almost all reported Fe-Sn binary phase diagrams. In this thesis, the phase relations were compared in accordance with the phase diagram reported in (Trehaux 1974) replotted in Figure 2-5. Two phases forming at room temperature are FeSn and Fe_2Sn which are antiferromagnetic and therefore are not of our interest. In the following, the crystal structures and magnetic properties of the three ferromagnetic phases reported in literature are given.

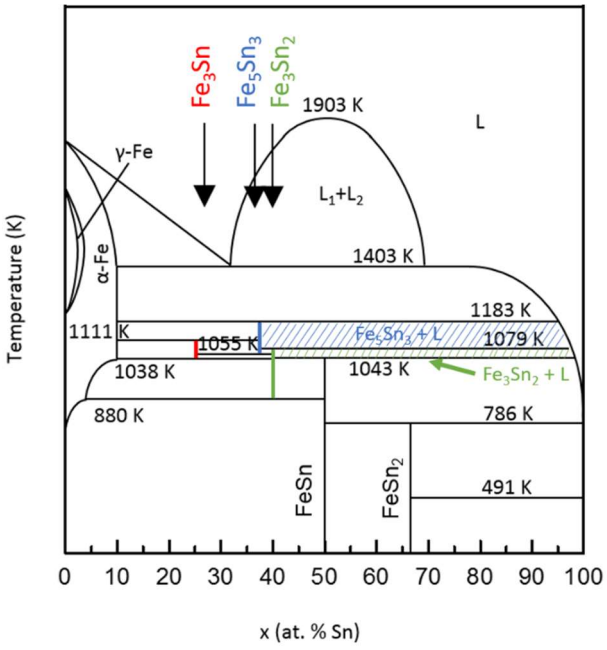

Figure 2-5. Phase diagram of the binary Fe-Sn system adapted from (Trehaux 1974). The dashed regions show the concentration and temperature intervals which could be used for single crystal growing of the Fe_5Sn_3 and Fe_3Sn_2 phases.

Fe_3Sn

The crystal structure of Fe_3Sn (3:1) is Mg_3Cd-type hexagonal in space group $P6_3/mmc$ with lattice parameters of a = 5.464 Å, c = 4.352 Å (Giefers 2006). The phase is stable between 1038 K and 1111 K. An early study with Mössbauer spectroscopy reported a uniaxial anisotropy of the compound (Trumpy 1970), however, later by measuring the oriented powder samples, it has been found that the easy magnetization direction lies in the hexagonal plane with quite different reported anisotropies of K_1 = -1.8 MJm^{-3} in (Sales 2014) and K_1 = -1.29 MJm^{-3} in (Echevarria-Bonet 2018). A precise investigation of magnetocrystalline anisotropy, which requires a magnetization measurement on high-quality single crystals along different crystallographic orientations, has not been reported prior to this thesis. Except for the reported planar anisotropy of the compound, which is not desirable, the rest magnetic properties are promising. The Curie temperature is T_C = 725 K and the saturation magnetization at room temperature is M_s = 1.48 T (Sales 2014). In addition, the large absolute value of magnetocrystalline anisotropy was a driving force for many researchers to investigate possible modifications to tune the anisotropy from planar to uniaxial. Based on theoretical calculations (Sales 2014, Vekilova 2019), tuning of anisotropy from planar to uniaxial is conceivable by alloying Fe_3Sn with Sb, As, Te. In addition, micromagnetic simulations (Fischbacher 2017) suggest that by nanostructuring of the planar Fe_3Sn material, an effective uniaxial anisotropy can be induced and therefore a hard magnetic material can be synthesized.

Fe_5Sn_3

The crystal structure of the Fe_5Sn_3 (5:3) is typically described in hexagonal structure ($P6_3/mmc$, Ni_2In-type) in various literatures (Dianoux 2017, Giefers 2006, Yamamoto 1966) where two Fe atoms occupy 2a sites and two Sn atoms occupy 2c and 2/3 of 2d sides are occupied with rest of Fe atoms (Figure 2-6). It has been reported that depending on heat treatment which leads to vacancy and Fe ordering of 2d sites, superstructure reflections may appear on the diffraction pattern of the sample which cannot be explained by the Ni_2In-type hexagonal structure (Giefers 2006, Sales 2014). The corresponding structural model is fully described for the first time in (Fayyazi 2019). The lattice parameters were reported to be different depending on different annealing temperatures and times. In (Giefers 2006), the lattice parameters vary from a = 4.220 Å and c = 5.246 Å for the sample annealed for 1 day at 1055 K to a = 4.232 and c = 5.227 Å for the sample annealed at 1175 K for 2 days. Furthermore, the Curie temperature is reported to be variable and ranged between 553 K and 632 K. Fe_5Sn_3 phase is stable between 1055 K and 1183 K. This compound has planar anisotropy with -0.35 MJ/m^3 and room temperature magnetization of 0.7 T (Sales 2014).

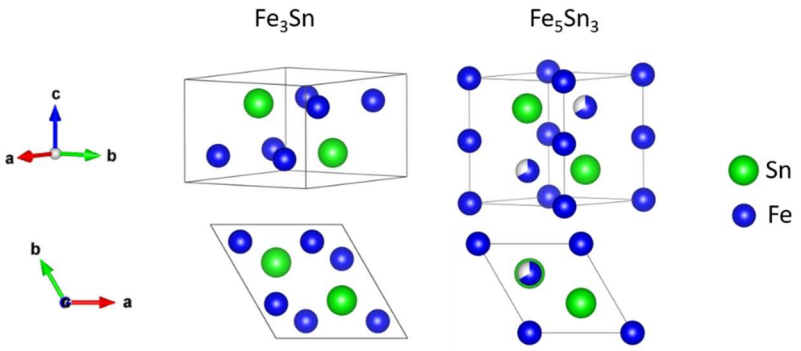

Figure 2-6. The crystal structure of Fe_3Sn (hexagonal-$P6_3/mmc$) and typically reported hexagonal $P6_3/mmc$ structure of Fe_5Sn_3. The crystallographic axes are shown as colored arrows.

Fe_3Sn_2

The Fe_3Sn_2 (3:2) crystallizes in the rhombohedral hR10-type structure (space group R-3m). The Fe atoms form kagomé planes which are made from equilateral triangles with different side lengths. The unit cell parameters are a = 5.340 Å, c = 19.797 Å (Giefers 2006, Trumpy 1970). As a result of its kagomé structure which is a two-dimensional network of corner-sharing triangles (Figure 2-7), Fe_3Sn_2 shows exotic quantum magnetic states which is extensively studied in recent years. The Fe_3Sn_2 phase exhibits many interesting physical properties, such as skyrmions, massive Dirac fermions, flatbands, and a giant topological Hall effect (Hou 2017, Kida 2011, Lin 2020, O'Neill 2019, Pereiro 2015, Wang 2016, Ye 2018). These physical phenomena have made Fe_3Sn_2 a candidate to be used in spintronic applications. The stability range of Fe_3Sn_2 is between 880 K and 1079 K, therefore it is metastable at room temperature. There are contradicting reports on the magnetic behavior of the phase. In (Sales 2014), the anisotropy is wrongly determined to be planar. However, the studies based on Mössbauer spectroscopy (Le Caer 1979, Trumpy 1970) as well as magnetometry (Fenner 2009, Malaman 1978), report the uniaxial anisotropy of the compound where moments lie along the *c* axis below the Curie temperature T_C = 657 K. In addition to high Curie temperature and uniaxial anisotropy, in (Goll 2015, Goll 2018), a considerable anisotropy of 1.7 MJ/m^3 was calculated for Fe_3Sn_2 with small Cr substitution using quantitative analysis of its surface domain structure and the compound is referred to a potential permanent magnetic material. The mentioned Mössbauer studies reported a continuous rotation of the magnetic moments from *c* axis towards the *ab* plane upon cooling below 250 K. However, in (Fenner 2009) by measuring the magnetic susceptibility, rotation of the magnetic moments towards the *ab* plane is reported to start at 520 K where at room temperature, the moment takes a small angle from the *c*-axis. At the same time, the moments are described to be non-collinear based on powder neutron diffraction study and a frustrated itinerant ferromagnetic with a spin glass transition at $T_f \approx 80$ is referred to Fe_3Sn_2 arising from its two-dimensional kagomé bilayer structure (Fenner 2009, Kida 2011).

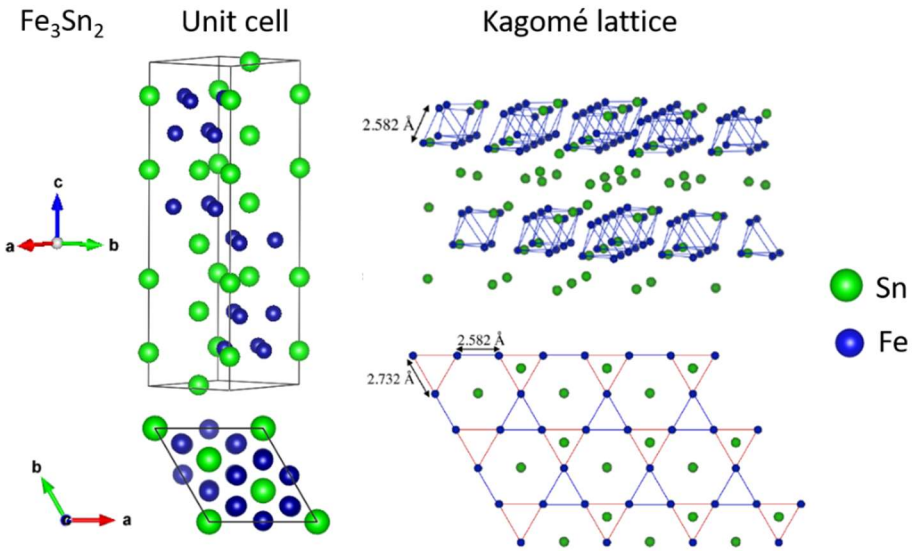

Figure 2-7. Crystal structure of Fe_3Sn_2 with the hR10-type rhombohedral structure. The formation of bilayered kagomé planes by Fe atoms made up of two sized triangles shown in red and blue. The Sn atoms locate within the kagomé planes and between bilayers (O'Neill 2019).

2.3.2. The RE-Fe-B ternary system

The crystal structure of the $Nd_2Fe_{14}B$ (2:14:1) is shown in Figure 2-8. The compound crystallizes in the $P4_2/mnm$ space group and has a tetragonal structure with lattice constants a = 8.80 Å and c = 12.21 Å (Herbst 1984). There exist 4 formula units in each unit cell with a total of 68 atoms. As can be seen in Figure 2-8, the structure has six Fe sites, two Nd sites (so-called 4g and 4f) and one B site which form a layered structure perpendicular to the *c*-axis. Except for Fe c-sites, the rest of Fe atoms form characteristic puckered hexagonal frames in two doubled layers where Nd and B atoms lie in between. All Nd and B atoms together with Fe c-site atoms are placed in z = 0 and z = 1/2. The atomic arrangement on these mirror planes are identical but with $\pi/2$ phase difference around the *c*-axis. Formation of this crystal structure is likely for all alloys consisting of Fe and B and a series of rare earth elements. In the $RE_2Fe_{14}B$ structure, The B atoms bring the thermodynamic stability of the structure.

RE 4f electrons are mainly responsible for magnetocrystalline anisotropy. For $RE_2Fe_{14}B$ with non-zero R moment and RE = Nd, Ce, Pr, Nd, Tb, Dy, Ho, the $K_1 > 0$ and for RE = Sm, Er, Tm and Yb, the resulting $K_1 < 0$ dictated by the single-ion anisotropy of R moments (see Figure 2-3). Those with negative K_1 should be excluded from applicable permanent magnetic materials. Among all $RE_2Fe_{14}B$, RE = Nd has the highest saturation magnetization. Although Fe ions provide most of the material's saturation magnetization (31 μ_B vs 6 μ_B for RE = Nd per f.u.) (Herbst 1991), the RE element also plays an important role. The RE contribution to the total moment of $RE_2Fe_{14}B$ can be estimated in $Y_2Fe_{14}B$ where Y is non-magnetic. To ensure high magnetization, the Fe moments should couple ferromagnetically with RE moments and as discussed already, this is the case for light rare earths whereas they couple antiferromagnetically with heavy RE moments, hence it is of interest to prevent HRE to retain magnetization. Therefore, RE = Tb, Dy and Ho are not of interest due to their resulting small total

magnetization. Hence, the RE candidates which fulfill the necessary conditions for permanent magnetic applications are Nd, Pr and Ce.

As both Nd and Pr are highly demanded RE elements (Pr being less abundant) and as discussed in the introduction, the main goal of the thesis is to substitute Nd with Ce which is not only the most abundant and cheapest RE but according to rare earth balance phenomenon, excess of this element is available to be used. As a result of different valance states of Nd which is trivalent (Nd^{3+}) in $Nd_2Fe_{14}B$ and Ce which shows a mixed state, their magnetism is quite distinct. Ce has only one electron in trivalent state and in metallic compounds, low energy electronic contribution can be often reached when this electron promotes to the conduction band and Ce adopts the tetravalent state Ce^{4+}- $4f^0$. This means that Ce loses its localized 4f electron and correspondingly the rare earth ion anisotropy. To improve intrinsic magnetic properties of $Ce_2Fe_{14}B$, Ce valence state should be favored towards +3 by e.g. proper engineering of the steric volume of Ce sites (Capehart 1993). The intrinsic magnetic properties of $Nd_2Fe_{14}B$ and $Ce_2Fe_{14}B$ compounds are listed in Table 2-1. Fe 3d electrons are also mainly responsible for Curie temperature as a result of delivering ferromagnetic coupling. The much smaller Curie temperatures of all $RE_2Fe_{14}B$ compounds in comparison to α-Fe (T_C = 1050 K) are attributed to strong distance dependence of Fe-Fe exchange energy which is generally shorter than 2.5 Å (the nearest neighbor distance in α-Fe) favoring antiferromagnetic exchange. The change of T_C within $RE_2Fe_{14}B$ compounds is also related to interatomic distances. In addition, for non-zero RE moment, it correlates with Fe-RE moment coupling and is a smooth function of the square root of De Gennes factor $G \equiv (g-1)^2J(J+1)$. The G factor is the effective RE spin and for Ce^{3+} is 0.18 (compare with 1.84 for Nd^{3+}) results in its very small contribution to finite-temperature magnetism and small Curie temperature (Herbst 1991).

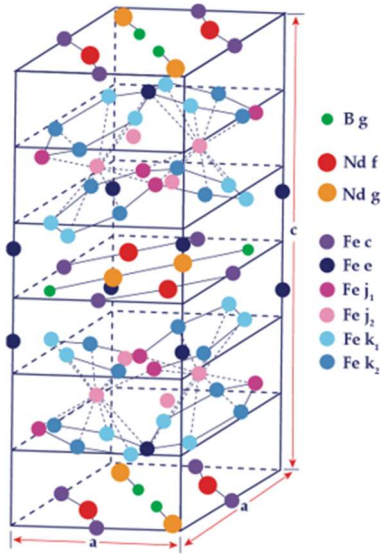

Figure 2-8. Crystal structure of $Nd_2Fe_{14}B$ (Herbst 1984)

To describe the magnetic behavior of $Nd_2Fe_{14}B$ and $Ce_2Fe_{14}B$ at different temperatures, a separate treatment of RE and Fe sublattices is necessary. The resulting appreciable uniaxial anisotropy in $RE_2Fe_{14}B$ with Ce and non-magnetic RE like La and Y, evidence the great contribution of Fe sublattice

anisotropy which favors the *c*-axis as an easy magnetization direction. A much greater anisotropy in these compounds in comparison to elemental Fe shows that the 3d electrons in this structure are not completely quenched. The anisotropy in $Ce_2Fe_{14}B$ remains uniaxial for the whole temperature range. In contrast, the easy magnetization direction in the $Nd_2Fe_{14}B$ compound exhibit a change at T_{SRT} temperature referred as Spin Reorientation Transition (SRT) temperature. At temperatures below T_{SRT} $\sim$ 135 K, the easy magnetization direction takes an angle to the *c*-axis (cants away towards [110] direction) which this angle increases by decreasing temperature to $\sim$ 30° at 4 K. The transition point can be identified by determination of inflection point of low field temperature-dependent magnetization curve. Alternatively, differential scanning calorimetry, heat capacity measurement and temperature-dependent ac susceptibility measurement were used to identify T_{SRT} of different materials.

Table 2-1. Intrinsic magnetic properties of selected $RE_2TM_{14}B$ compounds (Herbst 1991)

Compounds @295 K	$\mu_0 M_s$ (T)	$\mu_0 H_a$ (T)	T_c (K)
$Nd_2Fe_{14}B$	1.60	7.30	585
$Ce_2Fe_{14}B$	1.17	2.60	424
$Nd_2Co_{14}B$	0.81	4.5	1000

RE sublattice contribution to MCA dominates Fe sublattice anisotropy especially at low temperature. At RT and above, the spontaneous magnetization direction with respect to *c* axis can be explained by considering only 2nd order CEF term $B_2^0 O_2^0$, however, at low temperatures higher-order terms in the CEF become more important. As a result of temperature-induced competition between the higher-order CEF terms of Nd ions, their non-collinear arrangement towards perpendicular planes gets more favorable and as a consequence, easy magnetization direction becomes canted. By increasing temperature above T_{SRT}, exchange interactions exceed over CEF interaction favoring the collinear arrangement of Fe and Nd moments (Givord 1984).

Another important magnetic behavior observed in $Nd_2Fe_{14}B$ is the occurrence of the First Order Magnetization Process (FOMP). FOMP is a spontaneous rotation of magnetization vector when a sufficiently high magnetic field is applied along the hard axis. The nature of FOMP is strongly dependent on the direction of the applied field with respect to the crystallographic directions. This change in magnetization is field induced in contrast to spin reorientation which is temperature-induced. FOMP has its origin in the presence of two inequivalent minima in the free energy which system shifts from one minimum energy state to the other as the magnetization changes under the influence of a magnetic field. In $Nd_2Fe_{14}B$, FOMP begins to appear in the *M(H)* curves along the [100] axis at temperatures below 200 K. It can be described as an initial rotation of Nd moments in their local (001) easy planes which is followed by a sudden quasi-alignment of all the moments along [100] direction (Cadogan 1987). The critical field in which FOMP starts to occur is H_{cr} and it increases by

decreasing the temperature. For detection of FOMP in $Nd_2Fe_{14}B$, relatively high magnetic fields are required (H_{cr} = 17 T at 77 K) which cannot be provided by conventional lab magnetometers. Therefore, in this thesis, the magnetic measurements are performed in high field labor Dresden using pulse magnetometers. Neither spin reorientation transition nor FOMP occurs in $Ce_2Fe_{14}B$. Nevertheless, as a result of Ce having a mixed valance state of 3.44 (Capehart 1993) in the structure, Ce has a history of causing many unusual and strange phenomena.

Substitution of Ce in NdFeB magnets

The strong permanent magnetic performance of NdFeB magnets is governed by proper microstructural design. In general, Nd-Fe-B magnets consist of a major fraction of ferromagnetic $Nd_2Fe_{14}B$ phase (τ_1) which are decoupled by a certain amount of preferably well distributed paramagnetic amorphous Nd-rich phase. Sintered Nd-Fe-B magnets also often consist of $Nd_{1.1}Fe_4B_4$ which is paramagnetic at room temperature and its existence decreases the magnetization of the final magnet. As can be seen in Figure 2-9, the phase relations of the RE-Fe-B sintered magnets with composition remarked by a gray circle is quite different for R = Nd and Ce. In both systems, the 2:14:1 phase form along with the paramagnetic B-rich phases which in Ce-Fe-B ternary system is $CeFe_2B_2$. The third phase forming in the Ce-Fe-B system is binary the $CeFe_2$ Laves phase with the $MgCu_2$-type (C15) structure. The formation $CeFe_2$ phase (T_m = 1198 K) instead of low melting point Nd-rich (T_m = 928 K) phase which is essential for the densification of the magnet during sintering is quite detrimental as it leads to poor wettability and flowability during the sintering process (Li 2020).

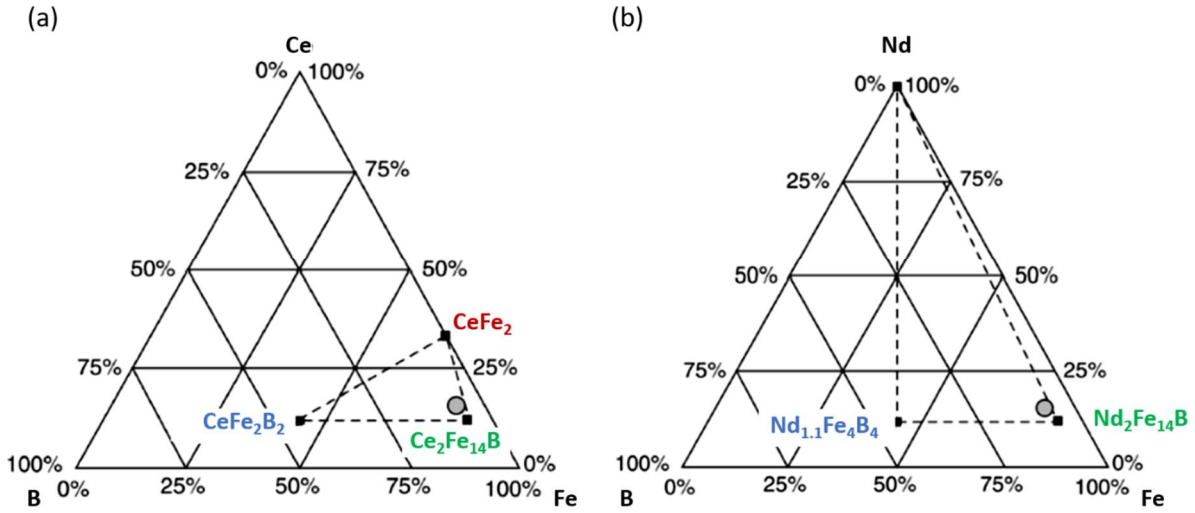

Figure 2-9. The phase components of (a) Nd-Fe-B and (b) Ce-Fe-B sintered magnets with the compositions shown by the gray circles (Li 2020)

The Laves $REFe_2$ phase is not stable at ambient pressure in most of LRE-Fe binary systems due to geometrical reasons. An ideal atomic radius ratio for the formation of the close-packed cubic Laves phase is √3/2 which for LRE-Fe is far beyond this value (Hynninen 2007). Stabilization of $REFe_2$ Laves phases including $NdFe_2$ was done by application of extreme pressure and temperature which resulted in a reduction of the rare earth ions radii (Tang 1998). The formation of $CeFe_2$ at ambient pressure is

an exception arising from its mixed-valence state. In contrast to other RE, Ce 4f electron is quasi delocalized and therefore participates in the construction of the conduction band. The stable Laves $(Nd_{1-x}Ce_x)Fe_2$ phase is synthesized for $x \geq 0.2$ (Tang 1998). The $CeFe_2$ phase is paramagnetic at room temperature (T_c = 235 K). The Curie temperature of $(Nd_{1-x}Ce_x)Fe_2$ increases linearly with decreasing x in which for $x < 0.8$ ferromagnetic ordering occurs at room temperature and for x = 0, T_c = 589 K is estimated. In the Nd-Fe-B system, Ce substitution shifts the phase boundaries and stabilizes the $(Nd,Ce)Fe_2$ Laves phase. If this cubic phase which might be ferromagnetic form instead of Nd, Ce-rich intergranular phase, it can drastically deteriorate extrinsic magnetic properties (Fayyazi 2016, Li 2020, Skokov 2018, Tang 2018). Although generally formation of the Laves phase is believed to be detrimental for extrinsic magnetic properties of Ce substituted magnets, some studies show that its existence can be beneficial. Ref. (Li 2016) shows that sintering at temperatures above the melting point of the $REFe_2$ phase could improve the wettability of 2:14:1 phase. In (Zhao 2017), it is shown that Ce tendency to enter 1:2 phase led to element segregation and enhancement of Nd content in the $(Nd,Ce)_2Fe_{14}B$ phase which retains desirable magnetic properties. From Ce-Fe binary phase diagram it can be seen that $CeFe_2$ forms at 1198 K which is well below the crystallization temperature of 2:14:1 phase from the melt (~ 1438 K). Therefore, low cooling rates promote 1:2 phase formation. The formation of the 1:2 phase can be partly overcome by rapid quenching techniques such as melt-spinning. In (Poenaru 2019), no indication of 1:2 formation was observed up to x = 0.7. Furthermore, reference (Zhou 2020) has reported that the partial doping of Fe with Ti in Ce-Fe-B alloys can substantially inhibit the formation of the 1:2 phase, instead promoting the formation of $Ce_2Fe_{14}B$ phase and therefore, improving the magnetic properties.

Another pitfall of Ce substitution for Nd-Fe-B magnet is the decrease in intrinsic properties of the main $(Nd_{1-x}Ce_x)_2Fe_{14}B$ phase with x (Li 2015, Susner 2017). The trend is followed while investigating the extrinsic properties of Ce substituted melt-spun ribbons (Li 2015), hot deformed magnets (Tang 2019) and sintered magnets (Zhang 2017). Meanwhile, a couple of studies report on abnormal coercivity enhancement in a certain range of Ce substitution for Nd. Literatures (Yang 2017) and (Pathak 2015) both show an abnormal increase in coercivity of $(Nd_{1-x}Ce_x)_2Fe_{14}B$ melt-spun ribbons at x = 0.2. The observation is related to the chemical miscibility gap for x = 0.14 - 0.4. Based on empirical alloying theory (Jacobsen 1996), as a result of small cell volume difference between $Nd_2Fe_{14}B$ and $Ce_2Fe_{14}B$ (2.5%), a full solid solution of one in another is possible. However, a study based on density functional theory calculations (Alam 2013) and neutron diffraction on single crystals show the preferential site occupancy of Ce atoms for larger 4g sites as a consequence of their different ionic radius which is Ce^{4+}(1.715 Å) < Nd^{3+}(1.821 Å) < Ce^{3+} (1.825Å) for 12-fold coordination. Therefore, Ce^{3+} rather occupies the larger 4g site than the smaller 4f site which leads to termination of its solubility and phase segregation at a specific concentration range. A contrary result is reported in (Colin 2016) by neutron study on rapidly quenched $(Nd_{1-x}Ce_x)_2Fe_{14}B$ alloys which suggest a continuous solid solution and preferential site occupancy of Ce for smaller 4f site. This discrepancy might be caused by a very different crystallization rate of the used synthesis method. Pathak et al. also showed an optimized coercivity of 0.94 T for x = 0.2 hot deformed $(Nd_{1-x}Ce_x)_2Fe_{14}B$ magnets (Pathak 2015). Our study in (Poenaru 2019) shows even further increase of Ce concentration (to x = 0.3) in hot deformed magnets led to the enhancement of remanence and coercivity compared to x = 0.2 as a result of less T_m of RE-rich grain boundary (GB) with higher Ce concentration which leads to better flowability and

deformability and subsequently better texturing of the final magnet. The anomaly in coercivity is also observed in Ce substituted sintered magnets at x = 0.25 whereas the remanent magnetization and energy product were gradually decreased (Yan 2014). The enhancement of coercivity was attributed to the stabilization of the $CeFe_2$ phase for x > 0.25 rather than 2:14:1 phase and consequently formation of thicker gain boundaries, beneficial for decoupling of ferromagnetic main compound (2:14:1) and correspondingly enhancement of coercivity. The magnetic properties of 25% Ce substituted NdFeB sintered magnets were further optimized by using Dual Alloy Method (DAM), which coercivity and remanence could be enhanced in comparison to single alloy method as a consequence of the coexistence of Ce-lean (where remanence and anisotropy are maintained) and Ce-rich 2:14:1 phase separated by well-distributed Ce content amorphous GB phase (Fan 2016). The advantageous application of the DAM method for preparing high abundant rare earth magnets was reported by other studies (Jiang 2019, Xiaodong 2016, Zhang 2016, Zhu 2014). It is reported that Ce tends to diffuse to the grain boundary region rather than the main 2:14:1 phase (Liao 2020) and as a result of the smaller melting point of (Nd,Ce)-rich grain boundary region than Nd-rich phase, the needed sintering temperature for full densification of the magnet can be kept lower. Consequently, a finer microstructure and more homogenous wetting of the grains beneficial for coercivity is resulted (Fan 2016). Improvement of magnetic properties is also reported in several researches investigating the grain boundary diffusion process in Nd-Ce-Fe-B magnets (Ito 2016, Tang 2018, Wang 2020).

Substitution of Co in (Nd,Ce)FeB magnets

Partial substitution of Fe by Co improves the magnetic properties of Nd-Fe-B magnet and almost all commercially available magnets include some amount of Co (e.g. MQU.F powder has 6.6 at.%). A complete solid solubility of Fe by Co is possible in $Nd_2(Fe_{1-x}Co_x)_{14}B$ compound. Co substitution increases the Curie temperature of the compound significantly (about 10 K/at% for x < 0.5). The saturation magnetization at room temperature decreases with increasing x with only a slight increase for x = 0.1 (Sagawa 1987, Sepehri-Amin 2018). The initial increase of M_s with 10% Co substitution in Fe site was not effectively used in sintered magnets due to the formation of nonmagnetic Nd_3Co in the GB region as a result of the large affinity of Co and Nd. The anisotropy field of $Nd_2(Fe_{1-x}Co_x)_{14}B$ for x < 0.8 is not changing significantly at a temperature range between [300-400 K], however for T > 400 K, it increases slightly with increasing x. Substitution of Co for Fe in NdFeB sintered magnets is often found detrimental for the coercivity which attributes to microstructural factors such as precipitation of Co-rich Nd-Co intermetallic compounds rather than the decreased in anisotropy (Sagawa 1987).

Substitution of Co for Fe in Ce content NdFeB magnets is of particular interest as it compensates the diminished T_c of the compound. Other positive impacts are also found while substitution of both Ce and Co in recent years which some are reviewed here. One of the initial studies concerning co-doping of Ce and Co reported the enhanced coercivity of $(Nd_{1-x}Ce_x)_2(Fe_{1-y}Co_y)_{14}B$, x = 0.2 and y = 0.15 hot deformed magnets for high temperatures in which at 450 K the coercivity of 0.7 T which is 35% higher than that in 4% Dy doped NdFeB sintered magnets (0.5 T) was achieved (Pathak 2015). Enhancement of thermal stability of co-doped Ce/Co magnets were reported in (Pathak 2016, Pathak 2016). For the first time, (Tang 2019) reported the hard-magnetic properties of $(Nd_{1-x}Ce_x)_2(Fe_{1-y}Co_y)_{14}B$ magnets prior to those of their Nd-Fe-B counterparts with x = 0.1 and y = 0.05. It has been shown that the improved coercivity attributes to a higher concentration of RE in GB regions when the magnet consists Ce.

Furthermore, ab-initio calculations showed that when Co and Co are both involved, the magnetization can be retained if Ce occupies 4g site selectively which is proved to be the case by atom-resolved STEM-EDS Mapping.

2.4. Combinatorial methods

Unlimited worldwide demand for new and improved materials brought the idea of introducing a highly efficient way of investigating different materials. Studying of the phase diagram using the traditional equilibrated alloy method that there is one sample under investigation at a time is a time-consuming and expensive task. This is the reason why many phase diagrams especially in the systems with more than two components are not studied so far. Combinatorial materials science is an emerging paradigm of research methodology introduced in order to speed up the discovery, examination, and the optimization of the new materials. In these approaches, large numbers of samples with multiple alloy compositions are synthesized together (material libraries) and, in parallel or series, the structure-property relationship of the multiple materials under variable conditions is screened. The very first use of combinatorial approaches goes back to 1955 where by employing thin film deposition with composition gradient and identification of the formed phases with electron diffraction, phase diagrams of several materials were developed (Boettcher 1955). Although since then the method was further applied for construction of the phase diagrams (Kennedy 1965), however, its workflow was first stated by Hanak in 1970 (Hanak 1970). The principles are announced to be (i) the complete compositional mapping of the sample consisting of multiple components, (ii) rapid chemical analysis in a non-destructive way, (iii) screening of the properties and data processing. Thin-film deposition combinatorial approaches have been extensively used for the development of different materials such as superconductors, ferromagnets, photovoltaic and catalysts (Hanak 1970, Thomas 1980) and also widely used in the fields of biology and chemistry for discovery and drug development (Xiang 1995). In (Enokido 2020) a high-throughput screening method for thin-film $R_2Fe_{14}B$- based magnets is proposed. Due to several disadvantages of deposition techniques such as their high cost, relatively large incorporation of substrate-induced stresses, a large number of defects, and most importantly, the dependency of the microstructure and physical properties on the deposition parameters, these methods are rather exclusive and their application should be carefully handled, especially when the study focuses on the exploration of equilibrium phase diagrams.

In order to construct the ternary phase diagrams, the bulk diffusion method was introduced in (Hasebe 1978). The procedure of the work was attaching three pure metals to form a tri-junction which were subsequently heat-treated to make diffusion occur. The thermal diffusion of elements leads to the formation of intermetallic phases due to solid-state reaction. These studies reported many isothermal sections of the ternary phase diagrams however, due to lack of sophisticated techniques, no property determination was performed and the method remained not well-known. Only after the combination of the method with a localized micro-scale property measurement system where the phases with desired characteristics could be selected, the approach became widely known and named as “diffusion-multiple” (Zhao 2001). A similar concept is used in the “reaction sintering” method where elemental powder mixtures are compacted, heat-treated and during an intermediate sintering state, different diffusional regions are formed and characterized (Groß 2004, Lüdtke 2001). The main

drawback of this method is a slow diffusion process, as all contributing components are in the solid state. The material properties of a wide spectrum of materials which are discovered and optimized using combinatorial methods are recorded in databases (Maier 2007, Potyrailo 2011). Recently, additive manufacturing techniques are also applied as bulk high-throughput synthesis methods for the discovery of new materials. In (Chaudhary 2020), for the development of mischmetal containing NdFeB permanent magnetic materials, bulk combinatorial synthesis via Laser Engineered Net Shape (LENZ) printing was employed. For characterization of hard magnetic materials, the high-throughput synthesis methods should be followed by rapid, high-quality magnetic characterization techniques such as magneto-optical Kerr effect magnetometry (MOKE) for measurement of magnetic hysteresis loops locally (Niarchos 2015), magnetization mapping by means of scanning superconducting quantum interference device (SQUID) microscopy (Takeuchi 2003) and magnetic domain analysis using Kerr microscopy (Goll 2014).

2.4.1. Reactive Crucible Melting (RCM)

The high-throughput method used in this thesis is a bulk combinatorial approach known as “Reactive Crucible Melting (RCM)” which is developed in the beginning of the 2000s and combines an efficient synthesis route with high-throughput characterization techniques such as scanning electron microscopy (SEM) for phase identification and Kerr microscopy for magnetic characterization (Goll 2015, Goll 2014, Lüdtke 2001, Lüdtke 2000). In contrast to the reactive diffusion pair techniques with solid-state reactions, inside of the reactive crucible which itself is made of the chemical element with the highest melting temperature, one or two other components can be in a liquid state during annealing, thus significantly accelerating the formation of intermediate phases. The strategy for high-throughput discovery of new hard magnetic materials is the identification of ferromagnetic phases with uniaxial anisotropy directly from their characteristic domain pattern which can be analyzed further for evaluation of the material’s intrinsic magnetic properties. The estimation of magnetocrystalline anisotropy from the domain structure is one of the main focuses of this thesis and described in detail in the next section. Whereas, estimation of the saturation magnetization from domain contrast and Curie temperature from the temperature dependence of domain contrast are investigated elsewhere (Goll 2014, Simon 2019). A wide range of RE-T-X ternary and quaternary systems were screened in Refs. (Groß 2004, Lüdtke 2001). This method is also used for the construction of room temperature phase diagrams of Ni-Mn-Ga and Fe-Mn-Ga ternary Heusler systems (Ener 2016).

2.4.2. Estimation of magnetic anisotropy based on domain theory

In the macroscopic scale, magnetic imaging allows the most direct view into the magnetic properties. As mentioned previously, domains forming in a magnetic material create a specific pattern which can be illustrated using different domain imaging techniques such as Kerr and MFM, both will be introduced in the next chapter. Ferromagnetic phases and most interestingly those with uniaxial anisotropy can be distinguished from the other phases since they possess characteristic domain pattern which can differ depending on the sample geometry, intrinsic properties and magnetic history.

Figure 2-10 shows the typical domain structures forming in a uniaxial ferromagnet with different thicknesses. For thin samples (a), band domains with alternating out of plane magnetization are formed and the domain pattern looks like stripes of alternating magnetization. This structure can be

described by the previously introduced Kittel open structure model. The observed pattern is often called Kittel structure also referred as maze-like domains. Based on the theoretical description by Goodenough (Goodenough 1967), as the thickness of the sample increases, the domain walls initially start to undulate to decrease the magnetic free energy. However, after a critical thickness L_s, bulk domains split into smaller domains when they approach the surface in order to reduce the magnetostatic energy while they stay wide in bulk to save part of domain wall energy. This process is known as branching and the obtained pattern is referred as the branched domain (also called star-like, spike-like domains). The branching process can be also clearly visualized when the easy magnetization direction lies in the observation plane. The corresponding domain pattern is called a stripe-like pattern (Hubert 2014).

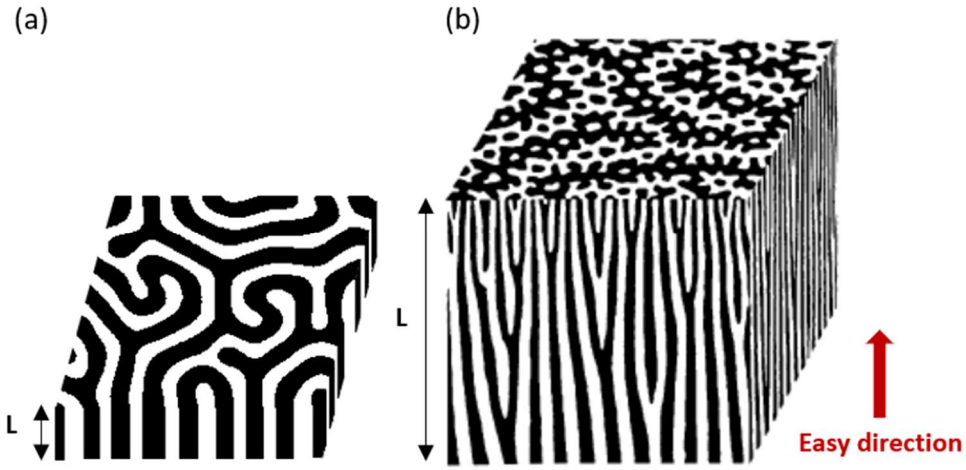

Figure 2-10. Domain structure of a uniaxial ferromagnet with small (a) and large (b) thickness. The formed structure in (a) is known as Kittel or maze-like structure. By increasing thickness, domain branching leads to the formation of branched domain or spike-like domains. Figure (b) is adapted from (Groß 2004).

As mentioned, the origin of domain formation, size and arrangement of them depends on the minimization of the total energy which can be written as an integral of acting energy terms over the sample volume.

$$E_{total} = \int_{Sample} [exchange + anisotropy + magnetostatic + domain\ wall + Zeeman + magnetistriction]\ dv$$

Accordingly, several theoretical models which link different material parameters to their corresponding domain structure were developed. The domain width *D* is related to the domain wall energy $\gamma = 4\sqrt{AK}$ and therefore to the magnetocrystalline anisotropy *K* and material exchange stiffness *A*. In this thesis, to estimate the magnetocrystalline anisotropy of the materials of interest, different theoretical models were employed. It has additionally been examined whether this estimation is trustworthy to be used as a high-throughput characterization of potential permanent magnetic materials as in (Goll 2015, Goll 2014). For analysis of the domain structure, one should select a proper domain model depending on the formed domain structure, grain size and relative anisotropy of the material.

A very basic model of domain structure has been developed by Kittel (Kittel 1946) related to open structure. This model can be applied on samples with thickness below L_s where no branching occurs and moments are uniaxial with easy axis perpendicular to the plate surface. The basic domain width D_b can be calculated as:

$$D_b = (\frac{\gamma L}{1.7 M_S^2})^{1/2} \qquad \textit{Equation 16}$$

with *L* being the grain thickness. For thin samples, the basic domain width increases exponentially with half power with the thickness of the sample. As the thickness increases (above L_s) and branching of domains become favorable *($D_b > D_s$)*, the basic domain width increases stronger following the $L^{2/3}$ law. The intersection point of the two asymptotic laws can be defined mathematically as a critical thickness. For high anisotropy materials ($Q \geq 1$), L_s can be written as:

$$L_s = 5000 Q \sqrt{A/K} \qquad \textit{Equation 17}$$

For the analysis of bulk stripes with domain splitting, a domain model developed by Szymczak is applicable (Szymczak 1973).

$$D_b = 0.395 (\frac{\gamma \mu^*}{M_S^2})^{1/3} L^{2/3} \qquad \textit{Equation 18}$$

In this equation, $\mu^* = 1+1/Q$ is the rotational permeability and *L* is the length of the stripe. μ^* can be approximated as 1 when $Q > 1$. However, for materials with low anisotropy, μ^* correction should be considered as the magnetization vector is no longer frozen along the easy axis and rotates with the permeability of μ^* under the influence of the field produced by charge distribution.

For sufficiently thick samples, the surface domain width is no longer thickness dependent. For out of plane easy direction crystal, the surface domain width can be calculated based on the Bodenberger-Hubert model (Bodenberger 1977) and can be written as:

$$D_s = \beta 4\pi\gamma / M_s^2 \qquad \textit{Equation 19}$$

Here, D_s is the average surface domain width, M_s is saturation magnetization and β is a phenomenological fitting parameter depending on the geometrical arrangement of the magnetic domains at the surface. The structure of surface domains is strongly dependent on the relative anisotropy of the material which can be expressed by quality factor *Q*. For high anisotropy materials with $Q >> 1$ where the surface domain structure of materials contains pure two-phase branching (magnetization up and down), β can be approximated as 0.3 ± 0.02.

In addition to magnetocrystalline anisotropy, other intrinsic properties such as saturation magnetization and Curie temperature can be estimated by analysis of magnetic domain contrast which is not the focus of this thesis.

3. Experimental methods

3.1. Sample preparation

3.1.1. Reactive crucible melting method

The production route of the reactive crucible melting is schematically shown in Figure 3-1. The crucibles should be made of the highest melting point element of the system under investigation and filled with the rest elements in the form of crushed pieces or powders of high purity. The filled crucibles are closed under argon atmosphere with properly designed lids which can be tightened and therefore minimize the leakage. The crucibles are then wrapped in metal foils, sealed in an evacuated silica tube and subsequently heat-treated at different temperatures. During the annealing, the filling elements with lower melting points melt and diffuse into the solid-state crucible. By the formation of a concentration gradient and depending on the composition range between the melt and the crucible, according to thermodynamically guided diffusion processes, intermediate intermetallic phases will form between the liquid and the crucible. The existence of melt in this method enhances the diffusion speed. Furthermore, the reaction can be performed under an argon atmosphere and therefore it has a big advantage for the investigation of reactive substances. As the crucibles are tightly closed by fitting lids, no leakage is expected and investigation of easily evaporating materials is possible. In addition, in such a well-maintained condition, the degree of impurity is very low.

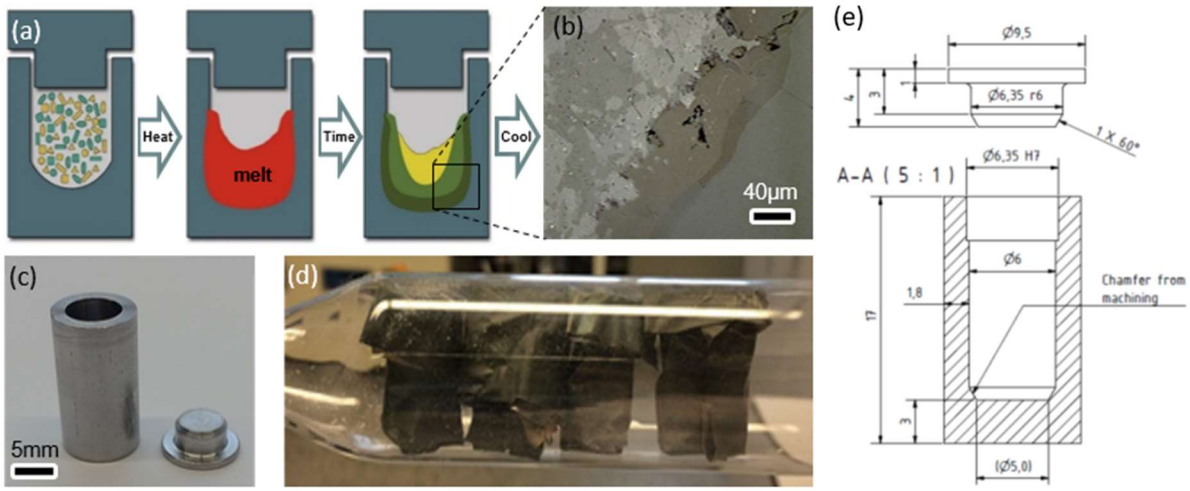

Figure 3-1. (a) Schematic representation of the production procedure for reactive crucible melting, (b) the optical microscopy image of diffusion zones of a reactive crucible, (c) a Fe crucible, (d) the crucibles were wrapped in metal foils, sealed in silica tubes under the vacuum and subsequently annealed at desired temperatures, (e) technical details of the designed crucibles and lids for RCM.

In this work, the crucibles are self-designed, and all are made of Iron. The design of the crucibles is optimized by the consideration of diffusion behavior of investigated materials under the most extreme used condition. By overestimation of the size of the diffusion zone, the thickness of the bottom part of

the crucible is chosen to be the largest while for having a prompt quenching, the wall thickness is chosen as thin as possible compromised with the diffusion depth. The crucibles were manufactured by the materials science faculty workshop of TU Darmstadt.

3.1.2. Single crystal growth

Single crystal growing requires detailed knowledge of the equilibrium phase diagrams. There are several growth methods that one can utilize to obtain high-quality single crystals. The most frequently used single crystal growing methods are based on solidification from its own melt which enabling the growth of pretty large single crystals (up to several kilograms) with very high growth rate (up to several millimeters per minute) by using methods such as in Czochralski, floating zone and Bridgman techniques. In these techniques, the growth rate is defined by temperature gradients which need to be precisely controlled as it may cause crystal imperfections because of significant thermal stresses. Therefore, these growth apparatuses should be supported by computer modeling tools which overall make them economically efficient only for single crystal growth laboratories and industries (Müller 2001). Moreover, melt growth methods cannot be used for single crystal fabrication of a material which has no congruent melting point. In these cases, single crystal growing from melt solutions (fluxes) can be used which at the same time does not require sophisticated and costly equipment. In this method, for a single crystal to be grown, the reactant diffusion is increased by allowing soluble starting materials to react in a molten solvent. When the molten flux acts not only as a solvent but also as a reactant that incorporates in the formation of the single crystal, the method is called the “reactive flux” method (Kanatzidis 2005).

In this work, all single crystals except for the Fe_3Sn compound are grown using this method. The apparatus consists of a furnace whose temperature can be precisely controlled and a crucible holding the molten flux. For the selection of a proper metal flux, some factors should be considered; (i) the flux material should have a low melting point reasonably below its boiling point, (ii) it should have low reactivity with container material, (iii) it should be possible to separate the flux from the formed single crystals by means of a chemical dissolution, physical reactions or mechanical removal and (iv) most importantly the metal flux should not form highly stable compounds with any of the reactants. The selection of low melting point Ga, Sb, Pb and Bi as flux metals for single crystal growth of Fe-Sn binary compounds led to the formation of undesirable phases. Figure 3-2 shows two examples of wrong flux selection where with Ga, Fe_3Ga binary single crystals form and Sn remains unreacted whereas with Sb, ternary $Fe_5(Sn,Sb)_3$ single crystals form as Sb substitutes Sn in the desired phase.

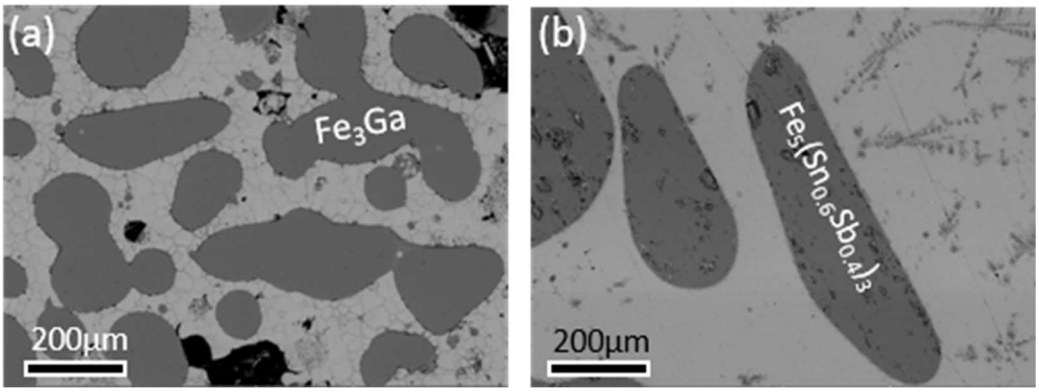

Figure 3-2. The SEM BSE image of the microstructure obtained for single crystal growing of Fe_3Sn_2 using (a) Ga and (b) Sb as flux materials. In (a) Fe_3Ga single crystals (gray) were formed which were surrounded by Sn-Ga mixture and in (b) $Fe_5(Sn,Sb)_3$ single crystals were grown in a Sn-Sb matrix.

According to the Fe-Sn phase diagram (Trehaux 1974), the binary compounds melt incongruently and they undergo phase transition before melting (Figure 2-5). Crystallization of the Fe_5Sn_3 and Fe_3Sn_2 compounds occur via peritectic reactions:

$$\alpha\text{-Fe} + \text{Liquid phase} \overset{1183\ K}{\Longleftrightarrow} Fe_5Sn_3$$

$$Fe_5Sn_3 + \text{Liquid phase} \overset{1079\ K}{\Longleftrightarrow} Fe_3Sn_2$$

By long-term annealing of the stoichiometric as-cast ingots in a temperature range [1055-1183 K] for Fe_5Sn_3 and [880-1079 K] for Fe_3Sn_2, a single-phase state samples with limited grain sizes are achievable (see Figure 4-19 b). However, mm-sized single crystals of these compounds were grown by using an excess of Sn as a reactive flux. It has been marked in the Fe-Sn binary phase diagram (Figure 2-5) (dashed regions) that both Fe_5Sn_3 and Fe_3Sn_2 compounds coexist with the Sn-rich liquid phase in off-stoichiometric Fe_3Sn_{2+x} alloys at a specific temperature interval. The starting alloys with composition $Fe_{50}Sn_{50}$ were prepared by induction melting of high-purity elements (Fe: 99.9%, Sn: 99.99%) under a purified argon atmosphere. The obtained ingots were placed in alumina crucibles, sealed in evacuated quartz tubes, and annealed in resistive furnaces. To grow "Fe_5Sn_3" (Fe_3Sn_2), the samples were heated up to 1173 K (1073 K) with a rate of 5 K/h. Subsequently, they were slowly cooled down to 1093 K (1053 K) during 23 days and kept at this temperature for 7 days and eventually quenched in water. After this procedure, taking more than a month of annealing, several well-shaped mm-large crystals were found which were embedded in solidified Sn-rich matrix (Figure 3-3 a). For separation of single crystals from Sn-rich flux, initially, the effect of different chemical solvents such as HCl, HNO_3, Nital and NH_4Cl selected from the handbook of metal etchants (Walker 1990) were investigated. The problem with this method of separation is that these acids are not only effective on the removal of Sn-rich flux but also etch the desirable single crystals containing Sn. The mechanical separation led to the breaking of crystals into small pieces while part of the surface was still covered by Sn-rich phases. According to the binary Fe-Ga phase diagram (Figure 3-4), $Sn_{8.4}Ga_{91.6}$ melts at almost room temperature. Taking advantage of this reaction, a piece of the ingot was covered by a large amount of Ga and heated up to

400 K to accelerate the reaction. Only after a couple of minutes, the floated single crystals in the molten Ga-Sn were extracted using a permanent magnet.

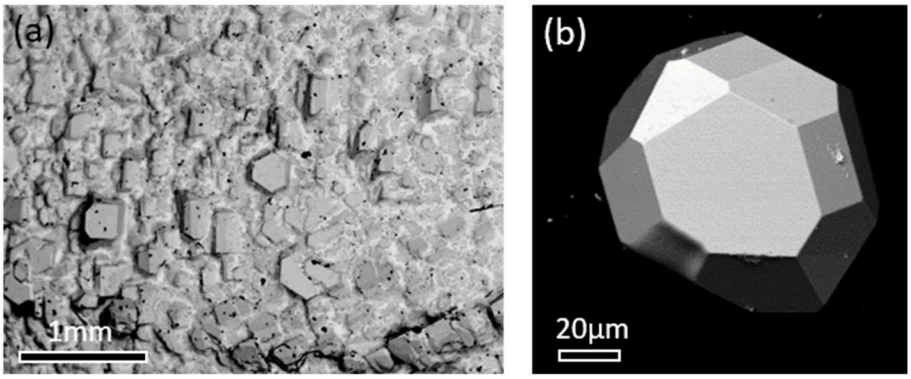

Figure 3-3. (a) The SEM images of well-shaped mm-size single crystals of Fe_3Sn_2 grown in the Sn flux. (b) The typical size of Fe_3Sn single crystals which made their handling and measurement difficult.

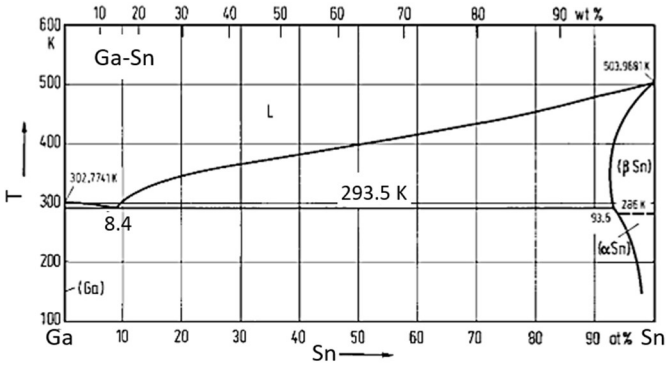

Figure 3-4. Phase diagram of the binary Ga-Sn system (Predel 1995)

The Fe_3Sn compound forms via peritectoid reaction α-Fe + Fe_5Sn_3 $\overset{1111\,K}{\Longleftrightarrow}$ Fe_3Sn. This solid-state transformation makes the single crystal growth of this compound very challenging. Moreover, the temperature range in which Fe_3Sn is stable is very narrow and as all products in this temperature range are in a solid state, much longer heat treatment than for other two binary compounds is required. To grow single crystals of this compound, the stoichiometric Fe_3Sn alloy was prepared by induction melting of high-purity elements. The annealing was done for two months at a constant temperature of 1073 K. After 2 months, the sample was quenched in water and almost a single phase Fe_3Sn structure with an average grain size of 100 µm was obtained. In this case, the single crystals were extracted from pores and cavities of the ingot with maximum a mass of 0.01 mg. Therefore, handling, aligning and measuring them were very challenging. It is worthy to mention that although this compound was counted as an attractive candidate for magnetic applications, it could not be synthesized in the form

of single crystal to be evaluated in respect of its intrinsic magnetic properties by any other research group before.

To grow $(Nd,Ce)_2(Fe,Co)_{14}B$ single crystals, the flux was chosen to be the RE metals with Nd:Ce ratio of the desired 2:14:1 phase. To select an optimum composition, the ternary Nd-Fe-B phase diagrams were carefully screened. From the temperature-composition section of the Nd-Fe-B phase diagram with fixed 4 at. % B (Figure 3-5), the composition with the largest temperature stability in the binary (2:14:1 + L) region was selected (Malfliet 2008). The alloys with the composition of $(Nd,Ce)_{33.5}(Fe,Co)_{62.5}B_4$ were melted by a high-frequency induction melter in zirconia crucibles under argon atmosphere. The subsequent slow cooling of the alloys leads to a coarse-grained microstructure. The precursors were sealed in an evacuated quartz ampule, homogenized at 1343 K (1070°C) for 2 days and subsequently slowly cooled down (0.5 K/h) to 963 K (690°C) for Nd-(Fe,Co)-B samples and to 1213 K (940°C) for Ce containing samples to avoid $CeFe_2$ phase formation. The samples were annealed for 100 hours at the final temperature and subsequently quenched in water. Several numbers of well-shaped and large single crystals were formed in the ingots. For separation of the single crystals from RE-rich flux, the samples were kept in the ambient atmosphere for a couple of weeks which after, the RE-rich phase was oxidized and powdered and the single crystals were extracted.

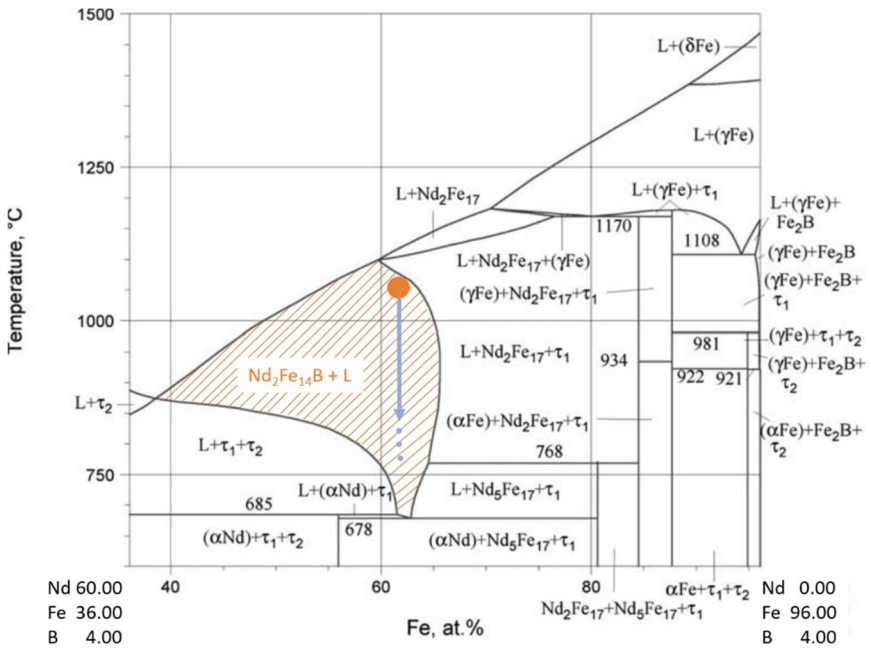

Figure 3-5. The ternary Nd-Fe-B phase diagram with constant concentration of B as 4 at % (Malfliet 2008)

3.1.3. Mechanochemical synthesis of magnetic nanoparticles

Chemical and physicochemical transformations on the materials which are driven by mechanical energy are defined as mechanochemistry (Petruschke 1985). Mechanochemical synthesis is a novel synthesis route for the production of single-crystalline particles with tunable particle size. By

fabrication of particles within the range of single-domain particle size where the coercivity is defined by the uniform rotation of magnetic moments (Stoner and Wohlfarth model (Stoner 1948)), the coercivity can be maximized. This approach enables the bottom-up fabrication of anisotropic particles which are well separated and can be used for the production of exchange-coupled nanocomposite permanent magnets (Gabay 2015, Gabay 2013). For materials including rare earth elements, as a result of their high oxygen sensitivity, fabrication of nanoparticles using mechanical alloying or ball milling (top-down methods) is a challenging task. Usage of precursors in oxide form and having a reduction agent in the mechanochemical synthesis method (reduction - diffusion with a high-energy mechanical activation) eases the production of nanoparticles in these materials specifically. Furthermore, fewer defects can be introduced using mechanochemical synthesis than the two other mentioned methods as the particles are grown rather than ground which would lead to a higher coercivity.

For the fabrication of Ce and Co substituted Nd-Fe-B 2:14:1 nanoparticle, commercially available high purity oxides of Nd_2O_3, Ce_2O_3, Fe_2O_3, Co_2O_3, B_2O_3 were chosen as precursors to produce nanoparticles. The rare earth oxides get hydrated in the laboratory atmosphere therefore for moisture removal they were heat-treated for 4 hours at 1000°C and subsequently stored in a glovebox with Ar atmosphere. The relative molar ratios between the added elements were calculated as; Fe/B = 14 equal to stoichiometric composition, Fe/RE = 3 having an excess of RE to compensate its loss during the synthesis process and Ce/RE = 0, 15, 25 and 50 %. For the reduction of oxides, Al, Mg and Ca can be utilized as reducing agent however, since Mg and Al are not soluble neither in water nor in ethanol, they cannot be removed simply from the final product. The CaO however, is removable with water as it reacts with water and forms calcium hydroxide. Therefore, one gram of the precursors was mixed with metallic Ca as a reducing agent and CaO powder as dispersant material. In an ideal case, one Ca atom reduces one O atom. However, the degree of reduction is limited due to the nature of the solid-state reaction, therefore, to ensure the complete reduction an excess of Ca is considered. The amount of CaO is chosen to be 3 times of the oxide precursors. The mixture was loaded to a steel milling vail (powder to ball ratio of 1:10) in an argon chamber and collected as well under a protected atmosphere as the resulting product is pyrophoric. The High Energy Ball Milling (HEBM) was done with a Spex-8000 shaker mill for 4 hours. During the HEBM process, oxides can be reduced and nucleation of the $RE_2Fe_{14}B$ phase initiates. The pyrophoric powder is then purged with 0.1 bar of Ar and sealed in a quartz tube. The annealing temperature is chosen to be in the stability range of the $RE_2Fe_{14}B$ structure and at the same time higher than the melting point of Ca (T_m = 842°C). Therefore, Ca is in a liquid state and accelerates the diffusion and reaction rate. The annealing was done for 6 minutes which after, the sample included the $RE_2TM_{14}B$ nanoparticles together with byproducts such as CaO, $Ca(OH)_2$ and Nd_2H_5.

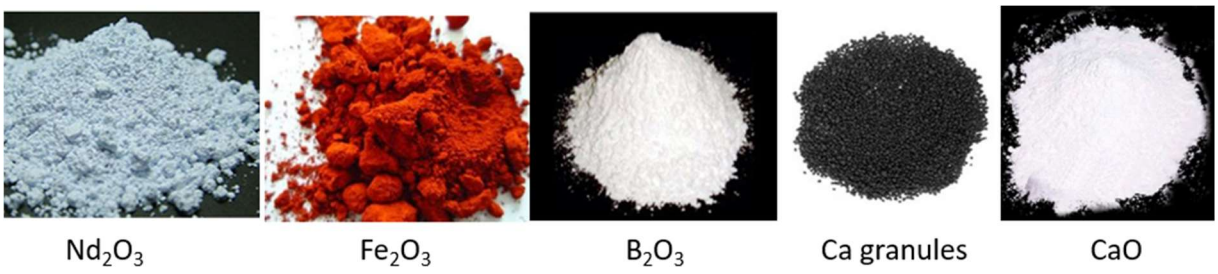

Figure 3-6. The powders used for mechanochemical synthesis of the $Nd_2Fe_{14}B$ nanoparticles

To collect the anisotropic nanoparticles and removal of the dispersant and byproducts, the washing protocol reported in (Gabay 2013) was used. At each step of the procedure, the powder was mixed with a relevant solvent and the solution was agitated by means of a sonicator (Sonics & Materials VCX750). After each washing step which has been taken about 7 minutes each, the ferromagnetic powder was collected using a strong magnetic field. To wash CaO, the powder was washed 5 to 7 times with 20 vol.% aqueous solution of glycerol and afterward washed 2 times with only water to remove residual glycerol. For removal of the excess RE (rare earth oxide and hydroxide), the washing was done with a dilute (0.1 vol.%) aqueous solution of acetic acid and followed by 2 times of washing with only water. Finally, the powder was washed 2 times with ethanol and let dried in the glove box.

As a result of washing with water, $RE_2TM_{14}B$ nanoparticles absorb hydrogen atoms therefore adding another step to the procedure is required to remove hydrogen. For removal of interstitial hydrogen, the $Nd_2Fe_{14}BH_x$ powders were annealed for 5 minutes at 300°C while being continuously pumped in a high vacuum.

3.2. Analysis methods

3.2.1. Microscopy techniques: SEM, TEM, Kerr and MFM

Scanning Electron Microscope (SEM)

To investigate the microstructural properties of the samples, a Tescan VEGA3-SBH scanning electron microscopy (SEM) with acceleration voltage between 15 to 30 kV was used in Secondary Electron (SE) mode for imaging the topology of the nanoparticles and single crystals whereas the Back-Scattered Electron (BSE) mode was utilized for chemical contrast imaging of the samples with multiple phases. The chemical composition of the phases was then determined using Energy Dispersive X-ray spectroscopy (EDX). The resolution of the SEM is limited to tens of nanometer.

Transmission Electron Microscope (TEM)

As the name suggests, the TEM microscopes generate a high energy electron beam (up to 1 MV) passing through a thin lamella (below 100 nm) of the sample enabling capturing of much higher resolutions than SEM. The sample preparation for the TEM analysis is done by *in-situ* lift-out technique using a Carl Zeiss XB-540 cross beam focused ion beam (FIB) system. The FIB-cutting was performed by Dr. Urban Rohrmann at the Fraunhofer Projektgruppe IWKS Alzenau. Electron microscopy was carried out in an aberration-corrected JEOL ARM 200F transmission electron microscope operated at

200 kV. The imaging was done by a focused electron beam that generates a probe size of 1 Å used to scan the sample to obtain a higher resolution using Scanning Transmission Electron Microscope (STEM). To image the atomic structure, the sample was aligned along the *c*-axis which set parallel to the focused beam and STEM- High Angle Annular Dark Field (HAADF) images were acquired. This method enables the detection of high angle, incoherently scattered electrons (Rutherford scattered from the nucleus of the atoms) and therefore is sensitive to atomic number enabling z-contrast imaging. Fourier-transformation of the HAADF image result is a diffractogram that can be used for the determination of the lattice parameters. For the HAADF image simulation, the QSTEM code was implemented. Electron energy-loss spectroscopy (EELS) was performed to determine the local sample thickness. The investigation by transmission electron microscopy has been done in cooperation with Dr. Michael Dürrschnabel at the TU Darmstadt, Institute of Applied Geosciences, Geomaterial Science research group.

Magneto-optical Kerr microscopy

Many characterization techniques are allowing to evaluate local magnetic properties of phases, for example, X-ray magnetic circular dichroism, electron holography, magnetic force microscopy and scanning Hall probe microscopy. These techniques are powerful but for high-throughput analyses of magnetic properties, they are too complex, expensive and have low acquisition rates and capacity. Very often they can operate only in a limited field of view and have other limitations that constrain their application as a high-throughput technique available in conventional labs. For the high-throughput characterization of magnetic domains, Kerr microscopy was used.

The change in the polarization state of the light beam when it is reflected from the magnetic specimen is the basic principle of Kerr microscopes. This phenomenon is known as Magneto-Optical Kerr Effect (MOKE). The light beam passes through the polarizer which only transmits plane-polarized light. The polarized light is incident on the magnetized specimen. Interaction of the electric field vector of the polarized light E with the magnetization vector of the material m, leads to additional oscillation of electrons according to Lorentz force $V_{lor} = -m \times E$. This vibrational motion is perpendicular to the direction of magnetization and the primary motion of the electrons. The resulting Lorentz motion generates the magneto-optical amplitude *K*. The interference of normally reflected component *N* and the Kerr component *K* leads to a small rotation of the reflected light beam. This rotation is magnetization dependent and since the rotation switches, if the magnetization is reversed, domain contrast is obtainable. The magnetic domain contrast of a Kerr image can be enhanced by digital means by subtracting the domain information from the non-magnetic background. The experiments can be performed using three different configurations in which the MOKE is different. The geometry of the measurement can be polar (magnetization is perpendicular to the sample plane and parallel to the plane of incidence), transverse or longitudinal (the magnetization is in the plane of the sample and parallel or perpendicular to the plane of incidence, respectively). In conventional Kerr microscopes, the Kerr sensitivity can be adjusted by proper positioning of a slit aperture. The polar configuration is sensitive to the out of plane magnetization component whereas, the transverse or longitudinal effects are additionally sensitive to the in-plane magnetization component. As the polar Kerr effect is always superimposed and is much stronger (about 10 times (Soldatov 2017)) than the other effects, in a mixed state (out-of-plane and in-plane magnetization component), the in-plane component might be

overlooked using conventional Kerr microscopy. In this thesis, the employed device for investigation of hard magnetic materials with strong uniaxial anisotropy is Evico magnetics Kerr microscope with Zeiss optics where the contrast of the images is enhanced by image processing capability of the KerrLab software. To investigate complex magnetic structures such as illustrated in Figure 4-23, an advanced design for contrast separation is utilized which is described below.

Selective Sensitivity in Kerr Microscopy

The contrast separation can be done by subtraction or addition of two Kerr images taken with the opposite direction of light incidence. Its principle is schematically shown in Figure 3-7. The in-plane contrast is reversed when the light incidence is inverted, while the polar contrast remains the same for both. Therefore, by capturing the Kerr images under the same illumination and contrast condition and subsequently processing of them to obtain sum or difference of the images, pure in-plane or pure polar contrast can be achieved, respectively.

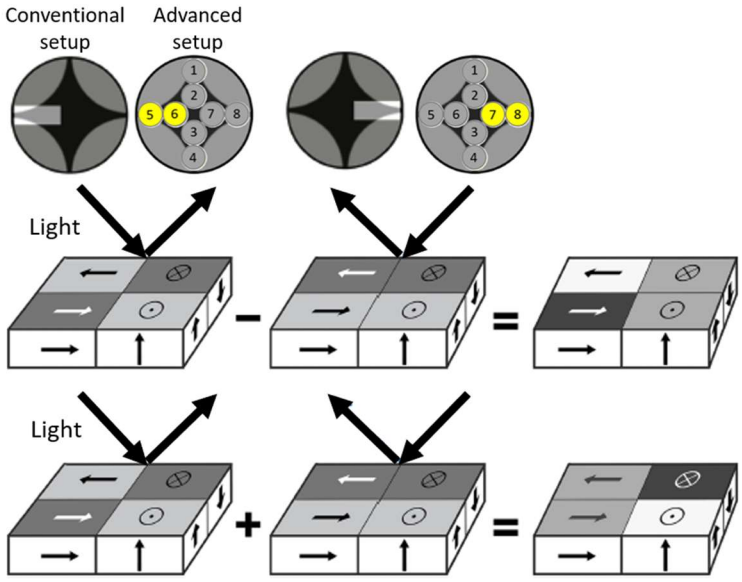

Figure 3-7. Schematic representation of contrast separation principle of selective Kerr microscopes based on subtraction (upper panel) and addition (lower panel) of two Kerr images captured with an incidence of opposite oblique light. By subtracting (adding) of the images, the polar (in-plane) contrast is eliminated and in-plane (polar) contrast remained. In a conventional set-up, an oblique incidence is realized by a displaced aperture slit whereas in an advance setup, as highlighted, the corresponding LED lights are switched on. The figure is adapted from (Soldatov 2017).

The setup consists of 8 Light Emitting Diodes (LED), substituting the light source and eliminating the necessity of using a slit aperture for altering the sensitivity. The lights of 8 LEDs are separately guided to the microscope and can be turned independently off or on resembling the function of a slit aperture (setting the incident angle and direction) using distinct arrangement. Figure 3-7 shows the arrangement of LEDs corresponding to longitudinal sensitivity in a conventional Kerr setup. The determined LEDs are required to be switched off and on synchronously with the camera exposure. The

switching time is in the microseconds range and the frame rate of the camera can be kept as fast as 10 frames/s which can be considered as real-time imaging. By in-situ subtraction of taken sequential images, contrast separation is applicable. Finally, the background image which was taken in a saturated state was subtracted from the final image.

The investigation by selective Kerr microscopy was done in cooperation with Dr. Ivan Soldatov from the Leibniz Institute for Solid State and Materials Research (IFW) Dresden.

Magnetic Force Microscope (MFM)

The out-of-plane magnetization component of the magnetic materials can be also imaged using magnetic force microscopy. MFM is a scanning probe technique utilizing an oscillating cantilever with a magnetic tip. For imaging, the initial step is the determination of topological features using the Atomic Force Microscopy (AFM) "tapping-mode" where the cantilever is in contact with the sample surface. The second step is scanning the same region while the tip of the cantilever takes a certain distance (30-50 nm) to the sample surface. During the second scan, as a result of the convolution of the magnetic stray field of the sample and the magnetic stray field of the MFM tip which its magnetization direction is perpendicular to the sample surface, out of plane component of the sample magnetization alter the resonance frequency of the cantilever slightly which can be measured and plotted to display the contrast between different domains. In this work, for temperature-dependent domain imaging, an MFM (attocube systems) was operated inside a Physical Property Measurement System PPMS (Quantum Design) enabling the measurement at temperatures down to 4 K. The used cantilever was coated with a magnetic CoPt/FePt having a coercivity of > 0.5 T. Prior to each image a magnetic field of 0.3 T was applied parallel to the magnetic easy axis of the sample followed by the field oscillation back to 0 T.

The magnetic force microscopy was done with the help of Dr. Tim Helbig at TU Darmstadt, Materials Science department, Functional Materials research group.

3.2.2. X-ray diffraction methods: Single crystal XRD, powder XRD, Laue XRD camera

X-Ray diffraction (XRD)

To study the crystal structure of materials, X-ray diffraction methods are very powerful tools since the wavelength of X-rays is on the same length scale as the interatomic spacings. Additional information such as quantitative phase distribution, crystallographic orientation and mean crystallite size can be characterized. The three XRD methods used in this work are (i) powder XRD, (ii) single crystal XRD and (iii) Laue XRD camera.

The two former ones make use of monochromatic radiation whereas the last one uses white radiation. Nevertheless, the basic principle of all is the same where for a given set of lattice planes with an inter-plane lattice distance d, the condition for diffraction to occur can be given by Bragg's law $2d\sin\theta = n\lambda$ where λ is the wavelength of the X-ray, θ is the scattering angle, and n is an integer number. A detailed description of diffraction methods is given in various literature and is not repeated here.

Powder XRD

For powder XRD with randomly oriented crystalline domains, the diffraction pattern is a 2D plot where the intensity of the diffracted beams was measured in a specific range of 2θ corresponding to the various *d* spacings in the crystal lattice. The method is used for quantitative and qualitative phase identification of some samples. The bulk samples were hand-ground and the powder X-ray diffraction patterns were collected by a STOE STADI P diffractometer using Mo $K_{\alpha 1}$ (λ = 0.70930 Å) with a Ge (111) monochromator in transmission geometry. For mechanochemically synthesized nanoparticles, the employed device is a Rigaku Ultima IV diffractometer with Cu $K_{\alpha 1}$ radiation (λ = 1.5405 Å) with the same geometry. The data were analyzed using the *Le Bail* (Le Bail 2005) and *Rietveld* methods (Rietveld 1969) using *FullProf* (Rodríguez-Carvajal 1993) and *Jana2006* (Petricek 2014).

Single crystal XRD

A more sophisticated structural analysis was done by single-crystal XRD to determine the crystal structure of an unknown material e.g. its symmetry and unit cell parameters. The diffraction pattern can be recorded on a film or CCD detector while the single crystal is rotated along different orientations with respect to the beam for a full diffraction data collection where later can be indexed to corresponding *hkl* planes. The diffraction spots correspond to reciprocal lattice points represented by reciprocal vectors. For an elastic scattering with the incident beam wave vector $\overrightarrow{K_i}$ and the reflected beam wave vector $\overrightarrow{K_d}$, the diffraction conditions are satisfied only if the endpoint of a reciprocal lattice vector $\overrightarrow{K_i}$ - $\overrightarrow{K_d}$ = $\overrightarrow{Q_{hkl}}$ is located on the surface of the (Ewald) sphere. The single-crystal XRD was done on single crystals in size of ~ 0.3 mm * 0.3 mm * 0.3 mm on an Oxford Diffraction Xcalibur™ diffractometer with a Sapphire CCD detector using Mo $K_{\alpha 1}$ radiation (λ = 0.71073 Å) with a graphite monochromator. Data collection was carried out with *CrysAlis CCD* (Oxford 2016) and data reduction was performed with the *CrysAlisPro* software (Oxford 2018). Crystal structures were solved by the charge-flipping method and refined on F^2 using the program *Jana2006* (Petricek 2014).

The investigation by single-crystal XRD was done by Dr. Tom Faske at TU Darmstadt, Materials Science department, Functional Materials research group.

Laue XRD camera

The single crystallinity as well as the orientation of the obtained single crystals were checked using a Laue X-ray diffraction camera. In this method, a single crystalline sample which is positioned on a precession goniometer head is irradiated with a white radiation collimated from an X-ray source. The beam is then reflected off (back-reflection Laue) or passes through (transmission Laue) the sample and forms a diffraction pattern on a film or a CCD screen. The employed Laue camera was adjusted to the back-reflection configuration in which the film is placed between the X-ray source and the single crystal. For the diffraction condition to be satisfied, each family of crystal planes picks and diffracts a particular wavelength from the white radiation for different values of *d* and θ. When the condition is fulfilled simultaneously for multiple sets of planes, the diffraction pattern as in Figure 3-8 can be observed. The high-intensity points which mark the intersection of several curves may define the directions in which the symmetry axes are expected. The single crystal position should be readjusted

after each acquisition until the desired orientation lies in the center of the screen i.e. along the primary beam. The single crystallinity as well as the orientation of the obtained single crystal in this work were checked with a Huber 801 Laue camera with Ag X-ray source and a CCD detector. The resulted diffraction patterns were analyzed using the Clip software which simulates the Laue pattern for a variety of crystal structures.

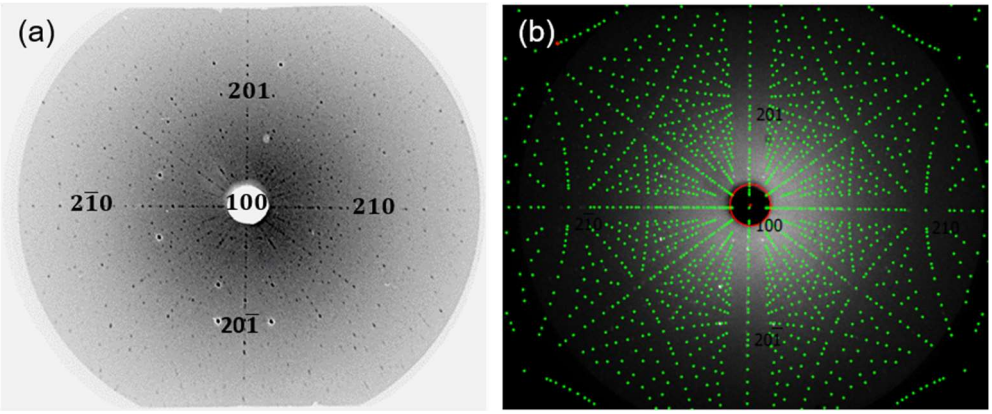

Figure 3-8. Laue X-ray diffraction of a $Nd_2Fe_{14}B$ single crystal. The quality and orientation of the single crystal were confirmed by observation of a clear Laue pattern. a) X-ray diffraction pattern with an incident beam along [100] of the crystal. b) Simulation pattern of tetragonal $Nd_2Fe_{14}B$ structure given by Clip software

3.2.3. Magnetic characterization methods: VSM, Pulsed field magnetometry

Vibrating Sample Magnetometry

The working principle of the VSM is based on Faraday's law of induction which states that a time-variant magnetic flux Φ in an electric circuit (e.g. a coil with N windings) would produce an electromotive force V. For this measurement, the sample is fixed to a non-magnetic rod which then is positioned between a set of oppositely wound pick-up coils in the region of a uniform magnetic field. The rod is attached to the oscillator providing a sinusoidal signal that is translated by the transducer assembly into vertical vibration. Originates from the vibrating movement of the magnetized sample, the time-varying magnetic flux generates an alternating voltage in the pick-up coils which is proportional to the magnetization of the sample.

$$V = -\frac{N\partial\Phi}{\partial t} = -\frac{N\mu_0\partial M}{\partial t}$$

In this work, two different VSM devices were utilized. (i) *LakeShore Cryotronics, Inc.* 7400 series VSM with the capability to generate the magnetic field of up to 2 T using two electromagnets. (ii) *Quantum-design* VSM system operated inside a PPMS equipped with a superconducting magnet with the field strength up to 14 T. Both have cryostat as well as oven option which enable the magnetic measurement from very low temperatures; liquid He temperature for PPMS and liquid N for LakeShore VSM to high temperatures ~ 1000°C.

Pulsed field magnetometer

For the measurement of NdFeB -based single crystals under an external magnetic field of more than 14 T, a pulsed field magnetometer at the High-field Laboratory in Dresden-Rossendorf (HZDR) was used. The magnetic field of up to 60 T was generated using a single 1.44 MJ capacitor module which was charged up to 22 kV and delivered a current with a maximum value of 30 kA. The total pulse duration was 25 ms with a rise time of 7 s. In this magnetometer, two series of pickup coils are used for the measurement. Two of the coils were connected in series relatively far above and below the sample to measure the magnetic field where the signal is proportional to the time derivative of the magnetic field. To obtain the largest detectable signal, the sample pickup coils are very close to the sample nevertheless the contribution of the generated magnetic field is much larger. Therefore, two properly balanced compensations coil wound in opposite directions are used to eliminate the effect of the magnetic field. To obtain a perfectly compensated effect and a reliable signal, a fine compensator is used in order to manually alter the voltage drop in the temperature-independent part of the signal at each temperature. In addition, the background measurement was also done for each temperature where the sample was absent, and the result is subtracted from the sample's magnetization curve. Every sample were remeasured using the VSM option of the PPMS to calibrate the absolute values of the magnetization.

3.2.4. Data evaluation

Sucksmith-Thompson method

For the determination of K_1 and K_2 anisotropy constants of the single crystals, the Sucksmith-Thompson method is used (Sucksmith 1954). In this method, by plotting the hard axis magnetization curve in the form of H/M vs M^2, the first 2 anisotropy constants can be deduced (when higher-order anisotropy terms are negligible). The principle is based on compromising two energies acting on the system (see Equation 10). One is the magnetic field exerting a torque $M_s H\cos\theta$ tending to increase θ and the other one is the torque tending to return the magnetization to its preferred direction which can be obtained by differentiating the anisotropy energy. Equating the two torques would lead to magnetic saturation at the field $H = \frac{2K_1+4K_2}{M_S}$ already shown in Equation 11.

This equation can be written in the form of:

$$\frac{H}{M_S} = \frac{2K_1}{M_S^2} + \frac{4K_2}{M_S^4} M_S^2 \qquad \textit{Equation 20}$$

If the anisotropy is uniaxial, H/M vs M^2 plot gives a straight line (as depicted in Figure 3-9) which cuts the y-axis in a = $\frac{2K_1}{M_S^2}$ and is inclined by angle α where tanα = $\frac{4K_2}{M_S^4}$. Extrapolation of a linear fit of high filed data to the x-axis would result in the square of M_s required for the calculation.

For easy-plane anisotropy, magnetic saturation occurs at the field $H = \frac{-2K_1}{M_S}$ and the technique is referred as the modified Sucksmith-Thompson method (Lyakhova 2017). By rewriting this equation in the form of $\frac{H}{M_S} = -\frac{2K_1+4K_2}{M_S^2} + \frac{4K_2}{M_S^4} M_S^2$, the anisotropy constants K_1 and K_2 can be calculated considering

a = $\frac{-2K_1-4K_2}{M_S^2}$ and tanα = $\frac{4K_2}{M_S^4}$. Different magnetization curves and therefore Sucksmith-Thompson curves might be achieved depending on the sign and magnitudes of K_1 and K_2. The computations of all are given in (Lyakhova 2017), and only those conditions found interest in this thesis were reviewed here.

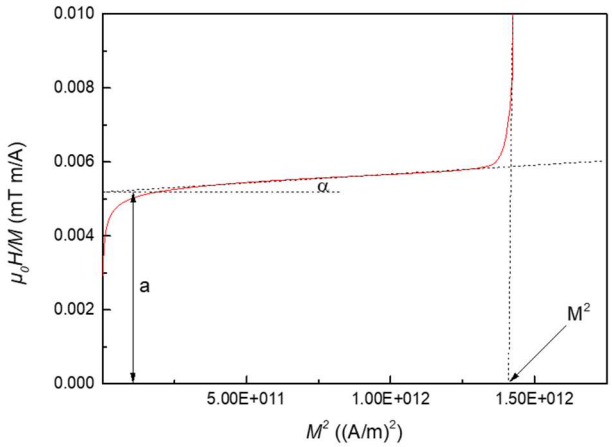

Figure 3-9. The Sucksmith-Thompson method for the evaluation of K_1 and K_2 by analysis of $Nd_2Fe_{14}B$ single crystal data measured along [100] direction at 300 K. Determination of a, α and M_s^2 is required for the calculation based on Equation 20.

Kuz'min fit to evaluate T_C and M_s(0K)

In this work, determination of Curie temperature T_C and spontaneous magnetization at zero Kelvin M_s(0K) was performed by plotting the Belov-Arrott graph (Arrott 1957, Belov 1956) and fitting the obtained M_s-T curves using Equation 21 developed by Kuz'min (Kuz'min 2010, Kuz'min 2005).

For this analysis, the field-dependent magnetization data measured along the easy magnetization direction needs to be plotted as H/M vs M^2. As an example, for $Nd_2Fe_{14}B$ single crystal, by processing the magnetization data obtained along [001] axis for some representative temperatures, the resulted curves are plotted in Figure 3-10. The dashed line in Figure 3-10 a is drawn in which all the low field data points coincide around the line. The spontaneous magnetization at each temperature was determined by linear fitting of higher field data points and determination of the crossing point of the fit with the dashed line. Curves related to the temperatures higher than Curie temperature lead to a negative intercept with the x-axis. As $Nd_2Fe_{14}B$ undergoes a spin reorientation transition at low temperatures, the M_s values obtained along [001] deviate from typical ferromagnetic M-T curves. In such cases, the measurement was done on a free-rotational single crystal meaning that the sample was free (not fixed to the measurement stick) to be able to align itself along its easy direction. The estimated M_s values by treating the magnetic data measured on a free rotational $Nd_2Fe_{14}B$ single crystals are plotted in Figure 3-10 b. The resulted M_S -T curves were then fitted to the equation developed by Kuz'min.

$$M_s(T) = M_s(0)\left[1 - s\left(\frac{T}{T_c}\right)^{\frac{3}{2}} - (1-s)\left(\frac{T}{T_c}\right)^{p}\right]^{\frac{1}{3}} \qquad \textit{Equation 21}$$

This equation is constructed to obey Bloch's $T^{3/2}$ -law (Bloch 1930) at low temperatures and power of 1/3 of the Heisenberg model in the high *T* region close to Curie temperature (Callen 1965), therefore it results in a more accurate evaluation. In this equation, *s* and *p* are fitting parameters which for most of the ferromagnets are in the range of [0 - 5/2] for s and close to 5/2 for p (Kuz'min 2010).

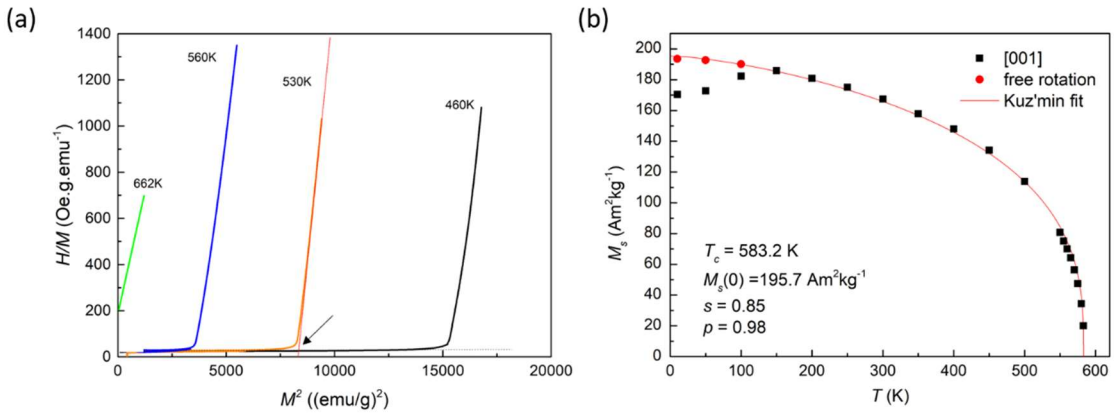

Figure 3-10. (a) Belov-Arrott graph plotted for 4 representative temperatures by analysis of $Nd_2Fe_{14}B$ single crystal data measured along [001] direction. The red line at 500 K is a fit to the high field data points. The dashed horizontal line corresponds to the demagnetization correction. The square of the spontaneous magnetization at 500 K is shown by an arrow. (b) The obtained spontaneous magnetization plotted as a function of temperature. The red line in (b) is a fit to Equation 21.

4. Fe-Sn system

Based on prominent magnetic properties found in Fe-rich ferromagnetic compounds in the Fe-Sn system, it is of particular interest to search through this material system to discover alternatives for permanent magnetic applications. This research was funded by European project Novamag (research Nr. 686056) which aimed for substitution of currently used NdFeB magnets with a proper RE-lean or RE-free material in which the Fe-Sn system was one of the candidates. Therefore, extensive studies have been carried out on this material system including theoretical calculations which will be shortly mentioned along with the experimental results. This chapter is divided into two main sub-chapters. In the first sub-chapter, the high-throughput RCM method is primarily verified by the investigation of the Fe-Sn binary system. Then, considering theoretical predictions as guidelines, the RCM method as well as other non-equilibrium techniques were implemented to search for a desirable hard magnetic material in Fe-Sn based systems. Finally, in the second sub-chapter, by synthesis and characterization of binary Fe-Sn ferromagnetic phases as single crystals, the structural and magnetic properties of them were investigated.

4.1. Searching for ferromagnetic Fe-Sn-X intermetallic compounds

4.1.1. Bulk combinatorial reactive crucible melting analysis applied to the Fe-Sn system

To search for Fe-Sn-X intermetallic compounds with desirable magnetic properties, I initially used the high-throughput RCM method to speed up the material discovery. Previous investigations by RCM only considered the room temperature stable phases as the samples were slowly cooled down to room temperature. In this work, for the first time this method is adapted for the exploration of complex phase diagram containing peritectic and peritectoid reactions, decompositions and etc. as in the Fe-Sn phase diagram (see Figure 2-5). At 800°C, based on Fe-Sn binary phase diagram (Trehaux 1974), all three ferromagnetic phases (Fe_3Sn, Fe_5Sn_3 and Fe_3Sn_2) are stable. To verify the phase diagram at this temperature, four compositions were selected namely $Fe_{85}Sn_{15}$, $Fe_{70}Sn_{30}$, $Fe_{55}Sn_{45}$ and $Fe_{40}Sn_{60}$ (they are highlighted by red crosses in a magnified version of Fe-Sn binary phase diagram shown in Figure 4-2) to be produced by conventional metallurgy (traditionally used for constructing the phase diagrams). The conventional samples were annealed for 10 days at 800°C and subsequently quenched. The microstructure forming in $Fe_{85}Sn_{15}$, $Fe_{70}Sn_{30}$, $Fe_{55}Sn_{45}$ and $Fe_{40}Sn_{60}$ conventional samples are shown in Figure 4-1. In the $Fe_{85}Sn_{15}$ sample, Fe_3Sn and α-Fe phases were formed consistent with the phase diagram. The formation of two intermetallic compounds Fe_3Sn and Fe_5Sn_3 in the $Fe_{70}Sn_{30}$ sample is also in agreement with the phase diagram. However, the existence of a large amount of unreacted α-Fe in the sample evidence that the equilibrium state was not achieved even after such long-term annealing. Two Sn-rich samples $Fe_{55}Sn_{45}$ and $Fe_{40}Sn_{60}$ include Fe_3Sn_2 intermetallic and Sn-rich phase also consistent with the phase diagram. The result confirms the formation of all three ferromagnetic compounds using the conventional method at this particular temperature.

Since the basic principle of a high-throughput method is a complete compositional mapping of the multiple material systems derived by thermodynamically guided diffusion processes, annealing of Sn filled Fe crucibles at various temperatures should be adequate to construct the binary Fe-Sn phase diagram. By high-temperature annealing of Fe-Sn crucible at 800°C and subsequent slow cooling down

to room temperature, the microstructure forming in the diffusion zone consists of 4 phases (Figure 4-1 f); two low-temperature intermetallic phases FeSn, $FeSn_2$, together with α-$Fe_{1-x}Sn_x$ solid solutions (x < 0.1) and elemental Sn. The darkest region represents the Fe crucible which a relatively large belt of FeSn phase is formed along it. Passing towards the Sn-rich region, the $FeSn_2$ phase is formed as a very thin layer on top of the FeSn phase. Some separated α-Fe rich regions were also observed in the Sn-rich part of the crucible where the FeSn and $FeSn_2$ phases were grown around it. As expected, by slow cooling of the crucible, the metastable phases existing at 800°C decompose to low-temperature stable phases and do not form in the crucible after slow cooling, which agrees with the phase diagram. For stabilization of the metastable phases, quenching of the Fe-Sn crucible was done after 10 days of annealing at 800°C. However, as can be seen in Figure 4-1 e, in the diffusion zone of the RCM sample, only two intermetallic Fe_3Sn and Fe_3Sn_2 compounds were formed and the intermediate phase which is Fe_5Sn_3 was missing. To investigate this problem further and verify the accuracy of the RCM method in reproducing reliable phase relations at various temperatures, in the next section, part of the Fe-Sn phase diagram with multiple transformations was reconstructed using homogenous samples and the results were compared with RCM outcome. The result of this investigation was published in (Fayyazi 2017).

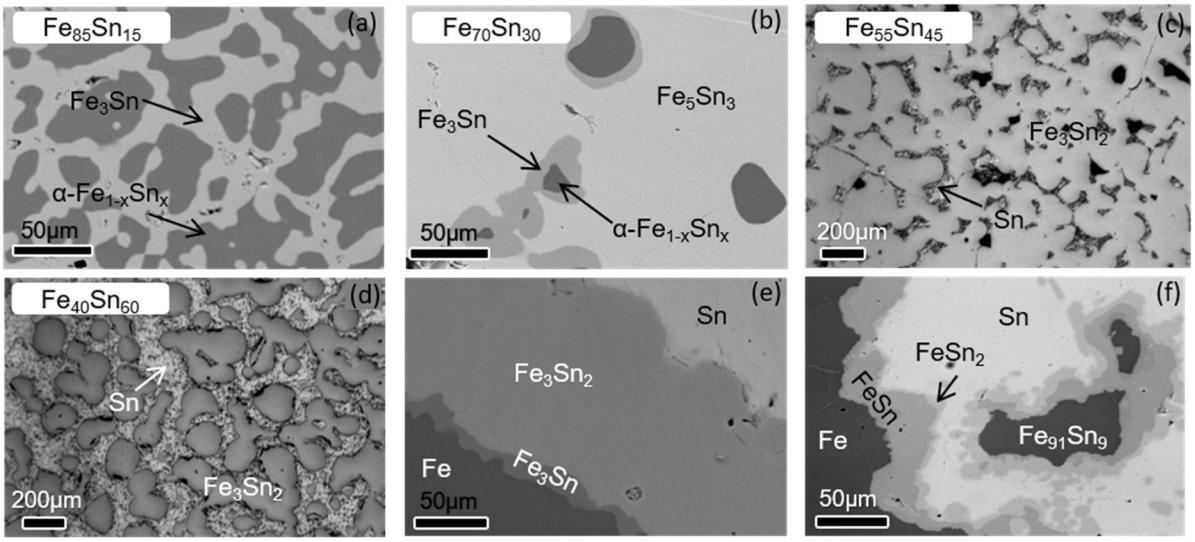

Figure 4-1. Microstructure forming after 10 days of annealing at 800°C in the conventionally prepared samples (a) $Fe_{85}Sn_{15}$, (b) $Fe_{70}Sn_{30}$, $Fe_{55}Sn_{45}$ (c) and $Fe_{40}Sn_{60}$ (d) and in the diffusion zone of Fe-Sn reactive crucibles (e and f). The metastable phases Fe_3Sn, Fe_5Sn_3 or Fe_3Sn_2 were formed in (a-e) as samples were rapidly quenched in water after heat treatment whereas decomposed to low-temperature phases in (f) which was furnace cooled to room temperature.

Reliability of RCM method in reconstruction of Fe-Sn binary phase diagram

To screen the phase diagram in a wide temperature range, two compositions $Fe_{70}Sn_{30}$ and $Fe_{57}Sn_{43}$ shown in Figure 4-2 were chosen to cover the region of interest in the phase diagram with multiple transformations. Due to the slow kinetics of peritectic reactions, to achieve equilibrium condition with

shorter annealing time, further investigations were done on samples prepared by melt spinning. This rapidly quenching technique is known to result in a refined microstructure, extended solute solubility and formation of metastable phases (Lyubina 2008). By application of large enough cooling rates which is induced to a molten material, highly disordered structures and therefore high diffusion rate can be achieved. After induction melting of $Fe_{70}Sn_{30}$ and $Fe_{57}Sn_{43}$ alloy, melt spinning was done by ejecting of the alloy to a rotating copper wheel. The melt spinning process parameters which had a significant impact on obtaining long and homogenous ribbons, such as processing temperature, overpressure and wheel speed were optimized. For homogenous melting of the ingot, a very high processing temperature of ~1500°C was required. Due to the low viscosity of the FeSn alloys, achieving continuous ribbons was only possible by keeping very small overpressure (0.1 bar) otherwise material was splashed on the copper wheel and resulted in inhomogeneous powder. On the other hand, although by increasing the wheel speed, a finer microstructure was expected, it has been found that the ribbon thickness decreased only by increasing the wheel speed up to 16 m/s and a further increase of the wheel speed resulted in a mixture of ribbons, flakes and granules with non-optimal microstructure. The optimized ribbons were then cold compacted and together with the Sn-filled reactive crucibles were sealed and annealed for 4 days at a selected temperature between 725°C and 825°C and subsequently quenched. For brevity sake, the compacted melt-spun samples will be shortly denoted as bulk samples.

Figure 4-3 shows the microstructure formed in the bulk $Fe_{70}Sn_{30}$ and $Fe_{57}Sn_{43}$ samples and simultaneously heat-treated Fe-Sn reactive crucibles at 3 selected temperatures, 750°C, 800°C, and 850°C. In addition, Table 4-1 lists the phases formed in the bulk samples, RCM and those predicted in the phase-diagram (Trehaux 1974). At 725°C and 750°C, the phase diagram predicts the formation of two intermetallic phases, Fe_3Sn_2 and FeSn together with α-Fe and Sn. However, in both RCM and bulk samples, in addition to the two mentioned intermetallic compounds, the Fe_3Sn phase was also present. For the Sn-rich bulk sample, in consistent with the phase diagram, Fe_3Sn_2 and FeSn were formed. However, based on the phase diagram, the Fe_3Sn phase is not stable at temperatures below 765°C which disagree with our observation where in the $Fe_{70}Sn_{30}$ sample annealed at 725°C and 750°C, the Fe_3Sn phase coexists with Fe_3Sn_2. Figure 4-3 c shows the microstructure obtained in the diffusion zone of the reactive crucible annealed at 750°C. As can be seen, a thin layer of the Fe_3Sn phase is formed along the crucible and on top of it, a relatively large belt of Fe_3Sn_2 phase is formed. In the top-left corner of the image, two phases, FeSn and Sn, are present. This shows that the reactive crucible reproduces the correct phase relations as in the bulk samples at 725°C and 750°C. An additional experiment on a stochiometric Fe_3Sn conventionally prepared sample shows no trace of Fe_3Sn formation after annealing at 700°C. Therefore, I suppose that the phase diagram reported in (Trehaux 1974), is inaccurate in the temperature interval [725°C-765°C]. For the RCM sample annealed at 725°C (Figure 4-8 b), in addition to the Fe_3Sn phase, further BSE contrasts were observed in the border of Fe crucible which according to EDX were richer in Fe than 3:1 phase. This observation will be investigated in detail in section 4.1.3.

The phase diagram predicts the formation of Fe_3Sn and Fe_3Sn_2 phases in the $Fe_{70}Sn_{30}$ sample and Fe_3Sn_2 and Sn phases in the $Fe_{57}Sn_{43}$ alloy at 775°C. The formation of these phases in both bulk samples and reactive crucibles is consistent with the phase diagram at this temperature.

For higher investigated temperatures 825°C and 850°C, all phase relations produced in both RCM and bulk samples are in agreement with the Fe-Sn binary phase diagram. At these temperatures, the Fe_3Sn_2 phase is no longer stable and it transforms to Fe_5Sn_3 and Sn.

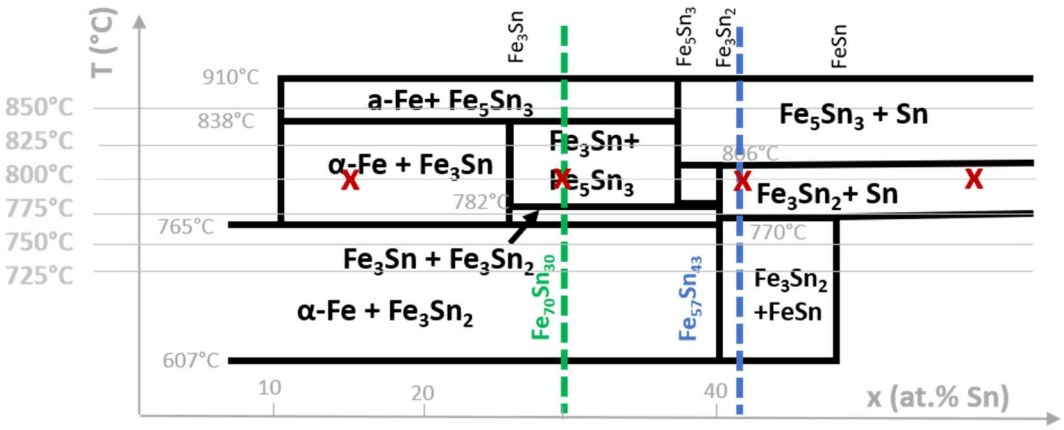

Figure 4-2. A selected area of the binary Fe-Sn phase diagram adapted from (Trehaux 1974). The composition of the prepared samples at 800°C (shown with red crosses) and two compositions $Fe_{70}Sn_{30}$ and $Fe_{57}Sn_{43}$ (shown by dashed lines) were chosen to study the phase diagram in a temperature range of [725°C -800°C] in a region of interest where metastable phases form.

Based on the phase diagram, only in a very small temperature window of [782°C- 806°C], all three ferromagnetic compounds are stable. At 800°C which lies in this temperature range, although all three phases were formed in the homogenously melted alloys annealed under an identical condition as the reactive crucible, the RCM sample fails to produce correct phase relations and the intermediate phase Fe_5Sn_3 phase which was expected to form at the interface between Fe_3Sn and Fe_3Sn_2 layers is missing. Non-attendance of Fe_5Sn_3 in the diffusion zone of RCM at 800°C was well reproducible. To exclude possible obstacles for nucleation of Fe_5Sn_3, different annealing times were used (from 2 days to 10 days). In addition, the annealing procedure was varied in case of approaching to the target temperature 800°C as (i) heating with 5 K/min rate, (ii) inserting into the furnace at 800°C (iii) overheating up to 1000°C (5 K/min) and then cooling down to 800°C (5 K/min). In all cases, the absence of the Fe_5Sn_3 phase was confirmed with accurate EDX analyses. In principle, the temperatures close to 800°C are special temperatures in the Fe-Sn phase diagram, where the situation of "missing phases" can be observed in the reactive crucible. The problem of "missing phases" was already reported in former studies dedicated to the diffusion multiple approach (another bulk high-throughput method) (Zhao 2004). The possible reasons behind the occurrence of this problem in samples with concentration gradients will be discussed in the coming section.

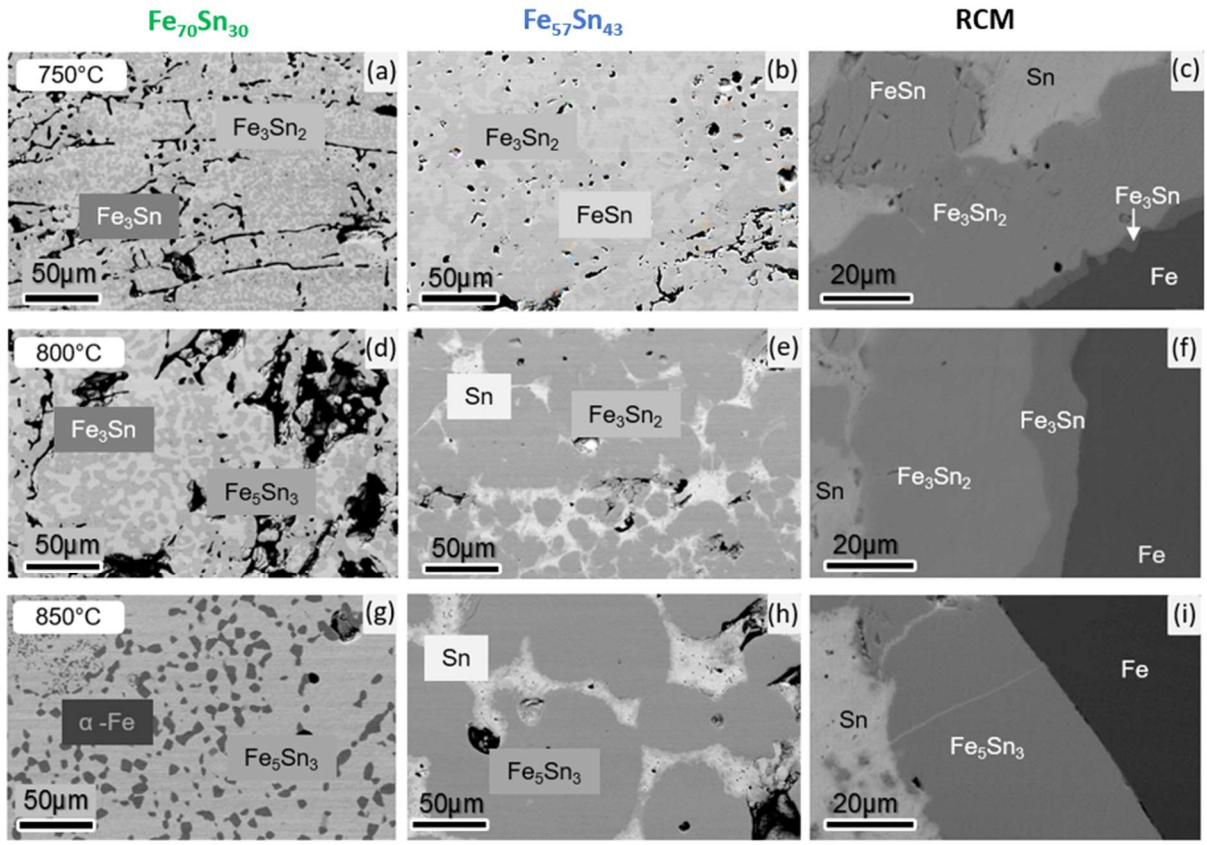

Figure 4-3. The BSE SEM images of samples prepared by melt spinning with the compositions $Fe_{70}Sn_{30}$ (left column), $Fe_{57}Sn_{43}$ (middle column) and reactive crucible samples (right column). Samples were annealed all together at 3 different temperatures for four days and subsequently quenched.

Table 4-1. The comparison of the intermetallic phases forming under an identical heat treatment in homogenous bulk samples, reactive crucibles and those known in the phase diagram.

Temperature	Equilibrated alloy	RCM	Phase diagram
725°C	3:1 - 3:2 1:1	3:1 (& 5:1?) - 3:2 1:1	X - 3:2 1:1
750°C	3:1 - 3:2 1:1	3:1 - 3:2 1:1	X - 3:2 1:1
775°C	3:1 - 3:2 -	3:1 - 3:2 -	3:1 - 3:2 -

Temperature	Equilibrated alloy	RCM	Phase diagram
800°C	3:1 5:3 3:2 -	3:1 X 3:2 -	3:1 5:3 3:2 -
825°C	3:1 5:3 - -	3:1 5:3 - -	3:1 5:3 - -
850°C	- 5:3 - -	- 5:3 - -	- 5:3 - -

Combinatorial analysis and the effect of missing phases

To investigate possible reasons behind the absence of Fe_5Sn_3 in the RCM sample, similar incidence reported in various literature were reviewed. In (van Loo 1973), interdiffusion between Ti and Al was investigated in the Al-Ti diffusion pair. They found that at 625°C, despite 6 expected phases based on the phase diagram (Al, Al_3Ti, Al_2Ti, AlTi, $AlTi_3$, Ti), only one intermetallic compound Al_3Ti exists in the diffusion zone between Al and Ti plates. Ref. (Zhao 2004), affirmed that in most cases of reported missing phases in diffusion couples, annealing was performed at temperatures below half of the homologous melting points. At low temperatures, the formation of intermetallic compounds with a high melting point can be very difficult due to low diffusion rates and slow kinetics. This criterion is not applicable in the case of Sn-Fe binary system, as the Fe_5Sn_3 phase is stable between 782°C and 910°C and therefore temperature of 800°C at which this phase is missing at, is very close to 910°C where this phase is formed by a peritectic reaction of α-Fe and liquid Sn-Fe solution.

Another possible explanation is based on the effect of lattice mismatch between the nucleating phase and the parent phase as in (Bhanumurthy 1990, Kale 1985). In (Bhanumurthy 1990), the interdiffusion behavior of Ni and Zr was investigated. It has been found that Ni_3Zr and $Ni_{21}Zr_8$ intermetallic compounds are forming in equilibrated alloys but do not nucleate in the interdiffusion zone of the Ni and Zr diffusion couple. The absence of $Ni_{21}Zr_8$ was attributed to its triclinic structure which causes a large lattice mismatch with the parent matrix. Change of free energy as a result of the formation of a new phase in the diffusion reaction can be divided into two term: (i) a chemical free energy change due to the formation of an ordered intermetallic compound which is negative and (ii) a change of non-chemical energy as a result of the formation of new interfaces, the introduction of strain, vacancy and supersaturation, which is positive (Bhanumurthy 1990). In our study, the growth of both Fe_5Sn_3 (at 850°C) and Fe_3Sn_2 (at 750-800°) phases on the parent phase of Fe_3Sn was observed. Hence, the absence of Fe_5Sn_3 with the orthorhombic crystal structure (a = 4.221 Å, b = 7.322 Å, c = 5.252 Å) in the diffusion zone at 800°C cannot be attributed to the lattice mismatch with the parent hexagonal Fe_3Sn (a = 5.464 Å, c = 4.352 Å).

The third possible explanation of the "missing phase" effect is based on the nucleation theory (Allen 2005, Gusak 2010). Nucleation theory proposes that for the formation of each phase, there exists an initial size which is equal to the critical nucleus size (about a nanometer). During reactive diffusion, the critical nuclei of an intermediate phase are expected to form in a strongly inhomogeneous region- the interface between other phases - in contrast to the equilibrium state. Hence, they are affected by sharp concentration and chemical potential gradients which account for diffusion fluxes at each interface (Langer 1975, Shatynski 1976). In such a situation, additional controlling factors on the growth rate of planar layers can be heat conduction, mass diffusion or interface source-limited conditions. As a result of heterophase fluctuations in the interface of two parent metals, successive layers of critical nucleus for all existing intermediate phases can appear. Among them, only those nuclei whose linear dimensions exceed a certain critical value will be stable. This critical radius corresponds to the condition, where the "gain" in the volume part of the system's free energy is in competition with the "loss" due to the surface energy. Nuclei smaller than critical size are thermodynamically unstable, thus, immediately disintegrate. Intermetallic phases with larger diffusivity and smaller critical size consume all the neighboring newly formed nuclei and make them be present only virtually – in the form of

constantly forming (due to heterophase fluctuations) and immediate vanishing (due to diffusive suppression by the neighbors) embryos. Criteria of suppression and growth for the simplest cases are discussed in (Gusak 2010). The suppression of Fe_5Sn_3 nucleation can be responsible for the observed discrepancy between the results obtained by the RCM combinatorial technique and the Fe-Sn equilibrium phase diagram.

Although combinatorial techniques play an important role in accelerating the material discovery with desirable properties and allow a rapid and efficient investigation of the phase evolution as a function of concentration and temperature, nevertheless, their reliability to provide accurate data should be validated. One should note that the RCM method is a relatively simple technique with experimental conditions close to conventional metallurgy. If the discrepancy has already been found here and the phase relationships have been reproduced incompletely, the problem of missing phases is likely to be exacerbated by more sophisticated methods of combinatorial analysis (e.g. deposition of thin films with composition gradients (Boettcher 1955), continuous phase diagramming (Zhao 2006), phase diagram on a chip (Xiang 2002) and etc).

High-throughput characterization for identification of uniaxial ferromagnetic phases

Competency of combinatorial methods is not only the high-throughput synthesis of material libraries but also prompt identification of those with desirable properties. In the RCM method, once the phase diagram is constructed, the functional magnetic properties of existing intermetallic compounds should be checked using an appropriate high-throughput technique working at a micrometer length scale. For observation of magnetic domains, Kerr microscopy is used as it offers very short image acquisition time and a spatial resolution of 0.6 µm. As shown in Figure 2-10, phases possessing a uniaxial magnetic anisotropy always demonstrate either typical stripe domain patterns if the magnetization lies in-plane, or branched/Kittel domains if the magnetization is perpendicular to the observation plane. Therefore, this distinguishing feature of uniaxial domain patterns can be used as a selection criterion for the identification of new hard magnetic phases in combinatorial analysis.

Figure 4-4 shows the Kerr images of the reactive crucibles annealed at 750°C, 800°C and 850°C. The forming phases show quite distinct domain patterns. The domain structure of the Fe_3Sn and Fe_5Sn_3 are typical for materials with magnetic anisotropy of easy plane type whereas Fe_3Sn_2 shows a well-pronounced uniaxial magnetic domain structure. A detailed investigation was done for interpretation of the domain structure of Fe_3Sn_2 on single crystalline samples which will be discussed in section 4.3. Furthermore, evaluation of the intrinsic magnetic properties of the Fe_3Sn_2 phase based on analytical models will be discussed in 2.4.2. Nevertheless, only based on the RCM technique, a quick assessment of anisotropy energy for Fe_3Sn_2 by the presumption of $Q > 1$ as in (Goll 2015) is possible. Quality factor Q is the ratio between the energy density of magnetic anisotropy K and the stray field energy density K_d. Considering $K_d = J_s/2\mu_0$ which is the stray field energy density for a plate that is uniformly magnetized perpendicular to its surface and J_s = 0.7 T for Fe_3Sn_2 (Sales 2014), an anisotropy constant of 1 MJ/m^3 or even higher can be estimated. This value is one order of magnitude larger than the actual anisotropy of this compound obtained by conventional magnetometry (see section 4.2.3). Under which conditions a reliable estimation of magnetic properties based on domain analysis of RCM samples might fail will be discussed in 4.3.1.

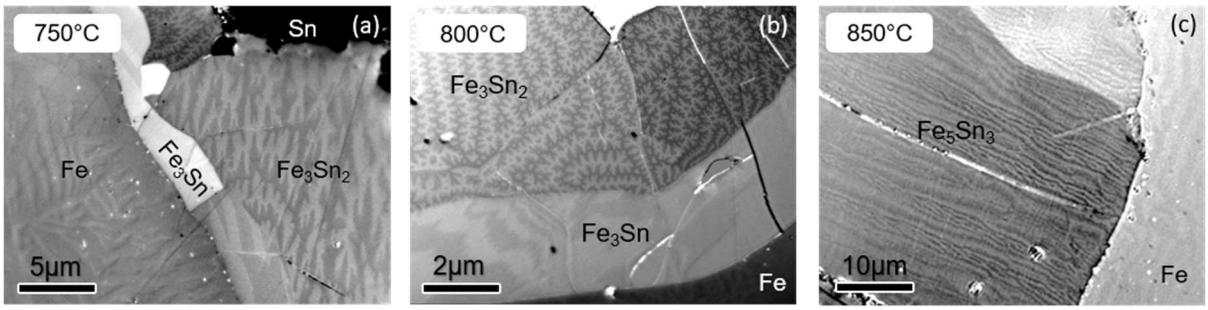

Figure 4-4. The Magneto-Optical Kerr images of the reactive crucibles annealed at 750°C (a), 800°C (b) and 850°C (c). The observed domain structures of different intermetallic compounds are distinct.

As already mentioned, the observed domain structure of Fe_3Sn represents its planar anisotropy as reported in (Sales 2014). The easy direction of magnetization of Fe_3Sn lies in the hexagonal plane which makes it impractical as a permanent magnetic material. Nevertheless, the large absolute value of MAE referred to this compound was a driving force for many researchers to check whether alloying of this Fe-rich compound can switch the anisotropy from planar to uniaxial. In the next section, the influence of different dopants on the phase stability and MAE of Fe_3Sn is discussed.

4.1.2. Searching for uniaxial $(Fe,X)_3(Sn,Y)$ compound

This study was performed under the framework of the NOVAMAG project mainly in collaboration with Uppsala university and resulted in a joint publication (Vekilova 2019). The effect of partial substitution of Sn in Fe_3Sn by elements around it in the periodic table which can likely turn the anisotropy to uniaxial was investigated by experiment and theory. The theoretical calculations were done by Dr. Olga Vekilova based on Density Functional Theory (DFT). Figure 4-5 shows the calculated MAE in $Fe_3Sn_{0.75}Y_{0.25}$ compounds as a function of the number of valence electrons color-coded for dopants from different rows of the periodic table. The results show a drastic variation of MAE with partial substitution of Sn by its neighboring elements whereas the sign of anisotropy can be tuned to positive (uniaxial anisotropy) for Y = Sb, Te and As. A similar trend was shown for the anisotropy in all considered rows starting from the largest but negative (planar) anisotropy from the group IIIA (Ga and In) towards uniaxial MAE anisotropy with an increase of the number of valance electrons. The maximum theoretical MAE was obtained for dopants belonging to Group VA but anisotropy started to decrease with a further increase of the number of valance electrons (e.g. Group VIA). Calculation of anisotropy in $Fe_3Sn_{0.5}Sb_{0.5}$ showed a decrease in anisotropy as a result of more valance electrons which is shown with a red square in Figure 4-5. Therefore, it was concluded that anisotropy depends more on the number of valence electrons than on the choice of a particular dopant. Hence, for experiments, several dopants were considered. For the investigation of $Fe_3(Sn,Y)$, the RCM method was employed. Although RCM failed in the formation of the intermediate Fe_5Sn_3 phase in the binary system, Fe_3Sn phase was observed in a temperature range between 725°C and 800°C in the reactive crucibles. Therefore, in the quest for uniaxial anisotropy, RCM samples with Y = Sb, Si, Ga, Ge, In, Pb and Bi were synthesized. The Sn:Y of 1:1 ratio was considered as RCM produces diffusion gradients. Due to the

toxicity of As and Te, they were excluded from experimental investigations. To provide the required condition for stabilization of the 3:1 phase, the crucibles were annealed at three selected temperatures of 740°C, 770°C and 800°C for 5 days and subsequently quenched. The phases formed in the diffusion zone of the crucible are listed in Table 4-2.

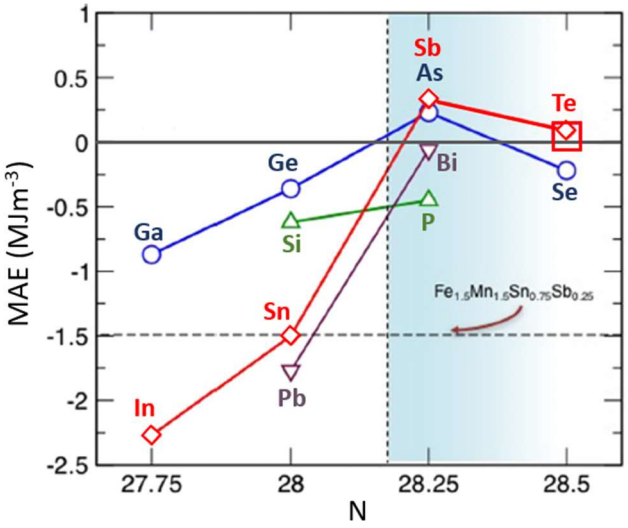

Figure 4-5. The calculated magnetocrystalline anisotropy energy (MAE) in $Fe_3Sn_{0.75}Y_{0.25}$ compounds as a function of the number of valence electrons, N. The color coding separates the doping elements which are from different rows (period) of the periodic table. The favorable area where the easy magnetization axis is uniaxial is shown with the gradient background. The calculated MAE of $Fe_{1.5}Mn_{1.5}Sn_{0.75}Sb_{0.25}$ is shown with a horizontal dashed line as its number of valance electron (26.75) is not in the range of the plotted graph. The large open square represents the anisotropy of $Fe_3Sn_{0.5}Sb_{0.5}$.

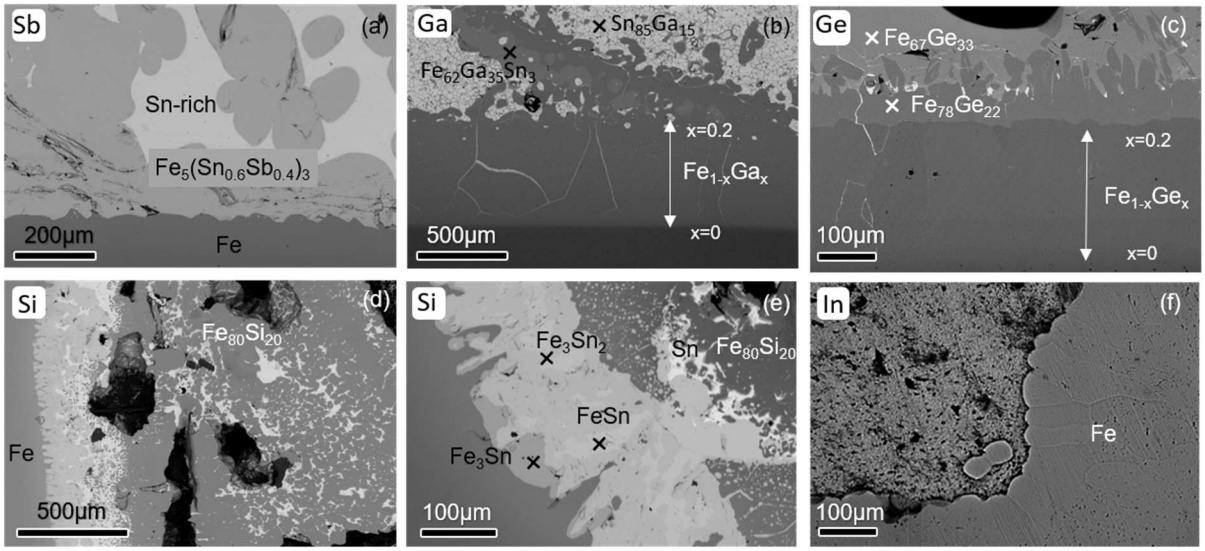

Figure 4-6. Diffusion zone of the Fe-Sn-Y (Sn:Y of 1:1) reactive crucibles annealed at 740°C in (a) Y = Sb, (b) Y = Ga and (c) Y = Ge and at 780°C in (d, e) Y = Si and (f) Y = In. Figure (d) and (e) are taken from an identical sample where (d) shows the overview image and (e) is the magnified image where Fe-Sn binary compounds were formed.

Figure 4-6 shows the microstructure of some representative Fe-Sn-Y Sn:Y; 1:1 RCM samples. It has been found that substitution of Sb for Sn destabilizes the formation of Fe_3Sn phase at all investigated temperatures and only $Fe_5(Sb,Sn)_3$ ternary compound was observed in the crucibles. This held true for additionally prepared RCM crucibles with Sn:Sb 3:1 and 5:1. As Sb was considered as the most promising dopants for inducing uniaxial anisotropy, further experiments were carried out on similarly heat-treated equilibrated alloys prepared by induction melting as well as HEBM with $Fe_3Sn_{0.75}Sb_{0.25}$ composition. In all cases, Sb acted as a destabilizer for the 3:1 phase and instead stabilized the 5:3 structure determined by powder XRD. A similar crystal structure as in Fe_5Sn_3 is reported in the binary Fe-Sb phase diagram which shows the existence of an off-stochiometric ε phase $Fe_{3+\delta}Sb_2$ with a hexagonal structure ($P6_3/mmc$) up to 1292 K (Okamoto 1999). However, no structure corresponding to 3:1 was reported in this binary system. The only available ternary Fe-Sb-Sn phase diagram which gives the isothermal section at 200°C (Raghavan 2001) also reports the formation of the ε phase with the same structure as in the binary Fe-Sb and Fe-Sn systems. Therefore, in Table 4-2, the formed ternary phase is denoted as 5:3.

The Fe-Sn-Ga crucibles annealed at 800 and 770°C show practically the same results where no intermetallic compounds were formed. In these crucibles, Sn remained unreacted whereas Fe and Ga formed solid solution $Fe_{1-x}Ga_x$ with x up to 28 atomic percent. At 740°C (Figure 4-6 b), in addition to $Fe_{1-x}Ga_x$ solid solution, $Fe_{62}Ga_{35}Sn_3$ phase (composition found by EDX) was identified. This phase corresponds to the so-called B2 (bcc, CsCl-type structure) in the Fe-Ga binary phase diagram (Matyunina 2018). Nevertheless, the $Fe_3(Sn,Ga)$ phase did not form at the attempted temperatures.

In the Ge containing crucibles, the microstructure obtained for all temperatures were quite similar. As can be seen in Figure 4-6 c, on the Fe-rich side of the crucible, a solid solution $Fe_{1-x}Ge_x$ region with x up to 22 atomic percent was formed. Moreover, distinct layers of Fe_3Ge (hexagonal, Ni_3Sn-type) and Fe_2Ge (hexagonal, $InNi_2$-type) (Predel 1995) intermetallic compounds were formed on top of the solid solution region. Larger stability of Fe-Ga (Ge) binary phases and/or higher diffusivity of Ga (Ge) in Fe might be the reason behind the non-attendance of Sn in the phase formation. Sn has remained unreacted in the Fe-poor region of the crucibles. As in Ga containing crucibles, in Fe-Sn-Ge crucibles, $Fe_3(Sn,Ge)$ was not observed in the diffusion zone of the crucibles.

The results from crucibles with Si substitution mimics the microstructure forming in the Fe-Sn binary crucibles. For these crucibles, Si is totally dissolved in Fe and does not diffuse to any of the formed Fe-Sn binary intermetallic compounds in the Fe-rich region of the crucible. As can be seen in the overview BSE image of the Si contained crucible (Figure 4-6 d), all added Si amount is consumed to form an intermetallic compound with a chemical composition of about $Fe_{80}Si_{20}$, determined by EDX scan in the various regions of the crucible. This phase is not reported as a line compound in any of the published binary Fe-Si phase diagram. Based on the Fe-Si phase diagram reported in (Predel 2013), at this concentration and temperature range, order-disorder reactions occur in the α-Fe region and α_1 phase (with up to 27 at % Si) with BiF_3-type superstructure exist. As Si was fully consumed to form a binary compound with Fe, in the binary Fe-Sn crucible, the Fe_3Sn phase (with no Si substitution) was formed in the diffusion zone of the crucible annealed at 770°C.

It is important to note that this study considered only a small temperature range which was found desirable for the formation of the binary Fe_3Sn and hence might be not appropriate for the formation of a doped structure. In addition, RCM provides an unlimited source of Fe which differs significantly from equilibrated alloys; therefore, it is expected that the RCM filling elements are primarily consumed to form most stable phases and might not react to form less stable ones.

Table 4-2. Formed phases in the diffusion zone of the Fe-Sn-Y Y = Sn, Sb, Ga, Ge and Si RCM samples

Crucibles	740°C	780°C	800°C
Fe-Sn	α- Fe, 3:1, 3:2, L (Sn)	α- Fe, 3:1, 3:2, L (Sn)	α- Fe, 3:1, 3:2, L (Sn)
Fe-1Sn-1Sb	α- Fe, $Fe_5(Sn_{0.6}Sb_{0.4})_3$, L (Sn+Sb)	α- Fe, $Fe_5(Sn_{0.6}Sb_{0.4})_3$, L (Sn+Sb)	α- Fe, $Fe_5(Sn_{0.6}Sb_{0.4})_3$, L (Sn+Sb)
Fe-1Sn-1Ga	α- $Fe_{1-x}Ga_x$ x<0.2, $Fe_{62}Ga_{35}Sn_3$, L (Sn+Ga)	α- $Fe_{1-x}Ga_x$ x<0.24, L (Sn+Ga)	α- $Fe_{1-x}Ga_x$ x<0.28, L (Sn+Ga)
Fe-1Sn-1Ge	α- $Fe_{1-x}Ga_x$ x<0.2, $Fe_{74}Ge_{26}$, $Fe_{67}Ge_{33}$, L (Sn+Ge)	α- $Fe_{1-x}Ga_x$ x<0.22, $Fe_{78}Ge_{22}$, $Fe_{67}Ge_{33}$, L (Sn+Ge)	α- $Fe_{1-x}Ga_x$ x<0.22, $Fe_{74}Ge_{26}$, $Fe_{66}Ge_{34}$, L (Sn+Ge)
Fe-1Sn-1Si	α- Fe, α-$Fe_{80}Si_{20}$, FeSn, L (Sn)	α- Fe, $Fe_{80}Si_{20}$, Fe_3Sn, Fe_3Sn_2, FeSn, L (Sn)	α- Fe, $Fe_{80}Si_{20}$, Fe_3Sn_2, FeSn, L (Sn)

For Fe-Sn-Y crucibles which contained In, Pb and Bi, no reaction has occurred. Investigation of Fe-Y and Sn-Y binary phase diagrams revealed that the formation of no binary intermetallic compounds is expected in these binary systems. In the ternary system based on the RCM experiments, the additional Y element also prohibited the diffusion of Sn into Fe crucible and always, a mixture of these elements remained in a liquid state during the heat treatment. An example of the obtained microstructure is shown for Fe-Sn-In in Figure 4-6 f.

Further experiments considered the partial substitution of Fe by its neighboring elements Co and Mn in Fe-X-Sn crucibles (X:Sn 1:10 and 1:1). Figure 4-7 a shows the diffusion zone of the Fe-Co-Sn crucible with Co:Sn 1:10 annealed at 800°C. It can be observed that for even a small amount of Co substitution, 3:1 phase was not formed in the sample and only 3:2 intermetallic phase exists. It should be noted that contrary to Co_3Sn_2, the Co_3Sn phase does not exist in this binary system (Ishida 1991). With a higher amount of Co substitution (Co:Sn 1:1), the only observed phase was $Fe_{0.8}Co_{0.2}Sn$ (1:1) phase which although is considered as low-temperature phase in the binary Fe-Sn phase diagram but form at temperatures up to 936°C in the Co-Sn system. RCM results of Fe-Mn-Sn crucibles shows that Mn acts as a stabilizer in the formation of the 3:1 structure. As can be seen in Figure 4-7 b, a much thicker (∼150 µm) layer of 3:1 phase was formed in the sample with Mn:Sn 1:1 in comparison to binary Fe-Sn RCM (∼10 µm) synthesized under the same annealing condition.

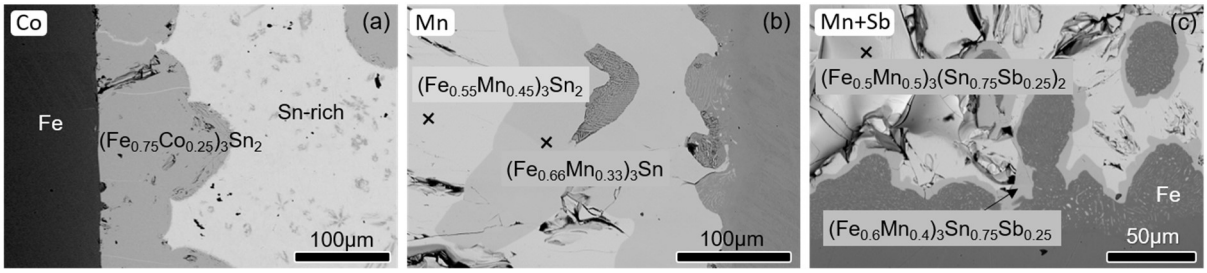

Figure 4-7. Diffusion zone of the (a) Fe-Co-Sn reactive crucible with Co:Sn 1:10, (b) Fe-Mn-Sn RCM with Mn:Sn 1:1 and (c) Fe-Co-Sn-Sb with Co:Sn:Sb 3:3:1. A narrow layer of $(Fe_{0.6}Mn_{0.4})_3(Sn_{0.75}Sb_{0.25})$ is formed although the 3:2 phase is the dominant forming phase in the crucible

As Mn is found to act as a stabilizer of the 3:1 phase, it was assumed that substitution of Mn (with one electron less than Fe) for Fe can compensate 1 electron excess of Sb rather than Sn and might stabilize the desirable 3:1 phase in Sb containing samples. Therefore, Fe-Mn-Sn-Sb RCM samples have been synthesized with Mn:Sn:Sb filling atomic ratio of 3:3:1 (denoted as Fe-Mn3-Sn3-Sb1) as the desirable composition was chosen to be $(Fe_{0.75}Mn_{0.25})_3(Sn_{0.75}Sb_{0.25})$. Figure 4-7 c shows the BSE image of Fe-Mn3-Sn3-Sb1 crucible annealed at 740°C for 5 days and subsequently quenched. By partial substitution of Mn for Fe, Sb was doped in the 3:1 structure and the hexagonal Mg_3Cd -type structure was preserved. A thin layer of $(Fe_{0.6}Mn_{0.4})_3Sn_{0.75}Sb_{0.25}$ phase is formed which bordered by Fe crucible. However, the most stable phase which has been formed in large quantity is found to be $(Fe,Mn)_3(Sn,Sb)_2$. Thus, by means of the RCM method, the phase stability of the Sb-Mn co-doped Fe_3Sn compound was confirmed. However, further attempts for the synthesis of the single phase 3:1 sample with co-doping of Mn and Sb using mechanical alloying which was performed by another project partner (Vekilova 2019) was not successful and all $Fe_xMn_{1-x}Sn_ySb_{1-y}$ (x = 3 and y = 1; x = 2.25, 2, 1.5, and y = 0.75; and x = 1.5, and y = 0.9) samples contained a large amount of secondary 3:2 phase in agreement with RCM results.

To examine whether the addition of Mn to the $Fe_3(Sn,Sb)$ compound preserves the predicted uniaxial anisotropy of the compound, Kerr microscopy was done on the formed Mn/Sb substituted 3:1 phase in the RCM sample. Our Kerr analysis showed a non-uniaxial domain structure of the compound. In agreement with the experimental observation, further theoretical calculations by DFT found a negative theoretical value of MAE for the $Fe_{1.5}Mn_{1.5}Sn_{0.75}Sb_{0.25}$ system with the same value as in the Fe_3Sn compound (Figure 4-5). It can be concluded that although Mn stabilizes the Sb-doped 3:1 structure, however, it flips the anisotropy back to the planar anisotropy value of the undoped compound.

To summarize, theoretical calculations showed that the anisotropy of the Fe_3Sn compound can be tuned by partial substitution of Sn with its neighboring elements. Based on the theoretical calculations, the substitution of 25% of Sn by Sb, As and Te results in a uniaxial anisotropy with Sb giving the largest absolute value. Nevertheless, the experimental study using the RCM and equilibrated alloy method showed destabilization of the structure with Sb substitution. It has been found that co-doping of Sb and Mn stabilizes the system experimentally, however, turns the anisotropy back to planar. Therefore, further search for better stabilizers or their combinations might be considered to find a compromise between the stability and the desired uniaxial MAE.

4.1.3. Stabilization of Fe_5Sn compound

The attempt to stabilize Fe_5Sn compound was also done under the framework of the NOVAMAG project and was motivated mainly by theoretical calculations. The theoretical analyses were done by Dr. Ingo Opahle from TU Darmstadt and Dr. Sergiu Arapan from UBU-ICCRAM. As already discussed, the high T_C as well as the large absolute value of MAE in Fe_3Sn compound as a result of the interplay of Fe 3d magnetism and strong spin-orbit coupling of the Sn 5p states, demonstrate a certain potential of Fe-Sn based alloys as permanent magnet materials. A DFT high-throughput screening was done for Fe-Sn binary compounds with more than 150 structures (including common structure types reported in chemically similar systems). Figure 4-8 a shows the calculated zero-Kelvin phase stability of the trial structures. Potentially (meta)stable phases with a distance to the convex hull of less than 50 meV/atom are shown with colored circles. These compounds have the potential to be stabilized at high temperatures or upon moderate alloying. In addition to the known intermetallic compounds $FeSn_2$ ($CuAl_2$-type), FeSn (CoSn-type), Fe_3Sn_2 (Fe_3Sn_2-type) and Fe_3Sn (Mg_3Cd_2-type) phases, four phases are found close to the convex hull of stable compounds which one is an orthorhombic Fe_3Sn_2 (Ni_3Sn_2-type). It should be noted that the disordered hexagonal Fe_5Sn_3 (Ni_2In-type) phase reported in the literature has about 80 meV/atom distance from the convex hull and therefore should be energetically less favorable than Fe_3Sn_2 (Ni_3Sn_2-type) which is so far not reported in the Fe-Sn system. This point will be pursued in section 4.2.2.

Three further Fe-rich compounds which are found in the vicinity of the convex hull are $Fe_{13}Sn_3$ ($Fe_{13}Ge_3$-type) structure, a monoclinic Fe_5Sn (Pd_5As-type) structure and a hexagonal Fe_5Sn (space group #164, (P-3 2/m 1)). The latter structure has not been observed in any similar 5:1 structure-type up to now. This hexagonal Fe_5Sn (shown with a red circle in Figure 4-8 a) has higher stability (comparable with Fe_3Sn) in comparison to the former ones. Furthermore, the theoretical calculation for the estimation of its magnetic properties predicts a saturation magnetization of 1.7 T, and magnetocrystalline anisotropy energy of 1.5 MJm^{-3}, making it a very promising potential candidate as a permanent magnetic material. Therefore, this section is dedicated to searching for the Fe_5Sn theoretically predicted compound.

As already mentioned, the Fe-Sn RCM sample annealed at 725°C showed several BSE contrasts in the Fe-rich region of the diffusion zone. Figure 4-8 b shows these contrasts which according to EDX analysis, their compositions were determined as; (1) $Fe_{82}Sn_{18}$, (2) $Fe_{78}Sn_{22}$, (3) $Fe_{80}Sn_{20}$. Due to the very small diffusion length of these phases (~ 1.5 µm) which is close to the spatial resolution of the used EDX system, highly accurate determination of the chemical composition was not feasible. As can be seen, the darkest contrast (3) which was expected to correspond to the compound with the largest Fe content is not correctly evaluated using EDX analysis. This is due to its small surface area which is fully surrounded by Fe-deficient compound (Fe_3Sn_2) in contrast to (3) which is bordered with Fe crucible. As the solubility of Sn in Fe is not more than 10 % based on Fe-Sn binary phase diagram, the formed regions were considered to correspond to highly metastable phases which are spontaneously formed and decomposed to another stable phase such as Fe_3Sn_2. The same behavior is known for the MnAl system, where favorable hard magnetic $L1_0$ τ-phase is quite unstable and only can be obtained under the special condition and by short term annealing otherwise decomposes into γ(Al_8Mn_5) and β-(Mn) phases only after 1 hour of annealing at about 500°C (Pareti 1986).

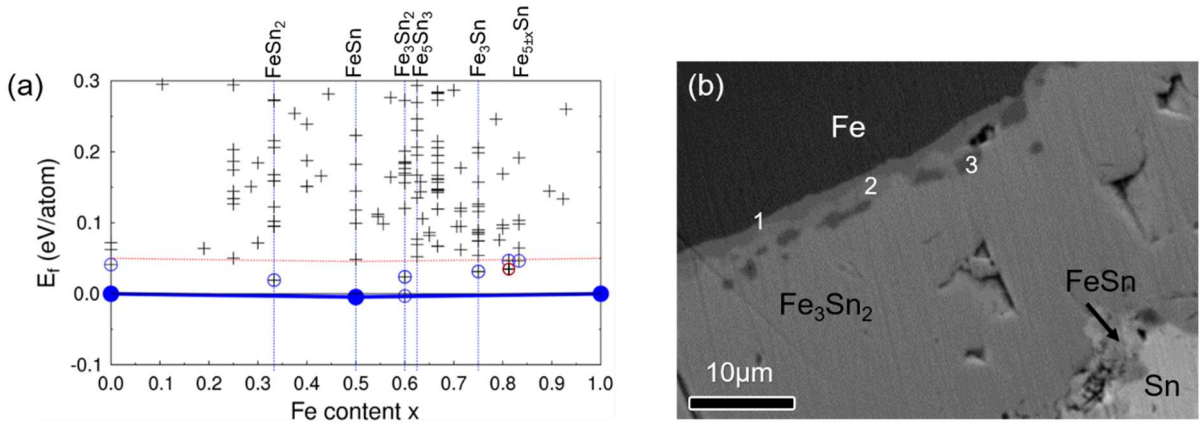

Figure 4-8. Formation energies of several structures calculated for binary Fe-Sn system plotted as a function of Fe content. The stable compounds are shown with filled blue circles on the convex hull. Potentially metastable phases which showed formation energy of less than 50 meV/atom further from the convex hull are shown by open blue circles. Many other structures which were calculated in the study are shown with black pluses. Two Fe-rich compounds with compositions close to Fe_5Sn were found to be of great interest to be explored experimentally. (b) The Diffusion zone of Fe-Sn crucible annealed at 725°C for one week and subsequently quenched. Three different contrasts observed in BSE mode of the SEM in the Fe-rich region of the reactive crucible were numbered and according to EDX analysis are 1. $Fe_{82}Sn_{18}$, 2. $Fe_{78}Sn_{22}$, 3. $Fe_{80}Sn_{20}$

For experimental screening of new phases, in addition to combinatorial methods based on composition gradients, the application of non-equilibrium bulk techniques such as melt spinning and mechanical alloying is quite common. In melt spinning, by controlling the speed of the wheel, one can change the structure from amorphous to nanocrystalline to microcrystalline state. In mechanical alloying**,** the material (in the form of coarse alloy powders or powders of the constituent elements) is put in a jar with or without surfactants mixed with hard stainless-steel balls and shaken for different times. By adjusting the powder/ball ratio, the size of the balls and milling time, different microstructures can be obtained all the way from amorphous to microcrystalline. The idea here was to obtain first an amorphous/disordered structure in the system of interest which after crystallization would lead to the equilibrium/metastable phases that exist in the system. This approach had been used in the past and led to the discovery of Nd-Fe-B magnets (Hadjipanayis 1983).

To search for Fe_5Sn and at the same time accelerating the diffusion rates, highly disordered samples were produced. The stochiometric Fe_5Sn was initially melted using induction melting and subsequently melt spun with a copper wheel speed of 16 m/s and chamber overpressure of 0.1 bar. Figure 4-9 a shows the XRD pattern of the Fe_5Sn melt-spun ribbons which demonstrates a mixture of phases. Accelerating the wheel speed to obtain an amorphous sample was not feasible as it led to a change in morphology of the ribbons to flakes and granules with segregated microstructure. By the introduction of more defects to melt-spun ribbons using HEBM, oversaturated Fe with bcc structure is obtained, which can be realized from the appeared relatively broad peaks in the corresponding XRD patterns (red pattern). The HEBM was done for 24 hours using SPEX 8000 D with 875 cycle/min and an optimal ball-to-powder ratio of 5:1. A similar result was obtained by direct HEBM of the high purity Fe and Sn

powders with Fe:Sn 5:1 atomic ratio under the same condition as for the as-spun sample. As the Fe structure is quite stable, the amorphization of the Fe-rich alloy was unfavorable even with longer milling times. All samples investigated in this study were synthesized by 24 h HEBM of mixed high purity powders with subsequent cold compaction.

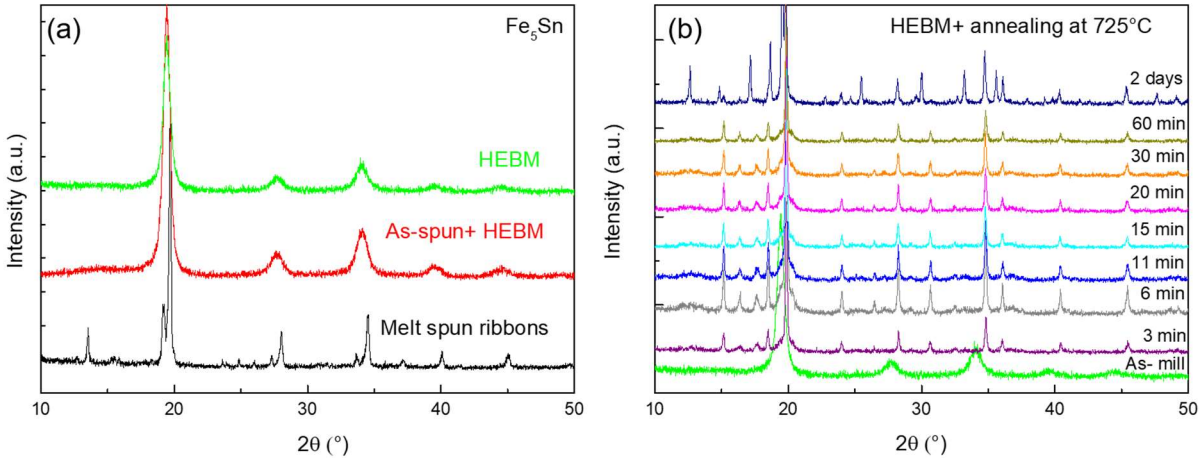

Figure 4-9. Powder X-ray diffraction pattern of the (a) Fe_5Sn melt-spun ribbons (black), as-spun Fe_5Sn after 24 hours high energy ball milling (red) and Fe_5Sn mixed fine powders after 24 hours of HEBM- mechanical alloying (green) and (b) Fe_5Sn as-milled sample after heat treatment at 725°C for 3 minutes up to 2days.

Initially, the incidence of any magnetic transition was checked by *M-T* measurement using static magnetic fields up to 1000°C. With heating and cooling rates of 2 K/min, the only detected transition was attributed to the Curie temperature of Fe. To check whether Fe-rich predicted phase forms at 725°C, the temperature at which RCM showed the appearance of Fe-rich regions, the as-milled samples were annealed at 725°C for different durations from 3 minutes to 2 days and subsequently quenched. XRD patterns of the samples are shown in Figure 4-9 b. The structure of the samples annealed for 3 to 60 minutes are similar and clearly different from the sample annealed for 2 days. The microstructure of the samples annealed for 2 days and the one annealed for 6 minutes together with their corresponding XRD patterns are shown in Figure 4-10. Rietveld refinement of the XRD pattern of the sample annealed for 2 days shows 60 % of α-Fe and 40 % of hexagonal Fe_3Sn phase ($P6_3/mmc$, a = 5.47122 Å, c = 4.36305).

The XRD pattern of the samples obtained after 3 to 60 minutes of annealing could not be refined using the Rietveld method as the intensity of none of the possible binary compounds were matching the pattern. Using Lebail refinement which is a phase-matching method, not taking the atoms and atomic positions into account, the XRD pattern of these samples could be indexed with α-Fe and Fe_3Sn_2 phases. The high-intensity peaks of the Fe_3Sn_2 compound are the (0 2 4) and (2 0 5) reflections at 2θ = 19.5° and 20.5° respectively. The intensity of these reflections is in the range of measurement noise and therefore made the identification of the phase difficult. On the other hand, a very small amount of secondary phase was found in the microstructure of the sample (BSE image in Figure 4-10 b) where

the α-Fe fraction of the sample was estimated to be at least 85 %. The reason behind the incompatibility of the peak intensities might be the short annealing time of the sample which led to the formation of highly disordered Fe_3Sn_2 compound. No structure attributing to the predicted Fe_5Sn was not formed at this specific temperature.

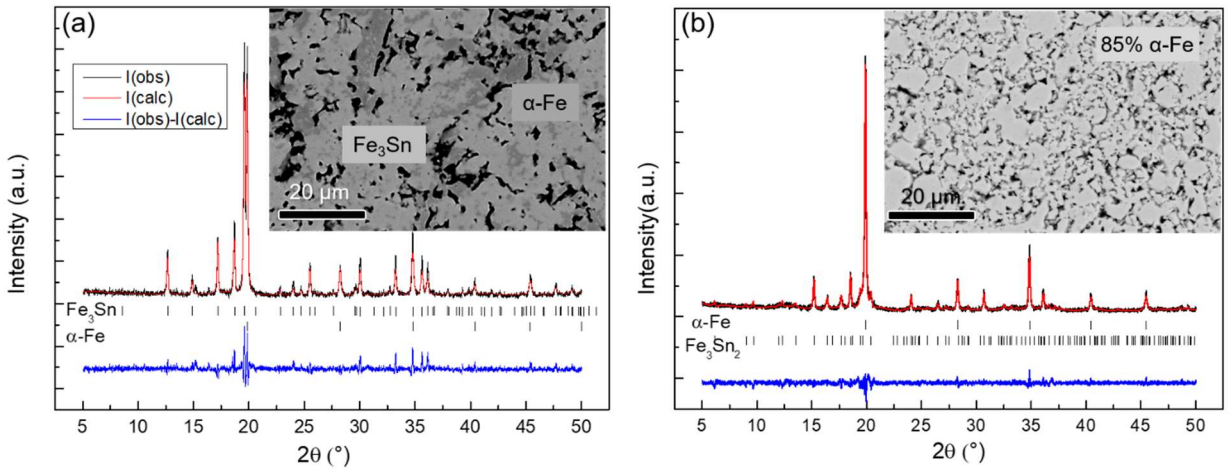

Figure 4-10. (a) Rietveld refinement of a powder XRD pattern of the Fe_5Sn sample annealed at 725° C for 2 days. (b) Le Bail fit of a powder XRD patterns of the Fe_5Sn samples annealed at 725° C for 6 minutes where the pattern could be indexed with α-Fe and highly distorted Fe_3Sn_2 phase. The inset in each figure shows the microstructure observed in BSE SEM of the corresponding sample. Observed data points, calculated and difference curves and reflection markers, respectively.

Further theoretical calculations were performed to investigate the effect of a ternary element substitution on the stabilization of Fe_5Sn. For these calculations, a supercell made of 8 unit cells of Fe_5Sn (space group #164) was considered where one Fe atom was replaced by an impurity (2.08 % at.), that is, $Fe_{39}Sn_8X$ at different sites: (i) (1/3,2/3,0.20753) labeled by 2d(1) , (ii) (1/3,2/3,0.66713) labeled by 2d(2), and (iii) 1b (0,0,1/2) (see Figure 4-11 a). The supercell structures were relaxed allowing ionic positions, cell volume, and cell shape to change. The computed enthalpy of formation of $Fe_{39}Sn_8X$ for many different impurities is presented in Figure 4-11 e. In this figure, the dashed line represents the corresponding value of predicted Fe_5Sn. It has been observed that the energy per atom is decreased with respect to Fe_5Sn using transition metals like Ti, V, Cr, Mn, Nb and Mo as impurities. As part of our task in the NOVAMAG project, the substitution of TM metals was attempted for the stabilization of Fe_5Sn.

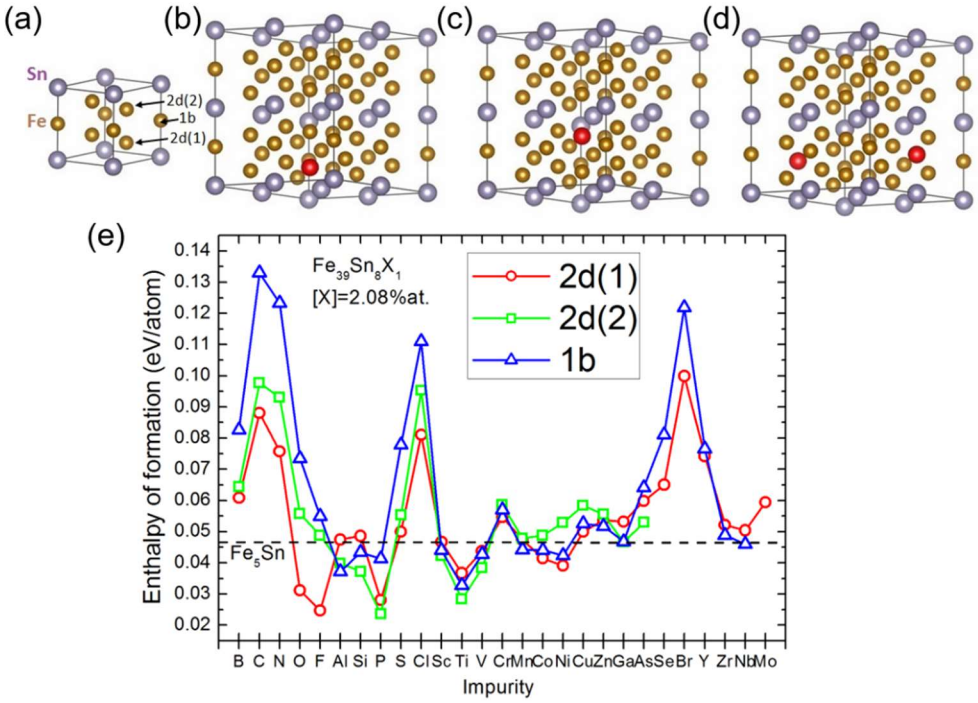

Figure 4-11. (a) Predicted Fe_5Sn unit cell (space group #164) and supercell $Fe_{39}Sn_8X$ where impurity (red atom) replaces a Fe atom at: (b) site 2d (1/3,2/3,0.20753), (c) site 2d (1/3,2/3,0.66713) and (d) site 1b (0,0,1/2). (b) Energy per atom of supercell $Fe_{39}Sn_8X$ where an impurity X is placed either at site 2d (1/3,2/3,0.20753), site 2d (1/3,2/3,0.66713) or site 1b (0,0,1/2). The dash line represents the energy per atom of predicted Fe_5Sn.

For experimental screening of theoretically recommended doping elements, extensive study has been carried out by fabrication of samples with $Fe_{39}Sn_8X$ composition where X = Fe, Ti, V, Cr, Mn, Co, Nb and Mo. The samples were synthesized by HEBM under the same condition as previously mentioned and heat-treated in a temperature range of [550°C - 900°C] for 24h and subsequently quenched. In total, 64 samples were synthesized and characterized.

By annealing at low temperatures, 500°C, 550°C, 600°C, 650°C and 700°C, due to a slow diffusion rate, a very fine microstructure was obtained. At these temperatures, all samples show a very similar microstructure with two-phase contrast with almost identical volume fraction observed by BSE imaging. As an example, the BSE image of the $Fe_{39}Sn_8Co$ sample annealed at 600°C is given in Figure 4-12 a. As grains are in nanometer size, quantification of the chemical composition was not feasible by EDX analysis. Nevertheless, based on BSE analysis and by observation of two-phase contrast, one can judge that $(Fe,X)_5Sn$ is not formed at these temperatures. By annealing at higher temperatures, the diffusion rate increases, and coarser microstructures are obtained. Figure 4-12 shows the grain growth in $Fe_{39}Sn_8Co$ samples with increasing temperature. The chemical compositions of the formed phases were determined using EDX analysis and are listed in Table 4-3 for samples annealed in a temperature range of [750°C- 900°C]. Two main phases with the majority volume fraction are bolded in the table. It should be noted that to distinguish the 3:2 phase from 5:3 which possess very close chemical composition, XRD measurements were done. Unfortunately, no trace of Fe_5Sn formation was observed

in any of the prepared samples. Either Fe_5Sn does not exist at all or the formation conditions were not fulfilled.

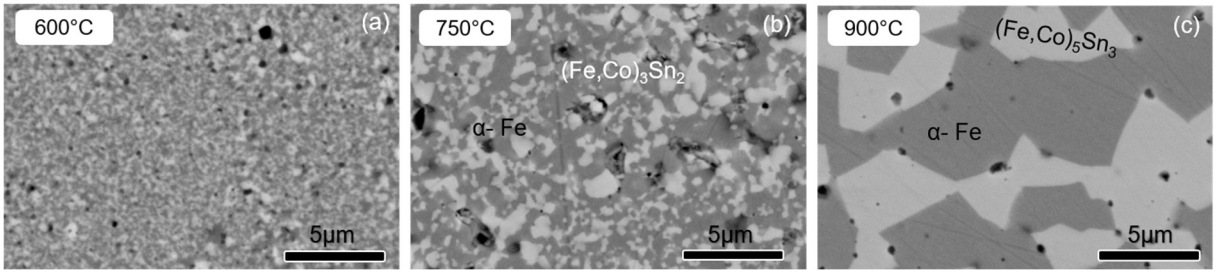

Figure 4-12. The BSE images of the $Fe_{39}Sn_8Co$ samples prepared by HEBM after annealing at (a) 600°C, (b) 750°C and (c) 900°C for 24 hours

The effect of alloying elements on the phase formation of $Fe_{39}Sn_8X$ is summarized in the following. In all investigated systems including binary Fe_5Sn, the 3:1 phase was stable up to 850°C. This is while our investigation in 4.1.1 on Sn-richer equilibrated sample ($Fe_{70}Sn_{30}$) showed decomposition of this phase to high temperature 5:3 compound above 825°C. The result shows higher temperature stability of the 3:1 phase in the Fe-rich region of the phase diagram. Furthermore, the stability of the 3:1 phase was improved by a substitutional element such as Mn and Ti. By Mn substitution larger 3:1 phase fraction was observed in comparison to the binary system in each investigated temperature in agreement with the observation in 4.1.2. For Ti contained sample, some traces of 3:1 was remained up to 900°C. Alloying elements such as Cr, Nb and V did not affect the phase formation considerably and the same intermetallic compounds as observed in the binary system were formed in the samples. Except for Mo, all substitutional elements diffused to the formed intermetallic compounds. However, by alloying with Mo, the whole Mo amount was consumed to form a solid solution with Fe. Nevertheless, its presence in the microstructure totally changed the phase formation as no 3:1 was formed in the whole temperature range and 3:2 was decomposed to 5:3 compound at a temperature above 800°C. The effect of Co substitution was in accordance with 4.1.2 where even a small Co substitution destabilizes the formation of Fe_3Sn structure.

Although this extensive study was not able to discover the theoretically predicted 5:1 structure in Fe-Sn -based system, it might guide other researches in respect of phase formations in these binary and ternary systems. As mentioned in 2.3.1, to the best of our knowledge all reported Fe-Sn binary phase diagrams in the literature except for (Trehaux 1974) did not consider the Fe_3Sn compound. Our observation shows the existence of this phase in the temperature range between [725°C and 850°C]. This means that especially the Fe-rich side of the phase diagram should be investigated in more detail and established further.

Table 4-3. List of forming phases in $Fe_{39}Sn_8X$ HEBM samples annealed in a temperature range between 750°C and 900°C. The samples were annealed for 24 hours and subsequently quenched. The phases with the majority volume fraction are bolded

$Fe_{39}Sn_8X$/ temperature	Fe	Ti	V	Cr	Mn	Co	Nb	Mo
750°C	**α-Fe** **Fe_3Sn** X Fe_3Sn_2	**α-Fe** **3:1** X 3:2	**α-Fe** **3:1** X 3:2	**α-Fe** **3:1** X 3:2	**α-Fe** **3:1** X X	**α-Fe** X X **3:2**	**α-Fe** **3:1** X 3:2	**α-Fe** X X **3:2**
800°C	**α-Fe** **Fe_3Sn** X X	**α-Fe** **3:1** X X	**α-Fe** **3:1** X X	**α-Fe** **3:1** X X	**α-Fe** **3:1** X X	**α-Fe** **3:2** X X	**α-Fe** **3:1** X X	**α-Fe** X **5:3** X
850°C	**α-Fe** **Fe_3Sn** X X	**α-Fe** **3:1** X X	**α-Fe** **3:1** X X	**α-Fe** **3:1** X X	**α-Fe** **3:1** X X	**α-Fe** X **5:3** X	**α-Fe** **3:1** 5:3 X	**α-Fe** X **5:3** X
900°C	**α-Fe** X **Fe_5Sn_3** X	**α-Fe** 3:1 **5:3** X	**α-Fe** X **5:3** X	**α-Fe** X **5:3** X	**α-Fe** X **5:3** X	**α-Fe** X **5:3** X	**α-Fe** X **5:3** X	**α-Fe** X **5:3** X

4.2. Structural and magnetic properties of binary Fe-Sn compound

In this section, the structural and magnetic properties of all three existing ferromagnetic compounds in the Fe-Sn system were investigated. Although in recent years, several studies were conducted to investigate this material in respect of magnetic and spintronic applications, to the best of our knowledge, this study which is also published in (Fayyazi 2019) is the only study characterizing the magnetic properties of all three ferromagnetic Fe-Sn compounds on single crystalline samples in a wide temperature range. Characterization of structural properties was performed by Dr. Tom Faske from TU Darmstadt, in case single-crystal XRD was applied.

4.2.1. Fe_3Sn

For Fe_3Sn single crystal, the well-established hexagonal Mg_3Cd-type structure in space group $P6_3/mmc$ was confirmed by single-crystal X-ray diffraction. The lattice parameters were found to be a = 5.4539 Å and c = 4.3429 Å.

For magnetic measurement, all single crystals were aligned along their crystallographic orientations using Laue XRD. The magnetization curves of a Fe_3Sn single crystal measured along the *a* [100], *b'* [210] and *c* [001] crystallographic directions at T = 300 K and 10 K are shown in Figure 4-13. The dotted lines represent the magnetization measured at 10 K and solid lines correspond to *M(H)* data obtained at room temperature. Based on the shape of the single crystal, demagnetizing fields were determined for each measured orientation. For all magnetization curves measured on single crystals shown in this section, the demagnetizing fields are subtracted. The obtained *M(H)* curves for Fe_3Sn single crystal

shows the typical behavior of an easy-plane magnetocrystalline anisotropy where [001] is the hard magnetization direction. No magnetic anisotropy is detected within the basal plane as the measured curves along the [100] and [210] are almost identical. The anisotropy remains of the easy-plane type for the whole measured temperature [10 K- 350 K]. By linear extrapolation of saturation magnetization along the [100] axis to zero internal magnetic field, the values of spontaneous magnetizations M_s were determined. The spontaneous magnetization decreases from 128 Am^2kg^{-1} (~ 2.2 μ_B/Fe) at T = 10 K to 120 Am^2kg^{-1} at T = 300 K. The anisotropy field $\mu_0 H_a$ was determined from the intersection of the low field linear section of the hard-axis *M(H)* curve to the easy-axis saturation magnetization. Estimation of anisotropy field at room temperature gives a large value of 2.2 T which decreases with decreasing temperature to 1.8 T at 10 K. The anisotropy energy E_a can be expressed in terms of a series expansion of the direction cosines of M_s relative to the crystal axes by defining anisotropy constants as in Equation 15; $E_a = K_1 \sin^2\theta + K_2 \sin^4\theta + K_3 \sin^6\theta + K_4 \sin^6\theta \cos 6\varphi + \cdots$ where θ and φ are the angles of the magnetization vector to the *c* axis and basal plane, respectively and K_i, i = 1, 2, 3,… are the anisotropy constants. The higher-order anisotropy constants are often negligible and therefore for our calculations, K_3 and K_4 are assumed to be zero.

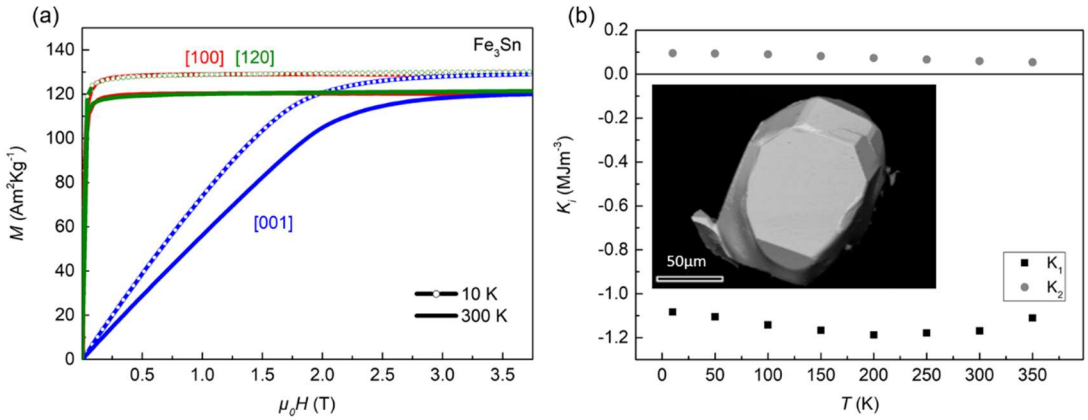

Figure 4-13. (a) Field-dependent magnetization curves of the Fe_3Sn single crystal measured at temperatures of 300 K and 10 K along the crystallographic axes a, b' and c under a magnetic field of up to 3.7 T. The anisotropy field at 300 K and 10 K is 2.2 T and 1.8 T, respectively. (b) Temperature-dependence of the anisotropy constants K_1 and K_2 calculated using the Sucksmith-Thompson method in the temperature range of [10-350 K]. The SEM image of the measured single crystal is shown as an inset to (b).

For calculation of the two first anisotropy constants K_1 and K_2 in all Fe-Sn ferromagnetic compounds, the Sucksmith-Thompson method was employed. As Fe_3Sn showed easy-plane anisotropy for the whole measured temperature range, a modified version of this method as explained in 3.2.4 was applied. The temperature dependencies of K_1 and K_2 for the Fe_3Sn single crystal is shown in Figure 4-13 b in the temperature range between 10 K to 350 K. As expected, K_2 is one order of magnitude smaller than the leading anisotropy constant K_1. The corresponding condition for an easy-plane type of magnetocrystalline anisotropy ($K_1 < 0$ and $0 < K_2 < -K_1/2$) was fulfilled for the whole temperature range. The resulting anisotropy energy at T = 300 K is found to be E_a = -1.2 MJm^{-3}. The reported values of

anisotropy in the literature which are obtained by measurement of oriented powders, overestimated the anisotropy as the reported values are -1.8 MJm^{-3} in (Sales 2014) and -1.3 in (Echevarria-Bonet 2018). This discrepancy affirms the necessity of single crystal data for the most reliable evaluation of the intrinsic magnetic properties. Although the absolute value of anisotropy constant K_1 in Fe_3Sn is considerable for a rare earth free compound, its negative sign makes this material impractical for permanent magnetic application.

Due to the small size of the Fe_3Sn single crystals, magnetic measurement at temperatures above 350 K, led to extremely noisy signal in the implemented PPMS high-temperature setup. Therefore, it was not feasible to report reliable magnetic data. Nevertheless, our magnetic data on Fe_3Sn covers a wide temperature range from 10 K, relevant for theoretical modeling, up to 350 K, important for the permanent magnetic application.

Theoretical investigations based on DFT calculation estimated the magnetocrystalline anisotropy of -1.5 MJm^{-3} as shown in Figure 4-5 in (Vekilova 2019). Combined with our experimental analysis of single crystals, further calculations were done by Dr. Ingo Opahle. Considering the lattice parameters of a = 5.4539 Å and c = 4.3429 Å measured on Fe_3Sn single crystal, MAE of -1.3 MJm^{-3} was calculated which is closer to the actual anisotropy of the compound. The larger estimation of anisotropy in (Vekilova 2019) is due to the different choice of lattice parameters as MAE can be quite sensitive to changes of the c/a-ratio signalized in (Vekilova 2019). The calculated in-plane anisotropy is negligible.

DFT calculation of Fe_3Sn total magnetic moment (Fayyazi 2019) gives a value of 7.21 μ_B/f.u with 97% contribution from spin magnetic moments (6.98 μ_B/f.u) and 0.23 μ_B/f.u from orbital magnetic moment. The theoretically obtained saturation magnetization of 2.4 μ_B/Fe is slightly higher than the experimentally deduced value at 10 K (2.2 μ_B/Fe). The local Fe spin magnetic moment is 2.42 μ_B whereas Sn carries only a small induced moment of -0.28 μ_B which is oppositely polarized to the Fe atoms. The Fe and Sn orbital moments are calculated as 0.077 μ_B and 0.003 μ_B. Although Sn orbital contribution is significantly lower than Fe, nevertheless, the Orbital Moment Anisotropy (OMA) between the easy [100] and hard [001] axis is comparable in absolute value for Sn and Fe (0.0006 μ_B), albeit with opposite sign. This result shows that Sn has a remarkable contribution to the total MAE, as the OMA is closely correlating with MAE.

4.2.2. Fe_5Sn_3

The crystal structure of Fe_5Sn_3 is typically assumed as hexagonal structure ($P6_3/mmc$, a = 4.223 Å, c = 5.253 Å) which is reported in Ref. (Yamamoto 1966). The Fe_5Sn_3 single crystals grown in this study exhibit a hexagonal morphology (Figure 4-14). The EDX analyses of the single crystals show chemical composition close to the stoichiometric value. Single-crystal XRD measurement on these single crystals reveals a diffraction pattern with a hexagonal array of reflections, matching the shape of the crystal. Indexation of the obtained pattern with the literature hexagonal structure leaves thousands of observed superstructure reflections in the *h-k* planes uncovered. This mismatching was not observed in the *h-l* and *k-l* planes, indicating that the [001] direction of the crystal is undistorted. In this study, a new structural model is developed by Dr. Tom Faske where the reflection pattern was treated as a twinned structure where the hexagonal *c**-axis is considered as a twinning axis for three orthorhombic twinned domains rotated by 120° with respect to each other. Each twin domain has a commensurately

modulated orthorhombic unit cell with lattice parameters of a = 4.221 Å, b = 7.322 Å, c = 5.252 Å and q = (0.5, 0, 0). A full description of the structure solution is given in (Fayyazi 2019).

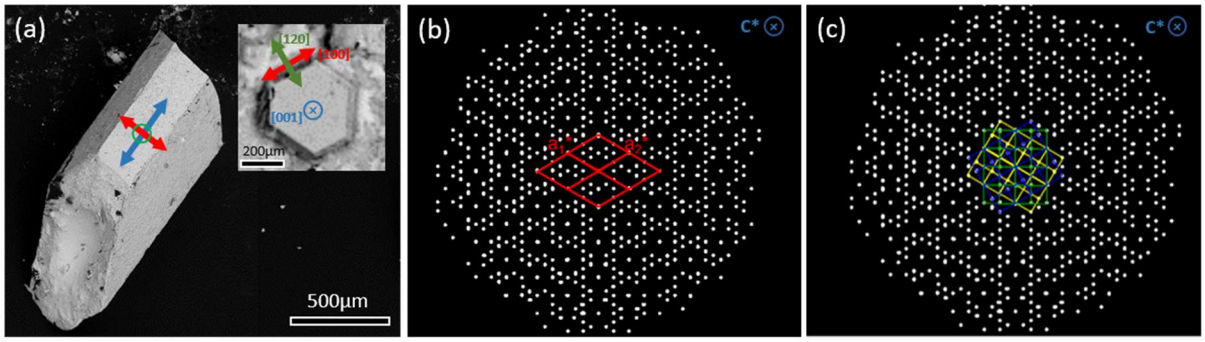

Figure 4-14. (a) BSE SEM image of a hexagonally shaped crystal grown with the stoichiometry of Fe_5Sn_3 with the c axis lying in the observation plane. The inset shows the same crystal where c-axis is out-of-plane. The crystal directions corresponding to a hexagonal coordinate system are shown with colored arrows. (b) and (c) Single-crystal XRD pattern of the full Ewald sphere of Fe_5Sn_3 along the c-axis with indexation according to the (a) hexagonal structure known in literature with lattice parameters of a = 4.22 Å and c = 5.25 Å and (b) with the twin approach using three commensurate (3+1)D orthorhombic unit cells with lattice parameters of a = 4.221 Å, b = 7.322 Å, c = 5.252 Å, q = (0.5, 0, 0). The orthorhombic unit cells are rotated by 120° with respect to each other along the c*-axis.*

To validate the proposed structural model, TEM analysis was done on a FIB lamella which was cut perpendicularly to the (pseudo)-hexagonal *c*-axis of the crystal. As can be seen in the overview low-magnification TEM bright-field image of FIB lamella (Figure 4-15), strong bending contours are present due to lamella's very small thickness. The thickness was measured by electron energy-loss spectroscopy as 27.4 nm. The sample was oriented such that the hexagonal *c**-axis is perpendicular to the image plane. The electron diffraction pattern was acquired from a selected representative area of 200 nm² which was free of bending as shown with a red circle. Similar superstructure reflections as the XRD pattern was observed by electron diffraction. The atomic structure was illustrated by STEM-HAADF imaging from a 50 x 50 nm² area (see Figure 4-15 c and d). Observation of different structural domains with stripe contrast tilted by 60°/120° towards each other confirms the proposed twinned structure. Analysis of Fast Fourier Transformation (FFT) diffractogram of a (50 x 50) nm² HAADF image, shows hexagonal reflection array and superstructure reflections similar to those observed by selected area diffraction. However, the FFT of a single domain highlighted in colored square frames reveals an orthorhombic diffraction pattern. As an example, the FFT diffractogram of a selected area (highlighted in a green frame in Figure 4-15 d) is shown in the inset of the corresponding image. The TEM analysis on the grown Fe_5Sn_3 crystal shows that the sample consists of multiple nano-twinned domains with an orthorhombic structure. Nevertheless, the particular arrangement of twin variants leads to a pseudo-hexagonal character in macroscopic X-ray and electron diffraction patterns. From the combined single-crystal diffraction data of all three orthorhombic twin variant, the crystal structure of Fe_5Sn_3 was solved and refined.

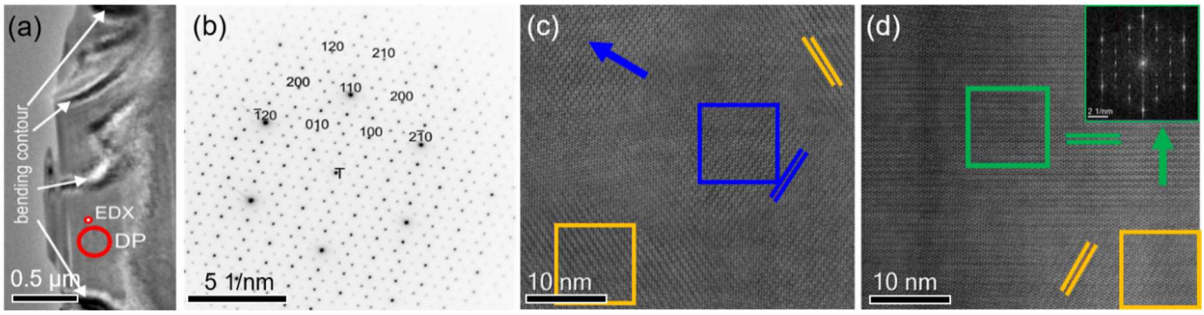

Figure 4-15. (a) The overview TEM image of "Fe_5Sn_3" lamella prepared by FIB with c axis out of observation plane. (b) Diffraction pattern of a selected area (red circle) with a representative region of 200 nm diameter indexed with the hexagonal unit cell parameters a = 4.22 Å and c = 5.25 Å. The superstructure reflections belong to a fourfold superstructure along a. (c) and (d) STEM-HAADF images of two representative areas in [001] zone axis orientation which show 3 particular atomic arrangement directions found in different regions of the sample. The directions are color-coded in accordance with the Figure 4-14. Inset of (d) shows the FFT of a representative twinned domain marked in green, revealing an orthorhombic diffraction pattern.*

A modified unit cell which is proposed for the Fe_5Sn_3 phase is a commensurately modulated orthorhombic unit cell with the lattice parameters of a = 4.221 Å, b = 7.322 Å, c = 5.252 Å and the space group *Pbcm(α00)0s0* with a modulation vector q = (0.5, 0, 0). The atomic arrangement of the typically assumed hexagonal structure of Fe_5Sn_3 is compared with the new model based on the orthorhombic crystal structure in Figure 4-16. Both structures are depicted along the *c** direction. A structural motif of the hexagonal phase is columns of Sn, Fe and disordered Fe atoms, which are randomly occupied on 2/3rd of the atomic positions (a). The main characteristic of the new structure is vacancy ordering in the columns of disordered Fe atoms so that every second position is fully occupied. This ordering causes Sn and Fe atoms in the vicinity of vacancies to relax their position and a wavelike atomic displacement in the columns of already ordered Sn and Fe atoms occur. Such a commensurate vacancy ordered structures were also reported for stoichiometric Ni_3Sn_2 and Co_3Sn_2 whereas incommensurate displacive atomic modulations have been observed for nonstoichiometric $Ni_{3-\delta}Sn_2$ and $Co_{3-\delta}Sn_2$ (Fjellvag 1986, Leineweber 2004).

Although EDX analysis of Fe_5Sn_3 crystal shows the chemical composition of $Fe_{62.x}Sn_{37.y}$ = Fe_5Sn_3, refinement of atomic occupancies result in a slightly different stoichiometry of Fe_3Sn_2. This deviation lies well within the experimental error of the EDX measurement. Nevertheless, one should note that this phase has a completely different crystal structure which is different from the well-established rhombohedral Fe_3Sn_2 phase forming at a lower temperature. The crystal structure and magnetic properties of the Fe_3Sn_2 phase will be discussed in the next section.

In 4.1.3, by high-throughput theoretical screening through several structures, it was mentioned that formation enthalpy of the literature reported hexagonal structure for Fe_5Sn_3 gets a relatively large distance from the convex hull. This is while an orthorhombic Fe_3Sn_2 (Ni_3Sn_2-type) phase stays only slightly higher in energy than the reported rhombohedral Fe_3Sn_2 phase. This theoretical finding agrees with the experiment, as the Fe_3Sn_2 (Ni_3Sn_2-type) structure is identical to an ordered approximant of the orthorhombic Fe_5Sn_3 structure observed experimentally on the obtained Fe_5Sn_3 crystals.

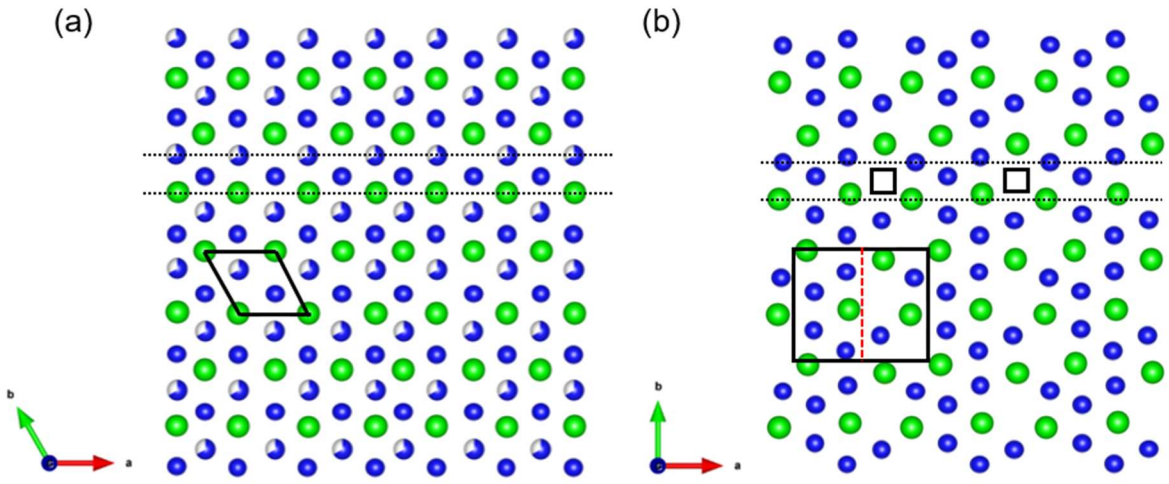

Figure 4-16. The atomic arrangement of (a) the crystal structure of Fe_5Sn_3 phase according to hexagonal structure reported in the literature and (b) the orthorhombic crystal structure of "Fe_5Sn_3" refined from single-crystal XRD both viewed along c. The Fe atoms are displayed in blue and Sn atoms in green. Fe atoms with an occupancy lower than 1 are displayed as partially filled spheres. The black rectangle clarifies the size of the modulated unit cell in the supercell. Black dotted lines are eye guides to indicate the displacement of atoms and black squares exemplarily mark positions of ordered Fe vacancies.*

Here, the question arises whether the twinned structure is a consequence of long-term annealing spent for single crystal growing of the Fe_3Sn_3 phase that led to vacancy ordering of the Fe atoms or such a structure is intrinsic and was also the case for the conventionally melted alloys discussed in section 4.1.1. Our investigation by powder XRD on equilibrated samples containing Fe_5Sn_3 for example rapidly quenched $Fe_{57}Sn_{43}$ sample annealed at 850°C for four days (Figure 4-3 h) shows several reflections which cannot be covered by the literature reported hexagonal structure. The powder XRD pattern of the $Fe_{57}Sn_{43}$ sample reveals a mixture of several phases. In addition to the main phases which attribute to Fe_5Sn_3 and Sn determined by EDX analysis, a small amount of (less than 4 %) low-temperature phases FeSn and $FeSn_2$ were detected by Le Bail fitting of the corresponding XRD pattern. The existence of these low-temperature phases must be due quenching rate of slower than an optimum value which led to partial decomposition of the high-temperature phase. Figure 4-17 shows the XRD pattern of the sample which is fitted in (a) with the literature structure hexagonal phase Fe_5Sn_3 ($P6_3/mmc$, a = 4.223 Å, c = 5.252 Å) and in (b) with the structural model developed based on single crystal data. In can be seen that the uncovered reflections in the fit with the unit cell of the hexagonal phase are considered by the modified unit cell which leads to an overall improvement of the quality of the fit.

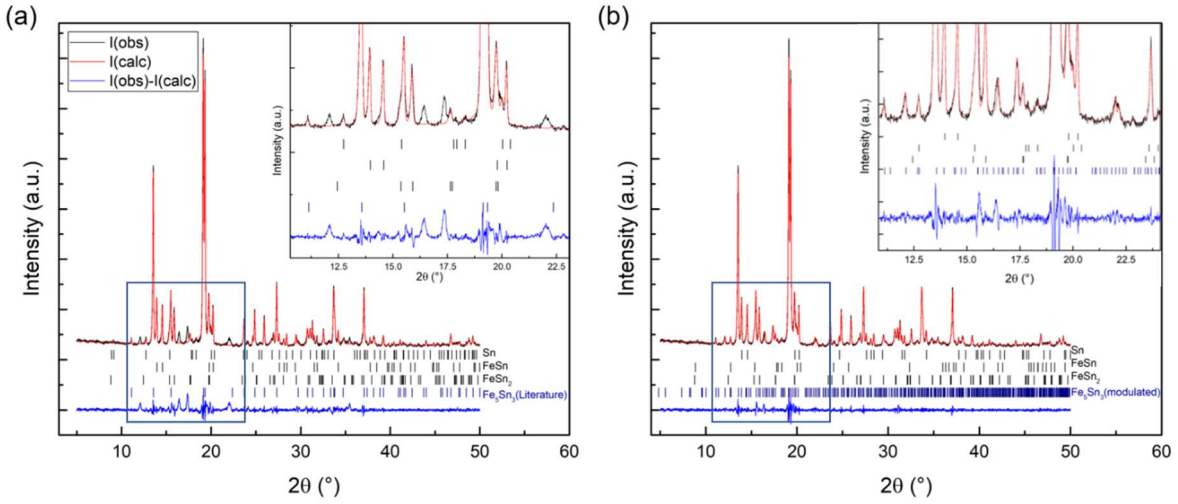

Figure 4-17. Le Bail fits of a powder XRD of a homogenously melted $Fe_{57}Sn_{43}$ sample annealed at 850°C. The sample consists of the main phase with Fe:Sn ratio of 1.74:1 and impurities of Sn, FeSn and $FeSn_2$. (a) Fit with the unit cell of the known phase in literature Fe_5Sn_3 ($P6_3/mmc$, a = 4.223 Å, c = 5.252 Å) and (b) fit with a 3 + 1D commensurably modulated orthorhombic unit cell of Fe_5Sn_3 in the supercell approach of JANA2006 (Pbcm(a00)0s0, a = 4.221 Å, b = 7.322 Å, c = 5.252 Å, q = (½,0,0)). Observed data points, calculated and difference curves and reflection markers, respectively.

The magnetic properties of the Fe_5Sn_3 compound were investigated on a grown single crystal. As the twinning feature is only present in the pseudo-hexagonal basal plane, the magnetic properties can still be determined anisotropically. The crystallographic orientations in which the magnetic properties were measured along, were *a* [100], *b'* [120] and *c* [001] of the old hexagonal description. These directions are indicated in the SE image of the measured Fe_5Sn_3 crystal (Figure 4-14 a). Figure 4-18 shows the field dependencies of magnetization which were measured in a temperature range of [10-700 K]. The *M(H)* curves for two representative temperatures of 10 and 300 K are shown. The magnetization curves along [100] and [120] which are the easy directions of magnetization are almost identical and no anisotropy between them was detected. The magnetization curve along [001] which is the hard axis, demonstrates a linear behavior, indicating the negligible role of the anisotropy constant K_2 in the overall anisotropy. For the whole temperature range, the anisotropy is of easy-plane type. At room temperature, the anisotropy field $\mu_0 H_a$ of Fe_5Sn_3 was found to be 1.1 T which decreases with increasing temperature. For the evaluation of anisotropy constants K_1 and K_2, the Sucksmith-Thompson method was used. The temperature dependencies of the anisotropy constants are plotted in Figure 4-18 b. The obtained K_2 values are in the range of 10^{-2} MJm^{-3}, which as mentioned, in comparison to the leading anisotropy constant K_1 are insignificant. As can be seen in Figure 4-18 b, first-order anisotropy constant K_1 remains negative for the whole temperature range, and the corresponding condition for an easy plane type of anisotropy is fulfilled. The magnitude of K_1 at T = 10 K and 300 K were found to be 0.48 and 0.35 MJm^{-3}, respectively. The anisotropy keeps decreasing with increasing temperature until it reaches zero at the Curie temperature.

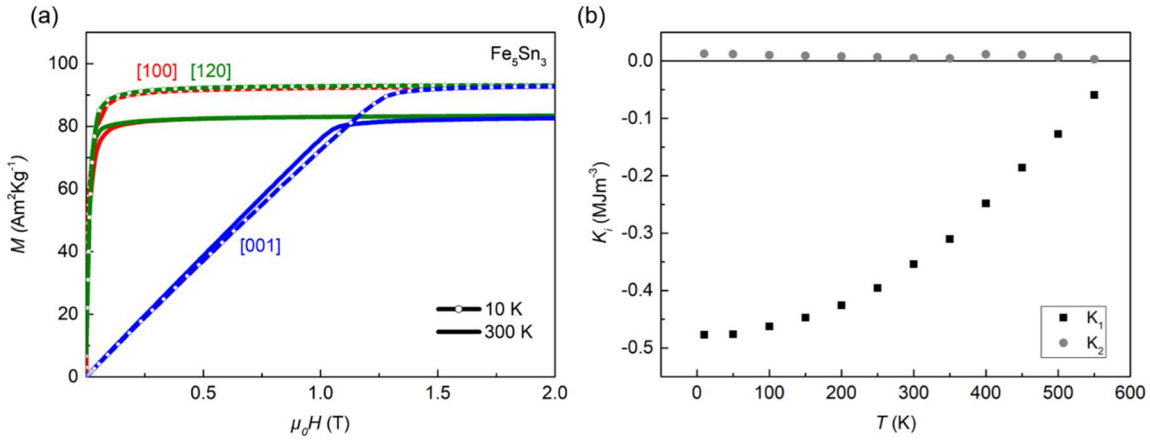

Figure 4-18. (a) Field dependent of magnetization isotherms of "Fe_5Sn_3" pseudo-crystal measured at T = 300 K and 10 K under a magnetic field of up to 2 T applied along the selected axes. (b) Temperature dependence of anisotropy constants of "Fe_5Sn_3" obtained from Sucksmith-Thompson analysis.

As explained in 3.2.4, to estimate the spontaneous magnetization M_s and T_C, isothermal magnetization data measured along the easy magnetization direction can be treated by plotting the Belov-Arrott graph (Arrott 1957). For Fe_5Sn_3 crystal, the *M(H)* curve along the [100] axis was processed which resulted in the temperature dependencies of the spontaneous magnetization plotted in Figure 4-21 a. The continuous line in the *M(H)* curves are the fit to Equation 21 proposed by Kuz'min (Kuz'min 2005). Such a shape of $M_s(T)$, with $s = 0.65$ and $p = 2.32$ is typical for Fe-based ferromagnets. Using the Kuz'min fit, T_C = 601 K and M_s (0K) = 92 emu/g (10.4 μ_B/f.u. ≈ 2.1 μ_B/Fe) were estimated. The obtained Curie temperature lies well in the range of previously reported values (Giefers 2006, Yamamoto 1966).

4.2.3. Fe_3Sn_2

The crystal structure of Fe_3Sn_2 was verified by analysis of the powder X-ray diffraction pattern of the polycrystalline Fe_3Sn_2 sample. The sample was synthesized by induction melting of stoichiometric composition and further melt spinning. The ribbons were cold compacted and annealed at 800°C for 2 weeks and subsequently water quenched. The sample contains the majority Fe_3Sn_2 phase with a small fraction of secondary phases (5 vol %) which the corresponding XRD peaks could be indexed by the low-temperature FeSn phase (see Figure 4-19 c). Some diffraction peaks of low intensity remained undefined. The BSE image and domain structure of the sample are shown in Figure 4-19. Rietveld refinement of the powder XRD pattern of the sample shows 95 vol % of Fe_3Sn_2 rhombohedral hR10-type (space group R-3m) phase. The unit cell parameters were found as a = 5.339 Å and c = 19.810 Å in good agreement with the earlier reported studies (Giefers 2006, Trumpy 1970). The magnetic measurement on the polycrystalline sample showed a very small anisotropy field in a range of demagnetizing field, disabling us to accurately estimate the MAE of the Fe_3Sn_2 phase.

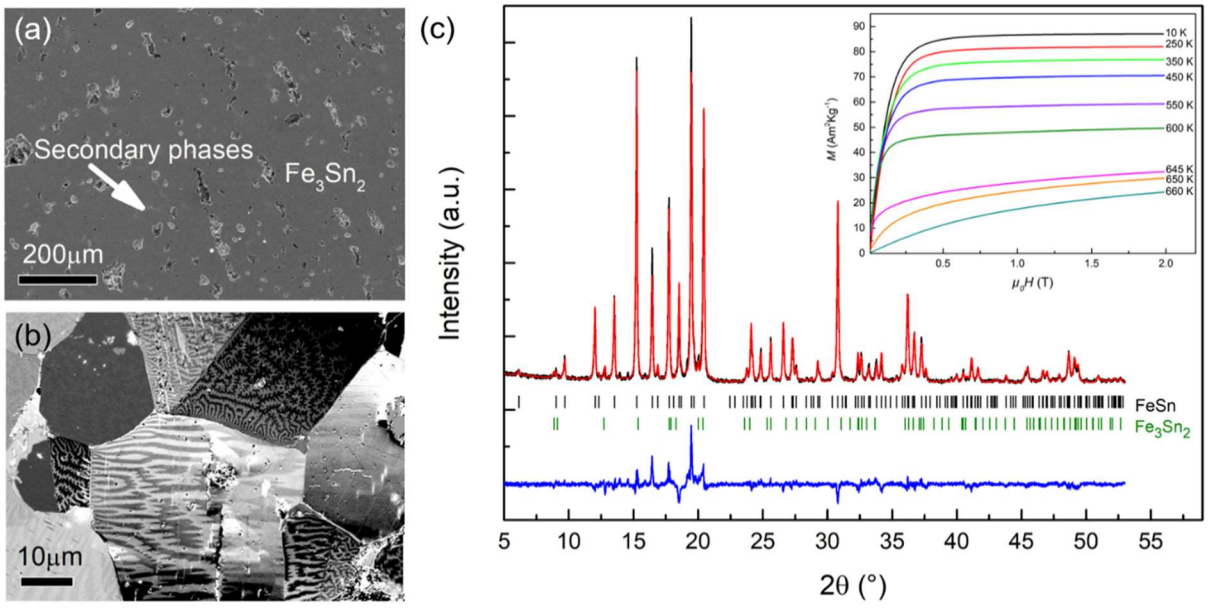

Figure 4-19. BSE (a) and Kerr (b) of a Fe_3Sn_2 polycrystalline sample annealed at 800°C. (c) Rietveld refinement of the XRD pattern of the sample showing 95 vol % of the main Fe_3Sn_2 phase with about 5% impurities. Inset of (c) is the field-dependent magnetization measurement on the sample in a temperature range between 10 and 660 K

To precisely measure the magnetic properties, the single crystalline Fe_3Sn_2 samples were grown and characterized. The crystal structure of the Fe_3Sn_2 single crystals was verified using single-crystal XRD and confirmed to be identical to the well-established Fe_3Sn_2 rhombohedral structure. The SE image of the measured single crystals with hexagonal morphology can be seen in Figure 4-20. The magnetic properties were measured along the *a* [100], *b'* [120] and *c* [001] crystallographic directions in the temperature interval [10-650 K]. The *M(H)* curves for two representative temperatures *T* = 10 K and *T* = 300 K are illustrated in Figure 4-20 a. The magnetocrystalline anisotropy is of uniaxial type at room temperature where the *c*-axis is the easy magnetization direction. The anisotropy remains uniaxial for temperatures above room temperature. However, by decreasing temperature, Fe_3Sn_2 undergoes a spin reorientation transition and the anisotropy switches from uniaxial to planar. The *M(H)* recorded along the [100] and [120] directions are practically identical, indicating a weak magnetic anisotropy within the basal plane for the whole temperature range.

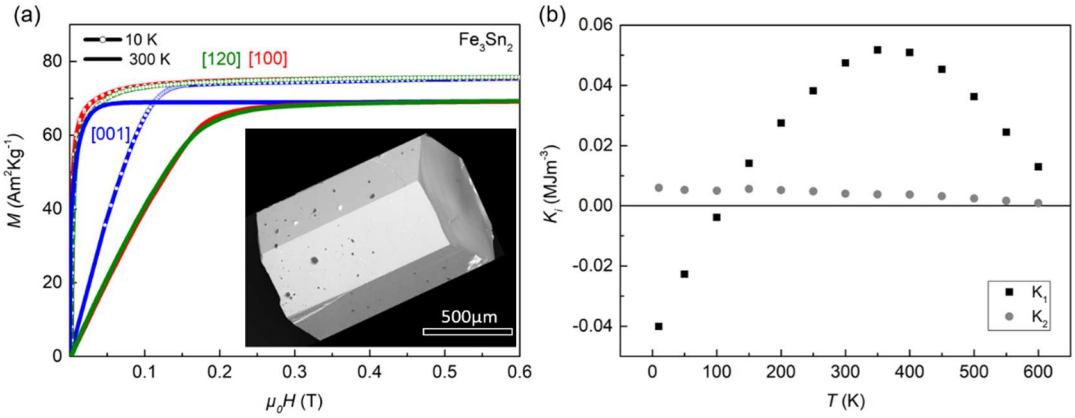

Figure 4-20. a) Field dependent magnetization measurement on Fe_3Sn_2 single crystal shown for T = 300 K and 10 K along the a, b' and c axes. Inset of (a) shows the hexagonal morphology of the measured Fe_3Sn_2 single crystal (b) Temperature dependencies of anisotropy constants of Fe_3Sn_2 obtained from Sucksmith-Thompson analysis. The sign of first anisotropy constant changes when it reaches the spin reorientation transition temperature T∼ 110 K.

For calculation of anisotropy constants K_1 and K_2 using the Sucksmith-Thompson technique, whether the anisotropy was uniaxial or planar, different equations were applied (Lyakhova 2017). The temperature evolution of K_1 and K_2 is shown in Figure 4-20 b. At room temperature, the anisotropy energy was calculated to be 0.05 MJm^{-3}. Although the anisotropy is uniaxial, the absolute value of anisotropy is too small to be applicable as a permanent magnetic material. Upon cooling, the first anisotropy constant changes sign when the temperature reaches T_{SRT} ∼110 K. The obtained T_{SRT} for this compound deviates significantly from the reported value T_{SRT} = 250 K in (Le Caer 1979, Malaman 1978). At temperatures above T_{SRT}, the conditions corresponding to a uniaxial-type of anisotropy ($K_1 > 0$ and $K_1 + 2K_2 > 0$) and below it, to a planar-type anisotropy ($K_1 < 0$ and $K_1 + 2K_2 < 0$) are fulfilled. The Curie temperature T_C and spontaneous magnetization M_s of Fe_3Sn_2 were determined using the Belov-Arrott graph by processing the magnetization data along the easiest magnetization direction (Belov 1956). Temperature dependencies of spontaneous magnetization together with a corresponding fit according to Equation 21 are shown in Figure 4-21 a. The fitting parameters s and p for Fe_3Sn_2 are found to be 0.65 and 3.36, respectively. The Curie temperature of the material is determined as 650 K in good agreement with Refs. (Le Caer 1979, Malaman 1978). The spontaneous magnetization at 0 K is 76 emu/g (∼1.9 μ_B/Fe) which is smaller than that expected value for Fe moments (2.22 μ_B/Fe). This observation might be related to the proposed frustrated ferromagnetism referred to this compound with a spin glass transition at $T_f \approx 80$ K (Fenner 2009).

As mentioned in 2.3.1, several works (Fenner 2009, Hou 2017, Kida 2011, Wang 2016) describe Fe_3Sn_2 as a non-collinear and frustrated itinerant ferromagnet based on its two-dimensional kagomé bilayer structure. To investigate this issue, the gradual change in *M(T)* in various applied fields were measured on an aligned Fe_3Sn_2 single crystal. Figure 4-21 b shows both zero-field-cooled (ZFC) and field-cooled (FC) *M(T)* curves. As can be seen, the *M(T)* curves measured under 0.01 T and 0.1 T field exhibit an anomaly around 100 K close to the determined T_{SRT} whereas under a magnetic field of 1 T, a typical ferromagnetic behavior occurs. The magnetic field of 1 T is strong enough to prevent magnetization

rotation in any other direction. Upon cooling, the *M(T)* curves measured under 0.01 T and 0.1 T show a relatively smooth susceptibility which increases with decreasing temperature until ~100 K where magnetization starts to decrease. Such behavior was also reported in (Fenner 2009, Hou 2017, Kida 2011, Wang 2016) where an increase in magnetization along the *ab* plane is referred to rotation of spins towards the *ab*-plane upon cooling, reaching its maximum at around 100 K. When the temperature decreases further, a decrease in magnetization can be attributed to the entrance into the spin-glass state. Separation of the ZFC and FC data observed for 0.01 T data, where the drop in magnetization is partially suppressed by field cooling is characteristic of a spin glass transition (Fenner 2009). Based on the geometrically frustrated feature of Fe_3Sn_2 and the observed properties such as anomalous Hall effect and topological spin textures, various studies highlight the potential of Fe_3Sn_2 for practical application in spintronics technology.

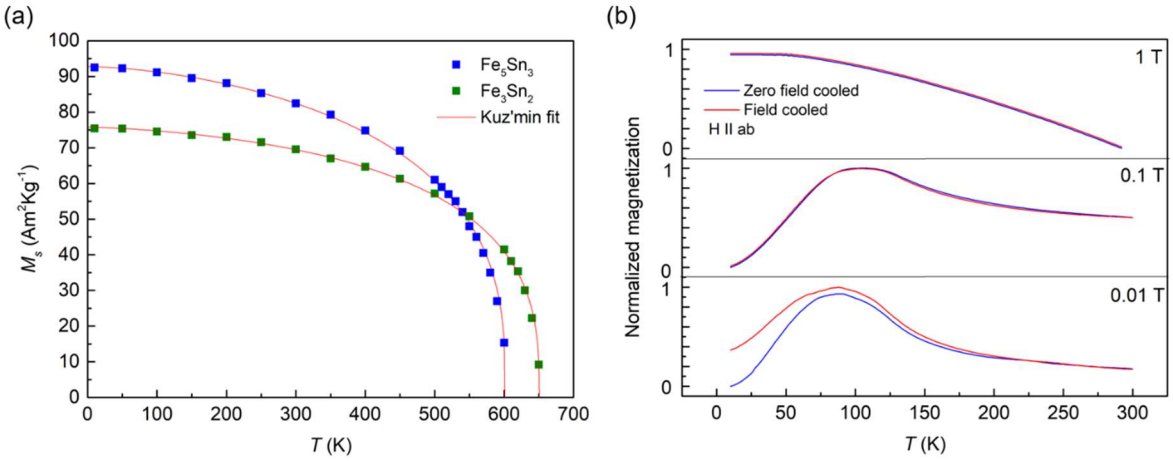

Figure 4-21. (a) Temperature-dependent spontaneous magnetization M_s of the Fe_5Sn_3 and Fe_3Sn_2 measured on single crystals. The red line is a fit using Equation 21 proposed by Kuz'min. (b) Temperature-dependent magnetization of an aligned Fe_3Sn_2 single crystal in applied magnetic fields of 1 T, 0.1 T and 0.01 T. Both zero-field-cooled (ZFC) and field-cooled (FC) curves were measured in the temperature range between 10 and 300 K.

In agreement with experimental results, DFT calculations at 0 K showed a small MAE of -0.015 meV/atom with easy plane anisotropy, while the in-plane anisotropy is negligible. The effect of temperature was not considered in the theoretical calculations, therefore, the driving force for the occurrence of spin reorientation transition remained unknown.

The local spin magnetic moments were calculated for Fe to be 2.22 μ_B and for two crystallographically distinct Sn atoms to be -0.30 μ_B and -0.201 μ_B. The orbital magnetic moments are 0.068 μ_B, 0.0036 μ_B and 0.0036 μ_B, respectively. This corresponds to a saturation magnetization of 2.13 μ_B/Fe which is slightly reduced compared to Fe_3Sn and Fe_5Sn_3 but still is higher than what is found experimentally for Fe_3Sn_2. Although the calculated OMA for the Fe atoms is 0.0003 μ_B which is significantly smaller than in Fe_3Sn, the averaged OMA of Sn (0.0007 μ_B) is of comparable size. In general, theoretical calculations showed a significant role of 5p orbital moments in anisotropy of all three investigated compounds as a result of strong spin-orbit interaction of Sn atoms.

To summarize this section, the intrinsic magnetic properties of Fe-Sn ferromagnetic compounds are listed in Table 4-4.

Table 4-4. Intrinsic magnetic properties of Fe-Sn binary ferromagnetic compounds measured on single crystals

Single crystal	M_s (Am^2Kg^{-1})/ (T) @300 K	M_s (Am^2Kg^{-1})/ (T) @0 K	$\mu_0 H_a$ (T) @300 K	$\mu_0 H_a$ (T) @10 K	K_1 (MJm^{-3}) @300 K	K_1 (MJm^{-3}) @10 K	T_c (K)
Fe_3Sn	120/ (1.27)	128/ (1.36)	-2.2	-1.8	-1.18	-1.07	735
Fe_5Sn_3	81/(0.80)	92/ (0.91)	-1.1	-1.3	-0.35	-0.48	601
Fe_3Sn_2	69/ (0.71)	76/ (0.78)	0.18	-0.1	0.05	-0.04	650

4.3. Characterization of magnetic domains in Fe_3Sn_2 single crystals

At room temperature, Fe_3Sn_2 shows a characteristic uniaxial domain structure as observed in RCM and polycrystalline samples with different orientations. In order to interpret the character of the Fe_3Sn_2 domain structure, detail characterization was done by application of Kerr (Figure 4-22 and Figure 4-23) and MFM (Figure 4-24) microscopy on an oriented Fe_3Sn_2 single crystal. The easy magnetization direction of the single crystal (*c*-axis) is oriented out of observation plane in Figure 4-22 a, b and c. Upon decreasing the sample thickness from ~ 200 µm (a) to ~ 60 µm (b) and to ~ 5 µm (c), different domain patterns were observed. In (a), the domain structure is of branched star-like whereas in (b) and (c) maze-like domains were observed. In (d) the sample is oriented in a way where easy magnetization direction lies in-plane and the stripe-like pattern appeared. The occurrence of such domains is typical for materials with uniaxial anisotropy as in Fe_3Sn_2 whose magnetic easy axis lies along the *c*-axis as shown above by VSM measurement. The change of domain character associating with the reduction of sample thickness is explained in 2.4.2. In (c), observation of band domains with alternating out of plane magnetization can be described by the previously introduced Kittel open structure model (Kittel 1946). With increasing thickness as in (b), the domain walls undulate to decrease the magnetic free energy. For thick enough sample with critical thickness $L > L_s$ (a), domain branching occurs in order to reduce the magnetostatic energy at the surface while in bulk, domains stay wide to save part of domain wall energy.

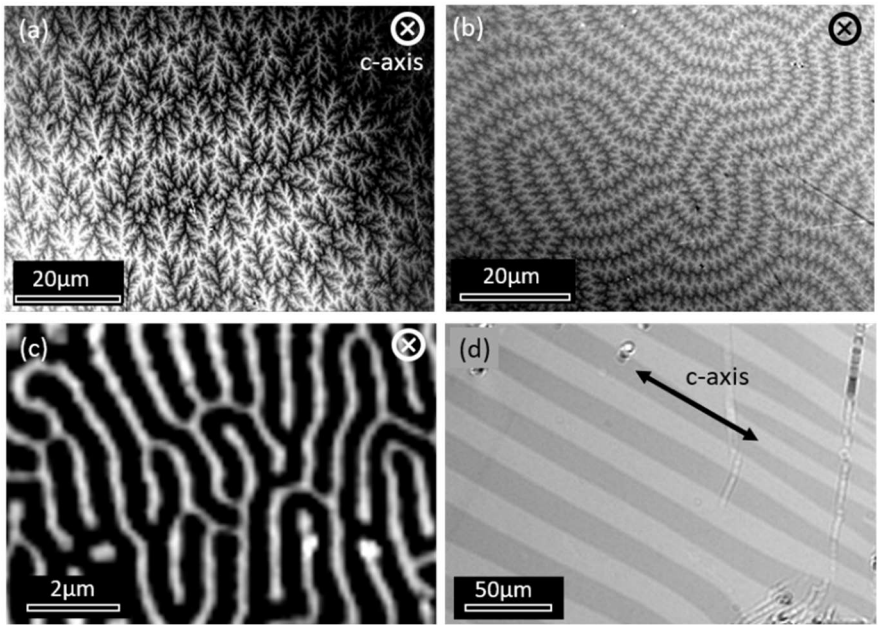

Figure 4-22. Kerr images of an aligned uniaxial Fe_3Sn_2 single crystal with c-axis lying out of the observation plane in (a), (b) and (c). The sample thickness is decreased from ~ 200 µm in (a) to ~ 60 µm in (b) and to ~ 5 µm in (c). In (d) the c-axis is parallel to the observation plane.

The observed branched domains in Fe_3Sn_2 might resemble the character of two-dimensional domains as in high anisotropic materials (Figure 2-10) in misoriented grains (e.g. polycrystalline samples (Figure 4-19 b)). However, on an oriented single crystal (a), domains show up as flower pattern with a high degree of fractal branching i.e. a more jagged appearance in comparison with the rounded shape of the branching protrusions (e.g. in $Nd_2Fe_{14}B$ (Figure 5-12.a)). To investigate this further and describe the surface domain structure of Fe_3Sn_2 crystal, selective Kerr microscopy (Soldatov 2017) was applied for a discriminated imaging of in-plane and out-of-plane magnetization components. Figure 4-23 shows the branched domain pattern of an identical region which was observed with pure polar (a) and pure in-plane sensitivity (b). The domain pattern observed with pure polar sensitivity is similar to (a) captured by conventional Kerr microscopy. In a conventional setup, as a result of the dominant polar Kerr effect, the in-plane component is disregarded. In the pure in-plane sensitivity image, a stripe-like oscillation of magnetization with multi-axial closure domains can be observed. Such a surface domain pattern is typical for material with intermediate anisotropy ($Q \approx 1$) and previously observed in Cobalt Q = 0.4 (Soldatov 2017). For these materials, anisotropy is not large enough to prohibit the magnetization rotation towards the surface which happens to minimize the magnetostatic energy. The schematic representation of magnetization orientation in Fe_3Sn_2 should be close to that illustrated in Figure 2-10. The information depth of Kerr microscopy on metals is around 20 nm and the fact that in Fe_3Sn_2, the oscillatory closure domains are even more pronounced than in cobalt (Soldatov 2017), suggests a smaller quality factor of Fe_3Sn_2 than that in Co. The quality factor of Fe_3Sn_2 is calculated using Equation 8 as $Q = \frac{2K}{\mu_0 M_S^2}$. Inserting the values obtained for K and M_s by magnetic measurement of

the Fe_3Sn_2 single crystal, the quality factor is calculated to be 0.25 which agrees well with our assumption.

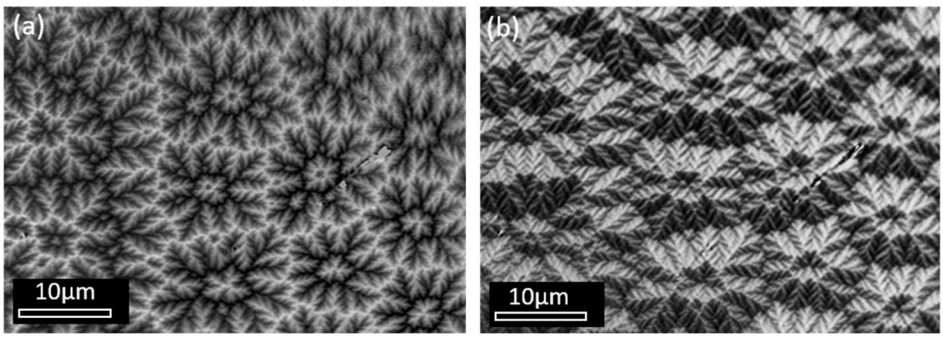

Figure 4-23. Kerr images of an aligned Fe_3Sn_2 single crystal with c-axis out of observation plane where polar (a) and in-plane (b) magnetization components of an identical domain pattern captured with a selective Kerr microscope.

To illustrate the rotation of spins in Fe_3Sn_2 from the *c*-axis towards the basal plane, temperature-dependent domain imaging was done using MFM on a ∼60 µm thick single crystal plate (*c*-axis out of plane). The evolution of the magnetic domain structure was recorded in a temperature range between 50 K and 300 K (Figure 4-24). To achieve the remanence state, a magnetic field of 0.3 T was initially applied parallel to the magnetic easy axis of the sample which was subsequently removed by a field oscillation back to 0 T. It can be clearly seen that the magnetization lies in-plane at T = 50 and 80 K where a domain structure typical for materials with planar anisotropy appeared. This is while the uniaxial feature of the magnetic domain became clear at temperatures above 110 K due to a change of magnetic anisotropy from 'easy plane' to 'easy axis' type. A recent analysis on the domain structure of Fe_3Sn_2 using MFM analysis revealed the first-order nature of the spin-reorientation transition in this compound by observation of a fine magnetic structure which is developed during cooling and has corresponded to the nucleation and growth of the low-temperature phase (easy plane) from the domain walls of the high-temperature phase (easy axis) (Heritage 2020). The evolution of such a fine magnetic structure within the domains was not observed in our investigation. At 300 K, the domains reveal the oscillatory maze-like character that was already found by Kerr microscopy (compare with Figure 4-22 b).

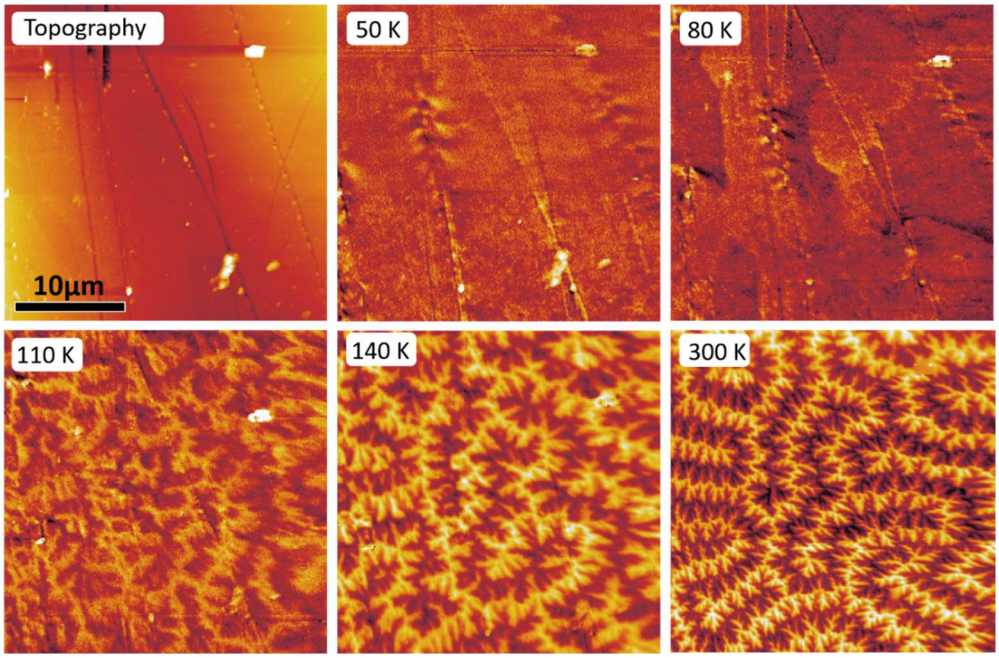

Figure 4-24. MFM images of an aligned Fe_3Sn_2 single crystal with c-axis out of observation plane captured in the temperature range of [50K-300 K]. For recording each image, a magnetic 0.3 T is initially applied parallel to the magnetic easy axis of the sample which was then followed by a field oscillation back to 0 T. The spin reorientation transition can be observed in the temperature range between [80 K-110 K] where the easy magnetization direction changes from in-plane to uniaxial.

4.3.1. Application of analytical domain models for evaluation of anisotropy

Domain imaging is not only beneficial in high-throughput identification of desired phases with uniaxial anisotropy but also can be used as a reliable tool for evaluation of their magnetocrystalline anisotropy based on domain theory. In 2.4.2, some analytical models aiming for interpretation of the domain structure of materials with uniaxial anisotropy were introduced. In this section, with the example of Fe_3Sn_2, the introduced domain models; "Kittel" (Kittel 1946), "Szymczak" (Szymczak 1973) and "Bodenberger-Hubert" (Bodenberger 1977) were employed for the assessment of magnetocrystalline anisotropy and check whether such domain analysis can be applied for high-throughput characterization of the magnetic properties as in (Goll 2014).

As a general working principle of such models is based on linking domain width *D* to the domain wall energy $\gamma = 4\sqrt{AK}$, initially, it is important to determine the exchange stiffness constant *A* which is the energy coefficient of exchange interaction. This material property is related to the Curie temperature of the material and can be calculated using a well-known formula introduced in Equation 2, $A = k_B T_C / 2a$ (Coey 2010) where k_B is Boltzmann constant and a is the lattice parameter in a simple structure (usually cubic). For calculation of *A* based on this equation, the number of atoms per unit cell should be taken into consideration (one for simple cubic, two for bcc and four for fcc, etc.) For Fe_3Sn_2 with a more complex structure however, this equation is not applicable. In this work, *A* is calculated using $A = k_B T_C / 4a$ where *a* is the average distance between the nearest iron atoms. The coefficient 4 in this equation is found empirically, comparing the *A* parameters known for different intermetallic

compounds (Karpenkov 2018). In Fe_3Sn_2 with average nearest Fe-Fe distance of a = 2.59 Å, exchange stiffness is calculated to be $A \approx 8.6$ pJ/m.

An alternative way for calculation of exchange stiffness which is considered to be more accurate is fitting of the low-temperature magnetization data by Bloch's $T^{3/2}$ -law (Bloch 1930). This law is based on the association of the long-wavelength spin waves energy with a gradual reduction of the magnetization. The temperature dependence of reduced magnetization according to Bloch's $T^{3/2}$ -law can be written as (Kittel 1986):

$$\frac{M_S(T)}{M_S(0)} = 1 - \frac{0.0587}{v}\left(\frac{k_B T}{2Is}\right)^{3/2} \qquad \textit{Equation 22}$$

where I is the exchange integral, s is spin quantum number and v is the number of atoms per unit cell. One can consider the average Fe-Fe distance (a) as a parameter and hence v = 1. The exchange stiffness can be then written as $A = vIs^2/a$ and Bloch's $T^{3/2}$ -law becomes as follow:

$$\frac{M_S(0)-M_S(T)}{M_S(0)} = 0.0587\left(\frac{k_B S}{2Aa}\right)^{3/2} T^{3/2} \qquad \textit{Equation 23}$$

For calculation of s which is the average spin per atom, $\mu_s = 2\mu_B\sqrt{s(s+1)}$, where μ_B is the Bohr magneton, $\mu_s = M_s(0)/3$ (3 magnetic atoms in the unit cell) is used. For Fe_3Sn_2, s is found to be 1.54. By plotting $\Delta M/M_s(0)$ versus $T^{3/2}$, which results at low temperature in a linear function with a slope of 2.15×10^{-5}, the exchange stiffness was determined as $A \approx 8.0$ pJ/m which is in good agreement with our primary estimation. The domain wall energy of Fe_3Sn_2 can then be calculated as $\gamma = 2.53\times10^{-3}$ J/m^2.

To explain the domain structure of Fe_3Sn_2 based on the well-known Kittel model (Kittel 1946), the thickness of the aligned Fe_3Sn_2 single crystal was reduced down to the point where no domain branching is allowed and only Kittel's open structure was appeared (Figure 4-22 c). Based on Equation 16, the anisotropy can be calculated as $K = 0.18^* \frac{D^4 M_S^4}{AL^2}$. For a 5 µm thick single crystal with $D \sim 0.4$ µm, application of the Kittel model results in $K \approx 0.02$ MJm^{-3} which gives a good estimation close to the actual anisotropy of the material, measured by conventional magnetometry.

Szymczak domain model (Szymczak 1973) can be applied to bulk stripes for a thick enough sample where domain branching is favorable. In bulk Fe_3Sn_2, the magnetic domains follow a two-phase branching scheme when approaching a surface perpendicular to the easy axis. In Figure 4-22 d, the onset of branching is observed on the right side of the image which was captured close to the sample edge. Based on Equation 18, the anisotropy can be calculated as $K = 16.6^* \frac{D^6 M_S^4}{A\mu^{*2} L^4}$. In this equation, L is the length of the stripe. The rotational permeability μ^* can be calculated as $1 + 1/Q$ which for high anisotropic materials with $Q > 1$, μ^* can be approximated as 1. However, for materials with low anisotropy, the determination of μ^* is essential. If the anisotropy of material is unknown, which is the case for high-throughput methods (e.g. RCM method) which aim for the discovery of new hard magnetic materials, insertion of $\mu^* = 1$ for quantitative domain analysis using the Szymczak equation, is erroneous. As an example, evaluation of anisotropy in Fe_3Sn_2 single crystal with D = 15 µm, L = 350 µm and assumption of $\mu^* \sim 1$, result in anisotropy of K = 1.61 MJm^{-3} which is two orders of magnitude larger than expected. In Ref. (Goll 2015), such a large value of anisotropy (K = 1.7 MJm^{-3}) is reported

for the $Fe_{53.3}Cr_{6.4}Sn_{40}$ compound synthesized by a reactive sintering high-throughput method and characterized by quantitative analysis of the Kerr images. Considering the Q = 0.25 ($\mu^* \sim 5$), the anisotropy of K = 0.06 MJm^{-3}, is in a good agreement with the actual anisotropy of the compound.

For the analysis of the branched domain pattern forming in bulk uniaxial samples, a theoretical domain model developed by Bodenberger and Hubert is widely used. This model considers the surface domain in which its width is independent of the sample thickness. Therefore, high-throughput evaluation of anisotropy based on this model is more straightforward in comparison to the two other methods. Based on Equation 19, $K = \frac{{D_S}^2 {M_S}^4}{256A\pi^2\beta^2}$. As β depends on the geometrical arrangement of the magnetic domains at the surface, it is determined phenomenologically (0.3 ± 0.02) for materials with $Q > 1$ where the branched domains are two dimensional. However, one can observe in Figure 4-23 that in Fe_3Sn_2, the spins are rotated towards the surface and strong in-plane magnetization components exist. Therefore, as expected, evaluation of anisotropy considering the $D_s \approx 0.6$ µm measured using the stereological line-cut method (will be explained in 5.1.4) on the Kerr image shown in Figure 4-22 a gives a value of = 0.2 MJ/m^3 which is not correct. Although this model fails in case of materials with intermediate and low anisotropy such as in Fe_3Sn_2, in 5.1.4 we will see that application of this model on high anisotropic materials i.e. $Nd_2Fe_{14}B$ leads to a reliable evaluation.

To summarize, in this section it has been shown that domain imaging techniques such as Kerr and MFM are very powerful tools enabling the identification of desired phases with the uniaxial type of anisotropy. Furthermore, phenomena such as spin reorientation transition can be detected by temperature-dependent domain imaging using these methods. Nevertheless, this work has shown that quantitative analysis of domain structure for the estimation of anisotropy can be significantly misleading in case the material is not highly anisotropic. Based on three established theoretical domain models ("Kittel", "Szymczak" and "Bodenberger-Hubert", the anisotropy of Fe_3Sn_2 was estimated which among them only the "Kittel" model resulted in a reliable result. The "Kittel" model, which is only applicable for very thin films, requires extensive sample preparation and very accurate determination of the thickness, therefore should not be considered as a high-throughput characterization tool. The reason behind the wrong assessment of anisotropy by the "Szymczak" and Bodenberger-Hubert" models was the consideration of only strict uniaxial magnetization. Application of selective Kerr microscopy and observation of in-plane magnetization component of (001) aligned Fe_3Sn_2 single crystal revealed the existence of multiaxial closure domains at the surface of the sample characteristic for medium anisotropic materials.

5. $(Nd,Ce)_2(Fe,Co)_{14}B$ system

5.1. Structural and magnetic properties measured on single crystals

It is of great interest to substitute RE elements with restricted supply chains such as Nd, Dy, and Tb in NdFeB magnets with the most abundant and cheapest RE element- cerium- without significant concurrent reduction of its material properties. Numerous numbers of publications have investigated the effect of Ce substitution as well as its co-doping with Co on the achievement of desirable extrinsic properties in NdFeB magnets. Very satisfying results were reported on the extrinsic magnetic properties of CeCo-doped NdFeB magnets and the effect of microstructure was extensively studied. However, the intrinsic origin of magnetic properties which is crucial for the further rational design of this class of materials is not carefully studied. In this chapter, the structural and intrinsic magnetic properties of ternary, quaternary and quinary $(Nd,Ce)_2(Fe,Co)_{14}B$ compounds were accurately measured on single crystalline samples in a wide concentration range. Five associating anisotropy constants were extracted by the combination of experimental results (field-dependent magnetization measurement along different crystallographic directions under the field of up to 60 T- measured at High field Labor Dresden) with theoretical models. This research was funded by MAGHEM project and the theoretical calculations were performed by our project partner Dr. Gabriel Gómez Eslava. In the final sub-section, extrinsic magnetic properties of $(Nd,Ce)_2(Fe,Co)_{14}B$ were investigated for the first time on the single domain particles synthesized by a mechanochemical method and the results were correlated to the intrinsic magnetic properties on the single crystals of the very same compositions.

5.1.1. $(Nd_{1-x}Ce_x)_2Fe_{14}B$ series

The 2:14:1 single crystals were grown using reactive flux method with flux being RE metals. The melted composition was selected by careful investigation of the ternary Nd-Fe-B phase diagram as discussed in section 3.1.2. The tetragonal 2:14:1 phase (space group $P4_2/mnm$) was formed over the entire Ce concentration range. The chosen melted compositions and the corresponding compositions of the obtained $(Nd_{1-x}Ce_x)_2Fe_{14}B$ single crystals determined by EDX analysis are listed in Table 5-1. The compositions of the single crystals were double-checked with 2 different EDX systems to ensure a correct quantification. For the sake of simplicity, the characterized single crystals are named in a digested way also listed in Table 5-1. This work is the first study covering the whole Ce concentration range for the investigation of structural and intrinsic magnetic properties measured on single crystals. The only other study available on synthesis and characterization of $(Nd_{1-x}Ce_x)_2Fe_{14}B$ single crystals (Susner 2017) covers the Ce doping up to x = 0.38.

Table 5-1. The composition of melted alloys for single crystal growing of 2:14:1 compound and the resulting composition of the obtained 2:14:1 single crystals and their corresponding sample names.

Melted composition	2:14:1 single crystal composition	Sample name
$Nd_{33.5}Fe_{62.5}B_4$	$Nd_2Fe_{14}B$	Nd
$(Nd_{0.80}Ce_{0.20})_{33.5}Fe_{62.5}B_4$	$(Nd_{0.85}Ce_{0.15})_2Fe_{14}B$	Ce15
$(Nd_{0.50}Ce_{0.50})_{33.5}Fe_{62.5}B_4$	$(Nd_{0.64}Ce_{0.36})_2Fe_{14}B$	Ce36
$(Nd_{0.25}Ce_{0.75})_{33.5}Fe_{62.5}B_4$	$(Nd_{0.37}Ce_{0.63})_2Fe_{14}B$	Ce63
$Ce_{33.5}Fe_{62.5}B_4$	$Ce_2Fe_{14}B$	Ce
$Nd_{33.5}(Fe_{0.85}Co_{0.15})_{62.5}B_4$	$Nd_2(Fe_{0.90}Co_{0.10})_{14}B$	Co10
$(Nd_{0.80}Ce_{0.20})_{33.5}(Fe_{0.85}Co_{0.15})_{62.5}B_4$	$(Nd_{0.85}Ce_{0.15})_2(Fe_{0.90}Co_{0.10})_{14}B$	Ce15Co10

The as-grown single crystals were well-shaped and typically elongated perpendicular to the *c*-axis. Employing Laue XRD, the quality of the single crystals was accurately verified. To investigate the effect of Ce substitution for Nd on the unit cell parameters of 2:14:1 structure, the powder XRD has been carried out. This investigation was done on the mixture of hand-ground 2:14:1 single crystals and the residual secondary phases which were mainly RE oxides. The resulting spectrum from each batch of samples was analyzed for extraction of the lattice parameters using LeBail fitting. As can be seen in Figure 5-1, lattice parameters a and c as well as tetragonality factor c/a decrease monotonically following the Vegard's law (Vegard 1921) with increasing Ce concentration. A small deviation occurs for Ce63 which appeared to be the sample with the lowest signal to noise ratio and largest error. A similar decreasing trend with Ce substitution is reported in Refs. (Poenaru 2019, Susner 2017). My result for $Nd_2Fe_{14}B$ lies within the literature data determined for from-the-melt-grown single crystals which typically fall in the range of 0.880 - 0.882 nm for a and 1.219 - 1.223 nm for c (Buschow 1988, Herbst 1991). Furthermore, the literature data for $Ce_2Fe_{14}B$, a = 0.876 and c = 1.211 nm (Herbst 1991) are in agreement with this work. The lattice parameters of $Ce_2Fe_{14}B$ do not follow lanthanide contraction and lies far below the trend which implies the tendency of Ce in +4 valance state as ionic radius of Ce^{4+}(1.715 Å) < Nd^{3+}(1.821 Å) < Ce^{3+} (1.825Å). The decrease of lattice parameters with Ce substitution is therefore expected when Nd^{3+} is substituted by Ce^{4+}. No anomalies in lattice parameters as reported by (Pathak 2015) with analysis of the polycrystalline samples related to phase segregation in Ce concentration range of $0.14 < x < 0.4$ was observed for Ce15 and Ce36 single crystals which lie within this interval.

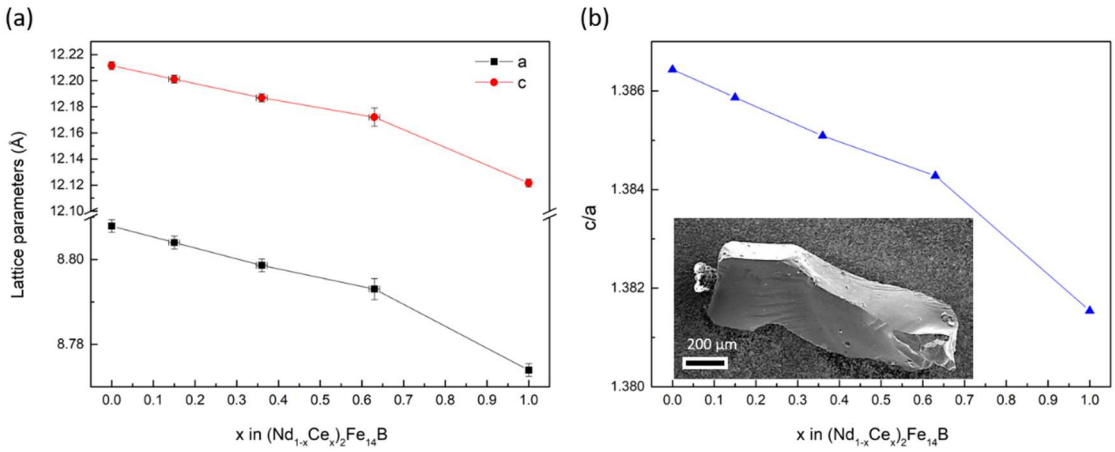

Figure 5-1. (a) Unit cell parameters and (b) tetragonality factor (c/a) of the 2:14:1 phase plotted against Ce concentration in $(Nd_{1-x}Ce_x)_2Fe_{14}B$ single crystals. Inset of (b) is the SEM image of a 2:14:1 single crystal shows the morphology of the typically obtained single crystals with columnar growth.

The magnetization measurement was performed for the whole Ce series along and perpendicular to the *c*-axis (room temperature easy axis). At room temperature and above, *M(H)* curves measured along the [100] and [110] crystallographic directions are almost identical (not shown). This means that there is no magnetic anisotropy within the basal plane. Therefore, for the determination of high temperature intrinsic magnetic properties of the single crystals, the crystals were oriented parallel and perpendicular to the *c*-axis by field aligning along the easy magnetization direction and 90° rotation from it, respectively.

Figure 5-2 a shows the *M(H)* curves for the Ce substituted single crystals at room temperature. The demagnetizing fields were subtracted based on the sample geometries. It can be seen that both M_s and H_a decrease with increasing Ce concentration. These properties are listed for some selective temperatures in Table 5-2. The reduction of spontaneous magnetization is in line with empirical predictions considering the alloying rules between the two end-members ($Nd_2Fe_{14}B$ and $Ce_2Fe_{14}B$). The anisotropy fields were determined from the kink in the hard magnetization curve and plotted as a function of temperature in Figure 5-2 b. The obtained anisotropy fields for $Nd_2Fe_{14}B$ and $Ce_2Fe_{14}B$ were compared with those reported in Refs. (Herbst 1991, Mushnikov 2007, Orimoloye 2018). Our values are relatively larger than (Herbst 1991), nevertheless in a good agreement with more recent publications, most probably due to more sophisticated measurement techniques and better quality of the single crystals.

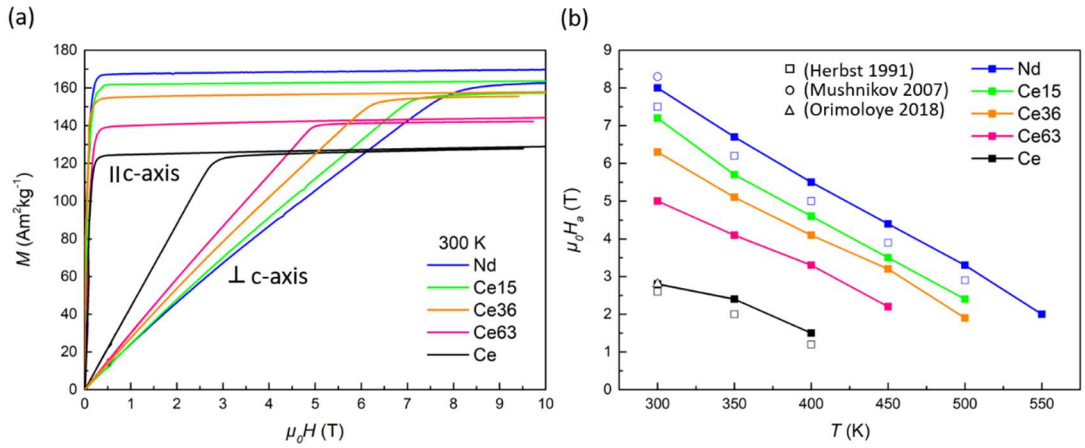

Figure 5-2. Room temperature field-dependent magnetization measurement of $(Nd_{1-x}Ce_x)_2Fe_{14}B$ single crystals along the easy and hard magnetization directions. (b) The anisotropy field of the single crystals as a function of Ce doping in a temperature range between 300 K up to 550 K. The obtained anisotropy fields for $Nd_2Fe_{14}B$ and $Ce_2Fe_{14}B$ were compared to the values reported in the literature.

Except for the ternary $Ce_2Fe_{14}B$ compound, four other Nd contained compounds undergo a spin reorientation transition at low temperature where easy magnetization direction takes an angle to the *c*-axis and becomes easy cone. Therefore, for the estimation of T_C and M_s(0K) using Kuz'min technique, the processing of magnetization data along [001] is not adequate and leads to a decrease in magnetization at low temperatures (see Figure 3-10 b). Hence, for this analysis, the magnetization curves were also measured for the whole temperature range on a free-rotational sample where the sample aligns itself along the easiest magnetization direction. By processing of the obtained *M(H)* curves and plotting the Belov-Arrott graph, the temperature dependencies of spontaneous magnetization were found as a function of temperature and plotted in Figure 5-3 a. The continuous black lines are the fits obtained based on Equation 21. The used fitting parameters *s* and *p* for all single crystals (given in Table 5-2) are typical for Fe-based ferromagnets. The obtained M_s(0K) and T_C (listed for all samples in Table 5-2) for $Nd_2Fe_{14}B$ and $Ce_2Fe_{14}B$ are in accordance with the literature values (Herbst 1991). The results from Ce doped single crystals were compared with (Susner 2017) in respect of anisotropy field and Curie temperature and plotted as a function of Ce concentration in Figure 5-3 b. By increasing Ce concentration, the diversity of the obtained Curie temperatures increases up to 10 K difference for x = 0.36. This discrepancy might arise from the application of different measurement techniques but most probably due to their large errors in identification of the actual Ce content of the crystal with x = 0.38 which is specifically noted in their paper to be higher than the other crystals (Susner 2017). In contrast to their statement, the reported lattice parameter for x = 0.38 sample is also much smaller than Vegard-like behavior. This issue also led to the most explicit discrepancy between the obtained anisotropy values. This works reports an anisotropy field of 6.3 T for Ce 36 being 1.2 T larger than x = 0.38 in (Susner 2017). On the other hand, the *M(H)* curves measured along the hard axis in (Susner 2017) are significantly non-linear, evidencing the bad quality of the crystals, also extrapolates the y-axis above the origin indicating the deviation of the hard axis from the direction of the field.

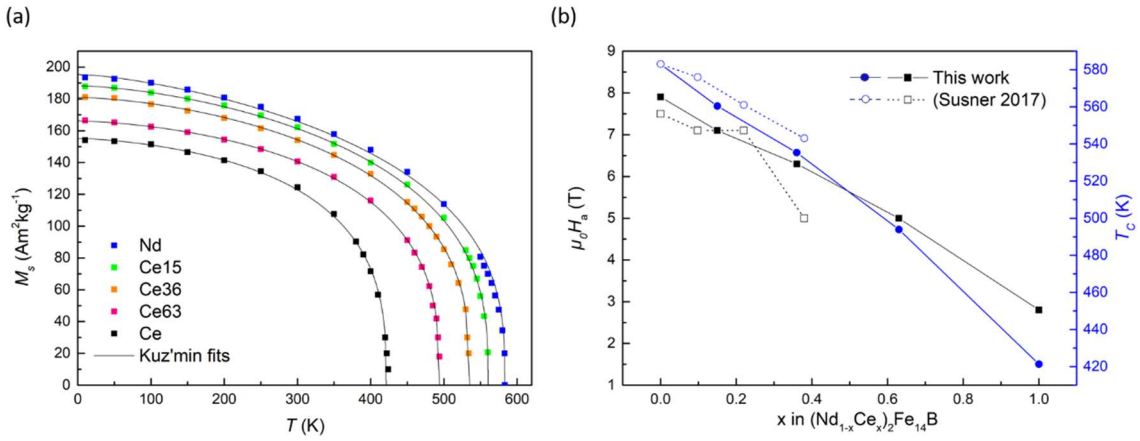

Figure 5-3. (a) Temperature-dependent spontaneous magnetization M_s of the $(Nd_{1-x}Ce_x)_2Fe_{14}B$ single crystals from 10 K up to the Curie temperature. The solid black lines are Kuz'min fits using Equation 21. (b) The comparison of the data obtained in this work and the reported values in (Susner 2017) for room temperature anisotropy fields and the estimated Curie temperatures as a function of Ce content in $(Nd_{1-x}Ce_x)_2Fe_{14}B$.

For high temperatures, it is adequate to consider the leading anisotropy constant K_1 only, as the higher order terms (K_2, K_3, …) are negligible. A difficulty for accurate determination of K_1 is the observed anisotropy in magnetization where the hard-axis magnetization curve does not fully approach the easy-axis above the anisotropy field (5% difference). This behavior which is more pronounced for single crystals with lower Ce concentration is reproducible and already reported in the literature for $Nd_2Fe_{14}B$ (Givord 1984) and other uniaxial materials (Kuz'min 2015). As implemented by (Kuz'min 2015), for estimation of K_1, in order to prevent under or over -estimation of the anisotropy, arithmetic mean value of M_s- easy-axis and M_s- hard-axis was considered. For calculation of the first order anisotropy constant for $Nd_2Fe_{14}B$, three different methods that are often used in literature were applied and compared in Figure 5-4 a. In the first method, ignoring K_2, Equation 11 is used for the estimation of $K_1 = \mu_0 H_a M_s/2$. In the second method, the anisotropy energy is estimated by calculation of the area between the magnetization curves measured along the easy and hard directions, which by neglecting higher order anisotropy terms can be considered as K_1. It can be clearly seen that both methods lead to an overestimation of K_1 especially for low temperatures due to an important role of K_2. The Sucksmith-Thompson method, considering both K_1 and K_2 led to more consistent values of anisotropy for $Nd_2Fe_{14}B$ compared to literature (Sagawa 1985). Furthermore, the inflection of K_1 by decreasing temperature below room temperature could be reproduced by the Sucksmith-Thompson method which is not the case for two other methods. Nevertheless, for accurate calculation of anisotropy at low temperatures, 5 anisotropy constants must be considered which will be discussed in section 5.1.3. In the high temperature range, first-order anisotropy constants of all Ce series were calculated using the Sucksmith-Thompson method and plotted as a function of temperature in Figure 5-4 b. The estimated K_1 of 4.4 MJm^{-3} for $Nd_2Fe_{14}B$, although fits perfectly to (Sagawa 1985) however is lower than the reported value of 4.9 MJ/m^3 in (Herbst 1991). For $Ce_2Fe_{14}B$ the K_1 is found to be 1.4 MJm^{-3} in a good agreement with a literature value of 1.5 MJ/m^3 reported in (Herbst 1991).

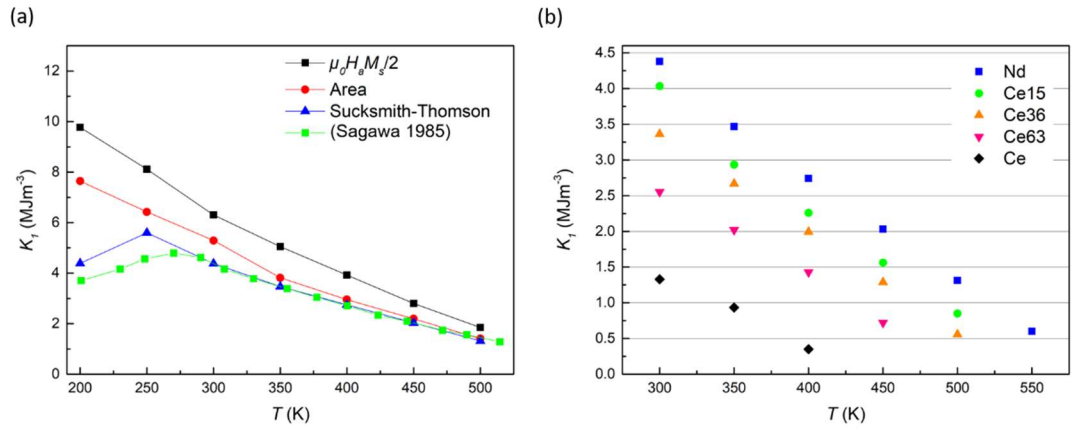

Figure 5-4. Comparison of the first order anisotropy constants calculated for $Nd_2Fe_{14}B$ using three different methods and literature values. (b) Temperature dependence of K_1 values estimated using the Sucksmith-Thompson method for the whole Ce concentration range.

It has been already mentioned that at low temperatures, due to a strong interplay between crystal field interactions and the exchange interactions on the RE ions, $Nd_2Fe_{14}B$ undergoes a spin reorientation transition where the anisotropy changes from uniaxial to easy-cone. The field-dependent magnetization measurements of $Nd_2Fe_{14}B$ single crystal along [001] and [100] are shown in Figure 5-5. Along [001], the change of easy magnetization direction can be directly realized by a sudden drop of low-field magnetization values (kink) when temperature decreased from 150 K to 100 K. Furthermore, a non-zero offset of magnetization in *M(H)* measured along [100] represents the change of anisotropy, which happens within the temperature range of 100 K – 150 K. Therefore, a low field temperature-dependent magnetization measurement along both directions would result in a change in magnetization enabling the determination of T_{SRT}.

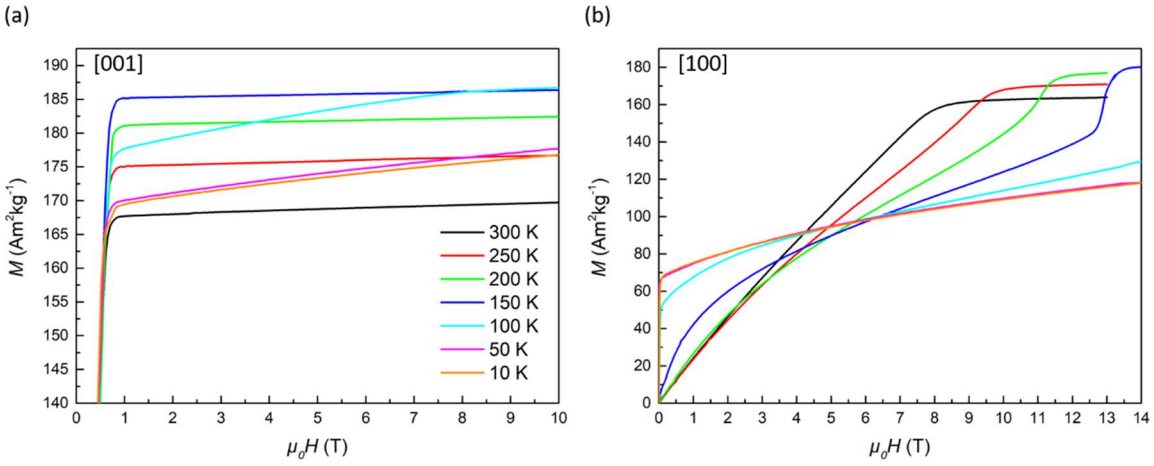

Figure 5-5. M(H) dependencies of $Nd_2Fe_{14}B$ single crystal measured along the [001] (a) and [100] (b) crystallographic directions in 10 K - 300 K temperature interval under a static magnetic field of up to 14 T. Note that for better illustration of magnetization behavior at low temperatures, the scale of magnetization is kept to upper range in (a).

To select a right field where the kink in [001] *M(H)* occurs, initially *M(H)* measurement was performed in order to identify the demagnetizing field. For a $Nd_2Fe_{14}B$ single crystal, a demagnetizing field of 0.6 T was evaluated along the [001] direction. Two *M(T)* curves recorded under the magnetic field of 0.5 T and 0.7 T slightly lower and higher (close to the kink) than the demagnetizing field are shown in Figure 5-6 a. Two distinct *M(T)* behavior were observed where the maximum point with application of 0.7 T field was found to be 127.5 K. This field which is applied along the *c*-axis is relatively large and favors the magnetization towards the *c*-axis, therefore is expected to underestimate the actual T_{SRT} which should be determined under 0 field.

The spin reorientation transition can be estimated from the inflection point of low field *M(T)* curves along [001]. However, a more accurate and common way is the processing of the hard direction magnetization evolution as a function of temperature (Abache 1986, Kou 1997). The field-dependent magnetization measurement was done on $Nd_2Fe_{14}B$ up to 1 T in a temperature range between 170 K and 122 K with 2 K increments (Figure 5-6 b). In this figure, the demagnetizing field is not subtracted (compare with Figure 5-5 b). The initial susceptibility increases with decreasing temperature up to a point where it does not change anymore (at 130 K). The subtraction of the demagnetizing field at this temperature leads to a non-zero magnetization offset. This phenomenon is directly reflected in the *M(T)* curve recorded under 0.01 T magnetic field, in which by decreasing temperature, the magnetization increases steeply until it reaches 130 K hereafter, it remains steady (Figure 5-6 c). The *M(T)* curves were also recorded under 0.7 T magnetic field which is strong enough to prohibit the magnetization rotation reflected by a linear *M(T)* behavior.

In order to study the effect of Ce doping on the spin reorientation transition temperature, the *M(T)* curves for all single crystals were measured along [100] direction under 0.1 T magnetic field. The reason for the selection of 0.1 T rather than 0.01 T was the small size of some of the measured single crystals which led to very noisy signals under such a small field. On the other hand, for $Nd_2Fe_{14}B$ (as an example), the inflection point in *M(T)* under 0.1 T was only 1 K higher than under 0.01 T. Therefore, for consistency of the results, the T_{SRT} values were determined by the inflection point of the *M(T)* curves under 0.1 T static magnetic field.

As can be seen in Figure 5-6 d, the substitution of Ce for Nd in $Nd_2Fe_{14}B$ shifts the T_{SRT} towards lower temperatures where for $Ce_2Fe_{14}B$ there exists no spin reorientation transition. It has been known that Fe sublattice in $Nd_2Fe_{14}B$ favors the axial anisotropy of this compound whereas the Nd sublattices anisotropies becoming dominant at low temperatures, compete with the axial alignment of magnetization and lead to a spin reorientation transition by decreasing *T*. This is while in $Ce_2Fe_{14}B$, the anisotropy originates mainly from TM sublattice. The weak contribution of Ce sublattice on the anisotropy can be realized by comparison of H_a(0 K) of 2.6 T in $Ce_2Fe_{14}B$ to 1.8 T for $Y_2Fe_{14}B$ which contains non-magnetic Y (also compare with H_a(0 K) = 17 T for $Nd_2Fe_{14}B$). The negligible contribution of Ce to the total anisotropy leads to uniaxial alignment for the whole temperature range. The increase of Ce concentration in $(Nd_{1-x}Ce_x)_2Fe_{14}B$ results in the maintenance of the uniaxial anisotropy and therefore decrease of T_{SRT} as proved to be the case experimentally.

The distinct role of RE sublattices on the incidence of SRT is studied for $Nd_2Fe_{14}B$ in (Abache 1986). It has been shown that the 4f sublattice -rather than the 4g sublattice (explained in section 2.3.2)- mainly

contribute to the planar alignment of magnetization. On the other hand, (Susner 2017) reported 70% preferential site occupancy of Ce atoms for larger 4g sites over the smaller 4f site resulted from their single crystal neutron diffraction analysis on $(Nd_{0.78}Ce_{0.22})_2Fe_{14}B$ single crystal. Linking these statements, it can be predicted that small Ce concentration does not significantly alter the T_{SRT} as it mainly occupies 4g site with axial anisotropy preference whereas its dependence (T_{SRT} to Ce content) would increase by increasing Ce content in $Nd_2Fe_{14}B$. Our results clearly show that the change of T_{SRT} is initially moderate for low x and increase promptly for higher x confirming this discussion.

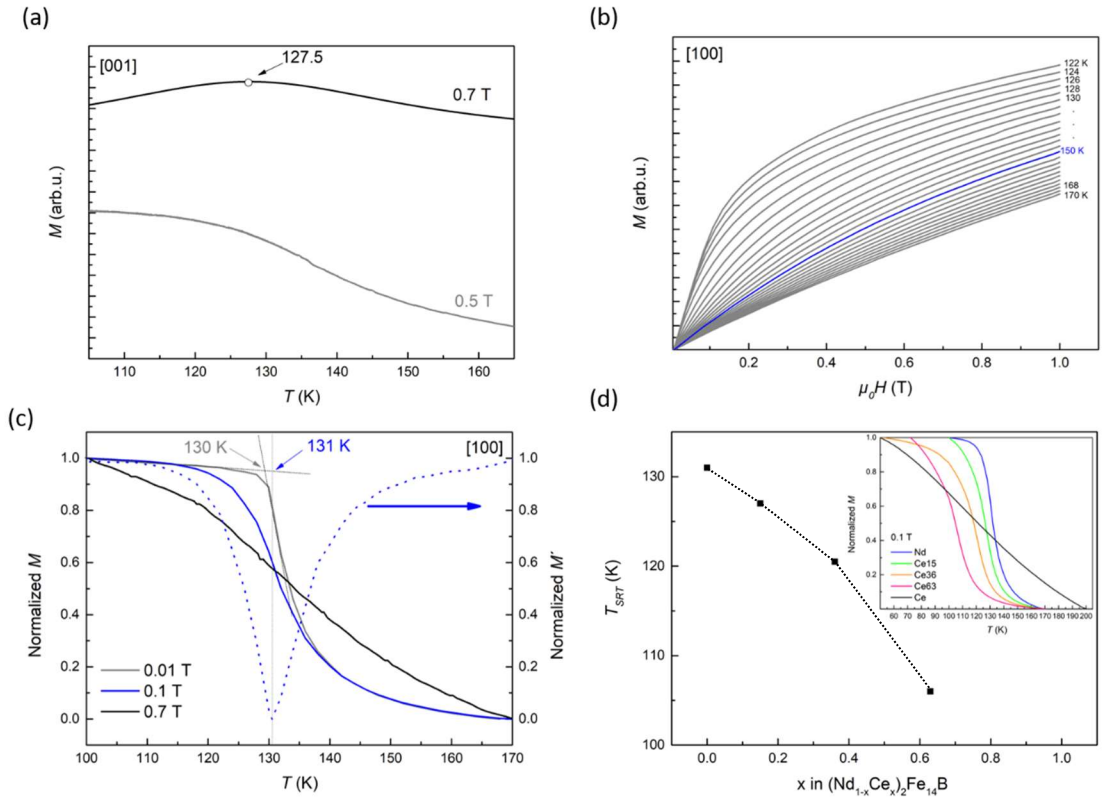

Figure 5-6. (a) The M(T) curves measured on a $Nd_2Fe_{14}B$ single crystal aligned along [001] direction under 0.7 T and 0.5 T magnetic field. (b) and (c) are the magnetic measurement of an identical $Nd_2Fe_{14}B$ single crystal aligned along [100] direction. In (b) the M(H) curves are measured up to 1 T in a temperature range between 122 K and 170 K. The demagnetizing field is not subtracted for these curves. The M(H) curve measured at 150 K is highlighted in blue to be compared with Figure 5-5 b. (c) is the M(T) curves measured under 0.01, 0.1 and 0.7 T magnetic field. The dotted line is the derivative of the M(T) curve measured under 0.1 T used for the identification of the T_{SRT}. (d) the determined T_{SRT} as a function of Ce content also listed in Table 5-2. The inset of (d) is the M(T) curves measured for Ce substituted single crystals aligned along the basal plane shift to lower temperature by increasing Ce concentration.

To summarize this section, the intrinsic magnetic properties of the $(Nd_{1-x}Ce_x)_2Fe_{14}B$ single crystals investigated in this section are listed in Table 5-2.

Table 5-2. Intrinsic magnetic properties of the $(Nd_{1-x}Ce_x)_2Fe_{14}B$ single crystals

Single crystal	M_s (Am^2Kg^{-1})/ (T) @300 K	M_s (Am^2Kg^{-1})/ (T) @0 K	H_a (T) @300 K	K_1 (MJm^{-3}) @300 K	T_c (K)	T_{SRT} (K)	Kuz'min fitting parameters	
							s	p
$Nd_2Fe_{14}B$	167.5/ (1.58)	195.7/ (1.85)	8	4.37	583	131	0.85	0.98
$(Nd_{0.85}Ce_{0.15})_2Fe_{14}B$	161.6/ (1.53)	188.2/ (1.78)	7.2	4.03	560	127	0.75	1.88
$(Nd_{0.64}Ce_{0.36})_2Fe_{14}B$	155/ (1.47)	180.9/ (1.71)	6.3	3.36	534	120	0.65	2.04
$(Nd_{0.37}Ce_{0.63})_2Fe_{14}B$	139.8/ (1.32)	166.3/ (1.57)	5	2.55	494	106	0.65	2.82
$Ce_2Fe_{14}B$	124.5/ (1.18)	155.1/ (1.47)	2.8	1.40	421	-	0.65	3.33

5.1.2. $(Nd,Ce)_2(Fe,Co)_{14}B$

It has been shown that Ce substitution for Nd deteriorates the intrinsic magnetic properties of the $Nd_2Fe_{14}B$ compound especially for high-temperature applications. The effect of further elemental substitutions to compensate losses resulting from Ce substitution has been reported in the literature. The substitution of Co in $Nd_2Fe_{14}B$ is known to increase Curie temperature, due to enhanced exchange interactions. In this section, the effect of partial Co substitution will be investigated by characterization of two Co doped single crystals with the composition of $Nd_2(Fe_{0.9}Co_{0.1})_{14}B$ and $(Nd_{0.85}Ce_{0.15})_2(Fe_{0.9}Co_{0.1})_{14}B$ referred as Co10 and Ce15Co10 to be compared with Nd and Ce15 single crystals.

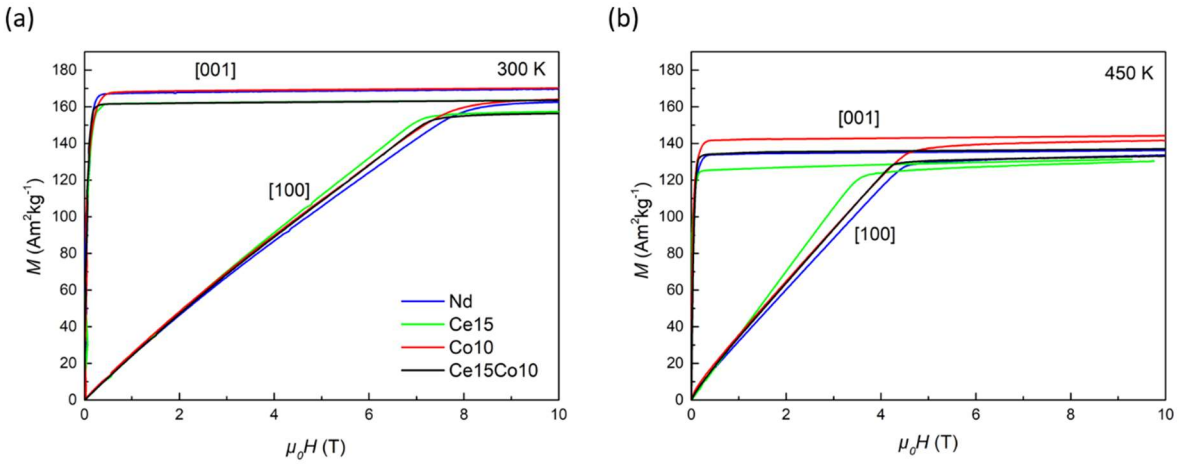

Figure 5-7. M(H) curves for $(Nd,Ce)_2(Fe,Co)_{14}B$ single crystals measured along [001] and [100] crystallographic direction at (a) 300 K and (b) 450 K.

Figure 5-7 a shows the room temperature field dependencies of magnetization measured on Nd, Ce15, Co10 and, Ce15Co10 single crystals aligned along [001] and [100] directions. One can see that 10% Co substitution only slightly increases the spontaneous magnetization of $Nd_2Fe_{14}B$ but decreases the anisotropy field from 8 T for pure $Nd_2Fe_{14}B$ to 7.8 T for Co10 in agreement with (Sagawa 1987). Simultaneous Ce and Co substitution results in the same spontaneous magnetization as in Ce15

indicating that Co practically does not affect the magnetization, similar to Co10 in comparison to Nd sample with only 1% difference. In Tang (Tang 2019), using ab-initio calculations it has been shown that the magnetization can be retained in $(Nd_{1-x}Ce_x)_2(Fe_{0.95}Co_{0.05})_{14}B$ compound when Ce occupies only 4g sites. The 4% decrease of magnetization in the Ce10Co15 sample in comparison to Nd and Co10 samples disagree with this hypothesis. Co substitution shows a contrary contribution to the anisotropy when it is solely substituted in $Nd_2Fe_{14}B$ than when is co-doped with Ce. The degradation of magnetic anisotropy in the Ce substituted sample is partially compensated when Ce and Co are both added to the structure. As reported in (Herbst 1986) and (Gómez Eslava 2021), Co shows a preferential occupancy for 4c, $8j_1$ and $16k_2$ sites in $Nd_2Fe_{14}B$ which in particular, 4c and $8j_1$ sites are more influenced by the RE atom, as they are surrounded by 4 and 3 RE atoms, respectively. It appears that the proximity between Ce and Co at low concentrations which leads to synergism between these two neighboring atoms is beneficial for the anisotropy of the compound as signaled by (Pathak 2015).

The most appreciable magnetic properties were observed for high temperatures as a result of Co higher exchange interactions which increased T_C to 653 K for Co10 and 642 K for Ce10Co15. The *M(H)* curves measured at 450 K show an enhancement of magnetic properties for both Co doped compounds. Comparing Nd with Co10 and Ce15 with Ce15Co10 in respect of spontaneous magnetization, it was found that although for low temperatures, the magnetization is not remarkably influenced by Co substitution , however, at temperatures above room temperature the magnetization for Co-doped samples starts to overtake and the difference is getting bigger with increasing temperature (see Figure 5-9 a). Similar to Ce substituted single crystals, the obtained *M(T)* curves were fitted using Kuz'min technique (using Equation 21) with fitting parameters of s = 0.65 and p = 1.09 for Co10 and s = 0.75 and p = 0.87 for Ce15Co, all typical for ferromagnetic materials. The effect of Co addition on change of magnetization for both pure and Ce-doped $Nd_2Fe_{14}B$ is very similar for the whole temperature range. As can be seen in Figure 5-7 b, although the slope of hard axis magnetization curve is not changed when 10% Co is substituted in $Nd_2Fe_{14}B$, however as a result of higher magnetization of Co10 sample, the estimated anisotropy field from the kink of *M(H)* curve along the hard axis is slightly higher. The higher anisotropy field of Co10 in comparison to Nd for temperatures above 400 K is in agreement with the results from (Sagawa 1987). The evolution of anisotropy fields as a function of temperature is shown in Figure 5-8. An interesting feature is a hasty enhancement of anisotropy fields for the Ce15Co10 sample in comparison to Ce15 which already starts at 350 K and reaches to the anisotropy of pure $Nd_2Fe_{14}B$ at 500 K. The leading anisotropy constant K_1 for Co substituted compounds were also calculated using the Sucksmith-Thompson method and plotted as a function of temperature along with their Co-free counterparts (Figure 5-8 b). The results show better thermal stability of anisotropy energy for co-doped (Ce15Co10) compounds making them a cost-efficient alternative candidate for high-temperature permanent magnet applications. The enhanced high-temperature performance of CeCo- doped NdFeB magnets (Pathak 2016, Tang 2019) is due to an improvement in intrinsic properties. A detailed investigation on the electronic structure of co-doped $(Nd,Ce)_2(Fe,Co)_{14}B$ should be done to be able to explain the physical origin of the enhanced magnetic properties.

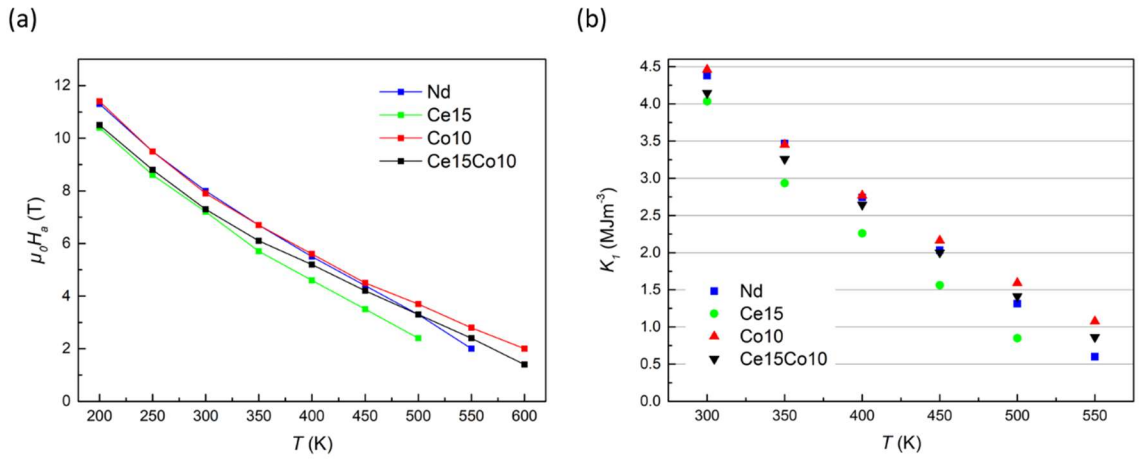

Figure 5-8. The temperature-dependence of anisotropy fields (a) and first anisotropy constants (b) of four grown $(Nd,Ce)_2(Fe,Co)_{14}B$ single crystals.

The effect of Co substitution for Fe on the SRT temperature of $Nd_2Fe_{14}B$ was also studied by low-field temperature measurement of magnetization as in Ce content single crystals. It has been found that T_{SRT} decreases with Co substitution and even further by co-doping of Ce and Co. As a result of a smaller mean magnetic moment of Co at 4 K (1.4 μ_B/atom) in $Nd_2Co_{14}B$ in comparison to Fe (2.2 μ_B/atom) in $Nd_2Fe_{14}B$, a weaker exchange field will be experienced by Nd ion in $Nd_2Co_{14}B$. This results in a much smaller T_{SRT} = 37 K for $Nd_2Co_{14}B$ (Sagawa 1987). Accordingly, a decrease in T_{SRT} was expected for Co substituted compounds. The angle in which easy magnetization direction takes from the *c*-axis below T_{SRT} was calculated for the $Nd_2Fe_{14}B$ and for the samples with partial substitution of Ce and Co. The calculation was done considering the spontaneous magnetization measured along the *c*-axis and free-rotational sample using the following Equation 24.

$$\theta = \cos^{-1}\left(\frac{M_s[001]}{M_s[free\_rot]}\right) \qquad \textit{Equation 24}$$

The angle between magnetization and the *c*-axis for $Nd_2Fe_{14}B$ using this method is found to be ~28° $\pm$ 0.5° at 10 K which is slightly smaller than the reported value of 30° at 4.2 K found by torque measurement (Tokuhara 1985). For Ce and Co doped samples, the easy magnetization direction is estimated to lie in a smaller angle of about 24°.

The intrinsic magnetic properties of Co substituted single crystals are listed in Table 5-3 together with their Co-free counterparts.

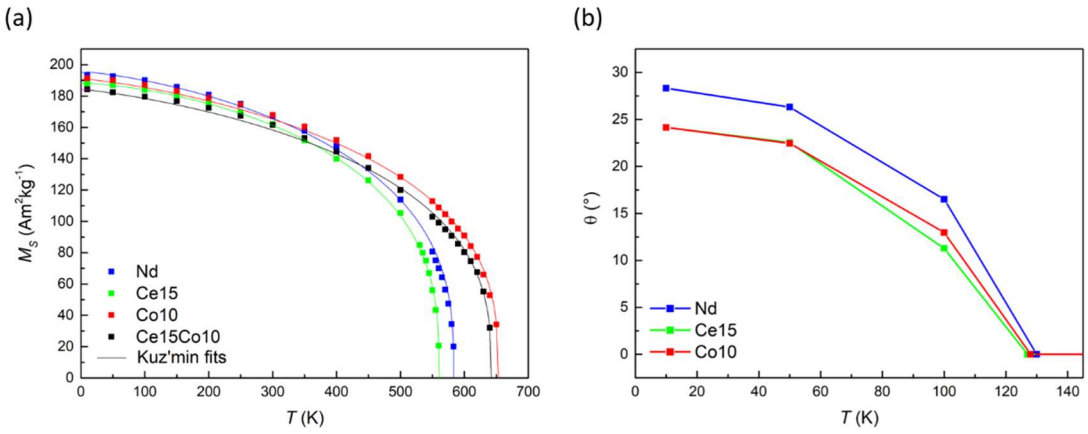

Figure 5-9. The temperature-dependence of spontaneous magnetization with the black solid lines being Kuz'min fits using Equation 21 (a) and the angle which easy magnetization direction takes from the c-axis for pure $Nd_2Fe_{14}B$ and partially doped compound with Ce and Co.

Table 5-3. The intrinsic magnetic properties of $(Nd,Ce)_2(Fe,Co)_{14}B$ single crystals for some selected temperatures

Single crystal	M_s (Am^{2}Kg^{-1})/ (T) @450 K	M_s (Am^{2}Kg^{-1})/ (T) @300 K	M_s (Am^{2}Kg^{-1})/ (T) @ 0 K	H_a (T) @450 K	H_a (T) @300 K	K_1 (MJm^{-3}) @450 K	K_1 (MJm^{-3}) @300 K	T_c (K)
$Nd_2Fe_{14}B$	134.1/ (1.27)	167.5/ (1.58)	195.7/ (1.85)	4.4	8	2.03	4.37	583
$(Nd_{0.85}Ce_{0.15})_2Fe_{14}B$	126.1/ (1.19)	161.6/ (1.53)	188.2/ (1.78)	3.5	7.2	1.56	4.03	560
$Nd_2(Fe_{0.9}Co_{0.1})_{14}B$	141.6/ (1.34)	167.9/ (1.59)	191/ (1.81)	4.5	7.8	2.16	4.45	653
$(Nd_{0.85}Ce_{0.15})_2(Fe_{0.9}Co_{0.1})_{14}B$	134.1/ (1.27)	161.6/ (1.53)	184.5/ (1.75)	4.2	7.3	2.00	4.14	642

5.1.3. Calculation of magnetocrystalline anisotropy constants at low temperatures

As already discussed, the low-temperature anisotropy energy of $Nd_2Fe_{14}B$ can no longer be expressed only by first anisotropy constant. However, due to acting of crystal electric field on RE ions, higher order anisotropy terms need to be considered. Determination of the magnetocrystalline anisotropy constants is of high importance specially for theoretical modeling. While the most reliable magnetic data can be obtained from measurements of high-quality single crystals, the synthesis and measurement procedures are not straightforward and are very time-consuming. Therefore, in recent years, modeling approaches have been developed for the calculation of intrinsic magnetic properties. Here, the low-temperature experimental analyses of the single crystals (shown for high *T* in the last section) were combined with theoretical models and five anisotropy constants of $Nd_2Fe_{14}B$ were extracted. The theoretical calculations were done by Dr. Gabriel Gómez Eslava and the results of this joint study is published in (Gómez Eslava 2021).

The field-dependent magnetization measurement was done along three crystallographic directions [001], [100] and [110] as well as on free rotatable single crystal providing data along the easiest magnetization direction. The *M(H)* curves were recorded in a temperature range between 10 K and 300 K and are shown for 200 K and 10 K in Figure 5-10. It can be seen that already at 200 K the magnetization along [110] direction does not saturate with a magnetic field of up to 14 T (the

maximum generated field with PPMS). Therefore, for T < 200 K, the magnetization curves were also measured up to 50 T using pulsed magnetic fields.

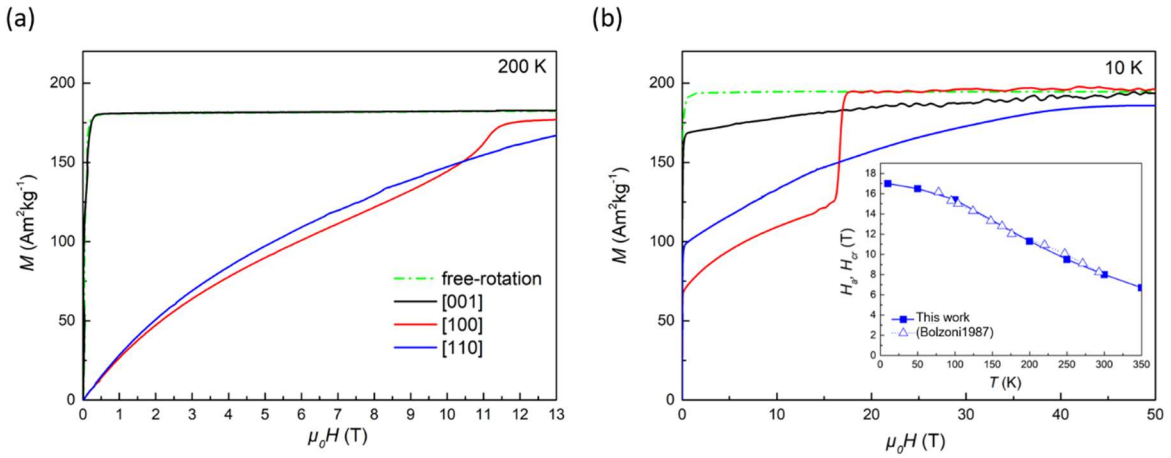

Figure 5-10. Magnetization curves of the $Nd_2Fe_{14}B$ single crystal along different crystallographic directions at 200 K (a) and 10 K (b). The inset of (b) shows the comparison of the values found for H_a and H_{cr} (from M(H) curves along [100]) with those reported in (Bolzoni 1987) for different temperatures).

First Order Magnetization Process (FOMP) was observed for *M(H)* curves along [100] direction at temperatures below 200 K. The critical field in which the FOMP happens increases with decreasing temperature where at 10 K, T_{cr} = 17 T. The inset of Figure 5-10 b shows a perfect agreement between our results and the literature values from (Bolzoni 1987).

To determine the anisotropy constants, the magnetization curves were simulated based on the minimization of the total energy of the system. For these calculations, the TM and RE moments are considered to be collinear for a given applied field and temperature and the contribution of each sublattice to the total anisotropy and magnetization is not discriminated as in most of the studies (Bolzoni 1987, Mushnikov 2007). This approach is known as Single-Lattice (SL) model. In this simplified model, the total energy of the system is considered as a sum of the anisotropy energy and Zeeman energy which can be expressed as:

$$E = K_1 \sin^2\theta + (K_2 + K_2' \cos 4\varphi) \sin^4\theta + (K_3 + K_3' \cos 4\varphi) \sin^6\theta - H_x M_x - H_y M_y - H_z M_z \qquad \textit{Equation 25}$$

here, θ is the angle between the magnetization vector and the *c*-axis, φ is the angle formed between the in-plane projection of the magnetization and [100] direction and M_x, M_y and M_z are:

$$M_x = M_s \sin\theta \cos\varphi,\ M_y = M_s \sin\theta \sin\varphi \text{ and } M_z = M_s \cos\theta \qquad \textit{Equation 26}$$

The orientation of external applied field vector can be determined with angles Θ and Ψ and H_x, H_y and H_z which can be written as:

$$H_x = H_{ext} \sin\Theta \cos\Psi,\ H_y = H_{ext} \sin\Theta \sin\Psi \text{ and } H_z = H_{ext} \cos\Theta \qquad \textit{Equation 27}$$

where Θ is the angle between the field vector and the *c*-axis, Ψ is the angle formed between the in-plane projection of the field and [100] direction. Angles Θ and Ψ are the parameters which are known from the experiment.

For the magnetic field applied along the [100] direction $\varphi = 0$, the anisotropy energy becomes:

$$E_A = K_1 sin^2\theta + K_2^+ sin^4\theta + K_3^+ sin^6\theta \quad \text{with } K_i^+ = K_i + K_i'; i = 2, 3 \qquad \textit{Equation 28}$$

For the magnetic field applied along the [110] direction $\varphi = 45$, and the anisotropy energy becomes:

$$E_A = K_1 sin^2\theta + K_2^- sin^4\theta + K_3^- sin^6\theta \quad \text{with } K_i^- = K_i - K_i'; i = 2, 3 \qquad \textit{Equation 29}$$

For each magnetic field magnitude, the equilibrium magnetization orientation was found by numerically minimizing the total energy with respect to θ and φ. For reproducing the experimental *M(H)* curves, the K_1, $K_2^{\pm}$, and $K_3^{\pm}$ constants were determined by adjusting these constants to proper values for each temperature and direction (fitting process) to reach the best agreement between the calculated and experimental curves. By combining the fitting parameters K_i^- and K_i^+ obtained at a given temperature, individual values of the anisotropy constants K_2, K_2', K_3, and K_3' are obtained, as shown in Figure 5-11 with dashed lines. The obtained results were compared with those reported in (Bolzoni 1987), also extracted from a SL model (open symbols in Figure 5-11). The uniaxial anisotropy constants K_1, K_2 and K_3 obtained by our SL model are in fair agreement with Bolzoni et al. However, for the in-plane constants K_2' and K_3' our SL model leads to slightly higher absolute values. From Figure 5-11, it can be seen that at temperatures near T_{SRT}, the sign of K_1 changes from negative to positive and it becomes the leading constant at temperatures above 200 K. The estimated K_1 for $Nd_2Fe_{14}B$ at room temperature using this method is 4.2 MJm^{-3} which is in a good agreement with the estimated value using Sucksmith-Thompson method. At lower temperatures, the dominant terms are the higher order constants K_2, K_2', K_3 and K_3'.

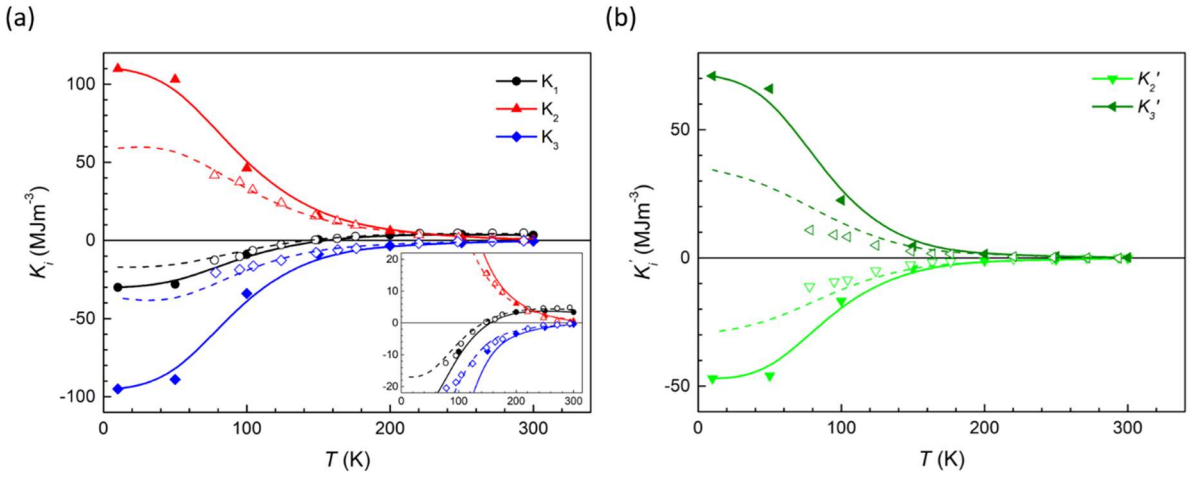

Figure 5-11. Anisotropy constants of $Nd_2Fe_{14}B$ single crystal as a function of the temperature, extracted from the SL model (dashed lines) and the TS model (solid symbols) and those reported in (Bolzoni 1987) from a SL model (open symbols). Solid lines are a guide to the eye. Inset of (a) magnifies the evolution of uniaxial anisotropy constants at higher temperatures.

In order to treat TM and RE sublattices individually, a more complicated model so-called Two-Sublattice (TS) model is developed. In the TS model, exchange energy between the two sublattices should be considered in the calculation of the total energy. Furthermore, 3d anisotropy needs to be considered as an individual term in the expression of the anisotropy energy. The temperature dependence of anisotropy and magnetization of TM sublattice can be taken from experimental measurements on $Y_2Fe_{14}B$ (Kuz'min 2005). Detail of these calculations are beyond the scope of this thesis but given in (Gómez Eslava 2021). The Nd anisotropy constants estimated from the TS model are shown in Figure 5-11 using solid symbols. It can be clearly seen that at low temperatures, the absolute values of the anisotropy constants obtained with the TS model are significantly higher than those obtained with the SL model. As the anisotropy of the Fe sublattice is much smaller than that of the RE sublattice, larger values of the anisotropy constants for RE sublattice was expected. This means that Fe moments tend to rotate towards the direction of the applied field easier (with lower fields) than the Nd moments. Nevertheless, as a result of exchange coupling between the two sublattices, the larger anisotropy of the RE atom prevents the rotation of both RE and TM magnetic moments.

It is important to note that the models aiming for predicting the intrinsic magnetic properties of TM-RE intermetallic compounds which use classical formalism based on the Stevens' operators by relating the anisotropy coefficients to the crystalline electric field parameters and exchange interactions also estimate higher values of the anisotropy constants at low temperatures (Ito 2016). The reason behind this is the consideration of only energy levels of the RE atom, related to its angular momentum. Therefore, the predicted values in the literature are related solely to the RE sublattice and not the compound as a whole as in experimental approaches. This work leads to a conclusion that the extraction of anisotropy constants using the TS model is more appreciable to be able to directly compare first principle calculations and experimental values.

5.1.4. Evaluation of magnetocrystalline anisotropy in $(Nd,Ce)_2Fe_{14}B$ using domain theory

In chapter 4, it has been shown how analytical models developed for interpretation of domain structure of materials with uniaxial anisotropy might fail for those with intermediate anisotropy like in Fe_3Sn_2.

In this section, with the example of highly anisotropic materials, the applicability of Bodenberger-Hubert model to reproduce the magnetic domain structure of $Nd_2Fe_{14}B$ (Q = 4.6) and $Ce_2Fe_{14}B$ (Q = 2.3) was investigated. Contrary to Kittel model, considering the simplicity of sample preparation required for application of this model, Bodenberger-Hubert approach can be used for high-throughput evaluation of anisotropy constant K_1 as in (Goll 2014, Goll 2015). Nevertheless, it is of high importance for such calculations that the sample under investigation is aligned properly with respect to its crystallographic directions. To ensure that there is no misalignment, the analysis was done on field-aligned single crystals. The domain structure of $Nd_2Fe_{14}B$ and $Ce_2Fe_{14}B$ single crystals is illustrated in Figure 5-12 where *c*-axis is out of observation plane. The Bodenberger-Hubert model considers the surface branched domains which their width is thickness-independent. For thick enough samples $L > L_s$ (~100 µm) (Bodenberger 1977) the size of fully developed branched domains D_s is measured by Kerr image analysis as shown in Figure 5-12. This analysis was done using stereological line-cut method in the horizontal and vertical directions. The mean surface domain width is found to be D_s = 0.570 µm for

$Nd_2Fe_{14}B$ and D_s = 0.406 for $Ce_2Fe_{14}B$. Using Bodenberger-Hubert model (Equation 19), K_1 can be calculated as:

$$K_1 = \frac{{D_s}^2 {M_s}^4}{256A\pi^2\beta^2} \qquad \textit{Equation 30}$$

The exchange stiffness A is calculated using $A = k_B T_C/4a$ and found to be 7.8 pJm^{-1} and 5.6 pJm^{-1} for $Nd_2Fe_{14}B$ and $Ce_2Fe_{14}B$, respectively. The used T_C as well as M_s values are those found by the measurement of corresponding single crystals. The estimated anisotropy of 4.30 MJm^{-3} found for $Nd_2Fe_{14}B$ and 1.03 MJm^{-3} found for $Ce_2Fe_{14}B$ are in a good agreement with the actual value found by conventional magnetometry which are 4.37 MJm^{-3} and 1.40 MJm^{-3}, respectively. This should be noted that the domain patterns were observed on a defected surface as a result of polishing. This is while, the magnetic measurements performed on single crystals are done on "defect-free" samples. Nevertheless, still a good agreement between both methods were resulted. Therefore, making use of a fully automated image processing for measurement of D_s, this method enables a high-throughput evaluation of magnetocrystalline anisotropy with acceptable accuracy.

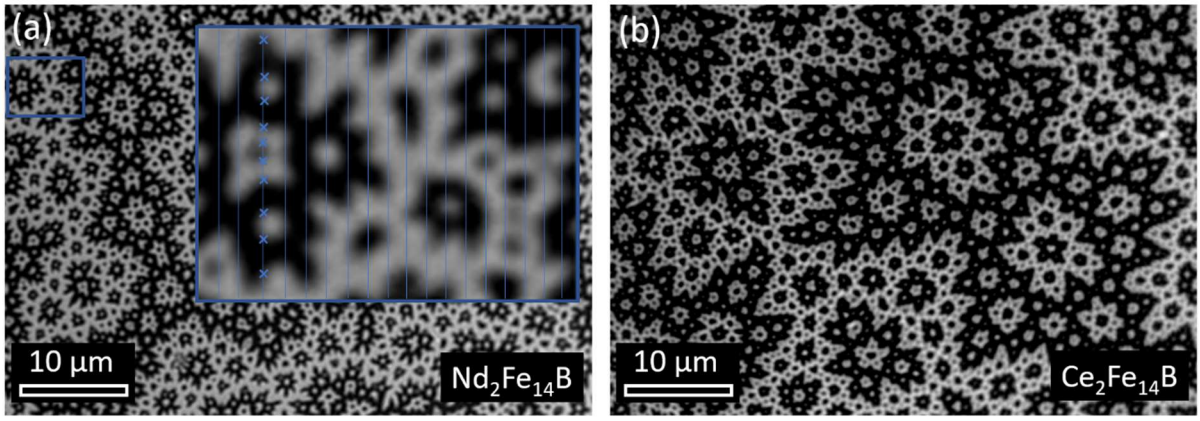

Figure 5-12. Kerr images of aligned $Nd_2Fe_{14}B$ (a) and $Ce_2Fe_{14}B$ (b) single crystals with c-axis being out of the observation plane. The marked area in (a) is magnified to schematically show the surface domain width determination using the line-cut method

5.2. Mechanochemical synthesis of sub-micron $(Nd,Ce)_2(Fe,Co)_{14}B$ particle

Mechanochemistry can be used to produce particles with a controllable submicron/nano range size. By fabrication of single-domain particles where the coercivity is defined by the uniform rotation of magnetic moments (Stoner and Wohlfarth model (Stoner 1948)), and at the same time a small amount of introduced defects in comparison to other top-down methods such as mechanical alloying and ball milling, high values of coercivity can be achieved. Therefore, one can introduce a direct link between the intrinsic and extrinsic properties of the Ce substituted 2:14:1 samples without consideration of the effect of grain boundary phases.

5.2.1. $Nd_2Fe_{14}B$ particles

For the synthesis of 2:14:1 particles, the relative molar ratios between the added elements were calculated as Fe/Nd = 3, Fe/B = 14. The amount of reducing agent Ca is altered from Ca/O of 1.5 as in (Gabay 2013) to 1.8 and 2. For Ca/O = 1.5, the appearance of a well-distinguished peak close to 2Θ = 45° corresponds to the existence of α-Fe in the sample which might evidence the in-complete reduction of Nd_2O_3. As shown in Figure 5-13, by increasing Ca/O ratio, α-Fe peak intensity decreases until for Ca/O = 2, it is almost eliminated. By Rietveld refinement of the XRD patterns of the samples, the weight fraction of α-Fe and $Nd_2Fe_{14}B$ were determined. For Ca/O = 2, the amount of $Nd_2Fe_{14}B$ formation reaches close to the calculated limit of 10.5 wt. % and therefore further increase of Ca only leads to an increase in particle size. This is due to the existence of Ca in the liquid state (T_m = 839 °C) at the annealing stage which accelerates the diffusion of the reduced RE, Fe, and B. The morphological analysis of the particles was done using SEM where after removal of the dispersant (after the washing process), their size was measured on more than 500 particles to obtain a reliable statistic. For the reference $Nd_2Fe_{14}B$ sample with Ca/O = 2, the average particle size is 224 nm (see Figure 5-14), where about 86 % of the particles are below 300 nm, the single domain particle size of $Nd_2Fe_{14}B$ (Gutfleisch 2000). This method enables the tuning of the particle size by application of different synthesis parameters.

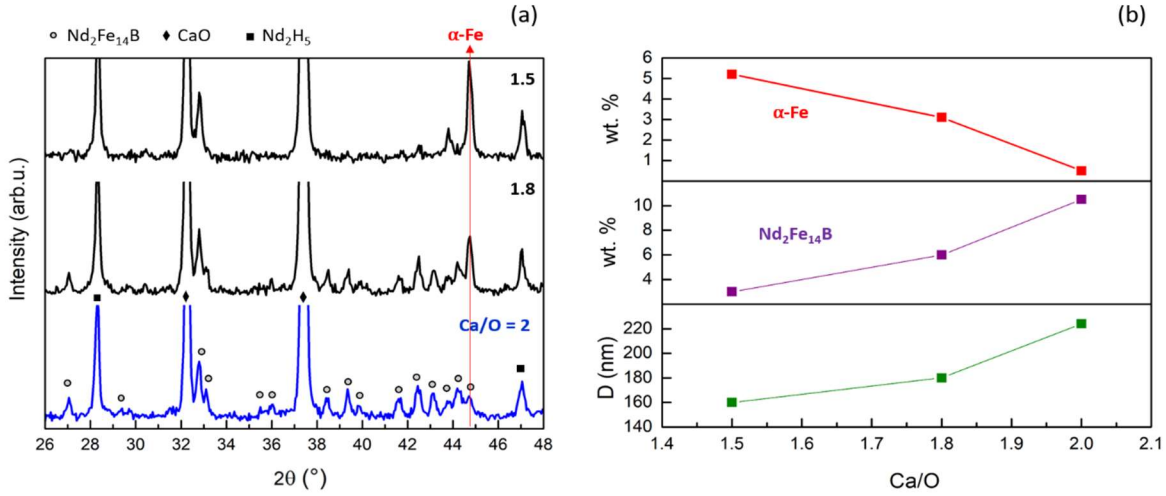

Figure 5-13. (a) XRD patterns of the as-synthesized powders with different Ca/O ratios and (b) its effect on the phase formation determined by Rietveld refinement of the XRD patterns plotted for Fe bcc (top row) and $Nd_2Fe_{14}B$ in wt. % (middle row). The bottom row in (b) is the average particle size as a function of the Ca/O ratio.

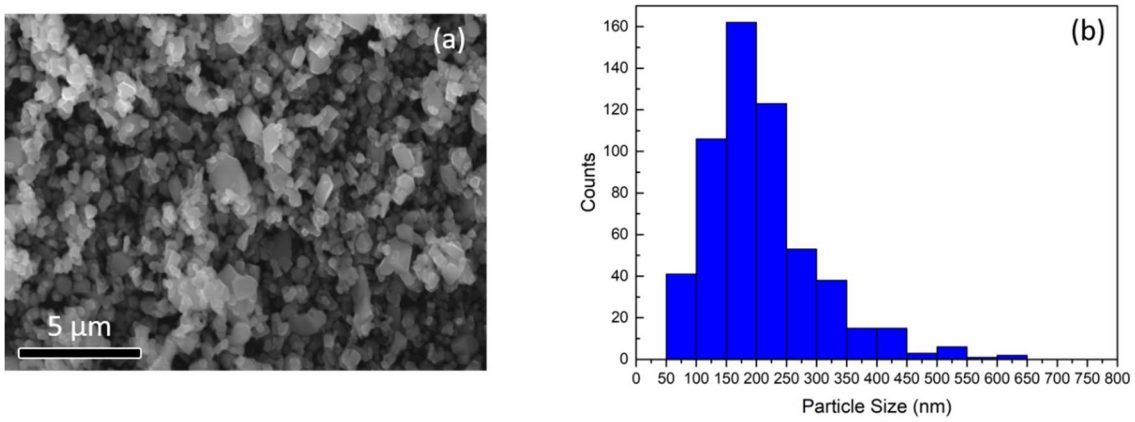

Figure 5-14. The SEM image of $Nd_2Fe_{14}B$ particles (a) and the corresponding size distribution with average particle size of 224 nm.

The XRD patterns of $Nd_2Fe_{14}B$ reference sample in the as-synthesized state, after washing procedure and after dehydrogenation are shown in Figure 5-15 a. In the as-synthesized state, in addition to the identified $Nd_2Fe_{14}B$ structure, the high-intensity peaks correspond to CaO and Nd_2H_5. The CaO is added to the sample in the initial state to act as dispersant material and prevent the particles to agglomerate. There may have been remaining metallic calcium in the as-synthesized sample right after synthesis, however, by exposing the powder to air during the XRD analysis, it decomposed to CaO and $Ca(OH)_2$. The $Ca(OH)_2$ peaks overlap with those of the Nd_2H_5 phase, which forms as a result of RE-rich phases reacting with air moisture. The removal of CaO and $Ca(OH)_2$ has been done by applying the washing procedure using a water-glycerol solution. Furthermore, the removal of Nd_2H_5 and possibly any existing RE-rich phases was done using a 0.1 vol.% acetic acid solution. Each washing procedure was repeated several times to ensure the complete removal of the byproducts and ended by the collection of magnetic particles using a magnetic field. The XRD peaks can be indexed with $Nd_2Fe_{14}B$ structure with enlarged lattice parameters corresponding to the hydrated $Nd_2Fe_{14}B$. This can be realized from the shift of corresponding peaks in the as-synthesized sample to lower angles in the washed state. Furthermore, a small peak corresponding to α-Fe becomes visible which could not be removed via the washing process. To recover $Nd_2Fe_{14}B$ structure, the dehydrogenation process (5 minutes of annealing at 300°C under continuous pumping) has been carried out which resulted in a 2:14:1 structure with very similar lattice parameters as in as-synthesized sample. The lattice parameters were extracted by Rietveld refinement of the XRD pattern and are given in Figure 5-16 b for as-synthesized and washed states.

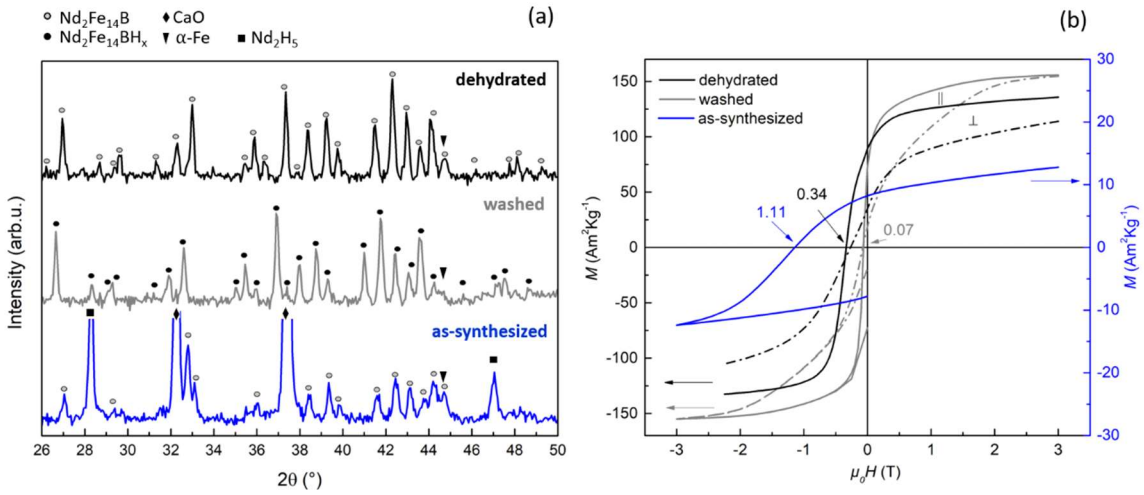

Figure 5-15. XRD patterns of the Nd-Fe-B sample shown for the as-synthesized, washed and dehydrated states. Identified XRD peaks correspond to $Nd_2Fe_{14}B$, $Nd_2Fe_{14}BH_x$, CaO, Nd_2H_5 and Fe bcc phases. (b) Field dependent magnetization measurement of Nd-Fe-B sample measured on isotropic as-synthesized powders (blue), anisotropic $Nd_2Fe_{14}BH_x$ particles (gray) and anisotropic $Nd_2Fe_{14}B$ particles (black). The magnetic curves for washed and dehydrated samples are recorded on aligned particles parallel (solid line) and perpendicular (dashed line) to the applied field.

The demagnetization curve measured on the as-synthesized sample consisting of $Nd_2Fe_{14}B$ particles with an average particle size of 224 nm embedded in the CaO/Nd_2H_5 matrix shows a coercivity of 1.11 T. This result is in agreement with the obtained value of coercivity for $Nd_2Fe_{14}B$ particles synthesized by mechanochemical synthesis method in Ref. (Gabay 2013). The low level of magnetization (12.8 Am^2kg^{-1} at 3 T) in the as-synthesized sample is due to the non-magnetic phases in the sample. Based on the XRD Rietveld refinement, the as-synthesized sample includes 9.1 wt% of 2:14:1 structure. By applying mass correction based on refinement results, the magnetization of 140 Am^2kg^{-1} at 3 T can be calculated which agrees with the obtained value of 139 Am^2kg^{-1} at 3 T in the dehydrogenated sample. The magnetization curves were measured after the washing process and after dehydrogenation on aligned particles along and perpendicular to the applied field. The washed sample exhibits a high saturation magnetization of 155 Am^2kg^{-1}. The increase of magnetization under the effect of hydrogenation in $Nd_2Fe_{14}B$ is reported in (Mushnikov 2007). A substantial decrease in coercivity has resulted from the hydrogenation of $Nd_2Fe_{14}B$ particles after washing. According to Ref. (Pareti 1988) and based on data obtained on textured powders, the anisotropy field of $Nd_2Fe_{14}B$ compound fall from 8 T down to 1.8 T upon hydrogenation. An anisotropy field of 2.5 T is estimated from *M(H)* curves of the washed sample which is the reason behind the decreased coercivity. After dehydrogenation, the coercivity could be recovered only to 0.34 T although the measured lattice parameters after dehydrogenation were almost equal to those of the as-synthesized state, indicating complete desorption of H atoms. The reason behind the irreversible coercivity might be the introduction of defects on the particle surface during the washing procedure which resulted in reduction of local magnetocrystalline anisotropy.

5.2.2. $(Nd_{1-x}Ce_x)_2(Fe,Co)_{14}B$ particles

In order to study the effect of Ce substitution on the magnetic properties of $Nd_2Fe_{14}B$ nanoparticles, $(Nd_{1-x}Ce_x)_2Fe_{14}B$, x = 0.15, 0.25 and 0.5 samples were synthesized by keeping the same synthesis parameters as in the ternary system (Fe/B = 14, Fe/RE = 3, Ca/O = 2, annealing @ 925°C-5min). No detectable peak corresponding to $REFe_2$ could be indexed in the collected XRD patterns of the samples (shown for washed particles in Figure 5-16 a). The shift of XRD peaks to higher angles reveals a decrease in lattice parameters with increasing Ce substitution. By performing Rietveld refinement on the XRD patterns of the as-synthesized and washed samples, the unit cell parameters were extracted and compared in Figure 5-16 b. The same trend as in Ce substituted single crystals were resulted in the particles, however, both a and c lattice parameters are smaller in the mechanochemically synthesized particles due to the introduction of defects during the ball milling process. It is common that different synthesis methods favor certain lattice order defects. In agreement with our results, lower lattice parameters were reported in (Ram 1992) for $Nd_2Fe_{14}B$ prepared through the reduction-diffusion process; in their case, a = 0.877 nm and b = 1.211 nm.

EDX analysis on the 2:14:1 particles shows that for all samples, the amount of substituted Ce is larger than the nominal composition which might be due to the higher diffusion rate of Ce in comparison to Nd or due to Ce content of the initial CeO being richer in Ce than its determined nominal composition. For $(Nd_{1-x}Ce_x)_2Fe_{14}B$ samples with nominal composition of x = 0.15, 0.25 and 0.5, the concentration determined using EDX analysis are x = 0.18, 0.3 and 0.54, respectively. The size distributions of Ce substituted 2:14:1 particles do not differ significantly and are found to increase to an average particle size of 241 nm for x = 0.5. The XRD analyses show a Vegard-like variation of lattice parameters with increasing Ce in $(Nd_{1-x}Ce_x)_2Fe_{14}B$ compounds, in agreement with the single crystal data. However, similar to the ternary compound, for the whole Ce substitutional range, the lattice parameters obtained on the mechanochemically synthesized particles are slightly lower than that in single crystals. No scattering behavior in the lattice parameters as reported in the literature (Pathak 2015, Yang 2017) were resulted for a specific Ce substitutional range.

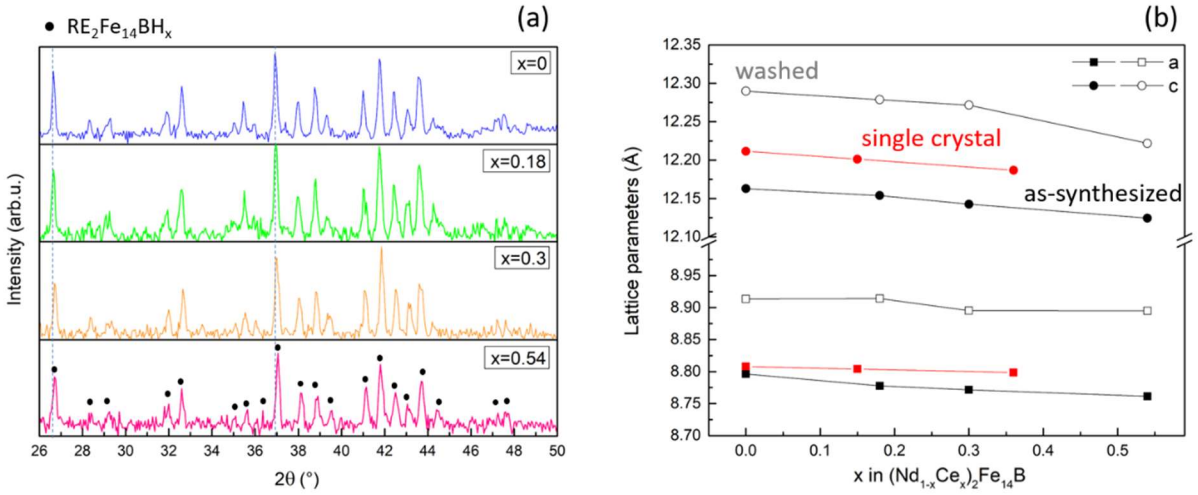

Figure 5-16. (a) XRD patterns of the washed $(Nd_{1-x}Ce_x)_2Fe_{14}B$, x = 0, 0.18, 0.3 and 0.54 samples. The dashed lines are the eye guides showing the peak shift resulted from Ce substitution. (b) Unit cell parameters of as-synthesized and washed sample compared with single crystal data plotted as a function of Ce concentration.

The room temperature demagnetization curves of the Ce substituted as-synthesized samples as well as the Nd-Fe-B sample (plotted as a reference) are shown in Figure 5-17 a. The magnetization is estimated by considering the wt. % fraction of 2:14:1 compound based on Rietveld refinement. The obtained coercivities were decreased by increasing the Ce content following the same trend as in magnetocrystalline anisotropy obtained on single crystals indicating a direct link between the intrinsic and extrinsic magnetic properties in the absence of grain boundary phases. Although, no anomalous enhancement of coercivity as in (Pathak 2015, Yang 2017) for melt-spun ribbons with 20 % Ce substitution was observed, nevertheless, the coercivity of $(Nd_{0.82}Ce_{0.18})_2Fe_{14}B$ particles only decreased slightly to 1 T in comparison to the un-doped sample with H_c = 1.1 T, indicating the great potential of Ce substituted magnets to overcome the well-known tradeoff relationship between magnetic properties and price.

The temperature stability of the Ce substituted samples was investigated by measuring the coercivity in the temperature range 300 K to 550 K. The temperature coefficient of coercivity (β) is employed to characterize the thermal stability of coercivity. β is calculated using the equation $\beta = \frac{H_c(T) - H_c(T_0)}{H_c(T_0) * (T - T_0)} * 100$ and plotted in Figure 5-18 for two temperature ranges (300-450 K) and (300-500 K), important for high-temperature applications. The temperature coefficient of coercivity (β for 300-500 K) degrades marginally from -0.441 %/K to -0.445 %/K by increasing x from 0 to 0.1, and β further decreases to -0.5479 %/K for x = 0.5. The same trend was observed for temperatures (300-450 K). Small degradation of β for a small amount of Ce substitution is of great interest for the production of Ce substituted magnets.

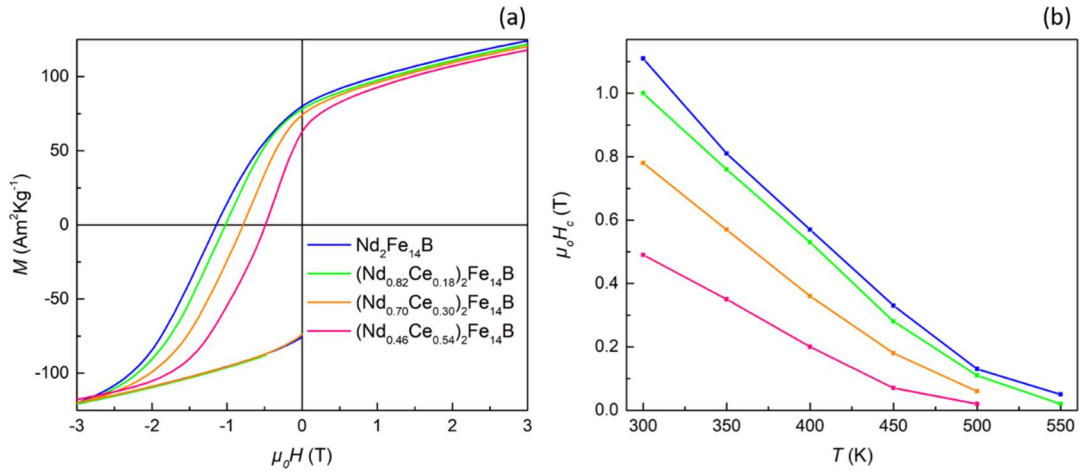

Figure 5-17. (a) Room temperature hysteresis curves and (b) temperature-dependence of coercivity in the as-synthesized $(Nd_{1-x}Ce_x)_2Fe_{14}B$ with x = 0, 0.18, 0.3 and 0.54 samples.

To investigate the effect of partial Co substitution for Fe on extrinsic magnetic properties of mechanochemically synthesized $(Nd_{1-x}Ce_x)_2Fe_{14}B$ particles, 15 % of Fe was substituted by Co in the samples with x = 0, 0.15 and 0.25. The EDX analysis shows that the actual concentration of Co in the 2:14:1 particles is the same as the nominal composition while Ce concentration being comparable to

the composition of the Co-free samples (within the experimental error of the EDX measurement). Therefore, the magnetic properties of the Co-doped samples could be compared in Figure 5-18 with their Co-free counterparts. The magnetic measurement of the as-synthesized $Nd_2(Fe_{0.85}Co_{0.15})_{14}B$ sample shows an enhanced coercivity in comparison to the ternary sample for the whole measured temperature range. The increase in coercivity for non-interacting $Nd_2(Fe_{0.85}Co_{0.15})_{14}B$ particles might be attributed to a preserved or even better intrinsic properties of the $Nd_2Fe_{14}B$ with small Co substitution (see Figure 5-8 b). Furthermore, Co is known to increase the corrosion resistivity which even for small substitution, plays an important role in the stability of nanoparticles (Abdelmoneim 2002). For Co-doped samples with x = 0.15 and x = 0.25, the coercivity has dropped slightly for low temperatures but overtook the values in the Co-free samples for high temperatures.

Thermal stability of $(Nd_{1-x}Ce_x)_2(Fe_{0.85}Co_{0.15})_{14}B$ particles was investigated and the obtained values of temperature coefficient of coercivity β were plotted in Figure 5-18 b. For all samples, an improvement of the thermal stability was obtained when Co was added in comparison to their Co free counterparts. The coefficient of coercivity β (300-500 K) increases from -0.44 %/K in the ternary system to -0.41 %/K in $Nd_2(Fe_{0.85}Co_{0.15})_{14}B$ particles. Nevertheless, the most considerable result is an improvement of temperature stability of coercivity where both Ce and Co are substituted in the sample with $(Nd_{0.82}Ce_{0.18})_2(Fe_{0.85}Co_{0.15})_{14}B$ composition with β (300-500 K) of -0.4%/K.

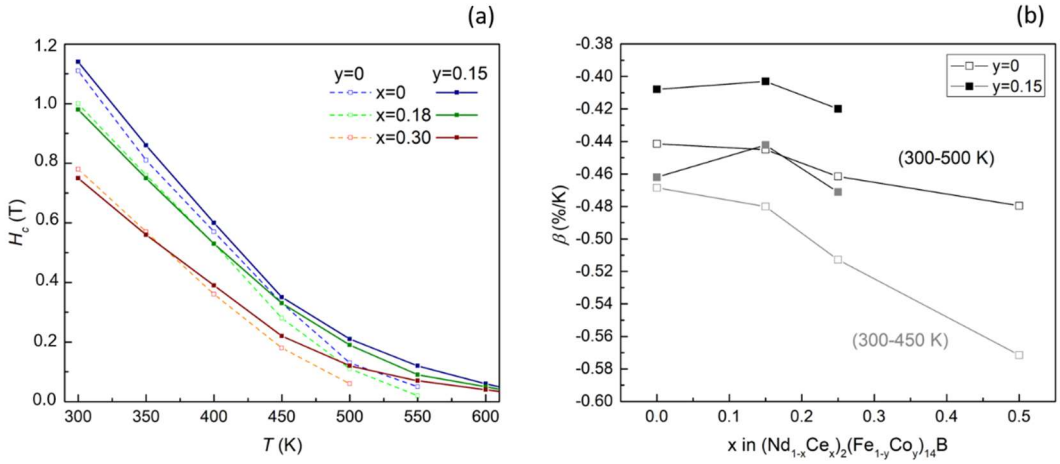

Figure 5-18. (a) Temperature-dependence of coercivity and (b) temperature coefficient of coercivity (β) of the mechanochemically synthesized $(Nd_{1-x}Ce_x)_2(Fe_{0.85}Co_{0.15})_{14}B$ particles with x = 0, 0.18, 0.3 and y = 0.15.

6. Summary and outlook

For the development of new hard magnetic materials with desirable intrinsic magnetic properties, two material systems (i) RE free Fe-Sn based system and (ii) rare earth balance Ce doped Nd-Fe-B system were studied.

For screening through the Fe-Sn based systems, high-throughput Reactive Crucible Melting (RCM) was employed. Using the example of the binary Fe-Sn system, the RCM technique was tested to check whether it produces reliable results. By comparison of the phases forming in the RCM and in the bulk alloys obtained by conventional metallurgical experiment, it has been found that the Fe_5Sn_3 phase, existing in equilibrium phase diagram at 800°C and forming in the bulk alloys, does not exist in the diffusion zone of the reactive crucible. The problem of "missing phase" is important to note as it may become more prominent while using more complex methods of combinatorial and high-throughput analyses and by their application on multinary material systems (Fayyazi 2017).

In addition to the RCM method, other non-equilibrium synthesis methods such as melt spinning and high energy ball milling were employed for the discovery of the desired hard magnetic phase in the Fe-Sn system. The followed experimental screening strategies were supported by DFT calculations of the magnetic and thermodynamic properties of Fe-Sn alloys which were performed by my project partners. All Fe-Sn binary ferromagnetic compounds; Fe_3Sn, Fe_5Sn_3, and Fe_3Sn_2 exhibit high Curie temperature of above 600 K and high saturation magnetization of above 0.7 T. Among them, the Fe_3Sn with the largest T_C = 735 K and M_s = 1.27 T also exhibits the strongest anisotropy however of planar type. To modify the electronic structure of Fe_3Sn and possibly induce uniaxial MAE, partial alloying of Sn with its neighboring elements such as Sb, Si, Ga, Ge, In, Pb and Bi was examined (Vekilova 2019). While theoretical calculations suggested the switching of anisotropy to uniaxial by partial substitution of Sb for Sn, the experimental results showed destabilization of 3:1 structure even by very small substitution of Sb for Sn in the Fe-Sn system. The Sb doped Fe_3Sn structure could only be stabilized by further doping of Mn into the Fe sublattice. Nevertheless, the predicted uniaxial anisotropy was flipped back to the planar anisotropy of an undoped system evidenced by observation of the nonuniaxial magnetic domain. The other screened Fe-Sn compound was Fe_5Sn which was predicted to have high potential to be stabilized at high temperatures or upon moderate alloying. The theoretical calculations predicted a saturation magnetization of 1.7 T and magnetocrystalline anisotropy energy of 1.5 MJm^{-3}, making it a very promising potential candidate as a permanent magnetic material to be explored. Guided by theoretical calculations, the phase relations of HEBM samples with $Fe_{39}Sn_8X$ composition with X = Fe, Ti, V, Cr, Mn, Co, Nb and Mo were screened in the temperature range between 500°C to 900°C. No trace of Fe_5Sn formation was observed in any of the 64 prepared samples. Either Fe_5Sn does not exist at all or the formation conditions could not be fulfilled.

Although in recent years so much effort has put into developing of a Fe-Sn hard magnetic material as a rare earth free gap magnet, so far, no compound which could fulfill all the requirements for a permanent magnetic application could be experimentally realized. Nevertheless, based on DFT calculations and due to the combination of Fe 3d magnetism and strong spin-orbit coupling of Sn 5p states, Fe-Sn based systems have intrinsically potential for inducing strong MAE. While the strong in-plane anisotropy of Fe_3Sn would require significant modification of the electronic structure to achieve

uniaxial anisotropy, Fe-Sn based phases with moderate MAE like Fe_5Sn_3 may be more suitable to achieve uniaxial MAE upon moderate alloying. Further experimental and theoretical studies are necessary in order to explore this potential.

To investigate the structural and intrinsic magnetic properties of Fe-Sn ferromagnetic compounds, the single crystals of Fe_3Sn, Fe_5Sn_3, and Fe_3Sn_2 were grown and characterized (Fayyazi 2019). While the crystal structures of Fe_3Sn and Fe_3Sn_2 compounds were found to be in agreement with the literature data, a new structural model for Fe_5Sn_3 which is different from its previously known structure (hexagonal, $P6_3/mmc$) was proposed. The combination of single crystal X-ray diffraction and Transmission Electron Microscope (TEM) provided evidence for threefold twinning of the orthorhombic unit cell with a (3 + 1) dimensional space group Pbcm(α00)0s0. The magnetic properties were measured on aligned single crystals and the spontaneous magnetization, Curie temperatures, and magnetocrystalline anisotropy energy were determined. In addition, the temperature dependencies of the anisotropy constants K_1 and K_2 were calculated using the Sucksmith-Thompson method. The result shows that Fe_3Sn possesses a large planar anisotropy of K_1 = 1.16 MJm^{-3} and 1.08 MJm^{-3} at room temperature and at a temperature of 10 K, respectively. The anisotropy of Fe_5Sn_3 phase is also in-plane with a constant of K_1 = 0.35 MJm^{-3} at room temperature and K_1 = 0.47 MJm^{-3} at 10 K. The Fe_3Sn_2 phase has a small uniaxial anisotropy of K_1 = 0.05 MJm^{-3}at room temperature and undergoes a spin reorientation transition at 110 K where the anisotropy changes sign and reaches K_1 = 0.04 MJm^{-3} at 10 K. The spin reorientation transition is also detected and confirmed by observing the magnetic domain structure using MFM. Although negligible anisotropy of Fe_3Sn_2 phase makes this compound not applicable as a permanent magnetic material, however this material began attracting attention as a candidate for spintronic applications due to its geometrically frustrated kagomé structure which resulted in various anomalous electronic characteristics such as a large topological Hall effect.

To investigate a mutual induction of orbital magnetic moments between Fe and Sn, as an outlook to this work and by owning Fe-Sn single crystals, the additional experimental techniques e.g. X-ray magnetic circular dichroism can be employed. Indeed, X-ray absorption spectroscopy offers insight into the element-specific magnetic properties like spin- and orbital moments of Sn and allows to disentangle contributions from different constituents in the Fe-Sn binary alloys. This will help in better understanding of the nature of magnetocrystalline anisotropy and role of Sn 5p electrons in incident of it.

Additionally, the applicability of magneto-optical Kerr microscopy as a tool for high-throughput evaluation of magnetic properties of phases appearing in the reactive crucible (or any bulk combinatorial technique) was investigated. It has been shown that Kerr microscopy is a proper characterization technique allowing the detection of uniaxial type of magnetic anisotropy on the micrometer length-scale. Nevertheless, the quantitative analysis of magnetic anisotropy from the domain structure can be erroneous. Using three established theoretical domain models (“Kittel”, “Szymczak” and “Bodenberger-Hubert”, I have shown that these theoretical models can be significantly misleading for the estimation of anisotropy in materials which are not highly anisotropic. It has been shown that the most reliable model among the three introduced ones for materials with intermediate anisotropy is the “Kittel” model, only applicable for thin films with the so-called Kittel band domain structure. This model, however, requires a very accurate determination of the thickness.

The estimation of the magnetic anisotropy of Fe_3Sn_2 on a 5 mm thick single crystal with D ~ 0.4 mm results in K_1 = 0.02 MJm^{-3} which is in a fair agreement with the actual anisotropy of the material determined by magnetometry. For this reason, the assessment of anisotropy by the "Szymczak" and Bodenberger-Hubert" models can be significantly erroneous as they only consider strict uniaxial magnetization. Application of selective Kerr microscopy and observation of in-plane magnetization component of (001) aligned Fe_3Sn_2 single crystal revealed the existence of multiaxial closure domain at the surface of the sample characteristic for moderately anisotropic materials. The "Szymczak" and Bodenberger-Hubert" models have nevertheless resulted in reliable results for high anisotropic $Nd_2Fe_{14}B$ and $Ce_2Fe_{14}B$ samples, investigated in the second part of the thesis.

The second investigated material was the Nd-Fe-B system where the effect of Ce substitution on the structural and intrinsic magnetic properties of $(Nd_{1-x}Ce_x)_2Fe_{14}B$ compounds was investigated by synthesis and characterization of single-crystalline samples with x = 0, 0.15, 0.36, 0.63 and 1. All investigated compounds crystallize in a tetragonal structure with a $P4_2/mnm$ space group with lattice parameters a and c as well as tetragonality factor c/a decreasing monotonically with increasing Ce concentration. Ce substitution has also decreased all intrinsic magnetic properties of the compound. The reduction of spontaneous magnetization was found to follow empirical predictions considering the alloying rules between the two end-members $Nd_2Fe_{14}B$ and $Ce_2Fe_{14}B$. The anisotropy field of $(Nd_{1-x}Ce_x)_2Fe_{14}B$ was found H_a = 8 T for x = 0 and H_a = 2.8 T for x = 1, both being in agreement with the literature values. However, an anisotropy field of 6.3 T for x = 0.36 was found to be 1.2 T larger than the reported value for $(Nd_{0.62}Ce_{0.38})_2Fe_{14}B$ single crystal in (Susner 2017). The temperature dependencies of the anisotropy constant K_1 was calculated using the Sucksmith-Thompson method for all compounds at room temperature and above. The first anisotropy constants were found to be 4.37, 4.03, 3.36, 2.55, 1.40 MJm^{-3} for x = 0, 0.15, 0.36, 0.63 and 1, respectively, which all decrease monotonically with increasing temperature.

Except for the ternary $Ce_2Fe_{14}B$ compound, four other Nd contained compounds undergo a spin reorientation transition at low temperature where the anisotropy changes from uniaxial to easy-cone. While the negligible contribution of Ce to the total anisotropy leads to uniaxial alignment for the whole temperature range, increase of Ce in $(Nd_{1-x}Ce_x)_2Fe_{14}B$ results in decrease of T_{SRT} from 131 K in x = 0 to 106 K in 0.63. Early studies on $Nd_2Fe_{14}B$ showed a distinct role of RE sublattices on the incidence of SRT as the 4f sublattice (compared to 4g) is dominantly contribute to the planar alignment of magnetization. Growing effect of Ce substitution in decrease of SRTT (the larger is the Ce proportion, the greater is the reduction of SPT), might indicate a preferential site occupancy of Ce atoms for larger 4g sites over the smaller 4f site.

To partially compensate the detrimental effect of Ce substitution on intrinsic magnetic properties of $(Nd_{1-x}Ce_x)_2Fe_{14}B$, 10% of Fe was doped with Co. Two additional single crystals $Nd_2(Fe_{0.9}Co_{0.1})_{14}B$ and $(Nd_{0.85}Ce_{0.15})_2(Fe_{0.9}Co_{0.1})_{14}B$ were investigated (Fayyazi 2016). The Curie temperature was increased by about 70 K in comparison to their Co free counterparts. The effect of 10% Co substitution on the spontaneous magnetization is negligible at room temperature. However, with increasing temperature, the magnetization for Co-doped samples starts to overtake and the difference is getting bigger with increasing temperature. At room temperature, 10 % Co doping slightly decreased the anisotropy field of $Nd_2Fe_{14}B$. In contrast, a favorable effect on anisotropy was obtained when Ce and Co are co-doped

in the structure. It has been observed that the degradation of magnetic anisotropy as a result of Ce substitution is partially compensated when it was co-doped with Co. The reason behind it can be the preferential occupancy of Co for 4c, $8j_1$ sites which are located in the affinity of RE elements. Therefore, the proximity between Ce and Co at low concentrations can lead to a synergism between these two neighboring atoms and result in an enhanced anisotropy. The substitution of Co has especially a positive impact on anisotropy energy at higher temperatures. The magnetic measurement of Co-doped single crystals clearly shows better thermal stability of anisotropy energy in comparison to their Co-free counterparts. A detailed investigation on the electronic structure of co-doped $(Nd,Ce)_2(Fe,Co)_{14}B$ should be done to be able to explain the physical origin of the enhanced magnetic properties. Owning the single crystal of this compound, a detailed investigation of the magnetic structure of Ce and Co doped $Nd_2Fe_{14}B$ can be done as an outlook to this work by neutron diffraction experiments which can shed a light for better undrestanding the mutual effect of Ce and Co in the 2:14:1 structure.

At low temperatures, the magnetization curves were measured under a magnetic field of up to 60 T applied by pulsed magnets. FOMP was observed in *M(H)* curves measured along [100] direction at temperatures below 200 K. It has been found that the field in which FOMP occurs increases with decreasing temperature, in agreement with the literature. By simulation and fitting process of *M(H)* curves at various temperatures and along different crystallographic directions based on the minimization of the total energy (sum of anisotropy and Zeeman energy was considered) of the system, 5 associating anisotropy constants were evaluated (Gómez Eslava 2021). The anisotropy constants were derived from Single Lattice (SL) and Two Sublattice (TS) models. As in the TS model, RE and TM sublattices need to be treated individually, the exchange energy between them should have been additionally considered in the calculation of the total energy. Therefore, the development of such calculations is more complex but is of great importance as it delivers the anisotropy constants of RE sublattice. The first principle calculations based on crystalline-electric field effect and the molecular field approximation which are widely used for the predication of intrinsic magnetic properties are also solely related to the RE sublattice. Therefore, the approach based on the TS model enables the direct comparison of the experimental results and those obtained by first principle calculations. At low temperature, the absolute values of the anisotropy constants obtained with the TS model and those estimated by first principle calculation are both higher than that in the SL model which determines the anisotropy constant of the compound as a whole. This approach of extracting anisotropy constants from single crystal measurements may be used to guide the development of permanent magnets which are less dependent on critical materials.

The intrinsic magnetic properties of CeCo doped single crystals were compared to the extrinsic magnetic properties of single-domain size particles synthesized by mechanochemical synthesis method. The sub-micron $(Nd,Ce)_2(Fe,Co)_{14}$ particles with an average particle size of ~230 nm were grown by Ca-reduction of precurser oxides and diffusion process during a HEBM and further heat treatment procedure. In agreement with single crystal data, Ce substitution resulted in a reduction of lattice parameters, however, the lattice parameters obtained on mechanochemically synthesized particles are slightly lower than that of single crystals, resulting from the introduction of defects during the ball milling process. Ce substitution has also resulted in a decrease of coercivity following the same trend as in magnetocrystalline anisotropy obtained on single crystals indicating a direct link between

the intrinsic and extrinsic magnetic properties in the absence of grain boundary phases. Investigating $(Nd_{1-x}Ce_x)_2Fe_{14}B$ particles with x = 0, 0.18, 0.3 and 0.54, no anomalous enhancement of coercivity as in (Pathak 2015, Yang 2017) for x = 0.2 melt-spun ribbons were observed. Nevertheless, the coercivity of $(Nd_{0.82}Ce_{0.18})_2Fe_{14}B$ particles only decreased slightly 1 T in comparison to the un-doped sample with H_c = 1.1 T, indicating the great potential of Ce substituted magnets to overcome the well-known tradeoff relationship between magnetic properties and price. In agreement with single crystal data, partial substitution of Fe with Co resulted in the enhancement of coercivity, especially at high temperatures. Investigation of thermal stability of particle by determination of temperature coefficient of coercivity has shown an improvement of the thermal stability for all samples when Co was added in comparison to their Co free counterparts. The coefficient of coercivity β is improved from -0.441 %/K in the ternary system to -0.407 %/K in $Nd_2(Fe_{0.85}Co_{0.15})_{14}B$ particles. Further improvement of the temperature coefficient of coercivity was observed when both Ce and Co were substituted in the sample with $(Nd_{0.82}Ce_{0.18})_2(Fe_{0.85}Co_{0.15})_{14}B$ composition. The enhanced high-temperature performance of CeCo-doped NdFeB magnets has definitely its origin in intrinsic magnetic properties based on the single crystal data provided by this thesis.

This thesis has succeeded in the introduction of CeCo substituted NdFeB material as a strong candidate for permanent magnet application. It has been shown that Ce-substituted magnets have the potential to possess superior performance to their Nd-Fe-B-based counterparts when Co is co-doped. While this thesis has mainly focused on the intrinsic magnetic properties of the main compounds, optimal engineering of the microstructural is necessary to achieve desirable extrinsic properties. As all commercial permanent magnets contain some degree of Co, the development of CeCo co-doped NdFeB magnets with a lower price and better performance is possible. Nevertheless, optimization of the material composition to be produced with different manufacturing techniques should be studied in detail. Moreover, negative associated effect e.g. formation of 1:2 ferromagnetic phase at the grain boundary which is detrimental for decoupling of the main ferromagnetic phase should be faced, especially, in the case of sintered magnets. While Laves phase formation can be partially suppressed by rapidly quenching, in sintered magnets, the inclusion of alloying elements which destabilize the 1:2 phase and at the same time do not deteriorate the intrinsic magnetic properties of the main phase should be investigated.

Bibliography

(Abache 1986) Abache, C. and Oesterreicher, J. "*Magnetic anisotropies and spin reorientations of $R_2Fe_{14}B$-type compounds*", Journal of Applied Physics. **60** 10 (1986) 3671-3679

(Abdelmoneim 2002) Abdelmoneim, A., Gebert, A., Uhlemann, M., et al. "*The influence of Co and Ga additions on the corrosion behavior of nanocrystalline NdFeB magnets*", Corrosion Science. **44** (2002) 1857-1874

(Alam 2013) Alam, A., Khan, M., McCallum, R. W., et al. "*Site-preference and valency for rare-earth sites in $(R\text{-}Ce)_2Fe_{14}B$ magnets*", Applied Physics Letters. **102** 4 (2013) 042402

(Allen 2005) Allen, S., Carter, W. C. and Kemper, R. "*Kinetics of materials*". Hoboken, New Jersey, John Wiley & Sons (2005) 645-652

(Arrott 1957) Arrott, A. "*Criterion for Ferromagnetism from Observations of Magnetic Isotherms*", Physical Review. **108** 6 (1957) 1394-1396

(Belov 1956) Belov, K. P. and Goryaga, A. N. Fizika Metallov I Metallovedenie. **2** (1956) 3-9

(Bhanumurthy 1990) Bhanumurthy, K., Kale, G. B., Khera, S. K., et al. "*Solid-state diffusion reaction and formation of intermetallic compounds in the nickel-zirconium system*", Metallurgical Transactions a-Physical Metallurgy and Materials Science. **21** 11 (1990) 2897-2903

(Binnemans 2014) Binnemans, K. "*Economics of rare earths: The balance problem*". The 1st european rare earth resources conference Milos (Greece).(2014) 37-46

(Bloch 1930) Bloch, F. "*Zur Theorie des Ferromagnetismus*", Zeitschrift für Physik. **61** 3 (1930) 206-219

(Bodenberger 1977) Bodenberger, R. and Hubert, A. "*Zur Bestimmung der Blochwandenergie von einachsigen Ferromagneten*", physica status solidi (a). **44** 1 (1977) K7-K11

(Boettcher 1955) Boettcher, A., Haase, G. and Thun, R. "*Strukturuntersuchung von Mehrstoffsystemen durch kinematische Elektronenbeugung*", Zeitschrift Fur Metallkunde. **46** 5 (1955) 386-400

(Bolzoni 1987) Bolzoni, F., Moze, O. and Pareti, L. "*First-order field-induced magnetization transitions in single-crystal $Nd_2Fe_{14}B$*", Journal of Applied Physics. **62** (1987) 615-620

(Buschow 1988) Buschow, K. H. J. "*Chapter 1: Permanent magnet materials based on 3d-rich ternary compounds*". Handbook of Ferromagnetic Materials, Elsevier. **4** (1988) 1-129

(Buschow 2003) Buschow, K. H. J. and De Boer, F. R. "*Physics of Magnetism and Magnetic Materials*". New York, Springer (2003)

(Cadogan 1987) Cadogan, J. M., Coey, J. M. D., Gavigan, J. P., et al. "*Exchange and CEF interactions in $R_2Fe_{14}B$ compounds*" Journal of Applied Physics. **61** 8 (1987) 3974-3976

(Callen 1965) Callen, E. and Callen, H. "*Ferromagnetic transitions and one- third- power law*", Journal of Applied Physics. **36** 3P2 (1965) 1140-1162

(Capehart 1993) Capehart, T. W., Mishra, R. K., Meisner, G. P., et al. "*Steric variation of the cerium valence in $Ce_2Fe_{14}B$ and related compounds*", Applied Physics Letters. **63** (1993) 3642-3644

(Chaudhary 2020) Chaudhary, R. P., Gandha, K. H., Meng, F., et al. "*Development of Mischmetal–Fe–Co–B Permanent Magnet Alloys via High-Throughput Methods*", ACS Combinatorial Science. **22** 5 (2020) 248-254

(Coey 2010) Coey, J. M. "*Magnetism and magnetic materials*", Cambridge University Press (2010)

(Coey 2012) Coey, J. M. D. "*Permanent magnets: Plugging the gap*", Scripta Materialia. **67** 6 (2012) 524-529

(Colin 2016) Colin, C. V., Ito, M., Yano, M., et al. "*Solid-solution stability and preferential site-occupancy in $(R\text{-}R')_2Fe_{14}B$ compounds*", Applied Physics Letters. **108** 24 (2016) 242415

(Cui 2018) Cui, J., Kramer, M., Zhou, L., et al. "*Current progress and future challenges in rare-earth-free permanent magnets*", Acta Materialia. **158** (2018) 118-137

(Cullity 2008) Cullity, B. D. and Graham, C. D. "*Introduction to Magnetic Materials*", IEEE press (2008)

(Dianoux 2017) Dianoux, A., Malaman, B. and Mazet, T. "*Magnetic and magnetocaloric properties of $Fe_{5-x}Mn_xSn_3$*", Solid State Communications. **260** (2017) 40-44

(Echevarria-Bonet 2018) Echevarria-Bonet, C., Iglesias, N., Garitaonandia, J. S., et al. "*Structural and magnetic properties of hexagonal Fe_3Sn prepared by non-equilibrium techniques*", Journal of Alloys and Compounds. **769** (2018) 843-847

(Ener 2016) Ener, S., Kroder, J., Skokov, K. P., et al. "*The search for room temperature tetragonal phases of Fe-Mn-Ga: A reactive crucible melting approach*", Journal of Alloys and Compounds. **683** (2016) 198-204

(Enokido 2020) Enokido, Y., Hashimoto, R., Kitamura, T., et al. "*High-Throughput Screening Method for Thin-Film $R_2Fe_{14}B$ Magnet*", IEEE Transactions on Magnetics. **56** 4 (2020) 1-5

(EU-Commission 2017) EU-Commission (2017). Study on the review of the list of critical raw materials, Criticality Assessments. European publications.

(Fan 2016) Fan, X. D., Guo, S., Chen, K., et al. "*Tuning Ce distribution for high performanced Nd-Ce-Fe-B sintered magnets*", Journal of Magnetism and Magnetic Materials. **419** (2016) 394-399

(Fayyazi 2016) Fayyazi, B., Skokov, K., Loewe, K., et al. "*The Intrinsic and extrinsic magnetic properties of $(Nd,Ce)_2(Fe,Co)_{14}B$: From single crystals to sintered permanent magnets*". The 24th International Workshop on Rare-Earth and Future Permanent Magnets and Their Applications (REPM), Darmstadt, Germany.(2016) 113-117

(Fayyazi 2017) Fayyazi, B., Skokov, K. P., Faske, T., et al. "*Bulk combinatorial analysis for searching new rare-earth free permanent magnets: Reactive crucible melting applied to the Fe-Sn binary system*", Acta Materialia. **141** (2017) 434-443

(Fayyazi 2019) Fayyazi, B., Skokov, K. P., Faske, T., et al. "*Experimental and computational analysis of binary Fe-Sn ferromagnetic compounds*", Acta Materialia. **180** (2019) 126-140

(Fenner 2009) Fenner, L. A., Dee, A. A. and Wills, A. S. "*Non-collinearity and spin frustration in the itinerant kagome ferromagnet Fe_3Sn_2*", Journal of Physics-Condensed Matter. **21** 45 (2009) 452202

(Fischbacher 2017) Fischbacher, J., Kovacs, A., Oezelt, H., et al. "*Effective uniaxial anisotropy in easy-plane materials through nanostructuring*", Applied Physics Letters. **111** 19 (2017) 192-407

(Fjellvag 1986) Fjellvag, H. and Kjekshus, A. "*Structural-properties of Co_3Sn_2,Ni_3Sn_2 and some ternary derivatives*", Acta Chemica Scandinavica Series a-Physical and Inorganic Chemistry. **40** 1 (1986) 23-30

(Freeman 1979) Freeman, A. J. and Desclaux, J. P. "*Dirac-Fock studies of some electronic properties of rare-earth ions*", Journal of Magnetism and Magnetic Materials. **12** 1 (1979) 11-21

(Gabay 2015) Gabay, A. M. and Hadjipanayis, G. C. "*Application of Mechanochemical Synthesis to Manufacturing of Permanent Magnets*", JOM. **67** 6 (2015) 1329-1335

(Gabay 2013) Gabay, A. M., Hu, X. C. and Hadjipanayis, G. C. "*Mechanochemical synthesis of fine $R_2Fe_{14}BH_x$ and $R_2Fe_{14}B$ powders with R = Nd or Nd-Dy*", Journal of Alloys and Compounds. **574** (2013) 472-476

(Giefers 2006) Giefers, H. and Nicol, M. "*High pressure X-ray diffraction study of all Fe-Sn intermetallic compounds and one Fe-Sn solid solution*", Journal of Alloys and Compounds. **422** 1-2 (2006) 132-144

(Givord 1984) Givord, D., Li, H. S. and Moreau, J. M. "*Magnetic-properties and crystal-structure of $Nd_2Fe_{14}B$*", Solid State Communications. **50** 6 (1984) 497-499

(Givord 1984) Givord, D., Li, H. S. and Perrier de la Bâthie, R. "*Magnetic properties of $Y_2Fe_{14}B$ and $Nd_2Fe_{14}B$ single crystals*", Solid State Communications. **51** 11 (1984) 857-860

(Goll 2015) Goll, D., Loeffler, R., Herbst, J., et al. "*Magnetic properties of hard magnetic $(Fe,Cr)_3Sn_2$ intermetallic compound*", Physica Status Solidi-Rapid Research Letters. **9** 10 (2015) 603-606

(Goll 2014) Goll, D., Loeffler, R., Herbst, J., et al. "*High-throughput methods for searching new permanent magnet materials*", IEEE Transactions on Magnetics. **50** 11 (2014) 2103507

(Goll 2015) Goll, D., Loeffler, R., Herbst, J., et al. "*Novel Permanent Magnets by High-Throughput Experiments*", JOM. **67** 6 (2015) 1336-1343

(Goll 2014) Goll, D., Loeffler, R., Herbst, J., et al. "*High-throughput search for new permanent magnet materials*", Journal of Physics-Condensed Matter. **26** 6 (2014) 064208

(Goll 2018) Goll, D., Loeffler, R., Hohs, D., et al. "*Reaction sintering as a high-throughput approach for magnetic materials development*", Scripta Materialia. **146** (2018) 355-361

(Gómez Eslava 2021) Gómez Eslava, G., Fayyazi, B., Skokov, K., et al. "*A two-sublattice model for extracting rare-earth anisotropy constants from measurement on $(Nd,Ce)_2(Fe,Co)_{14}B$ single crystals*", Journal of Magnetism and Magnetic Materials. **520** (2021) 167470

(Gómez Eslava 2021) Gómez Eslava, G., Ito, M., Colin, C. V., et al. "*Preferential Co and Fe atom occupancy in $R_2(Fe_{1-x}Co_x)_{14}B$ intermetallic compounds (R = Nd, Y and Ce)*", Journal of Alloys and Compounds. **851** (2021) 156168

(Goodenough 1967) Goodenough, J. B. and Stickler, J. J. "*Theory of the Magnetic Properties of the Ilmenites $MTiO_3$*", Physical Review. **164** 2 (1967) 768-778

(Groß 2004) Groß, F. "*Search for new permanent magnetic phases by reaction crucible analysis and development of high throghput methods*". PhD thesis, The University of Birmingham (2004)

(Gusak 2010) Gusak, A. M., Zaporozhets, T. V., Lyshenko, Y. O., et al. "*Diffusion-controlled Solid State Reactions: In Alloys, Thin Films and Nanosystems*", Wiley-VCH Verlag GmbH & Co.(2010) 476

(Gutfleisch 2000) Gutfleisch, O. "*Controlling the properties of high energy density permanent magnetic materials by different processing routes*", Journal of Physics D-Applied Physics. **33** 17 (2000) R157-R172

(Gutfleisch 2011) Gutfleisch, O., Willard, M. A., Brück, E., et al. "*Magnetic Materials and Devices for the 21st Century: Stronger, Lighter, and More Energy Efficient*", Advanced Materials. **23** 7 (2011) 821-842

(Hadjipanayis 1983) Hadjipanayis, G. C., Hazelton, R. C. and Lawless, K. "*New iron-rare-earth based permanent-magnet materials*", Applied Physics Letters. **43** 8 (1983) 797-799

(Hanak 1970) Hanak, J. J. "*The multiple-sample-concept in materials research - synthesis, compositional analysis and testing of entire multicomponent systems*", Journal of Materials Science. **5** 11 (1970) 964-971

(Hasebe 1978) Hasebe, M. and Nishizawa, T. "*Analysis and synthesis of phase diagrams of the Fe-Cr-Ni, Fe-Cu-Mn and Fe-Cu-Ni systems*", Applications of Phase Diagrams in Metallurgy and Ceramics. (1978) 911-954

(Herbst 1991) Herbst, J. F. "*$R_2Fe_{14}B$ materials - intrinsic-properties and technological aspects*", Reviews of Modern Physics. **63** 4 (1991) 819-898

(Herbst 1984) Herbst, J. F., Croat, J. J., Pinkerton, F. E., et al. "*Relationships between crystal-structure and magnetic-properties in $Nd_2Fe_{14}B$*", Physical Review B. **29** 7 (1984) 4176-4178

(Herbst 1986) Herbst, J. F. and Yelon, W. B. "*Preferential site occupation and magnetic structure of $Nd_2(Co_xFe_{1-x})_{14}B$ systems*", Journal of Applied Physics. **60** 12 (1986) 4224-4229

(Heritage 2020) Heritage, K., Bryant, B., Fenner, L. A., et al. "*Images of a First-Order Spin-Reorientation Phase Transition in a Metallic Kagome Ferromagnet*". **30** 36 (2020) 1909163

(Hirayama 2017) Hirayama, Y., Takahashi, Y. K., Hirosawa, S., et al. "*Intrinsic hard magnetic properties of $Sm(Fe_{1-x}Co_x)_{12}$ compound with the $ThMn_{12}$ structure*", Scripta Materialia. **138** (2017) 62-65

(Hou 2017) Hou, Z. P., Ren, W. J., Ding, B., et al. "*Observation of Various and Spontaneous Magnetic Skyrmionic Bubbles at Room Temperature in a Frustrated Kagome Magnet with Uniaxial Magnetic Anisotropy*", Advanced Materials. **29** 29 (2017) 1701144

(Hubert 2014) Hubert, A. and Schäfer, R. "*Magnetic Domains -The Analysis of Magnetic Microstructures*". Berlin, Springer Berlin (2014)

(Hutchings 1964) Hutchings, M. T. "*Point-Charge Calculations of Energy Levels of Magnetic Ions in Crystalline Electric Fields*". Solid State Physics. F. Seitz and D. Turnbull, Academic Press. **16** (1964) 227-273

(Hynninen 2007) Hynninen, A.-P., Thijssen, J. H. J., Vermolen, E. C. M., et al. "*Self-assembly route for photonic crystals with a bandgap in the visible region*", Nature Materials. **6** 3 (2007) 202-205

(Ishida 1991) Ishida, K. and Nishizawa, T. "*The Co-Sn (Cobalt-Tin) System*", Journal of Phase Equilibria. **12** 1 (1991) 88-93

(Ito 2016) Ito, M., Yano, M., Dempsey, N. M., et al. "*Calculations of the magnetic properties of $R_2M_{14}B$ intermetallic compounds (R=rare earth, M=Fe, Co)*", Journal of Magnetism and Magnetic Materials. **400** (2016) 379-383

(Ito 2016) Ito, M., Yano, M., Sakuma, N., et al. "*Coercivity enhancement in Ce-Fe-B based magnets by core-shell grain structuring*", Aip Advances. **6** 5 (2016) 056029

(Jacobsen 1996) Jacobsen, K. W., Stoltze, P. and Nørskov, J. K. "*A semi-empirical effective medium theory for metals and alloys*", Surface Science. **366** 2 (1996) 394-402

(Jiang 2019) Jiang, Q. Z., He, L. K., Lei, W. K., et al. "*Microstructure and magnetic properties of multi-main-phase Ce-Fe-B spark plasma sintered magnets by dual alloy method*", Journal of Magnetism and Magnetic Materials. **475** (2019) 746-753

(Kale 1985) Kale, G., Khera, S. and Patil, R. "Phase stability in the diffusion zone". Materials Science Forum, Trans Tech Publ.(1985) 319-324

(Kanatzidis 2005) Kanatzidis, M. G., Pöttgen, R. and Jeitschko, W. "*The Metal Flux: A Preparative Tool for the Exploration of Intermetallic Compounds*", Angewandte Chemie International Edition. **44** 43 (2005) 6996-7023

(Karpenkov 2018) Karpenkov, D. Y., Skokov, K. P., Lyakhova, M. B., et al. "*Intrinsic magnetic properties of hydrided and non-hydrided Nd_5Fe_{17} single crystals*", Journal of Alloys and Compounds. **741** (2018) 1012-1020

(Kennedy 1965) Kennedy, K., Stefansk.T, Davy, G., et al. "*Rapid method for determining ternary-alloy phase diagrams*", Journal of Applied Physics. **36** 12 (1965) 3808-3810

(Kida 2011) Kida, T., Fenner, L. A., Dee, A. A., et al. "*The giant anomalous Hall effect in the ferromagnet Fe_3Sn_2-a frustrated kagome metal*", Journal of Physics-Condensed Matter. **23** 11 (2011) 112205

(Kittel 1946) Kittel, C. "*Theory of the structure of ferromagnetic domains in films and small particles*", Physical Review. **70** 11-1 (1946) 965-971

(Kittel 1986) Kittel, C. "*Introduction to solid state physics*". New York, Wiley (1986)

(Kou 1997) Kou, X. C., Dahlgren, M., Grössinger, R., et al. "*Spin-reorientation transition in nano-, micro- and single-crystalline $Nd_2Fe_{14}B$*", Journal of Applied Physics. **81** 8 (1997) 4428-4430

(Kuz'min 2010) Kuz'min, M. D., Givord, D. and Skumryev, V. "*Why the iron magnetization in $Gd_2Fe_{14}B$ and the spontaneous magnetization of $Y_2Fe_{14}B$ depend on temperature differently*", Journal of Applied Physics. **107** 11 (2010) 113924

(Kuz'min 2015) Kuz'min, M. D., Skokov, K. P., Radulov, I., et al. "*Magnetic anisotropy of La_2Co_7*", Journal of Applied Physics. **118** 5 (2015) 053905

(Kuz'min 2005) Kuz'min, M. D. "*Shape of Temperature Dependence of Spontaneous Magnetization of Ferromagnets: Quantitative Analysis*", Physical Review Letters. **94** 10 (2005) 107204

(Kuz'min 2014) Kuz'min, M. D., Skokov, K. P., Jian, H., et al. "*Towards high-performance permanent magnets without rare earths*", Journal of Physics: Condensed Matter. **26** 6 (2014) 064205

(Landau 1935) Landau, D. L., E. "*On the theory of the dispersion of magnetic permeability in ferromagnetic bodies*", Phys. Z. Sowjetunion. **8** 153 (1935)

(Langer 1975) Langer, J. and Sekerka, R. "*Theory of departure from local equilibrium at the interface of a two-phase diffusion couple*", Acta Metallurgica. **23** 10 (1975) 1225-1237

(Le Bail 2005) Le Bail, A. "*Whole powder pattern decomposition methods and applications: A retrospection*", Powder Diffraction. **20** 4 (2005) 316-326

(Le Caer 1979) Le Caer, G., Malaman, B., Haggstrom, L., et al. "*Magnetic-properties of Fe_3Sn_2 .3. Sn-119 mossbauer study*", Journal of Physics F-Metal Physics. **9** 9 (1979) 1905-1919

(Leineweber 2004) Leineweber, A. "*Variation of the crystal structures of incommensurate LT'-$Ni_{1+delta}Sn$ (delta=0.35, 0.38, 0.41) and commensurate LT-$Ni_{1+delta}Sn$ (delta=0.47, 0.50) with composition and annealing temperature*", Journal of Solid State Chemistry. **177** 4-5 (2004) 1197-1212

(Li 2020) Li, A.-h., Xi, L.-l., Feng, H.-b., et al. "*Development of Ce-based sintered magnets: review and prospect*", J. Iron Steel Res. Int. **27** (2020) 1-11

(Li 2016) Li, Z.-b., Zhang, M., Shen, B.-g., et al. "*Variations of phase constitution and magnetic properties with Ce content in Ce-Fe-B permanent magnets*", Materials Letters. **172** (2016) 102-104

(Li 2020) Li, Z., Liu, W., Chen, H., et al. "*Effect of inhibiting $CeFe_2$ on grain boundary diffusion of Ce/La-Ce containing Nd-Fe-B magnets*", Materials Letters. **261** (2020) 127017

(Li 2015) Li, Z., Liu, W. Q., Zha, S. S., et al. "*Effects of Ce substitution on the microstructures and intrinsic magnetic properties of Nd-Fe-B alloy*", Journal of Magnetism and Magnetic Materials. **393** (2015) 551-554

(Li 2015) Li, Z. B., Shen, B. G., Zhang, M., et al. "*Substitution of Ce for Nd in preparing $R_2Fe_{14}B$ nanocrystalline magnets*", Journal of Alloys and Compounds. **628** (2015) 325-328

(Liao 2020) Liao, S., Ding, G., Zheng, B., et al. "*Influences of element distribution on the magnetic properties in the (PrNd)–(YCe)–Fe–B sintered magnets*", Journal of Magnetism and Magnetic Materials. **497** (2020) 165901

(Lin 2020) Lin, Z.-Z. and Chen, X. "*Tunable Massive Dirac Fermions in Ferromagnetic Fe_3Sn_2 Kagome Lattice*", Phys. Status Solidi RRL. **14** 5 (2020) 1900705

(Lüdtke 2001) Lüdtke, A. "*Reaction crucible analysis and magnetic domain structures*". PhD thesis, The University of Birmingham (2001)

(Lüdtke 2000) Lüdtke, A., Stahl, B., Harris, I. R., et al. "*Relationships in the Fe-Nd/Sm/Pr-B Phase Diagrams determined by Iron Crucible Reaction Analysis (ICRA)*", Proceedings of the 16th International Workshop on Rare-Earth Magnets and their Applications, Japan Institute of Metals. (2000)

(Lyakhova 2017) Lyakhova, M. B. and Zhdanova, O. V. "*Analysis of Magnetization Curves and Magnetocrystalline Anisotropy of Uniaxial Ferromagnets*", Metal Science and Heat Treatment. **58** 9-10 (2017) 587-593

(Lyubina 2008) Lyubina, J., Gutfleisch, O., Kuz'min, M. D., et al. "*$La(Fe,Si)_{13}$-based magnetic refrigerants obtained by novel processing routes*", Journal of Magnetism and Magnetic Materials. **320** 18 (2008) 2252-2258

(Maier 2007) Maier, W. F., Stowe, K. and Sieg, S. "*Combinatorial and high-throughput materials science*", Angewandte Chemie-International Edition. **46** 32 (2007) 6016-6067

(Malaman 1978) Malaman, B., Lecaer, G. and Fruchart, D. "*Magnetic-properties of Fe_3Sn_2 .2. Neutron-diffraction study*", Journal of Physics F-Metal Physics. **8** 11 (1978) 2389-2399

(Malfliet 2008) Malfliet, A., Cacciamani, G. and Lebrun, N. R., P. "*Boron - Iron - Neodymium. Landolt-Börnstein- Ternary Alloy Systems*", Springer. **11, Subvolume D** (2008)

(Mancheri 2019) Mancheri, N. A., Sprecher, B., Bailey, G., et al. "*Effect of Chinese policies on rare earth supply chain resilience*", Resources, Conservation and Recycling. **142** (2019) 101-112

(Matyunina 2018) Matyunina, M., Zagrebin, M., Sokolovskiy, V., et al. "*Phase diagram of magnetostrictive Fe-Ga alloys: insights from theory and experiment*", Phase Transitions. (2018) 1-16

(Morgunov 2016) Morgunov, R. B., Kunitsyna, E. I., Kucheryaev, V. V., et al. "*Giant effect of Sm atoms on time stability of (NdDy)(FeCo)B magnet*", The European Physical Journal Plus. **131** 9 (2016) 344-350

(Müller 2001) Müller, G. and Rudolph, P. "*Crystal Growth from the Melt*". Oxford, Elsevier (2001)

(Mushnikov 2007) Mushnikov, N. V., Terent'ev, P. B., Rosenfel'd. "*Magnetic anisotropy of the $Nd_2Fe_{14}B$ compound and its hydride $Nd_2Fe_{14}BH_4$*", The Physics of Metals and Metallography. **103** 1 (2007) 39-50

(Niarchos 2015) Niarchos, D., Giannopoulos, G., Gjoka, M., et al. "*Toward Rare-Earth-Free Permanent Magnets: A Combinatorial Approach Exploiting the Possibilities of Modeling, Shape Anisotropy in Elongated Nanoparticles, and Combinatorial Thin-Film Approach*", JOM. **67** 6 (2015) 1318-1328

(O'Neill 2019) O'Neill, C. D., Wills, A. S. and Huxley, A. D. "*Possible topological contribution to the anomalous Hall effect of the noncollinear ferromagnet Fe_3Sn_2*", Physical Review B. **100** 17 (2019) 174420

(Okamoto 1999) Okamoto, H. "*Fe-Sb (Iron-Antimony)*", Journal of Phase Equilibria. **20** 2 (1999) 166-167

(Orimoloye 2018) Orimoloye, K., Ryan, D. H., Pinkerton, F. E., et al. "*Intrinsic Magnetic Properties of $Ce_2Fe_{14}B$ Modified by Al, Ni, or Si*", Applied Sciences. **8** 2 (2018) 205

(Pareti 1986) Pareti, L., Bolzoni, F., Leccabue, F., et al. "*Magnetic-anisotropy of MnAl and MnAlC permanent-magnet materials*", Journal of Applied Physics. **59** 11 (1986) 3824-3828

(Pareti 1988) Pareti, L., Moze, O. and Fruchart, D. "*Effect of Hydrogen Absorption on the 3d and 4f Anisotropies in $RE_2Fe_{14}B$ (RE = Y, Nd, Ho, Tm)*", J. Less-Common Met. **142** (1988) 187-194

(Pathak 2016) Pathak, A. K., Gschneidner, K. A., Khan, M., et al. "*High performance Nd-Fe-B permanent magnets without critical elements*", Journal of Alloys and Compounds. **668** (2016) 80-86

(Pathak 2016) Pathak, A. K., Khan, M., Gschneidner, K. A., et al. "*Magnetic properties of bulk, and rapidly solidified nanostructured $(Nd_{1-x}\ Ce_x)_2Fe_{14-y}Co_yB$ ribbons*", Acta Materialia. **103** (2016) 211-216

(Pathak 2015) Pathak, A. K., Khan, M., Gschneidner, K. A., et al. "*Cerium: An Unlikely Replacement of Dysprosium in High Performance Nd-Fe-B Permanent Magnets*", Advanced Materials. **27** 16 (2015) 2663-2667

(Pereiro 2015) Pereiro, M., Yudin, D., Chico, J., et al. "*Topological excitations in a kagome magnet*", Nature Communications. **5** (2015) 4815

(Petricek 2014) Petricek, V., Dusek, M. and Palatinus, L. "*Crystallographic Computing System JANA2006: General features*", Zeitschrift Fur Kristallographie. **229** 5 (2014) 345-352

(Petruschke 1985) Petruschke, M. "*Tribochemistry. von G. HEINICKE. Berlin: Akademie-Verlag 1984. Bestellnummer: 7631993(6746). 495 S., 329 Bilder, 106 Tabellen, 98,– M*", Acta Polym. **36** 7 (1985) 400-401

(Poenaru 2019) Poenaru, I., Lixandru, A., Riegg, S., et al. "*Ce and La as substitutes for Nd in $Nd_2Fe_{14}B$-based melt-spun alloys and hot-deformed magnets: a comparison of structural and magnetic properties*", Journal of Magnetism and Magnetic Materials. **478** (2019) 198-205

(Potyrailo 2011) Potyrailo, R., Rajan, K., Stoewe, K., et al. "*Combinatorial and High-Throughput Screening of Materials Libraries: Review of State of the Art*", Acs Combinatorial Science. **13** 6 (2011) 579-633

(Predel 1995) Predel, B. "*Fe-Ge (Iron-Germanium)*", Datasheet from Landolt-Börnstein - Group IV Physical Chemistry. **5E** (1995)

(Predel 2013) Predel, B. "*Fe-Si (Iron-Silicon)*", Datasheet from Landolt-Börnstein - Group IV Physical Chemistry. **12C** (2013)

(Raghavan 2001) Raghavan, V. "*Fe-Sb-Sn (iron-antimony-tin)*", Journal of Phase Equilibria. **22** 6 (2001) 669

(Ram 1992) Ram, S. and Joubert, J. C. "*Production of substantially stable Nd-Fe-B hydride (magnetic) powders using chemical dissociation of water*". **61** 5 (1992) 613-615

(Rietveld 1969) Rietveld, H. M. "*A profile refinement method for nuclear and magnetic structures*", Journal of Applied Crystallography. **2** (1969) 65-71

(Rodríguez-Carvajal 1993) Rodríguez-Carvajal, J. "*Recent advances in magnetic structure determination by neutron powder diffraction*", Physica B: Condensed Matter. **192** 1–2 (1993) 55-69

(Sagawa 1985) Sagawa, M., Fujimura, S., Yamamoto, H., et al. "*Magnetic properties of rare-earth-iron-boron permanent magnet materials*", Journal of Applied Physics. **57** 8 (1985) 4094-4096

(Sagawa 1987) Sagawa, M., Hirosawa, S., Tokuhara, K., et al. "*Dependence of coercivity on the anisotropy-field in the $Nd_2Fe_{14}B$-type sintered magnets*", Journal of Applied Physics. **61** 8 (1987) 3559-3561

(Sagawa 1987) Sagawa, M., Hirosawa, S., Yamamoto, H., et al. "*Nd-Fe-B permanent magnet materials*", Japanese Journal of Applied Physics Part 1-Regular Papers Brief Communications & Review Papers. **26** 6 (1987) 785-800

(Sales 2014) Sales, B. C., Saparov, B., McGuire, M. A., et al. "*Ferromagnetism of Fe_3Sn and Alloys*", Scientific Reports. **4** (2014) 7024

(Sepehri-Amin 2018) Sepehri-Amin, H., Hirosawa, S. and Hono, K. "*Chapter 4: Advances in Nd-Fe-B Based Permanent Magnets*", Elsevier **27** (2018)

(Shatynski 1976) Shatynski, S., Hirth, J. and Rapp, R. "*A theory of multiphase binary diffusion*", Acta Metallurgica. **24** 12 (1976) 1071-1078

(Simon 2019) Simon, D. "*Development and Assessment of Rare Earth-lean Th_1Mn_{12}-Phases for the Use in Permanent Magnets*", PhD thesis. (2019)

(Skokov 2018) Skokov, K. P. and Gutfleisch, O. "*Heavy rare earth free, free rare earth and rare earth free magnets - Vision and reality*", Scripta Materialia. **154** (2018) 289-294

(Skomski 2009) Skomski, R. and Sellmyer, D. J. "*Anisotropy of rare-earth magnets*", Journal of Rare Earths. **27** 4 (2009) 675-679

(Soldatov 2017) Soldatov, I. V. and Schäfer, R. "*Selective sensitivity in Kerr microscopy*", Review of Scientific Instruments. **88** 7 (2017) 073701

(Spaldin 2010) Spaldin, N. A. "*Magnetic Materials: Fundamentals and Applications*". Cambridge, Cambridge University Press (2010)

(Stoner 1948) Stoner, E. D. and Wohlfarth, E. P. "*A mechanism of magnetic hysteresis in heterogeneous alloys*", Phil. Trans. R. Soc. London. **240** 826 (1948) 599-642

(Sucksmith 1954) Sucksmith, W. and Thompson, J. E. "*The magnetic anisotropy of cobalt*", Proceedings of the Royal Society of London. Series A. Mathematical and Physical Sciences. **225** 1162 (1954) 362-375

(Susner 2017) Susner, M. A., Conner, B. S., Saparov, B. I., et al. "*2 Flux growth and characterization of Ce-substituted $Nd_2Fe_{14}B$ single crystals*", Journal of Magnetism and Magnetic Materials. **434** (2017) 1-9

(Szymczak 1973) Szymczak, R. "*Observation of internal domain structure of barium ferrite in infrared*", Acta Phys. Polon. A. **43** (1973) 571-578

(Takeuchi 2003) Takeuchi, I., Famodu, O. O., Read, J. C., et al. "*Identification of novel compositions of ferromagnetic shape-memory alloys using composition spreads*", Nat Mater. **2** 3 (2003) 180-184

(Tang 1998) Tang, C. C., Zhan, W. S., Li, Y. X., et al. "*The effect of substitution by cerium on the structure and magnetic properties of the compound $NdFe_2$*", Journal of Physics D-Applied Physics. **31** 19 (1998) 2426-2430

(Tang 2019) Tang, X., Sepehri-Amin, H., Matsumoto, M., et al. "*Role of Co on the magnetic properties of Ce-substituted Nd-Fe-B hot-deformed magnets*", Acta Materialia. **175** (2019) 1-10

(Tang 2018) Tang, X., Sepehri-Amin, H., Ohkubo, T., et al. "*Coercivity enhancement of hot-deformed Ce-Fe-B magnets by grain boundary infiltration of Nd-Cu eutectic alloy*", Acta Materialia. **144** (2018) 884-895

(Thomas 1980) Thomas, R., Moulijn, J. A., Debeer, V. H. J., et al. "*Structure-metathesis activity relations of silica supported Molybdenum and Tungsten oxide*", Journal of Molecular Catalysis. **8** 1-3 (1980) 161-174

(Tokuhara 1985) Tokuhara, K., Ohtsu, Y., Ono, F., et al. "*Magnetization and torque measurements on $Nd_2Fe_{14}B$ single crystals*", Solid State Communications. **56** 4 (1985) 333-336

(Trehaux 1974) Trehaux, D. and Guiraldend, P. Scrypta metallurgica. **4** (1974) 363-366

(Trumpy 1970) Trumpy, G., Both, E., Djega-Mariadassou, C., et al. "*Mossbauer-effect studies of iron-tin alloys*", Physical Review B-Solid State. **2** 9 (1970) 3477-3490

(van Loo 1973) van Loo, F. J. J. and Rieck, G. D. "*Diffusion in the titanium-aluminium system—I. Interdiffusion between solid Al and Ti or Ti-Al alloys*", Acta Metallurgica. **21** 1 (1973) 61-71

(Vegard 1921) Vegard, L. "*Die Konstitution der Mischkristalle und die Raumfüllung der Atome*", Zeitschrift für Physik. **5** 1 (1921) 17-26

(Vekilova 2019) Vekilova, O. Y., Fayyazi, B., Skokov, K. P., et al. "*Tuning the magnetocrystalline anisotropy of Fe_3Sn by alloying*", Physical Review B. **99** 2 (2019) 024421

(Walker 1990) Walker, P. T., W. H. "*Handbook of Metal Etchants*". Bocs Raton, CRC Press (1990) 1241-1247

(Wang 2020) Wang, J., Wang, G. and Zeng, D. "*Coercivity and corrosion resistance enhancement of multi-main-phase Nd-Ce-Fe-B sintered magnets by the grain*

boundary diffusion process using $Pr_{81.5}Ga_{19.5}$ and $Pr_{81.5}Ga_{14.5}Cu_5$ alloys", Journal of Magnetism and Magnetic Materials. **503** (2020) 166639

(Wang 2016) Wang, Q., Sun, S. S., Zhang, X., et al. "*Anomalous Hall effect in a ferromagnetic Fe_3Sn_2 single crystal with a geometrically frustrated Fe bilayer kagome lattice*", Physical Review B. **94** 7 (2016) 075135

(Xiang 2002) Xiang, X. D. "*Mapping of physical properties–composition phase diagrams of complex material systems using continuous composition material chips*", Applied Surface Science. **189** 3–4 (2002) 188-195

(Xiang 1995) Xiang, X. D., Sun, X. D., Briceno, G., et al. "*A combinatorial approach to materials discovery*", Science. **268** 5218 (1995) 1738-1740

(Xiaodong 2016) Xiaodong, F., Guo, S., Chen, K., et al. "*Tuning Ce distribution for high performanced Nd-Ce-Fe-B sintered magnets*", Journal of Magnetism and Magnetic Materials. **419** (2016) 394-399

(Yamamoto 1966) Yamamoto, H. "*Mossbauer effect measurement of intermetallic compounds in iron-tin system - Fe_5Sn_3 and FeSn*", Journal of the Physical Society of Japan. **21** 6 (1966) 1058-1062

(Yan 2014) Yan, C. J., Guo, S., Chen, R. J., et al. "*Effect of Ce on the magnetic properties and microstructure of sintered Didymium-Fe-B magnets*", IEEE Transactions on Magnetics. **50** 10 (2014) 1-5

(Yang 2017) Yang, M. N., Wang, H., Hu, Y. F., et al. "*Increased coercivity for Nd-Fe-B melt spun ribbons with 20 at.% Ce addition: The role of compositional fluctuation and Ce valence state*", Journal of Alloys and Compounds. **710** (2017) 519-527

(Yang 1991) Yang, Y. C., Zhang, X. D., Ge, S. L., et al. "*Magnetic and crystallographic properties of novel Fe-rich rare-earth nitrides of the type $RTiFe_{11}N_1$-delta*", Journal of Applied Physics. **70** 10 (1991) 6001-6005

(Ye 2018) Ye, L. D., Kang, M. G., Liu, J. W., et al. "*Massive Dirac fermions in a ferromagnetic kagome metal*", Nature. **555** 7698 (2018) 638–642

(Zhang 2016) Zhang, X. F., Lan, J. T., Li, Z. B., et al. "*Abnormal variation of magnetic properties with Ce content in $(PrNdCe)_2Fe_{14}B$ sintered magnets prepared by dual alloy method*", Chinese Physics B. **25** 5 (2016) 057502

(Zhang 2017) Zhang, Y. J., Ma, T. Y., Jin, J. Y., et al. "*Effects of $REFe_2$ on microstructure and magnetic properties of Nd-Ce-Fe-B sintered magnets*", Acta Materialia. **128** (2017) 22-30

(Zhao 2001) Zhao, J. C. "*A combinatorial approach for efficient mapping of phase diagrams and properties*", Journal of Materials Research. **16** 6 (2001) 1565-1578

(Zhao 2004) Zhao, J. C. "*Reliability of the diffusion-multiple approach for phase diagram mapping*", Journal of Materials Science. **39** 12 (2004) 3913-3925

(Zhao 2006) Zhao, J. C. "*Combinatorial approaches as effective tools in the study of phase diagrams and composition-structure-property relationships*", Progress in Materials Science. **51** 5 (2006) 557-631

(Zhao 2017) Zhao, L., Yu, H., Guo, W., et al. "*Phase and Hyperfine Structures of Melt-spun Nanocrystalline* $(Ce_{1-x}Nd_x)_{16}Fe_{78}B_6$ *Alloys*", IEEE Transactions on Magnetics. **53** 11 (2017) 1-5

(Zhou 2020) Zhou, C., Pan, M., Wu, Q., et al. "*Improvement of magnetic properties for Ti doped Ce-Fe-B alloys: Effectively inhibiting* $CeFe_2$ *phase formation*", Journal of Magnetism and Magnetic Materials. **502** (2020) 166564

(Zhu 2014) Zhu, M. G., Li, W., Wang, J. D., et al. "*Influence of Ce Content on the Rectangularity of Demagnetization Curves and Magnetic Properties of Re-Fe-B Magnets Sintered by Double Main Phase Alloy Method*", IEEE Transactions on Magnetics. **50** 1 (2014) 1-4

Own publications and conference contributions

Publications:

- G. Gómez Eslava, **B. Fayyazi**, K. P. Skokov, Y. Skourski, D. Gorbunov, O. Gutfleisch, N. Dempsey und D. Givord. "*A-two sublattice model for extracting rare-earth anisotropy constants from measurement on (Nd,Ce)2(Fe,Co)14B single crystals*", Journal of Magnetism and Magnetic Materials. 520 (2021) 167470
- **B. Fayyazi**, K. P. Skokov, T. Faske, I. Opahle, M. Duerrschnabel, T. Helbig, I. Soldatov, U. Rohrmann, L. Molina-Luna, K. Güth, H. Zhang, W. Donner, R. Schäfer and O. Gutfleisch. "*Experimental and computational analysis of binary Fe-Sn ferromagnetic compounds*", Acta Materialia. 180 (2019) 126-140
- I. Poenaru, A. Lixandru, S. Riegg, **B. Fayyazi**, A. Taubel, K. Güth, R. Gauss and O. Gutfleisch, O. "*Ce and La as substitutes for Nd in $Nd_2Fe_{14}B$-based melt-spun alloys and hot-deformed magnets: a comparison of structural and magnetic properties*", Journal of Magnetism and Magnetic Materials. 478 (2019) 198-205
- O. Vekilova, **B. Fayyazi**, K. P. Skokov, O. Gutfleisch, C. Echevarria-Bonet, J. M. Barandiaran, A. Kovacs, J. Fischbacher, T. Schrefl, O. Eriksson and H. C. Herper. "*Tuning magnetocrystalline anisotropy of Fe_3Sn by alloying*", Physical Review B. 99 (2019) 024421
- **B. Fayyazi**, K. P. Skokov, T. Faske, D. Karpenkov and O. Gutfleisch. "*Bulk combinatorial analysis for searching new rare-earth free permanent magnets: Reactive crucible melting applied to the Fe-Sn binary system*", Acta Materialia. 141 (2017) 437-443

Conference paper:

- **B. Fayyazi**, K. P. Skokov, K. Löwe, C.A. Schwöbel, O. Gutfleisch. "*The Intrinsic and extrinsic magnetic properties of $(Nd,Ce)_2(Fe,Co)_{14}B$: From single crystals to sintered permanent magnets*", Proceedings of REPM Conference, Darmstadt (2016) 113-117

Conferences:

- MMA'19: Magnetic Materials and Application, UK magnetic society workshop, 2019, Milan, Italy "*Fabrication of novel permanent magnets with high coercivity- highlights of EU project NOVAMAG"* (invited talk), **B. Fayyazi**, NOVAMAG consortium
- The 25th International Workshop on Rare-Earth and Future Permanent Magnets and Their Applications (REPM, Beijing, China, "*Fe-Sn as a candidate system for magnetic applications - from high-throughput methods to single crystals"* (talk), **B. Fayyazi**, T. Faske, M. Duerrschnabel, K. P. Skokov, O. Gutfleisch
- 82th Annual Conference of the DPG, 2018, Berlin, Germany, "*The structural and magnetic properties of Fe-Sn ferromagnetic compounds"* (Poster), **B. Fayyazi**, K. P. Skokov, T. Faske, O. Gutfleisch
- IEEE International Magnetics Confernece, Intermag, Dublin, Ireland, "*Ce substituted rare earth balance magnets, magnetocrystalline anisotropy vs. coercivity"* (Poster), **B. Fayyazi**, K. P. Skokov, O. Gutfleisch
- 81th Annual Conference of the DPG, 2017, Dresden, Germany, "*Reliability of bulk combinatorial reactive crucible melting approach to search for new permanent* magnets: *a Fe-Sn case study"* (Talk), **B. Fayyazi**, K. P. Skokov, D. Karpenkov, O. Gutfleisch
- The 24th International Workshop on Rare-Earth and Future Permanent Magnets and Their Applications (REPM), 2016, Darmstadt, Germany, "*The intrinsic and extrinsic magnetic properties of $(Nd,Ce)_2(Fe,Co)_{14}B$: From single crystals to sintered permanent magnets"* (Talk), **B. Fayyazi**, O, T. Faske and O. Gutfleisch
- 8th Joint European Magnetic symposia (JEMS), 2016, Glasgow, UK, "*Bulk combinatorial analysis for searching new rare-earth-free permanent magnet: Reactive crucible melting approach"* (Talk), B. Fayyazi, K. P. Skokov, D. Karpenkov, O. Gutfleisch
- 80th Annual Conference of the DPG, 2016, Regensburg, Germany, "*Magnetocrystalline anisotropy of the $(Nd,Ce)_2(Fe,Co)_{14}B$ single crystals"* (Talk), **B. Fayyazi**, K. P. Skokov, C. Schwoebel, K. Loewe, O. Gutfleisch
- 13th Joint MMM-Intermag Conference, 2016, San Diego, US, "*Magnetocrystalline anisotropy of $(Nd,Ce)_2$ $(Fe,Co)_{14}B$ single crystals"* (Talk), K. P. Skokov, **B. Fayyazi**, C. Schwoebel, K. Loewe, O. Gutfleisch
- 6th international Conference on Magnetic Refrigeration, Thermag, 2014, Victoria, BC Canada, "*Adiabatic Temperature Change in $LaPr(FeSi)_{13}$ and their hydrides"* (Talk), B. Kaeswurm, **B. Fayyazi**, O. Gutfleisch

Acknowledgement

First of all, I would like to thank Prof. Dr. Oliver Gutfleisch for the opportunity he gave me to carry on my research and writing my PhD thesis in his group Functional Materials at TU Darmstadt. Throughout my research, he provided valuable guidance and feedback which I gratefully acknowledge. I would like to thank him also for supporting my short-term visit in the university of Delaware and my participation to many beneficial conferences.

I also want to gratefully acknowledge Prof. George Hadjipanayis, who kindly agreed to co- referee my thesis. I met Prof. Hadjipanayis six years ago and he was the one who actually encouraged me to enter the field of magnetism and introduced me to Prof. Gutfleisch. He also gave me the opportunity to join his group as a guest scientist and profit from his great supervision and guidance.

I would like to express my sincere gratitude to Dr. Konstantin Skokov who has always provided excellent supervision and discussion. His experience and endless knowledge were of great help specially in growing single crystals and handling and characterizing these tiny beauties.

My gratitude also extends to the rest of the Functional Materials group for their constant support throughout the 4 years. For sure, there were no place other than FM for me in Germany where I felt like home. I would like to specially thank Semih Ener, Leopold Diop and Konrad Löwe for scientific discussions and helps in various areas, Tim Helbig for MFM measurement and Imants Dirba for XRD measurements. Also, many thanks to my beloved colleagues, Dimitri Benke, Franziska Staab, Lukas Pfeuffer, Lukas Schäfer and Fernando Maccari for their continuous support during writing my thesis and everyone else who helped to make this work possible. I appreciate every second of those who stopped by 109 to share positive energy.

I also acknowledge Dr. Alex Gabay for teaching me the mechanochemical method, Tom Faske for extensive XRD measurements, Michael Dürrschnabel for TEM characterization, Urban Rohrmann for FIB preparation, Ivan Soldatov for Kerr analysis, as well as Ingo Opahle, Gabriel Gómez Eslava and Olga Vekilova for theoretical calculations.

The same goes to the funding source, NOVAMAG project, under Grant Agreement No. 686056, EU Horizon 2020.

I owe thanks to a very special person, my husband, Morteza for his continued and unfailing love, support and understanding during my pursuit of PhD degree that made the completion of thesis possible. I thank my family especially my brother Ali for being always supportive and inspiring.